STATUS AND PERSPECTIVES OF THE FRENCH CRG-IF INTERFACE BEAMLINE BM32

REPORT FOR THE BEAMLINE REVIEW PANEL OF MAY 2020

November 2020

M. De Santis, O. Geaymond, L. Martinelli, J.-S. Micha, G. Renaud,

F. Rieutord, O. Robach, S. Tardif, O. Ulrich

Table des matières

1 Overview: history, role and impact of the beamline

The French CRG Interface (IF) Beam Line (BM 32) is dedicated to study the physics and chemistry of surfaces, interfaces, thin films and nanostructures and to investigate the mechanical properties at the micron scale. It was one of the first beamlines at the ESRF available to users, in 1994. It first held three monochromatic-beam experimental stations that were used alternatively, one equipped with a multipurpose goniometer (GMT), one dedicated to X-ray absorption spectroscopy (XAS) experiments, and one devoted to surface X-ray diffraction in ultra-high vacuum (UHV) called SUV (Surfaces under Vacuum). In 2000, the XAS station moved to a new, dedicated beamline BM30B (CRG-FAME), and SUV evolved toward INS (In situ Nanostructures on Surfaces), more oriented toward studying nanostructures. In 2006, the beamline optics was completely refurbished with two vertically focusing mirrors in addition to a two crystals sagittal focusing monochromator. A white beam microfocus configuration, producing a sub-micrometric beam in the GMT hutch, was added. In parallel, a micro-diffraction setup was developed (hereafter called µLaue).

The goniometer of the **GMT** station has three main characteristics, which makes it unique for some investigations. The goniometer is very accessible and versatile, so that many different scattering experiments can be performed, bulk or surface sensitive, with the sample surface either horizontal or vertical. Different sample environments such as a cryostat and a small vacuum chamber are available. Several others have already been used: magnet and cold finger, Langmuir trough, dilution fridge etc... The advantages of the IF beamline are the very clean X-ray beam with low background, and the possibility to work with hard X-rays (energies up to 30 keV), which is necessary for studies of interfaces between dense materials (liquid/liquid,liquid/solid or solid/solid). Because of its very versatile design, the GMT instrument is a user-oriented facility that fits the needs of a wide community. The research on the GMT diffractometer has been balanced between studies of « hard » and « soft » condensed matter.

The new **µLaue** instrument for Laue microdiffraction added in 2006, is used in alternance with the GMT goniometer in the same hutch (EH2). This setup is similar to the ones developed at APS by G.E. Ice, and at ALS by N. Tamura. To date, few comparable dedicated and operational stations exist worldwide: 2 in US (34-ID-E @ APS, BL12-3-2 @ ALS) 1 in Canada (VESPERS 07B2-1 @ CLS), and 1 in Taiwan (21A @ TPS). On BM32, a white (5-23 keV) microbeam (0.5x0.5 µm2) impinges on the surface of the polycrystalline sample, under an angle of 40°. A 2D plane detector is usually mounted on top of the sample in reflection geometry for most of the experiments. For poorly crystallized materials measurements can be carried out in transmission geometry but necessitate anticipated relatively heavy setup change. By scanning the sample, the recorded laue patterns can be analysed to provide routinely a 2D map of local orientation and deviatoric strain (angular unit cell deformation). Extensions of the standard Laue technique are being developed such as (1) to get access to all unit cell lattice parameters or equivalently the full strain tensor by means of Laue spot energy experimental measurements, (2) to locate in 3D the origin of scattering signal by depth resolved measurements from Differential Aperture X-ray Microscopy (DAXM). Materials and

Nano sciences are the main scientific fields covered by the studies with the µLaue instrument with both fundamental and applied aspects.

Finally, The INS2 endstation is based on a UHV diffractometer devoted to Surface X-Ray Diffraction (SXRD), Grazing Incidence X-ray Scattering at wide (GIXS) and Small (GISAXS) angles and X-ray reflectivity and possibly Surface X-ray Absorption Spectroscopy (S-XAS) on surfaces and interfaces, and during thin film and nanoparticle growth. More recently this set-up was also used for resonant x-ray diffraction experiments (RXD), taking advantage of the easy energy tunability of the beam line optics. The main advantages of INS2 with respect to other existing stations are the possibility to perform in situ deposition with up to seven sources in the X-ray chamber, as well as a very good RHEED system and Auger analysis under grazing incidence, which can be operated simultaneously with x-ray measurements during deposition or annealing. In addition to physical evaporation, an injector has been recently added opening the world of chemical vapor deposition (CVD) under ultra-high vacuum, also called Chemical Beam Epitaxy (CBE). This instrument has been completely refurbished in 2016 thanks to a funding from French government (Equipex).

With these three instruments, the beamline has a large impact in the French research community in nanoscience. In addition, these instruments serve each year as a support for practicals and tutorials dedicated to students during their Master at the local Grenoble University, and for HERCULES (the Higher European Research Course for Users of Large Experimental Facilities) students. The local team is then involved in the corresponding teaching. Note also that practicals on Laue techniques were organized within the CNRS training framework, on the µLaue instrument.

2 Organization, committees

The IF CRG beamline is part of a program established in 1991 by the two French research agencies: CNRS (Centre National de la Recherche Scientifique) and CEA (Commissariat à l'Energie Atomique et aux Energies Alternatives). Two CRG beamlines - IF and D2AM (BM02) – have been operational since 1994. A third beamline had a split radiation fan with one branch –FIP- (BM30A) operational since 1999, and the second branch equipped with the FAME beamline (BM30B). More recently a new spectroscopic beamline FAME-UHD opened in 2016. Due to the adaptation on the new source EBS lattice, FIP beamline moved to BM07 and FAME has now the BM30 port for itself. A CRG/French Council with representatives of the two agencies is responsible for financial, personnel and scientific policy of the entire program. The program is executed locally by a "structure d'exploitation" regrouping the three Department Head of "Institut Néel (CNRS)", "Service Modélisation et Exploration des Matériaux" (IRIG CEA-Grenoble) and "Institut de Biologie Structurale" (joint CEA-CNRS lab.), all established at Grenoble. The personnel working on the beam lines are employed by these local laboratories. As a consequence the concept of in-house research is slightly different from the one at ESRF. The beamline and instrument scientists perform research programs of their own laboratory in addition to assistance to external users selected by program committees. The facilities of the three labs (infrastructure, workshop, design, secretary...) act as a support since CRGs are not eligible to use the similar facilities of the ESRF.

Almost 25% of the total available beamtime is reserved for upgrade, maintenance and in-house research. One third of the remaining beam time is due to the European community, and is allocated by European committees through the usual application for beam time at the ESRF. The 2/3 of remaining beam time is open to the entire French community, and is allocated on the basis of merit of experiment proposals by the SOLEIL committees, twice a year, as for the ESRF beamtime. The available user beam time is calculated applying the rules observed at ESRF: time is reserved for in-house research (IHR), buffer between experiments and maintenance. Note that scientific staff often apply for beamitme like any users to pursue their research.

[section intentionally removed]

Similarly, at the same funding institution we have already submitted the MAGNIFIX project which should be in the process of evaluation. Description of MAGNIFIX is given in the perspectives section.

3 Beamline Optics

The configuration for the optics is of a classical layout where entrance slits are followed by a 3 optical element group (first mirror, monochromator and second mirror) in charge of X-ray white beam processing, and finally exit slits. To achieve a good harmonic rejection, both mirrors work at variable incidence, therefore adjusting cut-off energy to working energy. A good energy resolution is reached thanks to the first mirror that collimates the beam for the monochromator. The second mirror vertically focuses the beam either on the sample (normal mode) or on a micrometric 2-directions slit system located at the end of the optical hutch (pink micro-focus mode) and acting as a secondary source. The INS diffractometer needs a fixed beam vertical position. Therefore, the monochromator crystal gap is adapted to compensate for the vertical offset given by the variable angle of the mirrors.

The first mirror M1 is made of a single crystalline 1.3 m long Si bar, coated with 500Å Ir exhibiting a 3Å roughness, a slope error of 1.5 µrad rms on the full length, and only 1 µrad rms on the 300 mm central area. This mirror can be bent up to 5 km radius in order to vertically collimate the divergent beam from our bending magnet onto the first crystal of the monochromator. The cooling system consists in water circulation in copper blades, dipping in liquid InGaN ternary alloy placed in two channels dug on both sides of the Si bar, thus avoiding transmission of vibrations to the mirror. The maximal allowed thermal power for this mirror is 580W, corresponding to a ring current of 500mA.

The second mirror M2 is identical to the first, except for the absence of the cooling system and a higher maximum curvature (radius down to 2.5km) to allow vertical focusing on the micrometric slit.

The monochromator is a double crystal (DCM) Si(111) type with the whole optical block under vacuum. The rotation stage is equipped with a high resolution encoder to achieve 0.35 µrad resolution. It is mounted on a translation stage to follow the beam reflected from the first mirror when the incidence angle is adjusted to select the cut-off energy. The rotation stage carries the first and second crystal assembly.

The first crystal assembly is a 10mm thick Si crystal with an optimized shape allowing a drastic reduction of the thermal meridional bump [1]. It is glued on a copper plate cooled by water circulation. The roll of this plate can be adjusted by a piezo actuator to achieve a correction of the horizontal position of the beam against thermal drifts arising from ring current decrease (if needed before EBS).

The second crystal assembly is the standard Si ribs crystal mounted on an ESRF-CNRS bender type and is used for the sagittal focusing. The bender assembly can be moved by three rotations (weak links): two for crystal roll and yaw and one for the two crystals parallelism (pitch). This latter movement is finely adjusted by a piezo actuator to achieve automatic intensity maximization, thus compensating drifts as in [2]. Moreover, the bender is carried by two crossed translations: one adjusting the gap between the crystals and the second adjusting the shift between crystals along the beam propagation axis.

In pink microbeam mode, the mirrors M1 and M2 are working under a fixed 4mrad incidence angle (cut-off energy > 23 keV), the gap between the monochromator's crystals is opened to let the beam outgoing from the M1 mirror pass through the monochromator directly onto mirror M2 and the pink beam is vertically focused onto the micrometric slit. As the main scientific goals are to measure 2D-maps of grain orientation and deformation in thin polycrystalline materials with a lateral resolution of 0.5 µm, we have to take up 2 major challenges: achieve a pink microbeam of size 0.5x0.5µm2 and have it stabilized to better than 0.2µm.

To deliver the pink microbeam, a classical Kirkpatrick-Baez (KB hereafter) achromatic microfocusing device, composed of 2 fixed-curvature elliptic perpendicular mirrors, is used. The KB mirrors are Pt-coated (now Rh) and work under a fixed incidence angle of 2.9mrad (cut-off energy > 30keV, now 23 keV), the first KB mirror being 290 mm long and the second 140 mm. The KB works under real object / image condition by demagnifying the micrometric slit. The demagnification factor is simply the ratio between object distance and image distance. Therefore, the KB is brought as far as possible from the micrometric slit and as close as possible to the sample, leading to demagnification ratio in the vertical plane of 145 and 45 in the horizontal plane. Moreover, since beam spot size increases with the level of beamline mirror polishing slope errors or mirror bending defects, the slope errors of the mirrors M1 and M2 on their central 300mm are below 1µrad, and the KB mirror slope errors are lower than 0.2 µrad on full length.

For controlling and tuning the optics, specific software has been written, either at low level to support special device controllers, or at high level to have a user friendly and easily adjustable beamline. A feedback system was developed for automated tuning of the second crystal of the monochromator to maximize the flux and compensate for the long term drifts [2].

References

[1] J.S. Micha et al, Nucl. Instrum. Meth. A A 710, 155-160 (2013)
[2] O. Proux et al, J. Synch. Rad. 13 (2006) 59-68

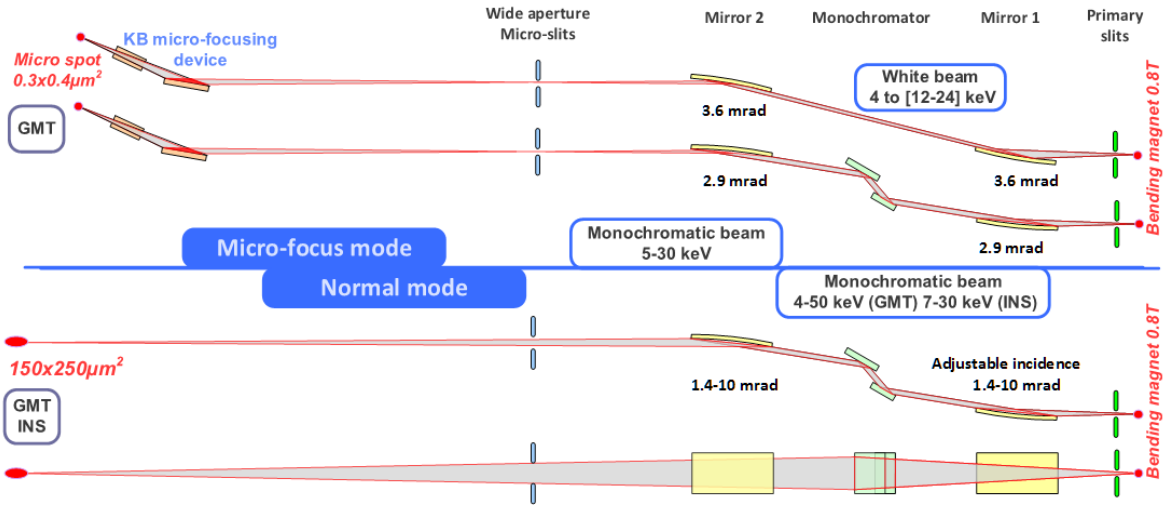

Figure 1: Schematic representation of the two configurations of the optical elements, mirrors and monochromator, providing either a sub-millimetric monochromatic beam of high energy resolution (the normal mode) or a sub-micronic beam that may be either white or monochromatic in the so-called micro-focus mode.

4 List of beamline staff, functions and scientific interest

[section intentionally removed]

5 Instrumentation and Techniques

5.1 The Laue Microdiffraction setup (µLaue)

The large demand for structural characterization of objects with ever decreasing sizes has driven the development of new methods to determine not only the average internal structure but also the local structure at submicron scale. Probing the local strain, shape (size, orientation) and composition of micro and nano materials is the main objective of our Laue micro-diffraction setup. This dedicated setup is unique in Europe. Such instrument takes full profit from the white beam source of bending magnets.

Two fixed-curvature elliptical KB mirrors are used to achieve a sub-micronic (hxv) =0.3x0.3 µm^2 white beam with a X-ray energy range of 5 to 23 keV (adjustable) up to 2018. Now (sept. 2020) thanks to EBS and new Rh-coated KBs: **(hxv) =0.2x0.2 µm^2 and energy band 5-22 keV**. A typical Laue pattern on a thick grain (>5µm) requires less than 0.5s counting time. Larger counting times are needed for low Z materials, smaller grains (< 0.5 µm), and grains with large orientation gradients (> 10 mrad/µm).

Selected regions of interest on the sample surface can be finely aligned on the x-ray beam by means of an optical microscope featuring a 50X objective and a 12X zoom, low depth of focus (< 1 µm) and high lateral resolution (0.3µm). In addition, x-ray fluorescence mapping can be used for locating micro-markers on the sample when the microscope is retracted.

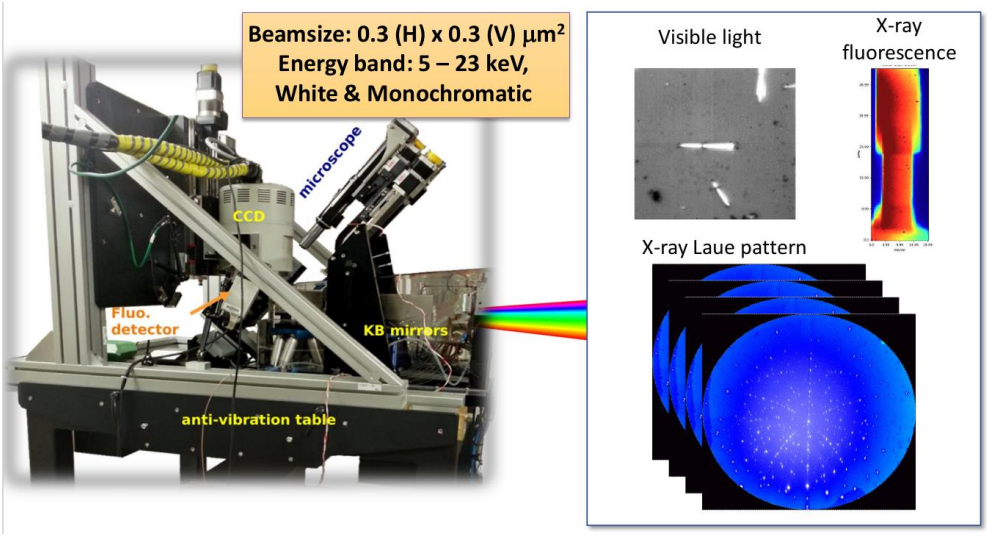

Figure 3. Laue Microscopy is based on the collection of Laue pattern of scattered beams coming from white and microsized beam sample illumination. Beam properties correspond to the 2015-2018 period.

The spot positions in the Laue pattern can be monitored as a function of time to detect *in situ* phase transitions, crystal deformation or reorientation. The mapping of the spots positions as a function of beam position on sample helps to localize regions where stresses or defects concentrate, e.g. after sample elaboration or after applying a load.

At a higher level of analysis, each single Laue pattern once indexed fully determines the grain orientation (3 Euler angles) and the deviatoric shape of the unit cell (i.e. b/a, c/a,). Large orientation maps (figure 3) built from a raster sample scan then provide e.g. the local texture and the relative strain levels of between grains of different orientations. Such maps also allow selecting particular grains for fine intra-grain mapping of orientation and strain gradients. Complementary methods for spot energy measurements (monochromator, energy dispersive detector, transmission Diamond monochromator) may then be used for local full strain tensor or line profile analysis. Moreover, 3D scan are now available thanks to optimized DAXM technique and new numerical algorithms developed on the beamline last years.

A home-developed open source software suite, *LaueTools*, facilitates the data analysis by means of several Graphical User Interfaces, scripts and jupyter-notebooks. During the experimental run, its online treatment tools help to choose the best data collection strategy. After the experiment its fast parallel computing modules allow the automatic analysis of several thousands of images.

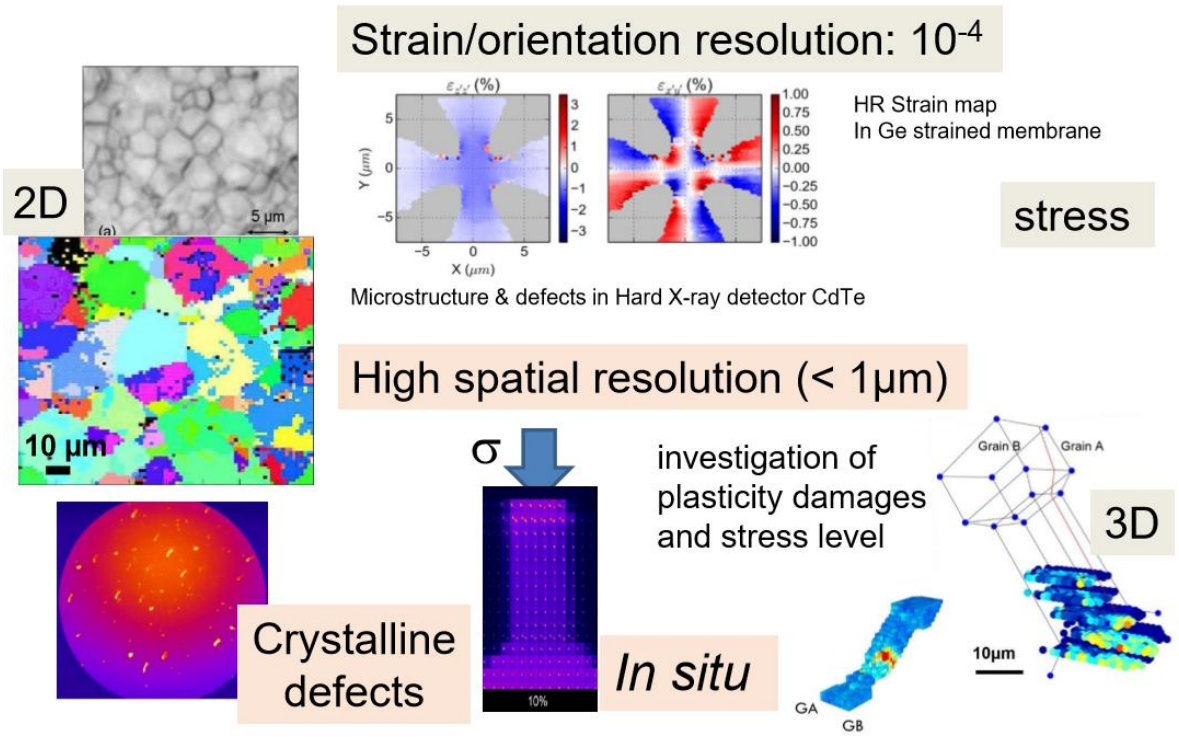

Figure 4. Laue Microscopy provides local structural parameters (orientation, strain and stress tensor) with high resolution on mono- and poly-crystals by 2D or 3D mapping. In situ experiments can be carried in various conditions.

Applications of this instrument are mostly in Materials Science: energy-related materials (Solid-oxide fuel cells, nuclear fuels, photovoltaic cells), complex integrated circuits from the

micro-electronics industry (2D and 3D interconnects), structural materials (superalloys for turbine blades, and other metallurgical compounds), biology-related materials (wood, tooth, nacre) for orientation and texture aspects. More fundamental studies include *in situ* mechanical testing on model macro, micro or nano objects (FIB-machined metallic micro-pillars, nanowires, whiskers, bi-crystals, tri-crystals), in view of improving the description of the mechanical properties of polycrystals or micro and nano objects in elastic or plastic regime (peak shape analysis).

5.2 The In situ Nanostructures and Surfaces (INS2) endstation

The INS station is devoted to studies of surfaces, interfaces, nanostructures and thin films in Ultra High Vacuum, in particular during their growth, by means of three techniques using hard X-rays: Grazing Incidence X-ray Scattering (GIXS, which here is generic for SXRD, GID, GIXRD etc…), Grazing Incidence Small Angle X-Ray Scattering (GISAXS), and X-ray Reflectivity (XR). In the recent years, a gas injector allowing for the injection of dangerous gases (silane, germane, H2S …) has been added to the existing MBE (up to seven sources) possibilities. The core diffractometer and UHV chamber has been completely renewed during the last years, thanks to a French Equipex.

These “Equipexs” were about 250 projects funded by the French government within its “Investments of Excellence” initiative, to develop or renew research platforms opened to the French research community. Basically the INS2 project, launched in 2012, consisted in completely rebuilding the instrument with a new faster and heavy-duty diffractometer coupled to a new larger UHV chamber equipped with Be windows (Fig. 5). It became operational during the year 2016, and was opened to external users for the two remaining years (2017 and 2018) before the ESRF shutdown.

Like the previous instrument, the new INS2 one is dedicated to *in situ* studies of the growth and structure of nanometric films, particles, nanowires or new 2D material, possibly *operando* and in real time, using diffusion/diffraction of hard X-rays. The growth is achieved using a combination of techniques including molecular beam epitaxy (MBE) and chemical vapor deposition (CVD). X-ray measurements allow, among other things, structural studies on the atomic scale by grazing incidence scattering at large angles (GIXS/GIXD/SXRD/XRR) and morphological studies on the scale of a few nanometers or tens of nanometers, by scattering at small angles in grazing incidence (GISAXS). The GIXS and GISAXS techniques can be used simultaneously in real time.

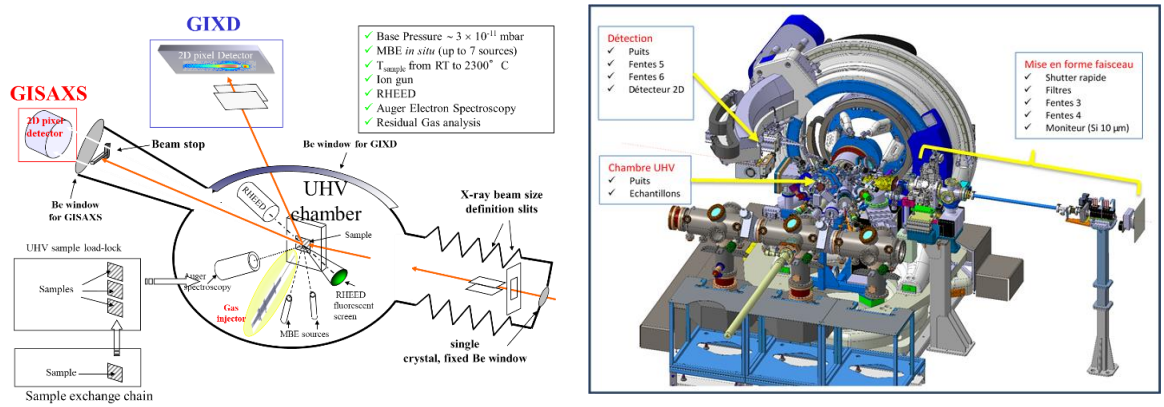

Fig. 5. Left: Schematic drawing of the principles of the INS2 setup, see text. Right: The CAD representation of the whole setup; see text for description

Compared to the previous instrument, INS2 can move the sample or the detectors 10 to 100 times faster, making it possible to study the nucleation/growth processes of quantum dots or 2D films or nanowires on a more relevant time scale. It also allows more structural and / or morphological information to be collected simultaneously by recording maps of the reciprocal space using fast 2D detectors. Finally, all these studies can be carried out under much better and more complex conditions.

The UHV chamber is designed as a hybrid system. First, it allows “classic” ultra-vacuum studies including heating up to high temperatures (1500°C standard; up to 2350°C with a special, non-transferable sample mount), ion bombardments, Auger electron spectroscopy and Reflection High Energy Electron Diffraction measurements, as well as measure of partial pressures of residual gases or of gases injected into the chamber. Second, it also accepts samples that are transferred from other processing chambers equipped with 1-inch Moly-block, thanks to two specific UHV transfer suitcases. Third it can be used to grow different nanomaterials by MBE or by CVD or by combining the two growth methods. A large number of evaporation sources are available, either of the "Knudsen" type or of the electron bombardment type. More than 8 can be simultaneously mounted on the chamber. A very specific injector associated with a versatile and secure gas distribution system is available for the CVD. Nitrogen and hydrogen plasma sources as well as a large source of silicon are also available. This chamber is fitted with a large number of flanges of different diameters and easily accessible, making it possible to envisage very varied configurations, rarely available on similar instruments.

The goniometer and the chamber were designed entirely in 3D CAD (Fig. 5) and are therefore perfectly integrated. The goniometer was produced by the *Symétrie* company. It comprises a basic rotation around a vertical axis making it possible to define the angle between the beam and the surface of the sample, kept vertical. This rotation moves the entire diffractometer. In addition to this, the detector can be positioned on a portion of a sphere by two other rotations, and the sample can rotate around the perpendicular to its surface, after it has been aligned using a hexapod. All these movements are very fast (up to 20 °/s), precise (better than 0.0005 °) and controlled by encoders. The detectors use hybrid pixel technology: Maxipix 5x1 for

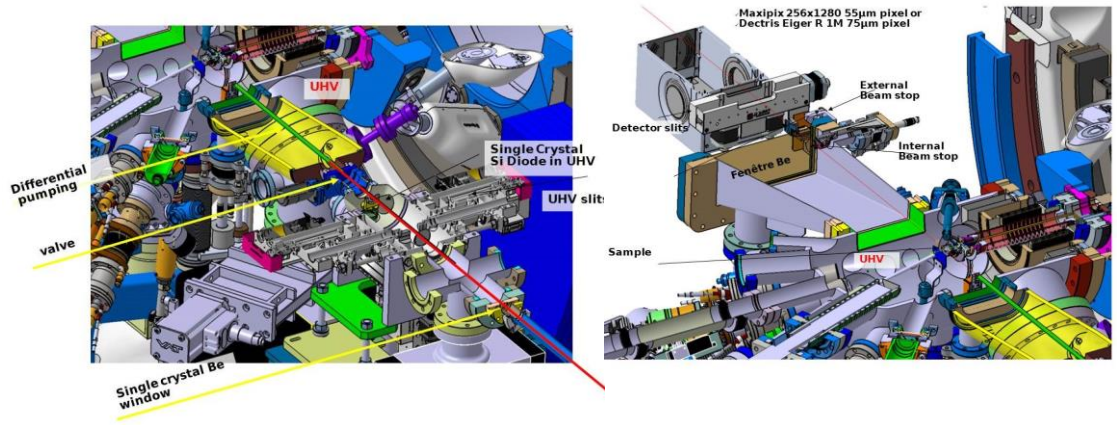

Fig. 6: Inside of the UHV chamber detailing the sample, sample holder, furnace, and inside slits and beam-stops, together with the wide rectangular exit Be window for low delta angles

diffraction and Eiger 1M for GISAXS. The circle supporting the hexapod is mounted on a large vertical axis that allows removing it from the inside of the circle in order to easily access the chamber *via* its large flange for instrument mounting and maintenance.

A specific feature of the INS instrument developed over the years were in-UHV slits, knife edge and beam stops that allowed minimizing the unwanted background scattered by all elements put in the beam prior to the sample. This was further developed in this new version (see Fig. 5 left) by using a fixed (as opposed to moving before) Be window about 3 meters before the sample. In addition, this Be windows is single-crystalline, and thus does not yield any background scattering (except for Bragg peaks that are out of the beam).

The use of two pairs of in vacuum slits before the monitor and of a single crystalline Si diode monitor (Fig. 5 right) help further minimizing the background. Finally, the large rotation of the whole instrument to define the incident angle chamber rotation over a wide range (-1 to 20°) is allowed by a large oval bellows. The remaining background is further suppressed thanks to slits, knife-edge and beam stops inside UHV that are precisely aligned thanks to UHV piezoelectric translation tables (Fig. 6). The large chamber beryllium window is made of a big cylindrical part as before, but, again, the background from the exit beam is suppressed by replacing the part of the Be window crossing the exit direct beam by a flat Be window that is 500 mm farther, just before the 2D detectors (for GIXD or for GISAXS). This has been developed at the expense of a complexification of the detector slits, since the anti-scattering slit is placed on a translation to move it out when measuring close to the direct beam. Altogether, these features provide really background free (except that coming from the sample) measurements, both at low and high angles, which is hard to achieve with this geometry except when using an extremely small beam such as from ID beamlines.

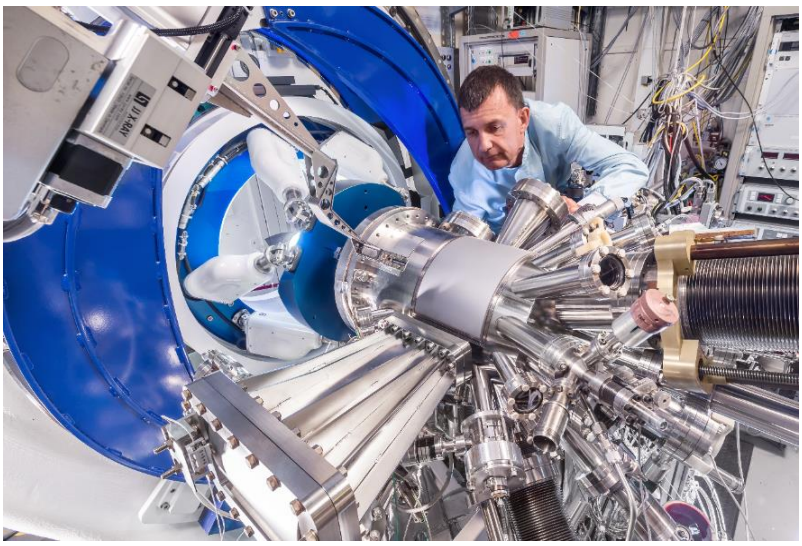

The sample holder is a long rod in UHV ended by the sample heater at one end, and by a CF63 mounting flange at the other end. This flange is connected to a differentially pumped rotary feedthrough, itself connected to a large, heavy duty hexapod in air for a 6-degrees of freedom sample alignment on the one end, and to a large bellows connected to the main chamber, that accommodate for these sample motions, on the other end. The hexapod allows for three perpendicular ±5° $_1$ and rotations of 0.001° accuracy and three X,Y,Z translations of m accuracy. All the other rotary motions have 0.005° absolute accuracy, lower than 0.001° resolution; axes parallel or perpendicular within 0.001°, and a sphere of confusion of 60 µm for the sample motions and 100 µm for the detector ones. The (±200°) sample rotation and the detector (-15°, +126°) rotation can reach speeds of 20°/s, and the out of plane detector rotation (-1, 45°) reaches 10°/s. The rotation defining the incident angle can be moved between -1 and 20°, without disconnecting the chamber from the Modutrack introduction system, thanks to a long bellows in between.

On the exit side, a large, rectangular flange mounted on the chamber let the beam travel toward a large, rectangular Be window placed 500 mm away from the sample. A T-shape beam stop is placed in UHV just before this exit Be windows (plus another one just after), allowing to stop the direct and reflected beams before they are scattered by the exit window. The low-angles lost in detector angle delta (from -1 to 12 degrees) because the hemispherical Be windows has to be discontinued to be allowed for this, is recovered on the negative side through the large rectangular Be window.

The detector arm holds a fully motorized slit placed just before the detector, which may be either a Maxipix 5x1 or an Eiger 1M R pixel detector, and a detector slit is placed as close as possible to the Be windows of the main chamber at large δ angles, and moved away for delta δ angles smaller than 12°. The slit opening is defined by the rotation of 2 parallel tungsten rolls around and axis perpendicular to the beam.

For its two years of use, the INS2 setup has proved to be perfectly adapted to a number of experiments performed either by the internal team or by external users. Among these studies, one may cite the growth of high quality oxide layers and their detailed quantitative structural determination by SXRD; the demonstration of organized growth of preformed FePt clusters when deposited on the moiré induced by the deposition of graphene on Ir(111) surfaces; the characterization of many different 2DMaterials like Te-based transition metals dichalcogenides like $MoTe_2$, $ZrTe_2$, $HfTe_2$,$TiTe_2$ etc…; the *in situ* growth of MoS_2 on Au111 using the injector to inject H_2S gas and the intercalation of Cs below it; the substitution of Se by S in $PtSe_2$ TMDCs leading to Janus type SPtSe etc.

5.3 The Multitechnique goniometer (GMT)

The MultiTechnique Goniometer GMT is a general purpose 2+2 axis surface diffractometer, well suited to most grazing incidence scattering techniques (GIXS, XRR, GISAXS). It is normally dedicated to samples elaborated ex-situ but it can also accommodate a wide range of sample environments due to the large open space available around the goniometer center. It has been used during the last years for solid/solid, solid/liquid and solid/air surface and interface studies, mostly using X-ray energies between 20 and 30 keV.

As opposed to the INS setup, the experiments taking place on GMT do not usually request lengthy surface preparations ahead of the beamtime. It is therefore located upstream of the INS endstation, sharing a hutch and alternatively using the beam with the µLaue setup while the INS setup is preparing samples or baking out.

Thanks to the large volume accessible at the sample position, the instrument can accommodate a large variety of sample environments, ranging from small enclosures (e.g. electrochemical cells) to a large UHV system with two chambers devoted to in-situ studies of catalytic processes. The goniometer can also handle vibration filtering tables for liquid surface studies, helium cryostats, magnets, and a variety of furnaces. The first µLaue experiments were actually run using the goniometer as a support for both focusing and sample movement elements, while the 2D detector was mounted on the detector arm.

The instrument has been used in the last years mainly for the study of buried interfaces *e.g.* liquid/solid or solid/solid interfaces. We make use of the 20-30 keV energy range of our bending magnet to access the interfaces, going through one side of the interface (*i.e.* one of the phases) over its whole width.

We have automated as much as possible sample changing. For solid/solid interfaces for example, samples are piled up and automatic alignment routines have been developed so as to be able to study series of about 20 samples. Routines for automatic data inversion (*e.g.* reflectivity data) have been developed in parallel.

The instrument has received little evolutions during the last 4 years. Its mechanics is still accurate enough and efforts have been put on developing or replacing the other beamline instruments. Only part of the motors electronics has been upgraded, *e.g.* with the installation of ESRF icepap controllers for detector slits motors.

More recently, we have started to use 2D pixel detectors for diffraction experiments. We use a 5-chip 256*1280 silicon pixel detector that can be mounted in both orientations regarding its long direction (generally along CTR direction, depending on sample orientation). The detector has been used for instance to record diffraction patterns from artificial gratings. Due to their small pixel size, low noise and high counting rates, these detectors are interesting and may speed up the acquisition of reciprocal space maps. Recent reports from SOLEIL have shown for example how to use low-diverging beams and 2D detectors to speed up reflectivity measurements [Mocuta *et al.*, J. Synchrotron Rad. (2018). **25**, 204-213]. However, the poor efficiency of Si pixel detectors limits their usage for the medium high energy experiments. We expect this limitation to be removed with today's availability of CdTe pixel detectors. Tests

have already been made and a small size pixel CdTe detector (Maxipix) has been acquired just before the EBS shutdown.

Many of the experiments performed on GMT have a link with applied research subjects. We have worked on the physics of several steps of the SmartCut™ technology developed at the CEA-Grenoble and its spin-off company SOITEC. In particular we investigate the ion implantation, wafer direct bonding and fracture. Other subjects of technological interest have been addressed, like SEI (Solid Electrolyte Interphase) formation at the interface between electrode and electrolyte in Li batteries. Strain (GID, RSM) and size measurements (SAXS, GISAXS) on microelectronics systems patterned using state-of-the-art lithography have also been recently performed to develop the Critical Dimension SAXS (CDSAXS) technique.

5.4 Detectors on BM32

On BM32 we have a large choice of detectors to cover a wide range of techniques. These are commercially available detectors. In some cases, integration and developments were necessary to control these detectors with the standard control system, previously SPEC and in a very near future BLISS, which will be the standard for next few years. These developments consist in electronics and software, in order to best match the experimental requirements of our 3 instruments.

For beam monitoring and data normalisation we are using standard silicon diodes, either in transmission or measuring scattered signals. The high accuracy electronic transforms the analogue value into pulses that are integrated by the counting cards. We are also using a 4-channel picoammeter to monitor the beam, and a lock in amplifier to make a feedback on the second crystal of the monochromator and keep the flux at its maximum value whatever the power load on the optics.

On the experiment side we have detectors, from the basic zero dimension detector, to two dimensions CCD or sCMOS and pixel detectors.

5.4.1 0D detector for diffraction:

The standard photomultiplier with NaI scintillator is still in use on GMT diffractometer behind slits that defines the analysis direction. Coupled to these detectors we also have an automatic filter system used to avoid detector saturation and to extend the dynamics of the detection chain. This kind of detecting is being replaced by a CdTe pixel detector.

In experiments that require high energy resolution we have a Rontec Si drift detector. This detector has a typical energy resolution of 250 eV at a counting rate up to 400 kcps with a 5mm2 detection area. It is mainly used on the microdiffraction experimental setup to monitor the fluorescence signal from the sample, either to build fluorescence maps or simply to locate on sample. We also acquired a second detector of this type, a Ketek XR-SDD read with a XIA electronics. The energy resolution is 125 eV at 5.6 keV and the throughput of 100kcp/s

5.4.2 2D detectors:

- CCDs

We have many CCD detectors with various input size, pixels number and size, sensitivity, readout speed. Detector choice is done by users and its local contact in order to best match the experiment requirements.

The QuadRo CCD detector from Princeton Instrument has not been repaired because the CCD chip was not available anymore. So, to make experiments we used a MAR CCD 165 camera (now Rayonix) and acquire a new sCMOS camera. This camera from Photonic Science is a quad camera with a 165mm input field. It has a readout time 20 times shorter than the MAR CCD. This was a real improvement on micro laue setup. To replace the MAR CCD, which is still our backup detector, we also bought a ImageStar 165. It's a wide input field 36 Mpixel sCMOS camera with a 0.5s readout time.

All CCD detectors are fully supported in the standard acquisition system. Some use ESRF software developments, others have required special developments by the BM32 team because they are not supported at ESRF or very specific features or control modes are required.

Other CCD detectors, VHR or ImageStar are still occasionally used to make alignments or calibration.

Detector model	**Input size (mm^2)**	**Nb Pixels**	**Pixel size (µm)**	**Readout Time (s)** (no binning)	**Readout Time (s)** binning 2x2	**Dyna-mic (bits)**	**Dyna-mic range (dB)**	**Features /comments**	**Instrumen t**
MAR 165 CCD	Φ 165	4 Mpixel	80	2.5		16	86		µLaue
sCMOS quad	Φ 165	16 Mpixel	40	0.25	0.1	16	79	On line image correction and rois integration	µLaue
sCMOS ImageStar 165	Φ 165	36 Mpixel	27.5	0.1	0.025	16	70	To be delivered in August 2020	µLaue
VHR CCD	Φ 81	7 Mpixel	30	1.2/2.4	0.3/0.6	12/16	70	Electronic shutter, Antiblooming x1000, pipeline readout mode, possibility to extend	µLaue

								dynamic up to 20 bits	
ImageStar CCD	square 67x67	9 Mpixel	22	2.5	0.6	16	82	Antiblooming x100	µlaue /GMT /INS

- Pixel detectors

Two 1280x256 (5x1 modules giving 70.4x14.08 mm2 detection area) Maxipix pixel detector are used on INS2 instruments. With a 55 μm^2 pixel size a 500 µm Si thickness, and 6.10^7 Xph/mm^2/s at 20% non-linerity, this detector is used for diffraction at energies under 25 keV, which cover 95% of experiments on INS2.

For GISAXS measurements on INS2 which requires large input field and very low noise we have a Dectris 1 Mpixel Eiger detector with a 77x77mm2 input size and a 75μm^2 pixel size. With 450µm thickness Si pixels, the count rate is up 22.10^7 Xph/mm^2/s at 20% non-linearity and a frame rate of 10 images/s.

On GMT, which can operate efficient experiments at 27 keV we bought in 2018 a 512x512 Maxipix CdTe detector to have a greater detection efficiency.

5.5 Data Acquisition & Analysis

Basic data analysis during the acquisition relies on ESRF tools such as PyMCA (formerly newplot) with the 3 instruments. Also 4 techniques are widely used on the beamline. For three of them in monochromatic mode, software exist and some are still improving. Then general GISAXS data are treated with isGISAXS (GUI developed by R Lazzari in Fortran when he was post-doc on the beamline) and surface diffraction one with PyROD (GUI based on rod written in python by T. Zhou during his phD on the beamline). For reflectivity curves several softwares are available for users for electronic density profile model fitting. For Laue diffraction a complete package LaueTools has been developed since 2009. Hosted on gitlab.esrf.fr, written in python, numerous modules allow to handle laue patterns images to extract structural parameters. LaueTools is open-source has gathered several functionalities requested by users for a decade such as GUIs and scripts, and more recently jupyter notebooks that call core computation (simulation, refinement) modules. It aims at favoring the learning curve of the analysis of Laue diffraction data set made of several 10000 images and amounted 5 To per campaign (6 days).

LaueTools Suite Software for Laue microdiffraction data analysis

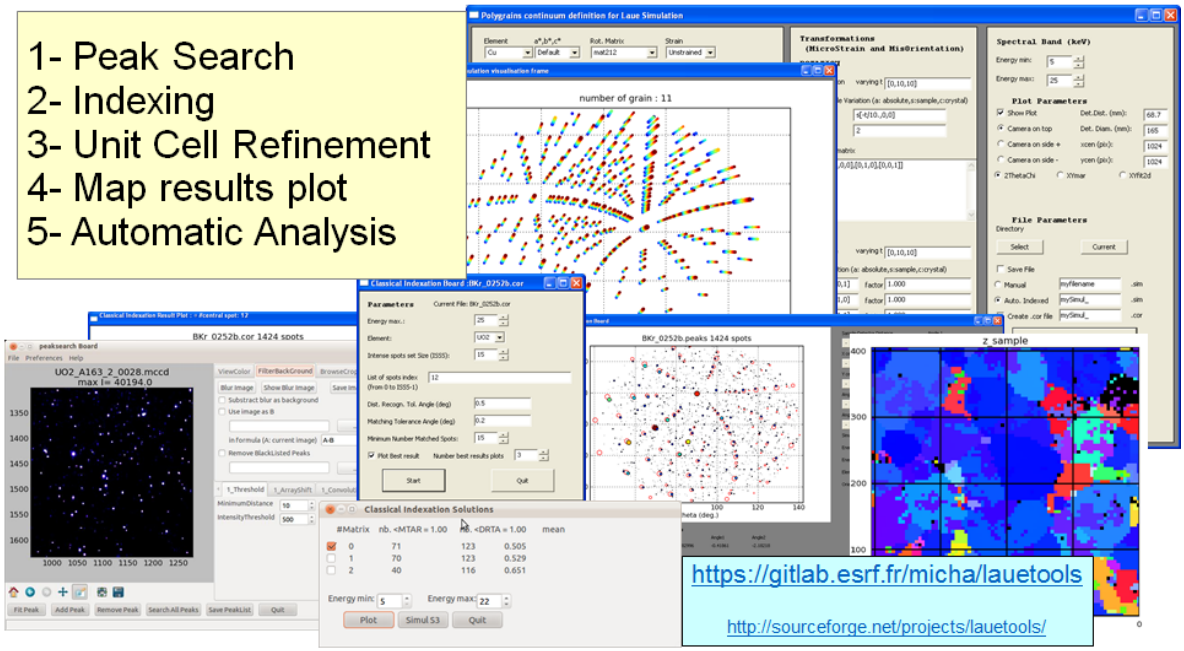

Started in 2009, LaueTools is a Home developed software package dedicated to microdiffraction Laue pattern images analysis (GUI, modules, scripts). More recently jupyter-notebooks lying on Lauetools core modules are provided to help users in handling images data set collected on the beamline.

6 Example of Scientific Research and Highlights

In the next pages a selection of scientific highlights on the three instruments for the period 2015-2020 is presented (3 highlights by instruments):

µLaue

HL1*: In situ* Laue microdiffraction experiments (Research in Collaboration)

HL2: 3D X-Ray Laue Microscopy (Research in Collaboration + beamline scientists)

HL3: Energy-resolved Laue microdiffraction (Research in Collaboration + beamline scientists)

GMT

HL4: Fluids in nanoconfinement (Research in Collaboration)

HL5: Solid/solid wafer bonding interfaces (Research of beamline scientists)

HL6: Energy storage materials (Research of beamline scientists)

INS

HL7: 2D Topological Semimetals Grown by Molecular Beam Epitaxy (Research in Collaboration + of beamline scientists)

HL8: Structure and chemical order in ultrathin films by resonant x-ray scattering (Research in Collaboration + of beamline scientists)

HL9: Atomic structure of ultrathin film solved by surface x-ray diffraction (Research in Collaboration +of beamline scientists)

6.1 HL1 In situ Laue microdiffraction experiments

The µLaue setup offers the possibility to carry out from simple (ex situ, single shot) to complex (in situ, 3D map). To meet the users needs the last five years have been devoted to the improvement of *in situ* experiments (eg following the scattering signal with time or as a function of an external load, such as temperature, electrical current or mechanical load), 3D mapping of microstructure and energy measurements. Significant achievements have been obtained in terms of acquisition time, data reliability and their visualisation & analysis.Note that there is a growing demand on measuring small crystals orientation prior to Bragg Coherent Diffraction Imaging experiments performed elsewhere (ID01@ESRF or at APS).

6.1.1 Example 1: Three-point bending behavior of a Au nanowire studied by in-situ Laue microdiffraction

T.W. Cornelius[1], Z. Ren[1], C. Leclere[1], F. Lauraux[1], A. Davydok[1], G. Richter[2], O. Thomas[1]

1 CNRS, IM2NP, Aix Marseille Univ., Univ. de Toulon, Marseille, France
2 Max Planck Institute for Intelligent Systems, Stuttgart, Germany

In the recent past the mechanical properties of nanostructures attracted enormous attention. Micro-compression testing on focused ion beam milled metal micropillars revealed an increasing yield strength with decreasing structure size, a tendency that became known in literature as “smaller is stronger”. These ultra-high yield strengths allow for deforming nano-objects to very high strains without inducing plasticity offering completely new opportunities for elastic strain engineering of physical properties. Since these pioneering works, the research focus moved to defect scarce nanostructures to better understand the nucleation and storage of the first defects and dislocations generated at ultra-high yield strengths of several GPa relaxing the elastic strain.

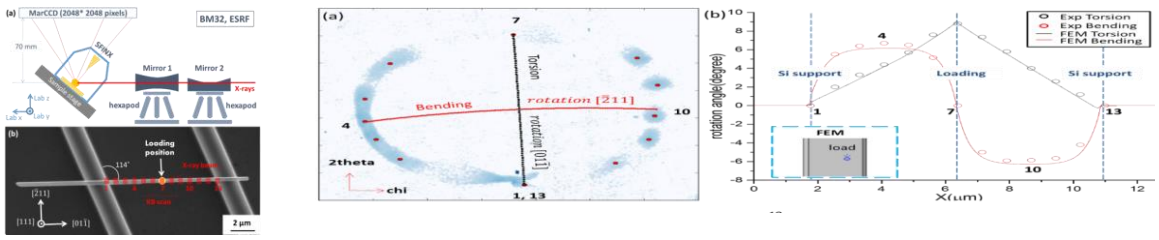

Fig. H1-1: (a) Schematic diagram of experimental configuration at BM32. (b) Scanning electron microscopy image of a self-suspended Au nanowire before deformation. The measurement positions along the nanowire during KB scans are marked by rectangles and the scanning direction is indicated by the arrow. (c) Enlarged view of the area around the Au 222 diffraction peak. The expected movements of the Laue spot on the detector for a pure vertical bending (rotation around Au direction) and a pure torsion (rotation around Au direction) are marked as red and black lines, respectively. (d) Bending and torsion profile along the suspended part of the nanowire inferred from the integrated Laue micro-diffraction pattern shown in (c) and calculated by finite element method simulations taking into account a force of 2.1 µN and a misalignment of the SFINX-tip with respect to the nanowire center of 57 nm [4].

Within the last decade, various in-situ nano-mechanical testing devices were developed allowing for applying the mechanical load and simultaneously visualizing the deformation of

the nanostructures by scanning electron microscopy, transmission electron microscopy, or synchrotron X-ray diffraction techniques. White beam Laue microdiffraction is highly sensitive to the crystalline orientation and defects such as geometrically necessary dislocations (GNDs). Thanks to the polychromaticity of the incident X-ray beam a multitude of diffraction spots can be measured simultaneously without any rotation of the sample in contrast to monochromatic X-ray diffraction where the incident angle and diffraction angle have to be adjusted for each Bragg reflection. This fact makes Laue microdiffraction very attractive for *in-situ* experiments, in particular, for *in-situ* micro- and nano-mechanical studies where every additional movement should be avoided for circumventing the generation of detrimental vibrations. Because of these constraints, typical *in-situ* experiments are performed with the focused X-ray beam illuminating a single spot of the sample, thus limiting the obtained information to one position on the structure under study. In order to map the deformation of a mechanically loaded nanostructure, the MNO group at IM2NP (Marseille) developed a novel method that allows for scanning the X-ray beam across the sample surface, similar to the electron beam in a SEM, by translating the Kirkpatrick-Baez (KB) mirrors used for focusing the incident polychromatic X-ray beam in the horizontal and vertical direction [1].

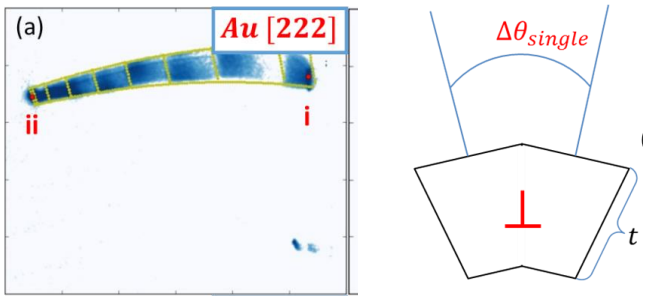

Fig. H1-2: a) Integrated diffraction patterns of the Au 222 Laue spot. The yellow lines mark the expected peak shapes generated by linearly combining rotations around the Au [2$\bar{1}$1] and the Au [121$\bar{]}$ axes. b) Schematic illustration of the lattice rotation induced by a single edge dislocation.

This same group recently developed a scanning force microscope that is compatible with Laue microdiffraction end-stations at the BM32 beamline [2]. While most nano-mechanical studies concentrate on uniaxial tensile and compression tests, we performed three-point bending experiments on suspended nanowires providing access to the flexure behaviour of the nanostructures which is of major importance for actual applications like flexible electronics [3].

A schematic of the experimental setup and a scanning electron microscope image of a gold nanowire suspended across silicon micro-trenches are presented in Fig. H1-1(a) and (b), respectively. The position where the mechanical load was applied by the AFM-tip is highlighted in the SEM images as well as the measurement positions along the nanowire where the KB scanning approach was used to displace the beam focus. During the loading of the nanowire, the Laue spots move on the detector. An integrated Laue microdiffraction pattern of the Au 222 Laue spot recorded along the mechanically loaded nanowire is displayed in Fig. H1-1(c) [1]. While pure bending results in a vertical movement of the Laue spot on the detector pure torsion leads to a horizontal spot displacement. The circular Laue spot movement indicates the presence of both bending and torsion of the nanowire which was confirmed by finite element method simulations considering a misalignment of the loading point of about 60 nm with respect to the center of the nanowire width generating the necessary torque.

For plastically deformed nanowires, the analysis of the Laue peak shapes (Fig. H1-2(a)) eventually allows for determining the activated slip systems and the number of geometrically necessary dislocations (GNDs) stored in the volume probed by the focused X-ray beam. GNDs actually induce a rotation of the crystal (as schematically shown in Fig. 2(b)) which translates to a broadening of the diffraction spot where the direction of the broadening is directly related to one of the 12 slip systems existing for FCC materials and the amount of broadening is

related to the number of GNDs. This analysis revealed that a maximum of 15 and 6 type GNDs is found close to the clamping point and the number of stored dislocations steadily decreases towards the loading position.

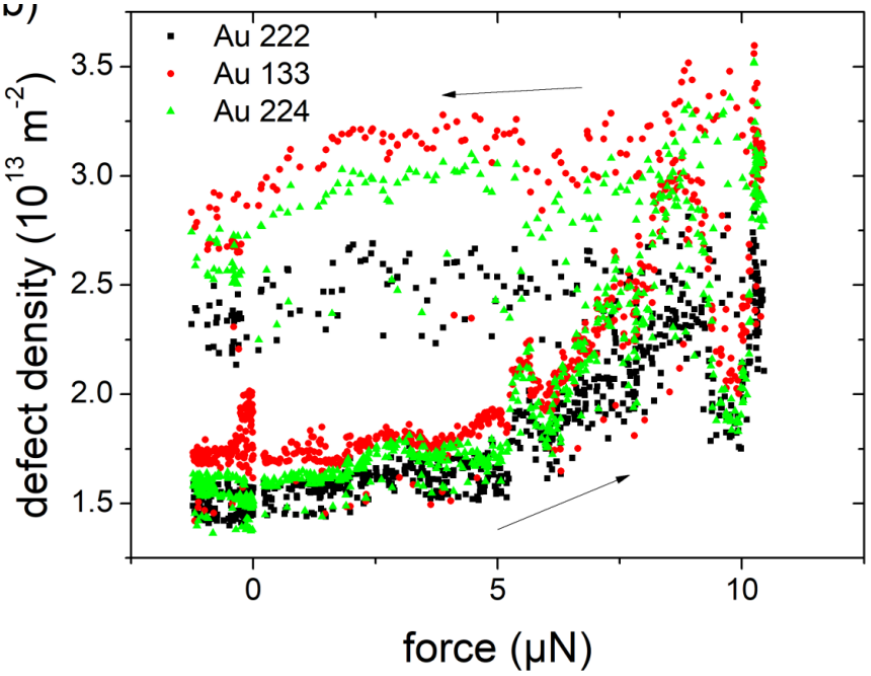

Fig. H1-3: Dislocation density in the indented Au crystal as a function of the applied force inferred from the elongation of the Au 222, Au 133, and Au 224 Laue spot.

Presently, the developed *in-situ* AFM does not allow for directly measuring the applied force due to the lack of the measurement of the deflection of the AFM cantilever, which is usually done by an optical laser feedback system in commercial AFMs. However, the MNO group recently developed a novel method to determine the deflection of the Si cantilever *in-situ* by Laue microdiffraction [1]. Thanks to a PhotonScience detector which bases on CMOS technology and which has a much lower noise level than the previous MarCCD detector, the researchers are actually able to measure the Laue diffraction spots originating from the Si cantilever and to determine the cantilever bending from the displacement of the Laue spots on the detector. They obtain force resolutions of better than 90 nN. These new developments represent a major step forward to actual nano-mechanical tests measuring both stress and strain at the same time. As an example of the capabilities offered by this new approach the MNO group performed *in-situ* nano-indentation experiments on single Au nano-crystals. Fig. H1-3 shows the GND density as a function of the applied force determined from the streaking of the Au Laue spots and from the displacement of the Si spots from the cantilever on the detector screen, respectively.

References

1 C. Leclere et al, J. Synchrotron Radiat. ***23*** *(2016) 1395 – 1400*
2 Z. Ren et al, J. Synchrotron Radiat. ***21*** *(2014) 1128 – 1133*
3 C. Leclere et al, J. Appl. Cryst. ***48*** *(2015) 291 – 296*
4 Z. Ren et al, J. Appl. Phys. ***124*** *(2018) 185104*
5 F. Lauraux et al, In-situ force measurement during nano-indentation combined with Laue microdiffraction, submitted to Nano Select (under review)

6.1.2 Example 2: First implementation of combined XEOL and µLaue measurements

J. Eymery, O. Ulrich, J.-S. Micha, O. Robach
Univ. Grenoble Alpes, CEA-INAC, F-38000 Grenoble, France

X-ray excited optical luminescence (XEOL) allows getting information on the intrinsic optical properties of materials. Up to now, this technique has been mainly combined with fluorescence and XANES spectroscopy to get composition and chemical environment mappings. For the first time in the world, we combined XEOL with the µLaue structural analysis on the French CRG-IF BM32@ESRF beamline taking advantages to recording a diffraction pattern *without aligning the sample* and measuring at the same time the optical emission. For good emitting crystals, only a few second counting time is needed. The exposure for structural and optical analyses are therefore very similar enabling fast scanning.

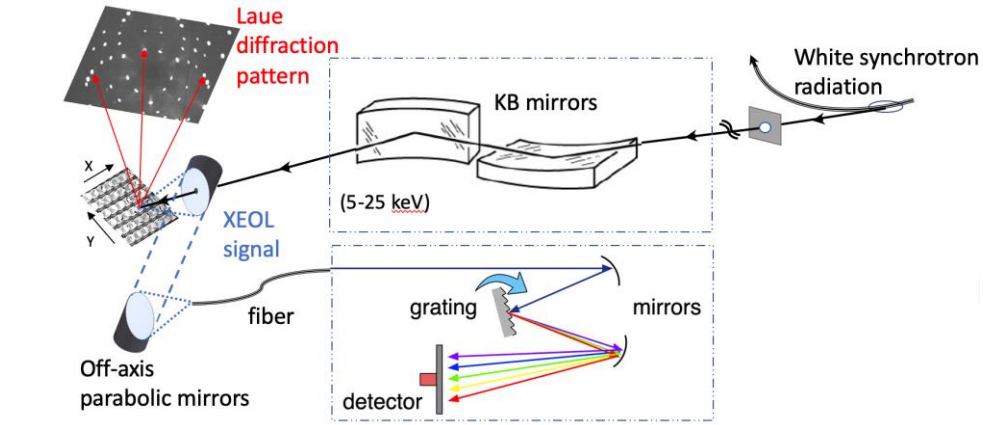

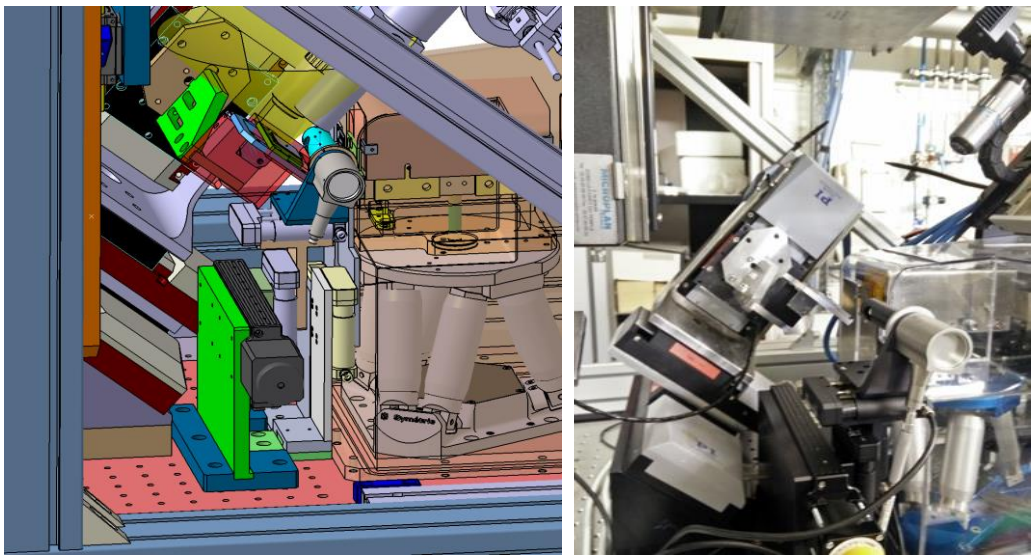

Fig. 1. Schematics, drawing and implementation of the XEOL measurement on the BM32@ESRF µLaue setup.

The sub-micrometer resolution range provided by the µ-Laue setup (250x300 nm^2 beam) is complementary with other ESRF nanobeams (e.g. ID16B beam < 50x50 nm^2) that perform fluorescence-emission mappings on very small areas (a few μm^2). In the framework of the CEA Bottom-Up project called LumiX (IRIG, MEM, NRS lab.), we developed a new setup on the diffractometer to record the light emission (see Fig. 1). The emitted photons are collected

by an off-axis parabolic Al-mirror (X-rays are going through a holed mirror), they are then focalized by a second parabolic mirror to the entrance of an optic fiber going to a QEPRO Oceanview spectrometer (350-925 nm). This light is then dispersed by a diffraction grating on a back-illuminated pixels CCD camera cooled with a Peltier device. A shutter mechanism allows selecting the acquisition time and acquiring the background for S/N improvement of XEOL spectra. The entire system (computer server, acquisition and analysis software) has been optimized to measure the visible range emission wavelength and Python Notebooks are written to help data analysis. This effort will be integrated in the data analysis roadmap of the beamline. Quite large mappings (mainly limited by data storage volume) can be obtained to get statistical information on a large number of objects.

The interest of this method has been successfully demonstrated before the ESRF-EBS shutdown within 4 different model systems: core-shell wires InGaN/GaN multiple quantum wells (MQWs) grown at CEA/IRIG, industrial 2D MQWs, µLEDs realized at CEA/DOPT and YAG:Ce “phosphor” materials that emit complementary colors to get white light in LEDs. A few examples of the two latter systems are illustrated in Fig. 2. It shows the collection efficiency of the system for the bright µ-LED emitters and weaker phosphors emitters (note sharp excitation of atomic states in the first type of phosphors). The full correlative data analyses are presently under way to link the emission features to the crystalline quality fluctuations of the materials. In the near future, other extensions of XEOL techniques such as polarized and time resolved analyses will be tested and implemented to have new insights on the properties of light emission.

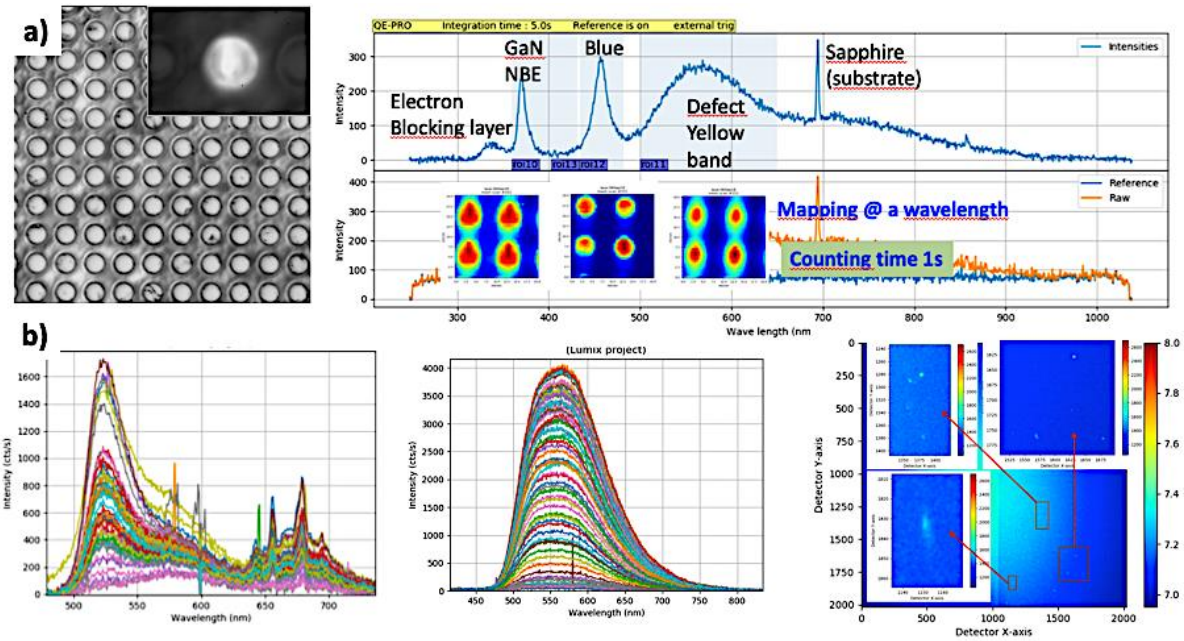

Fig. 2. a) XEOL measurements of µLEDs (6 µm diameter). A spectrum is measured at each point of the scan and allows wavelength mapping. b) Scans along two different types of phosphors (see features) and an example of Laue pattern.

6.2 HL2 3D X-Ray Laue Microscopy

Motivations Increasing the 3D capabilities of the Laue microdiffraction is a crucial importance to meet the growing needs of users for reliable captures of materials structure (orientation, strain, defects).

Due to X-ray penetration (even with intermediate photons energy, 5-25 keV), scattering intensities coming from different sample depths are superimposed. First, a full 3D picture of a microstructure with the grains absolute position and shape and boundaries is required to understand the mechanical properties of materials without any assumption usually done in 2D microstructure map. Second, the resulting Laue pattern made of superimposition of each probed individual grain Laue pattern is harder to analyse with single Laue pattern procedure due to the higher number of spots and their overlaps. Finally, in case of strain or orientation gradient within the gauge volume, peaks shape deviates strongly from the circular and symmetrical shape (described a single crystal model) leading to severe misestimation of the mean elastic strain. In all cases, better reliability on structural parameters assessment (namely on elastic strain one) is obtained by decomposing the scattering by sample depth, ie. by reconstructing the Laue pattern corresponding to a sample voxel.

Instruments and Methods

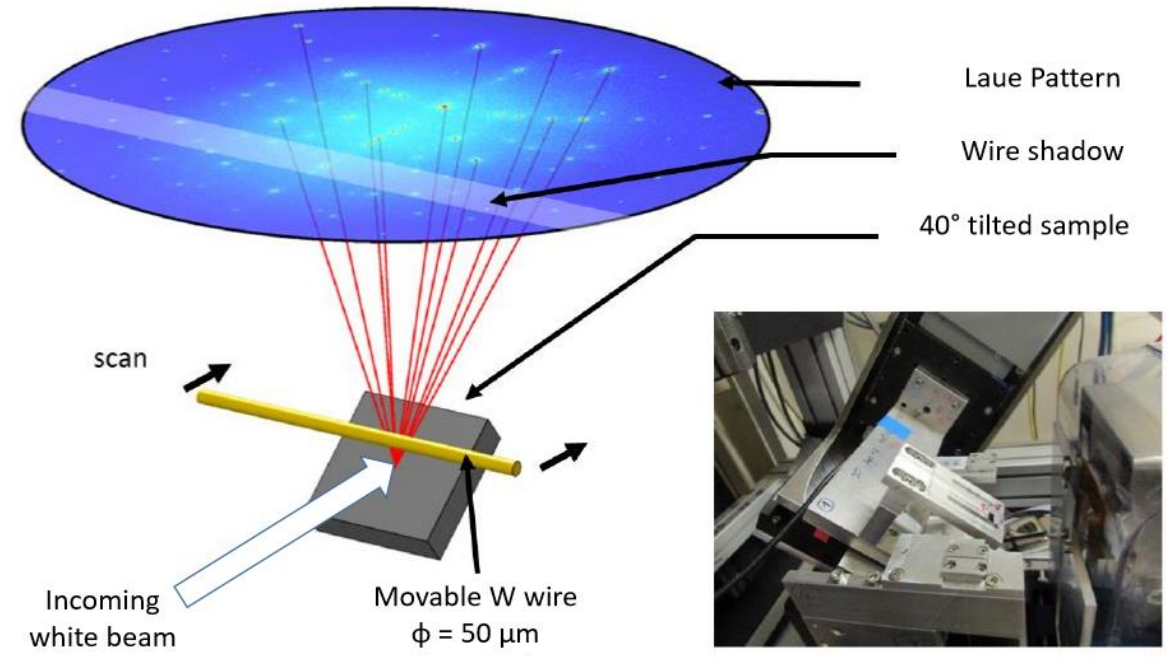

Figure HL1-1: Principles of 3D-µLaue. (a) Some X-ray scattered beams coming from the sample (tilted by 40°) are attenuated by a W movable wire. X-ray fluorescence intensity from illuminated sample volume (along incoming beam path) is seen on 2D detector placed at the top of sample. Similarly, Laue spot intensity profiles (pixel intensity as a function of wire position) show also dips which allow to retrieve the origin of scattering in sample depth by simple geometrical triangulation. (b) Photograph of one of the sample holder setups used on BM32 (X-ray comes horizontally from the right).

Thanks to ANR-DFG granted XMicroFatigue project (2017-2020) (Beamline staff and C. Kirchlechner group at MPIE Düsseldorf), the 3D-µLaue method has been improved intensely by L. Renversade (post-doc) on the basis of initial expertise on the development of DAXM method on BM32 since 2012. From the acquisition point of view, a faster 2D detector (sCMOS and simple wires scanning stages (several wires per holder) allow now the collection of few hundreds of images (for depth reconstruction with less than 1 µm resolution) in few minutes (Fig. HL1-1). Graphical user interfaces were designed to handle the calibration of wire trajectory and to assist the 3D scan acquisition strategy (to find the best compromise between the spatial depth resolution and measurement time). Moreover, a new algorithm to derive the scattering linear density (along the beam path beneath the sample surface) from the pixel intensity profiles has been designed. Inspired by algebraic methods of contrast diffraction or absorption tomography, it takes into account the wire transmission function and the large number of images. It significantly reduces the numerical noise which was overwhelming in the reconstructed scattering density profiles by the previous method (derivatives from finite differences).

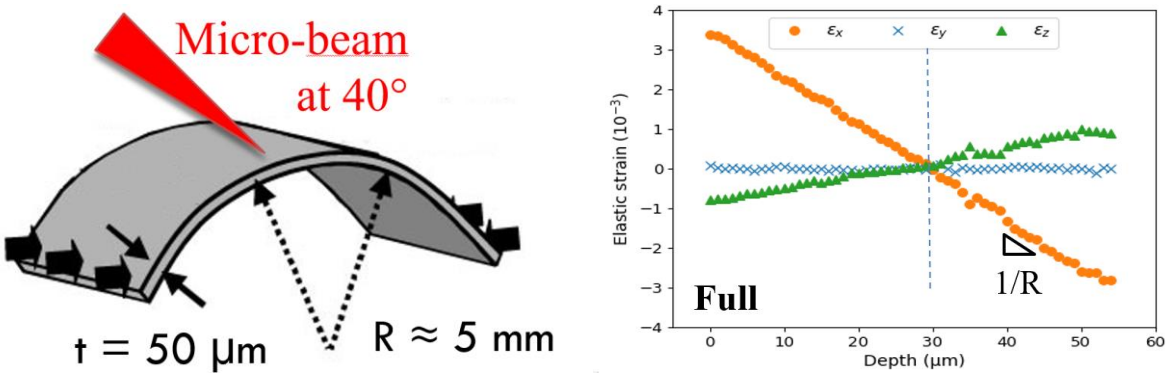

Fig. HL1-2: A bent Si 50 µm thick wafer (prepared by L. Michaud et al CEA-DRF/DRT) was used to qualify the strain sensitivity determined from reconstructed Laue patterns in each sample voxel crossed by the incoming beam. (b) Experimental strain components as a function of depth. Strains are zero on neutral fiber.

To assess the accuracy on strain determination from Laue pattern reconstructed in voxel, we measured the elastic strain profile through a bent Ge beam (fig HL1-2). Profiles of strain components are linear as expected by beam mechanics theory. Also, the relative and absolute level of strains are also in excellent agreement with analytical predictions. More importantly, the dispersion of the results is less than 10-4 which is of the same order with 2D strain map on unstrained Ge. More details will be published in a forthcoming article. To date, a 1 µm depth resolution profile is usually collected for 0.5 or 1 second exposure time, whereas a 0.3 µm resolution can be achieved by tripling the experimental time.

Thanks to these developments, we report two studies using DAXM. Example 1 deals with 3D strain measurements to investigate its effects on whisker growth. Ongoing analysis of in situ fatigue bending of Cu micropillars is presented in Example 2.

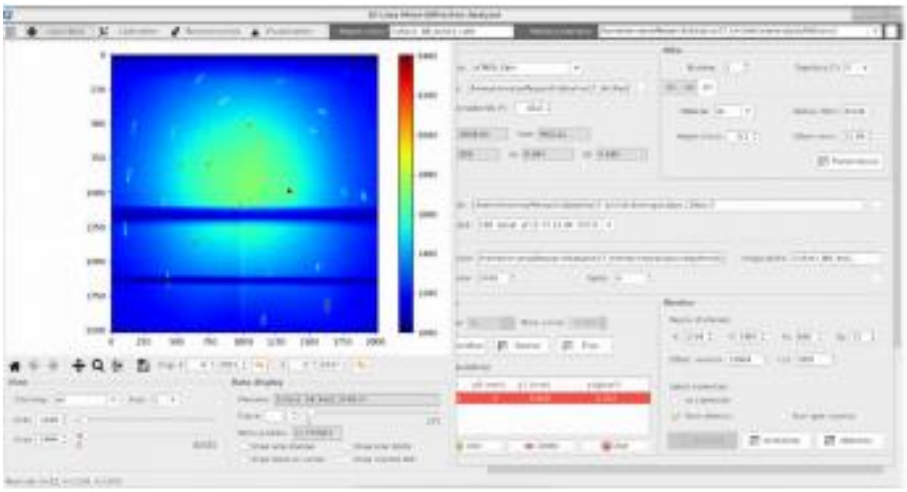

Figure HL1-3: Graphical user interface designed on BM32 to handle and visualize data for wire scan acquisition and calibration.

Example : 3D microstructure of in situ bent Cu pillars

C. Kirchlechner[1,2], J.-B. Molin[1], L. Renversade[3], O. Robach[3], O. Ulrich[3], J.-S. Micha[3]
[1]MPIE Düsseldorf, Germany, [2]KIT, Karlsruhe, Germany, [3]BM32 beamline

Abstract We present ongoing development and studies of in situ DAXM performed on micropillars during mechanical test. Few number of deformation fatigue cycles are performed and simultaneously Laue patterns are recorded each step to capture the evolving microstructure by 2D map and 3D volume.

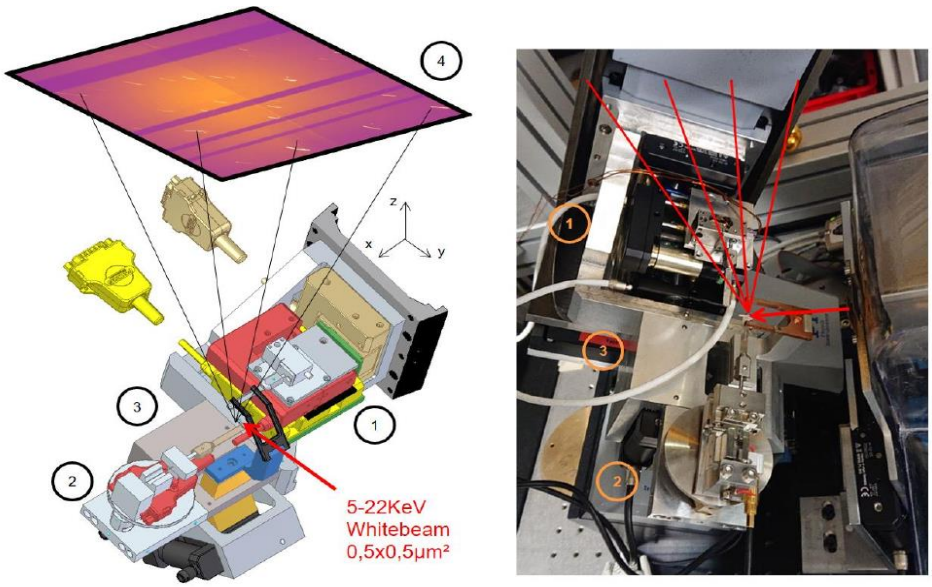

Figure HL-1-7: Setup of the in situ Straining Device 3D X-ray Laue microscope on BM32. Microsized sample are holded by left part (2) and deformed by actuators from the right one (3). A fork with one several wires can be moved independently by stages (3).

To understand the fundamental structural damage mechanisms of materials under fatigue load at the mesoscale, direct observations of atomic lattices transform are required. When decreasing objects size, dislocations interactions with grain boundaries and sample surface govern predominantly the mechanical behavior for which accurate predictive laws and experimental data are still missing to build models and for the properties optimization of this new class of grain boundaries engineering materials. Two major needs are required in this field: (1) access to structural parameters inside materials not only at its surface (e.g. by electronic microscopy), (2) follow the evolution of the same microstructure to get rid of experimental artefacts and for a better reliability in the interpretation of structural quantitative changes. Therefore in situ mechanical test save time (no sample realignment) and bring a better control of experiment geometry. The XMicroFatigue measurements campaigns were focused on the first fatigue cycles to observe a few number of dislocations and how they accumulate at a single grain boundary (or transmit through it). Two premiers have been done and will be published soon: (1) 3D map (1 µm3 voxel) on a microsized object and (2) in situ monitoring of 3D microstructure evolution (6 hours/3D map of 10*10*15 μm^3 with lateral resolution of 0.5x0.5 µm and depth resolution less than 1 µm).

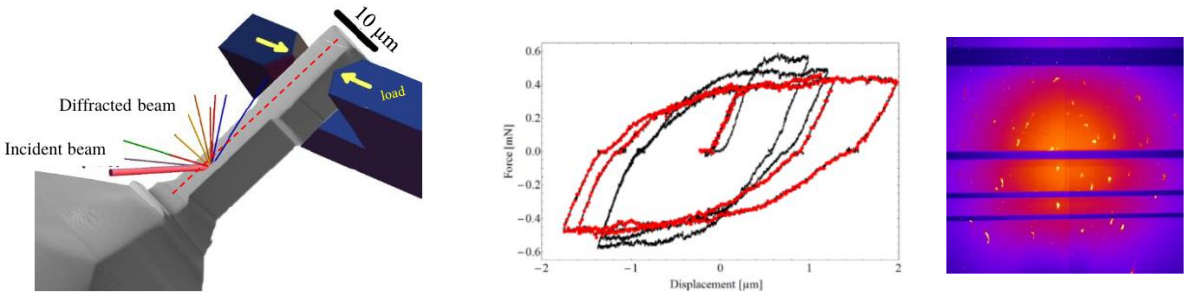

Figure HL1-8: (left) X-ray scattering (detector on top), grain boundary orientation (red dotted line) and mechanical test (bending of the pillar tip) geometry. (middle) Examples of force-displacement cycles corresponding to several percents of (plastic) strain in the region of interest (inferior half part of the pillar).

The subsequent experimental protocol was used during in situ experiments (Figure H1-8): The samples were submitted to one full fatigue cycle. During *in situ* loading mechanical data (force and displacement) and µLaue patterns were recorded simultaneously. The three dimensional scans were performed in the undeformed state (0 cycles) and, then, after ¼, ½, ¾ and 1 cycle in order to thoroughly investigate the local fatigue structure formed in single and bi-crystalline microsamples. During 3D scans a volume of ~10x10x15µm3 was scanned with the DAXM setup with a step size of 1µm and a polychromatic beam (5 to 22 keV), 0,5x0,5μm^2 sized. In total 12 micron sized samples, with 49 volumes scan. ~ 20TB of data had been collected during 4 beamtimes of several days. In Fig.4, a schematic reconstruction of a 3D volume scan is shown. The analysis was performed on one out of eight bi-crystalline sample. The analysis of acquired data is still ongoing, but already now it is clear that the data contains unique information on the 3D evolving microstructure of our material. We are confident to quantitatively assess local density of GND's, the local deviatoric strain and misorientations at the grain boundary (Figure HL1-9). Data treatment and analysis are still ongoing.

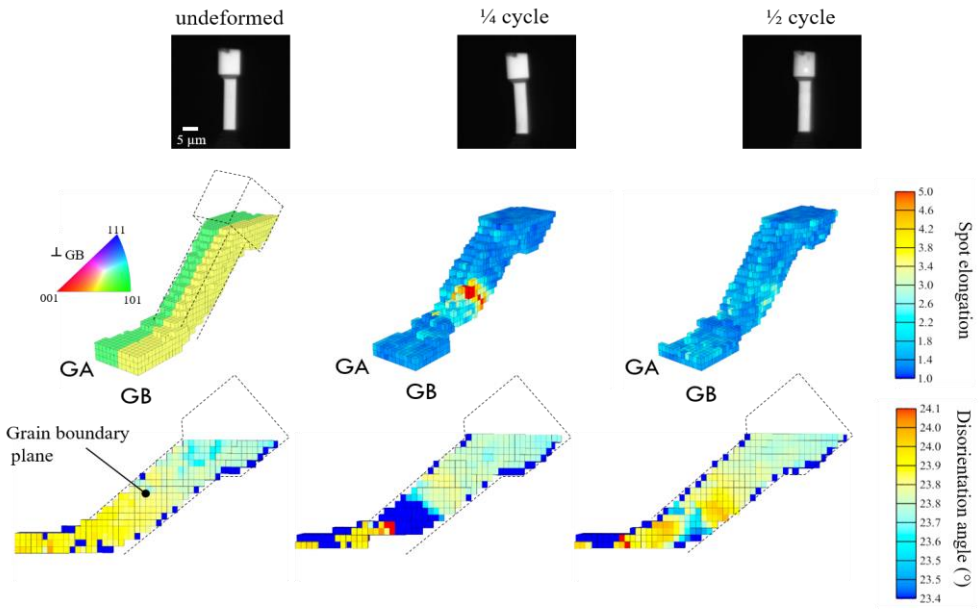

Fig. HL-1-9 : Microstructural evolution of (5X5x25 µm³) micropillar composed by 2 grains GA and GB (whose misorientation corresponds to an impenetrable high-angle grain boundary) during the first steps of fatigue cycle. Each column correspond to a given deformation step (central column with the highest strain). First row: visible light images of the pillar. Second row: (left) 3D orientation map. (middle and right) 3D map of Laue spot elongation related to dislocations storage volumic density. (right) Initial microstructure is almost recovered in terms of defects (damages) density. Third row: 2D GA/GB misorientation map at the grain boundary plane de cross section. (right) The remaining fine internal misorientation heterogeneities (introduced by crystalline defects) can be used in dislocations dynamical simulations to calibrate and improve greatly interactions potentials.

6.3 HL3 Energy-resolved Laue microdiffraction

As for 3D-Laue which decomposes the scattered intensities for each pixel over sample depth, energy measurements allow their decomposition over the d-spacing of lattice spaces.

Motivations: The complete knowledge of structural parameters is often required since they control the physical and mechanical properties of materials. Moreover, the numerical comparison of the unit cell parameters with reference ones - expressed by the full symmetric strain tensor of rank 2 with 6 independent parameters - is a ground quantity when describing mechanical properties in materials science. Finally, the full stress tensor can be determined from the strain tensor and the elastic constants representing valuable data for both fundamental and engineering aspects.

In standard Laue diffraction, the positions on the detector plane of Laue spots corresponding to Bragg reflection onto atomic planes are given directly by the orientation of lattice planes. They are used to determine the local crystal orientation and next to the local strain state or the shape of the unit cell by means of mutual angles between spots. However, the unit cell volume or equivalently the absolute length of any reciprocal space unit cell vector remains undetermined because the corresponding d-spacing - measured in standard monochromatic

techniques remain unknown due to the lack of photon energy (or wavelength) direct measurement.

To overcome this limitation, a mechanical assumption can be made for crystal located at the sample surface where normal to surface stress component (szz) can be considered as zero. Given the elastic constants Cij, this allows to solve the unknown hydrostatic strain from the Hooke's law ($\sigma=C\varepsilon$) (fulfilled by the full stress and strain tensors). However, even if this method has been successfully applied in several cases [1 Tardif, 2 Hektor 2019], it can be hardly give reliable full lattice parameters estimation for thick or buried objects.

Then, several experimental methods have been developed to obtain the full set of unit cell parameters. They all combine the measurement of the standard Laue pattern to retrieve the deviatoric strain (5 over 6 lattice parameters or strain components) with the measurement of at least one Laue spot energy. The insertion of the beamline monochromator (located in the optics hutch far upstream) was first tested but switching from white to monochromatic beam was too slow due to the lack of beam spot position reproducibility for microobject studies. O. Robach *et al* developed then two methods keeping a stable (in time) illumination at the same sample location during the measurement of Laue spot energy either by using (1) a 0D movable SSD detector ("fluorescence detector") or (2) monitoring spot intensity while rotating a diamond monochromator in transmission geometry ("Rainbow technique"). Results obtained with these methods are presented in examples 1.

More recently, the fluorescence detector principles has been followed and extended for higher speed and reliability by using 2D energy dispersive detector. On BM32 beamline two teams have used pnCCD (from pnSensors company) technology which exhibits the finest energy resolution (less than 150 eV @ 5 keV) as shown in examples 2.

References
*[1] S. Tardif et al, J. Appl. Cryst. (2016). **49**, 1402–1411*
[2] J. Hektor et al, Acta Materialia 168 (2019) 210e221

6.3.1 Examples 1: Energy resolution using movable 0D Energy Dispersive detector or light monochromator in transmission

6.3.1.1 Residual stress measurements by X-ray Laue microdiffraction in superalloy.

G. Altinkurt[1], M. Fèvre[1], G. Geandier[2] et al,
[1]LEM-ONERA, [2]Inst. J. Lamour Nancy

Abstract The Laue microdiffraction technique was used to investigate the strain field caused by the shot-peening operation and its redistribution after thermal hold or fatigue in a model nickel-based superalloy with an average grain size of 40 µm. This superalloy and shot-peening are widely used in aeroengine applications.This work aims at improving the characterization and the understanding of stress relaxations in high temperature alloys and to assess the ability of the Laue microdiffraction technique to quantify residual stresses in coarse-grained microstructures.

In this 2 phase alloy, recording the Laue diffraction patterns permitted to measure separately the strains related to the average alloy (γ+γ') and to the γ' phase and complemented structural studies performed in the laboratory. Even if there are small stresses in the inner part of the

samples, the sensitivity of the Laue microdiffraction method was large enough to quantitatively characterize the crystal misorientations and the deviatoric strain redistributions. Useful data were provided not only at the grain scale but also at the mesoscopic scale, thus bridging the gap between the $\sin^2 \psi$ and Ortner's methods used to determine residual stresses respectively in fine and single grain microstructures. The obtained results are also of first interest for a quantitative comparison with HR-EBSD measurements in the scanning electron microscope.

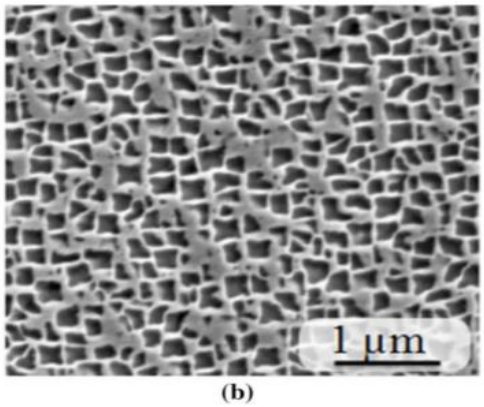

Figure HL-2-1: Observation of the coarse-grained microstructure in the N18 superalloy. (a): EBSD map revealing γ grains (random colors) with an average size of 40 µm. (b): Secondary electron image showing γ' precipitates (dark gray) with an average size of 200 nm embedded in the γ matrix (light gray).

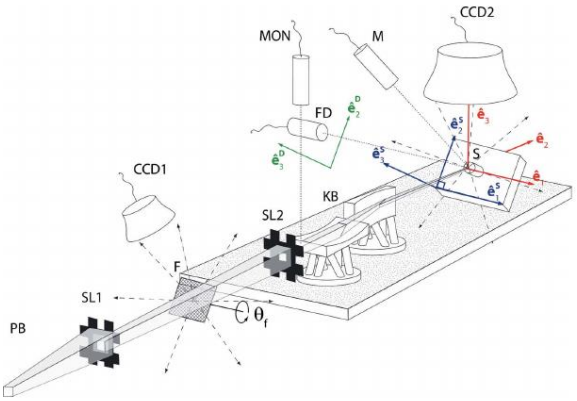

Fig. HL2-2 Schematic of the diffractometer setup with polychromatic incident x-ray beam, slits, Kirkpatrick-Baez focusing mirrors (KB) mounted on hexapods, polycrystalline sample, 2D CCD detector and energy dispersive point detector (FD). A diamond slab working in transmission (F) can be rotated to attenuate transmitted white beam at some energies. Calibratio

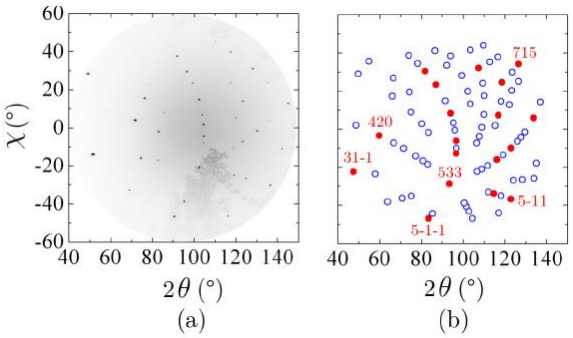

Fig. HL2-3 Laue patterns in the CDD detector coordinate system (2θ,χ). (a): Raw data. (b): Simulated pattern with the fundamental (closed symbols) and superstructure (open symbols) reflections.

Several states of the superalloy were investigated: initial, shot-peened (with and without annealing) and after fatigue loading (300 cycles up to 1% deformation at 450°C) with and without prior shot-peening treatment. These states simulate the material state from its elaboration to working conditions (at high temperature). Radial elastic strain profiles were measured. Figure HL2-4 reports orientation and deviatoric strain map measured at sample surface in shot-peened + fatigued state and only fatigued one. It shows that the surface is damaged due to shot-peening up to 300 µm depth (from map left border). Note the cylindrical shape of sample (sliced perpendicularly to z and polished) and corresponding frame: tensile fatigue along axis z, radial shot-peening). Because no difference was observed between the

two deviatoric strain fields, two energy measurements were used to determine the last unknown parameter of the full strain or stress tensors. In a two experiments [1,2], energy coupled measurements with an energy point fluorescence detector (Figure HL2-2) and with rainbow method were performed to determine the full elastic strain tensors associated with the γ and γ' phases. Thanks to the presence of separated Laue spots from γ and γ' superstructure phases stress measurements were carried out (Figure HL2-3).

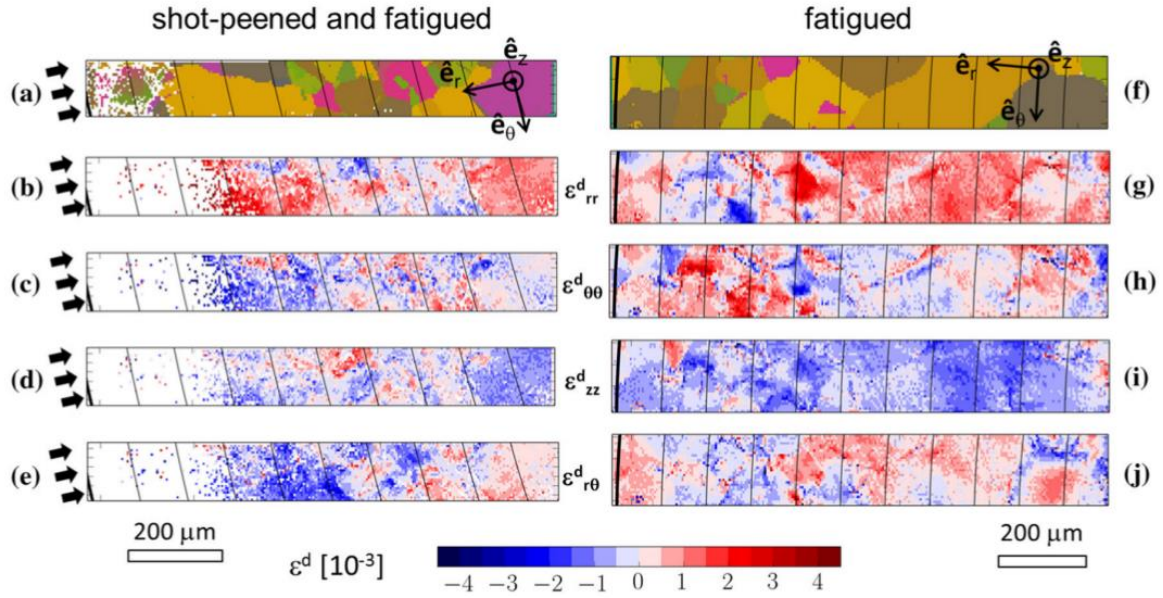

Fig. HL2-4 Grain orientation and deviatoric elastic strain components associated with (a-e) the shot-peened and fatigued sample S4, (f-j) the fatigued sample S5. The components are represented in the cylindrical coordinate system (êr, êθ, êz) related to the sample surface. They correspond to the average alloy (γ+γ' phases). The sample edge is at left. The isoradius contour lines have a spacing of 100 µm. Arrows indicate the average direction of the shot-peening. A 5µm step size was used during the µ-XRD measurements.

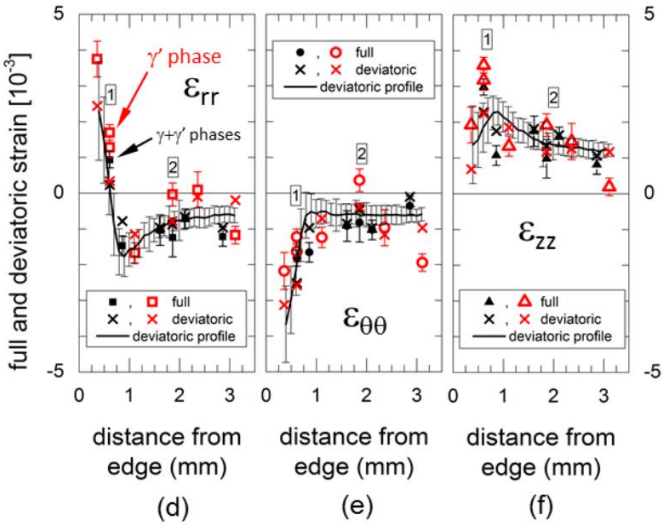

Fig. HL2-5 (d)-(f): Full and deviatoric strain components ε_{rr}, $\varepsilon_{\theta\theta}$ and ε_{zz}. The symbols correspond to the values obtained from energy measurements, open for the γ' phase and closed for the average alloy (γ+γ') with lattice parameter 3.592 A°.

Figure HL2-5 compares radial full and deviatoric elastic strain for each phase (measured over few grains) and the average deviatoric strain derived from the large number of grains of map. Discussions on the results can be found in [1]. Comparison of energy resolution with fluorescence detector and rainbow method are presented in [2] (Figure HL2-6).

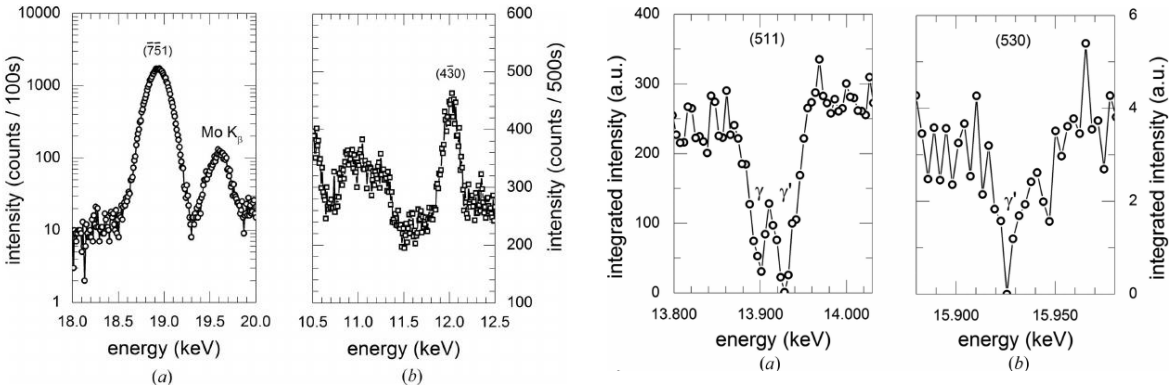

Figure HL2-6 (left) Fluorescence spectrum associated with (a) the -7-51 fundamental reflection (γ+γ') and (b) the 4-30 superstructure reflection. (right) By means of the diamond filter, Laue spot energy associated with (a) the 511 fundamental separated reflection of fcc-γ and sc-γ' phases (b) the 530 superstructure γ' phas reflection from measurements performed.

From the analysis of fundamental reflections in samples with average precipitate sizes of 200 or 2000 nm, we demonstrated that the 1 eV energy resolution provided by the filter-based rainbow technique is suited for distinguishing the γ phase from the γ' phase when the lattice mismatch is larger than 2.10-3 Å. This was not feasible with the energy dispersive detector because of its 150 eV energy resolution, which results in uncertainties of up to 10 eV for the energy of hkl reflections. In that case, the collected data refer to the average alloy. The uncertainty related to the unknown crystal lattice parameter in the four-spot analysis was close to +- 2.5 10-3 Å for the two methods.

From a technical perspective, we also demonstrated that the translation range and acquisition time of the energy dispersive point detector lead to important limitations on the number of measurable reflections and the compatibility with automatic operation. In addition, energy measurements were not always feasible owing to the crystal orientation, its symmetry and the experimental setup. With the 'rainbow' filter, the energy of several hkl reflections can be determined irrespective of the crystal orientation and symmetry after a 15–30 min acquisition. This leads to better confidence in the data analysis. The technique is adapted to automatic data acquisition and therefore suitable for sample mapping.

γ+γ' coherency strains and their relationship with the mechanical response of a material have been investigated in depth using diffraction techniques based on peak profile analyses in single crystals of nickel-based superalloys. In this study, we showed that Laue microdiffraction is now able to perform a similar task, but at the grain scale in polycrystals and with mapping capacities. This provides helpful data for understanding the relationship between the alloy microstructure of grains and precipitates and its damage resistance (e.g. creep, fatigue).

References

[1] G. Altinkurt et al, Journal of Materials Science 53, (2018) 8567-8589
[2] G. Altinkurt et al, J. Appl. Cryst. (2017). 50, 1754–1765

6.3.1.2 Accurate crystallographic metrology on strained Ge for electronic bandgap engineering. S. Tardif, A. Gassenq, K. Guilloy et al, CEA-IRIG/DRT

It has been theoretically predicted and experimentally observed that tensile strain in Si or Ge can induce a change in the electronic structure leading to reduced band gap at the Γ point. Owing to the already small energy difference between the Γ and L valley, Ge could thus become a direct band gap semiconducting material. The typical tensile strain theoretically required to achieve this are on the order of 2% biaxial (001) or 4% uniaxial [100]. Such high strain values are not trivial to reach in single crystal materials and could only be obtained in micro or nanostructures so far.

Here we investigated Ge microbridges prepared using direct bonding of a Ge layer on an oxidized Si substrate, and electron lithography for high precision patterning. The aim of the patterning is to concentrate the small residual biaxial strain in the Ge layer in small constrictions by underetching the oxide layer, either microbridges (uniaxial) or microcrosses (biaxial). A typical microbridge is shown in Fig. 1a: the two large strips are relaxed and the strain is concentrated in the small center microbridge. In order to measure the local strain at the micron scale, one needs to use localised probes. Optical Raman spectroscopy is a standard technique to measure locally the Ge-Ge bond frequency shift, and thus estimate the strain. However it is indirect as the shape of the strain tensor has to be known a priori and the validity range of the relation between the frequency shift and the strain value is limited, as we will show later. Diffraction techniques are directly sensitive to the interplanar distances and therefore are the tool of choice to probe strain. Here we used the Laue microdiffraction technique to obtain in a single measurement both the local orientation and strain state in several types of suspended Ge microstructures.[1] Typical results in 5 different bridges, corresponding to five different lengths of the stretching arm are shown in Fig. HL2-7b,c. The tetragonalization of the lattice can readily be seen from the comparative evolution of the h0l and 0hl Bragg reflections, as illustrated in Fig. HL2-71c. Indexing the Laue diffraction patterns gives the relative lattice parameters (e.g. b/a and c/a), the three lattice angles (α, β and γ) and the orientations angles (e.g. R_x, R_y and R_z), as illustrated for a microcross in Fig. HL2-7.

In order to obtain quantitative values for the full strain tensor, we used either a numerical approach under the assumption of no normal stress on the free surface, or an experimental approach using energy-resolved Laue techniques, as described hereafter.

For the numerical approach, neglecting the normal stress on the *z* oriented surfaces removes one unknown from the six equations describing the mechanical equilibrium between stress and strain. Only six unknowns remain (5 stress components and 1 strain component - the hydrostatic strain), and thus the system can be analytically solved. The underlying assumption is that the mechanical constants (compliance or stiffness tensor) are indeed constant in the strain range considered.

For the determination of the energy of individual Bragg reflection from the white beam measurements, we used either by the “rainbow-filter” (RF) method, or direct energy measurement using an additional energy-resolved detector. The RF consists in placing a band stop filter in the beam and scanning the position of the attenuated energies. Experimentally, this is achieved by placing a diamond single crystal in the beam in Laue diffraction condition and rotating it while recording the Laue patterns of the sample. Once calibrated, the rotation angle of the diamond and corresponding aligned reflections give the attenuated energies of the transmitted beam. Thus, the energy of given peaks in the Laue patterns can be accessed by monitoring the decrease in their intensity and the corresponding diamond angle. The

resolution and accuracy is typically limited by the angular increment of the diamond, and by the angular dependence of the reflection energy.

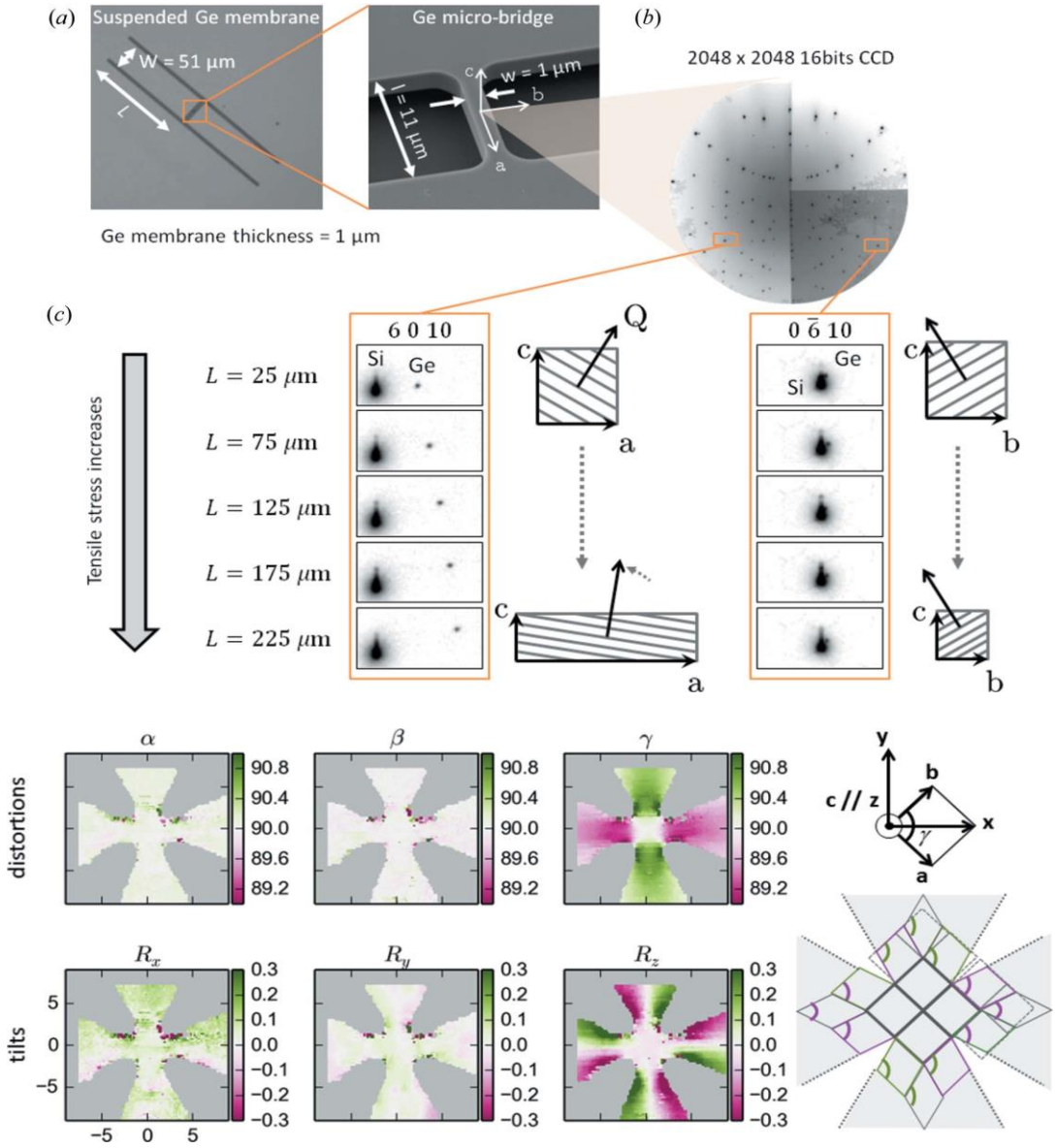

Figure HL2-7. ***Top*** *: (a) SEM micrographs of a <100> micro-bridge, showing the design parameters W (51 mm), w (1 mm), L and l (11 mm). L was tuned between 25 and 225 mm to change the strain amplification. The direct space lattice vectors are indicated by a, b and c. (b) Raw Laue pattern, as measured in the center region of the micro-bridge, and (c) details on two different Bragg peaks, showing the diffraction from both the Ge micro-bridge and the underlying Si substrate as a function of the tensile stress.* ***Bottom*** *: Crystallographic angles alpha, beta and gamma and lattice orientation angles Rx , Ry and Rz measured in a micro-cross and in a micro-bridge. Inset: orientation of the basis and direct space lattice vectors, and sketch of the strained micro-structure.[1]*

A secondary energy-resolved point detector (Silicon-Drift Detector, SDD) can also be used to directly measure the energy of the peak.Typically, the usual Laue pattern is acquired and indexed, thus the angles of all possible diffraction peaks can be estimated. The SDD can then be positioned at one or several of such locations to obtain a direct energy measurement. The resolution of a SDD is usually in the 100 eV range, much larger than required for a 10^{-4} strain resolution with peak energies on the order of 10 keV. However the center of mass of the peak can be determined with a much better resolution, on the order of a few eV. This requires a fine

tuning of the channel/energy conversion of the multichannel analyzer (MCA) connected to the SDD. The approximate energy calibration can be performed using the fluorescence of the elements present. Quite conveniently the Ge $K_{\alpha,}$ fluorescence lines lie in the 10-11 keV range, right in the middle of the 0-20 keV detection range of the MCA. To achieve the best calibration, we found that having a second peak of known energy close to the peak of interest was beneficial for the finer calibration of the MCA. Luckily, in our system of interest, the diffraction of the Si substrate is almost aligned with that of the Ge layer (Fig. HL2-7b) and therefore can be measured simultaneously.

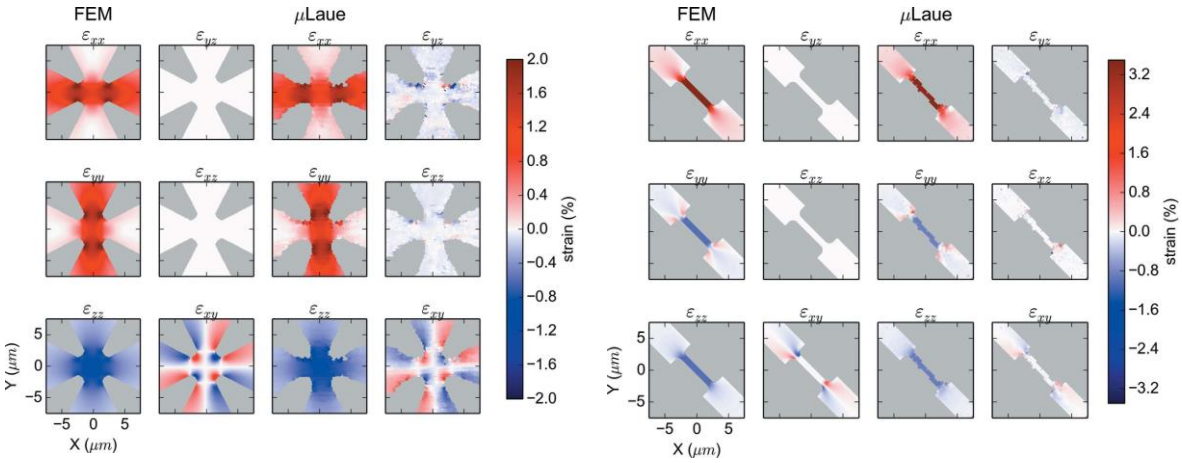

Figure HL2-8. Components of the full strain tensor in a micro-cross expressed in the x = [110], y = [110], z = [001] basis, and of the micro-bridge expressed in the x = [100], y = [010], z = [001] as obtained by FEM simulations and rainbow-filtered Laue micro-diffraction measurements [1].

Using the quantitative energy measurements, we could retrieve the full strain tensor in different microstructures and validate the assumption behind the numerical analysis. We could perform extended strain tensor mapping (Figure HL2-8) and we obtained an excellent agreement with the simulations using finite elements method over all the components of the strain tensor. Furthermore, by performing the measurements on different microbridges, we could experimentally measure for the first time uniaxial strain up to about 5%. Interestingly, we observed nonlinear behaviors in the high strain regime. For example, we evidenced that the relationship between the observed Raman spectral shift and the measured strain amplitude was not linear for <100>-uniaxial strain above about 2%, as shown in Figure HL2-9a. Higher order terms need to be considered, which is consistent with the Density Functional Theory calculations that we performed. This result is significant, as the Raman shift increases faster for larger strain, which leads to an overestimation of the strain for values above 2%.[2] Similar effects were also investigated for other strain orientation.[3] Another important effect of high amplitude strain is the band edge shift. Above 2% <100>-uniaxial strain, usual deformation potentials are not accurate enough to predict the measured band edges and one has to use a tight-binding approach to compute consistent values, as shown in Figure HL2-9b.[4]

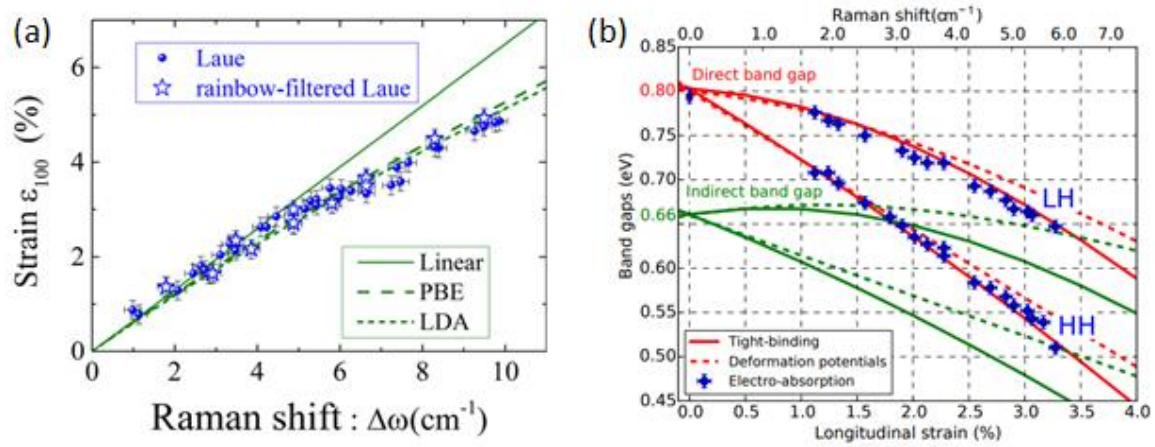

Figure HL2-9. (a) <100>-uniaxial strain as a function of the Raman spectral shift. The strain values are either numerically calculated (solid circles, see text) or experimentally measured using the "Rainbow-filter" method (empty stars), DFT calculations using two different types of exchange correlation potentials (dashed lines), and usual linear approximation (solid line). [2] (b) Direct (red) and indirect (green) band gap measured using electroabsorption (symbols) and calculated using deformation potentials (dashed lines) or tight-binding calculations (solid lines).[4]

In conclusion, the ability to measure in a single shot the deviatoric strain tensor and the sample orientation, combined with the possibility to extract the last missing parameter by additional measurements or calculation has proven highly effective in the study of strained Ge microstructures. The usual framework for Raman spectroscopy, the more accessible standard laboratory local strain probe, was shown to require taking into account higher order terms in the high strain regime. Other monochromatic nanodiffraction techniques, such as the K-map on ID01, could have (and actually have) been used for the accurate determination of the full strain tensor, at the cost of mapping several peaks for each microstructure. Here, the ability of microLaue to probe many samples over a relatively short time was key to establish a detailed strain-dependence of several other materials parameters (Raman shift, band edge shift, photoluminescence..). Additionally, while not described here, temperature effects were also investigated using either cryogas cooling or furnace heating, thanks to the versatility of the microLaue setup.

References:

*[1] S. Tardif et al., Journal of Applied Crystallography **49**, 5 (2016)*
*[2] A. Gassenq et al., Applied Physics Letters **108**, no. 24 (2016): 241902*
*[3] A. Gassenq et al, Journal of Applied Physics **121**, no. 5 (2017): 055702*
*[4] K. Guilloy et al., ACS photonics **3** (10), 1907-1911 (2016)*

6.3.2 Example 2: Energy resolution using pnCCD 2D detector

The fast acquisition with a single 2D detector of scattered intensities with scattering angles and corresponding photons energy at each pixel is the ultimate way of practising X-ray Laue Diffraction. This wealth of information allows one to determine (ideally in a single shot) the full unit cell parameters or equivalently all the 6 components of strain tensor (so-called full strain tensor). The larger the number of measured Laue spots the higher the reliability on the structural parameters determination. This will overcome the limitations of energy measurements with the punctual fluorescence detector presented above by decreasing significantly the acquisition time. Combining a minimum of X-ray optics (no monochromator, only collimating and focusing elements), the absence of sample rotations or prior alignment, with the use of a fully adapted energy resolved detector for whitebeam experiments is also a clear advantage for speed and reliable measurements.

6.3.2.1 Single-shot full strain tensor determination with microbeam X-ray Laue diffraction and a two-dimensional energy-dispersive detector

A. Abboud[1], T. Conka Nurdan[2], S. Send[1], R. Hartmann[3], L. Strüder[3] and U. Pietsch[1]

[1] Univ. Siegen Germany, [2] Univ Turkey German Istanbul, Turkey, [3] pnSENSOR Gmbh, Germany

Abstract. The full strain and stress tensor determination in a triaxially stressed single crystal using X-ray diffraction requires a series of lattice spacing measurements at different crystal orientations. Usually this can be achieved using a tunable X-ray source. A novel experimental procedure for single-shot full strain tensor determination is reported using polychromatic synchrotron radiation with an energy range from 5 to 23 keV. Microbeam X-ray Laue diffraction patterns were collected from a copper micro-bending beam along the central axis (centroid of the cross section). Taking advantage of a two-dimensional energy-dispersive X-ray detector (pnCCD), the position and energy of the collected Laue spots were measured for multiple positions on the sample, allowing the measurement of variations in the local microstructure. At the same time, both the deviatoric and hydrostatic components of the elastic strain and stress tensors were respectively measured and calculated.

Recently, full elastic stress and strain tensor measurements were performed on a copper through-silicon via with a combination of mono- and polychromatic X-rays to scan the energy of Laue spots (Levine et al., 2015). This scheme has been proposed earlier and installed at ALS, APS and our beamline at ESRF. These studies provide ground breaking results. However, switching and tuning the X-ray beam is a time-consuming procedure that does not fully guarantee a fixed footprint of the beam on the sample, which prohibits the application of this approach for in situ sub-micrometre full strain measurements.

The sample used for the present experiment is a copper single crystal shaped by means of a focused ion beam. The specimen is shown in Fig. HL2-10A. It has a gauge length of 20 µm in height and widths of 7 and 9 µm at the center. Prior to this experiment, the sample was milled with the [361] crystallographic axis parallel to the central axis and the [841] crystallographic direction parallel to the loading axis. By means of a PicoIndenter a doped diamond Berkovich indenter tip was used for the bending experiment.

An energy-dispersive pnCCD detector was used to acquire the µLaue scattering data. Its active volume is made from a 450 mm weakly doped n-type silicon. The front side is divided into 384 x 384 pixels, each of 75 75 mm in size. The spatial resolution is limited by the pixel size but can be further reduced by dedicated algorithms handling charge sharing among adjacent pixels, while the energy resolution (FWHM) is limited by the electronic noise and the Fano limit of silicon. The latter is measured to be 136.5 eV at 8040 eV. Further details on this type of pnCCD are given by Send et al. (2013).

In the first attempt, Abboud et al mounted a 2D pnCCD detector (384x384 pixels, pixel size =75 µm) in addition to the standard detector (Abboud et al., RSI 2014). It allowed only the collection of 2 Laue spots from Cu micropillar. More recently, by replacing the standard by their pnCCD closer to the sample, they achieved to measure 5 spots on the Cu micropillars as shown in Figure HL2-10A with a comparable angular resolution. In principles, to obtain the best energy resolution, incoming flux must be reduced so that a pixel gets a unique photon during the frame duration of about 10 ms (at 92 Hz).

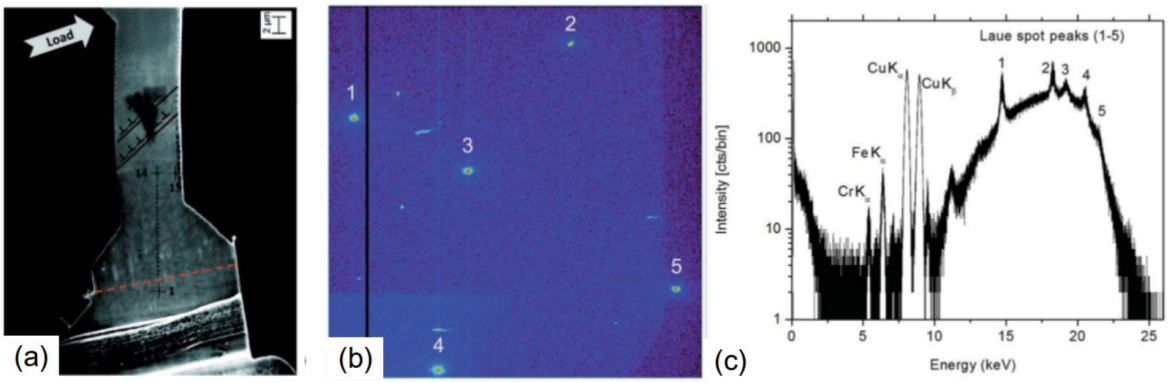

Figure HL2-10 (a) Cu micropillar sample milled by Ga by Focussed Ion Beam (FIB), (b) : Energy accumulated (over the 5-23keV energy bandpass) Laue pattern from 50000 frames (exposure time 543s). (c) : Pixels accumulated energy spectrum (over 384x384 pixels). 5 X-ray (scattered beam) lines are clearly visible and separated above 15 keV allowing the evaluation of 5 d-spacings from a single shot. The peaks FWHMs ranged from 280 to 425 eV (by considering only pixels in 10x10 pixels centered on peaks) corresponding to 3% of energy resolution.

As a function of the position along the neutral fiber, 14 energy resolved Laue patterns were then measured (Fig H2-10B top). The full strain and stress tensors were obtained (Fig H2-10B bottom). A calibration point where Cu structure was the least deformed was chosen to calibrate the detection geometry. Due to the limited number of spots measured in the Cu Laue pattern calibration parameters are less accurate than those obtained by standard Ge wafer unstrained with a laue pattern of several dozen of peaks. Together with these uncertainties, Cu structure at calibration point was not ideal and is likely to be a in a residual deformation state, leading to a overestimation of the strain level. However better normal strain and stress components evaluation is achieved by taking into account strain at calibration point. This full strain and stress assessment methodology can greatly be improved (in speed and reliability) by combining the current standard large sCMOS camera with a larger 2D pnCCD detector than that used with this team.

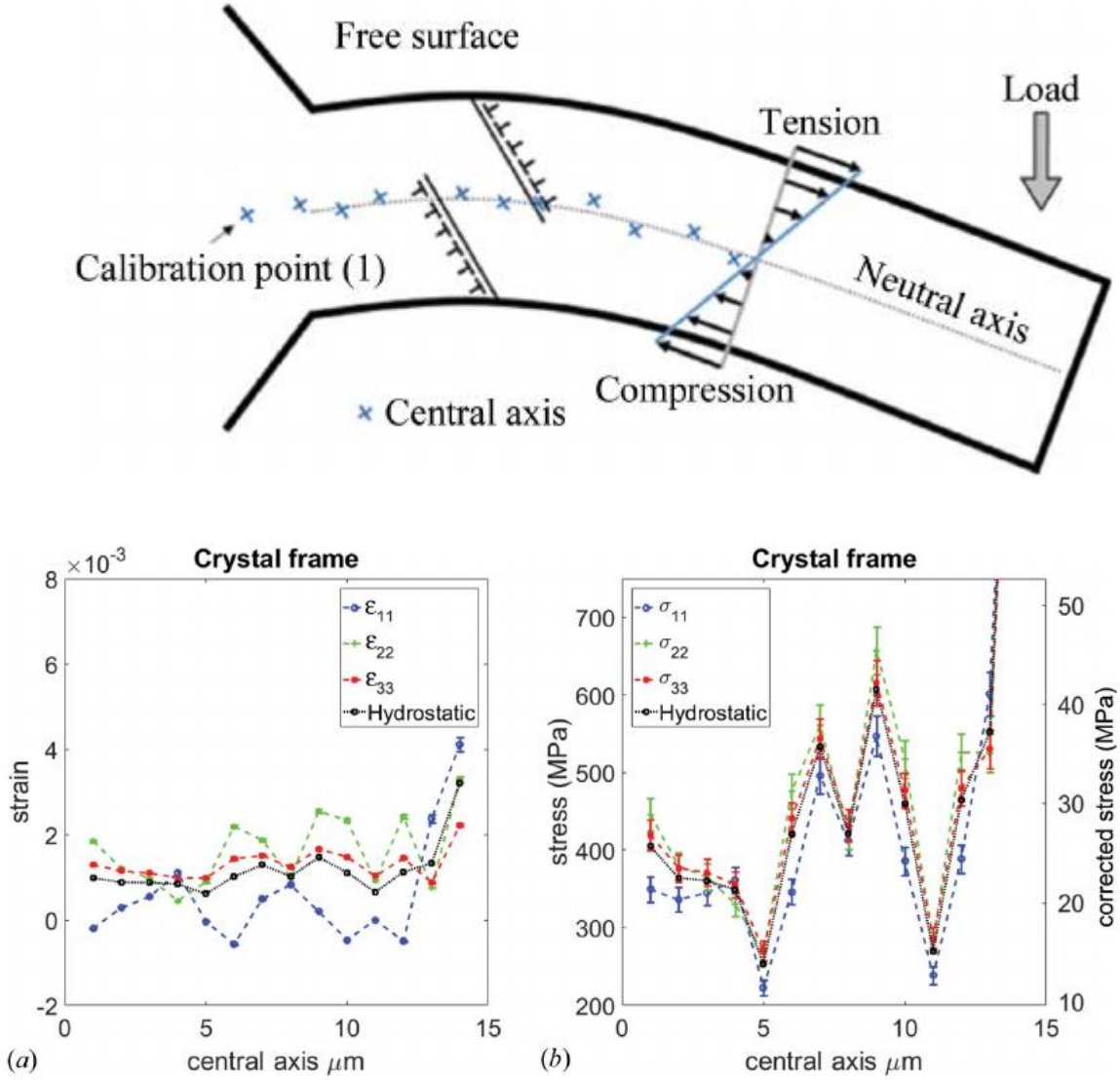

Figure HL2-10B (top) A simplified sketch of the bending beam and two glide planes (one with positive and one with negative Burger's vectors). The dotted line shows the expected location of the neutral axis, and the crosses show the measurement points, i.e. possible deviation from the neutral axis. (bottom) (a) Normal strain components ε_{xx} ; ε_{yy}; ε_{zz}, plotted as a function of distance along the central axis. The uncertainties are one standard deviation. The sawtooth pattern can be interpreted as the presence of a strain gradient along the central axis (see top sketch). (b) The strain pattern translated to the normal stress components, showing a similar response. The right-hand y axis shows the corrected stress values after taking into account the uncertainty in the calibration measurement. The last stress value is around 100 MPa.

References

Abboud, A. et al, J. Appl. Cryst. (2017) ***50****, 901–908*
Abboud, A. et al, Rev. Sci. Instrum. (2014) ***85****, 113901.*
Send, S., et al., Nucl. Instrum. Methods ***A*** *(2013),* ***711****, 132–142.*
Levine, L. et al. ,. IUCrJ (2015) ***2****, 635–642.*

6.3.2.2 White beam Rapid Texture scanning using Energy dispersive detector

T. Grünewald[1,2], P. Tack[3], H. Lichtennegger[1] *et al*,

[1] BOKU Wien Austria, [2] ESRF, [3] Ghent Univ., Belgium

Summary. A 3D texture scanning setup was implemented using a white X-ray beam and an energy dispersive 2D detector (SLCam) for energy dispersive Laue diffraction (EDLD) measurements. The setup was designed and manufactured in Vienna and commissioned prior to the beam time. Focusing elements were used with different parameters from usual conditions to obtain a broader focal spot size of 2x3 µm. One were able to measure the crystallite orientation in biomimetic $CaCO_3$ spherulites as one-shot orientation maps in reciprocal space. For the first time successful mapping of significant areas of the sample were obtained using the inherent speed advantage over conventional texture determination with a monochromatic beam in a rotational setup.

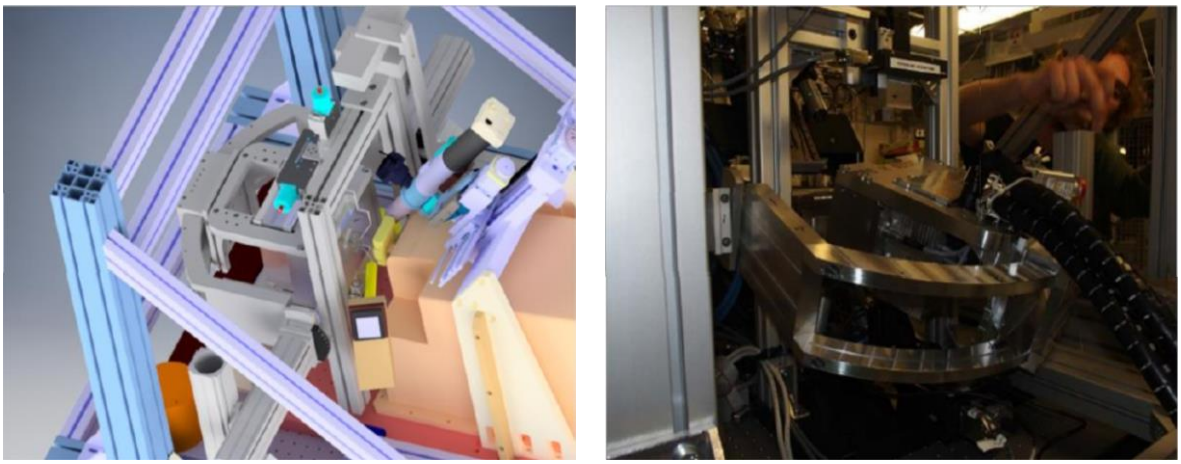

Figure HL2-11: 3D rendering of the setup, showing the sample, beamstop and aperture stages long with the tiltable detector b) Actual implementation of the setup at BM32 in the micro laue setup with a tilted detector.

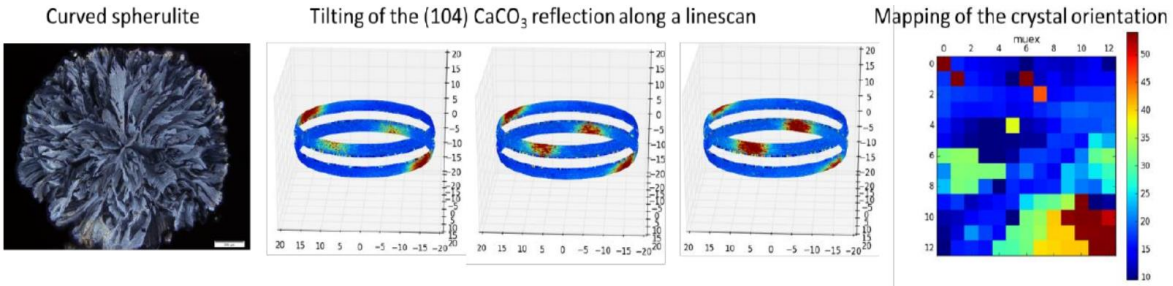

Figure HL2-12 (a) A curved CaCO3 spherulite, (b) The tilting of the (104) reflection over three points in one scan (c) A map of the (104) crystal orientation.

Samples and Setup. The aim of this experiment was to develop and implement a scanning setup for the BM32 micro laue setup in order to be able to use a small, focused white x-ray beam together with a mapping approach to carry out EDLD measurement on structurally heterogeneous samples. Users managed to measure the textural changes in biomimetic

CaCO3 and elucidate how the stress of the “cake-like” wedge structure is mediated during growth (see Fig IF-17 a).

The setup employed a white beam spectrum from a bending magnet, shaped by a pre-focusing mirror in the energy range from 5 to 22 keV. As the necessary setup for the detector did in part not comply with the optical parameters of the KB focusing optics, one had to move the focal spot downstream by 27mm (which is the reason why the final spot size was 2x3 µm and not 300x300nm as usual). Due to the small active area of the SLCam detector a diffractometer-like stage was implemented to tilt the sample. This was specifically designed for this experiment and implemented (see Figure IF-16). In addition users put new PI M 111,OWIS 120 and Mics MT 60 scanning stages (which were in part borrowed from ID13) to be able to move the sample adequately, beamstop and beam cleaning aperture respectively. A rendering of the setup can be seen in Fig IF-16 a). In order to reduce air scatter as much as possible we used thin ultralene windows and flushed these paths with He. In order to detect fluorescence from the sample, a Ketek XRF detector was employed. It is obvious that the setup is quite intricate and required a bit of commissioning time during the shutdown. For future improvements it would be advantageous to optimize the beam cleaning apertures introduced here for the first time with a better collimation scheme.

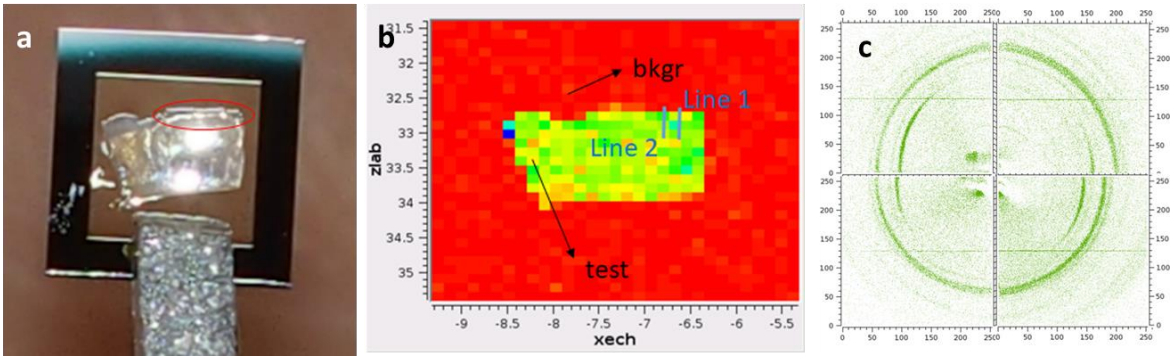

Fig. HL2-13: EDLD on healthy tooth enamel. (a) Silicon nitride window holding a thinly ground section of a tooth. The area marked with a red oval is the region of interest with the enamel and dentin enamel junction (DEJ). (b) prior to measurement a Ca fluo map was recorded. The blue lines indicate the position of linear scans performed across the enamel and DEJ. (c) Typical diffraction pattern showing the peaks of hydroxyapatite (HAP) and revealing strong texture. Note that the pattern consists of 4 quadrants, corresponding to 4 different tilt/rotation positions of the SLCam on the rack to cover as much of reciprocal space as possible. The offset is then internally corrected by an evaluation algorithm.

Principal outcome. Figure HL2-12 shows the 104 reflection from $CaCO_3$ along a scan line in the spherulites. It is visible that the orientation of the crystal axis is not only tilting in one but two directions, which is very hard to analyze with conventional texture analysis. The preliminary data analysis indicated that distinct zones with abruptly changing crystal orientation are existing (Fig HL2-12c). Users are currently in the process of evaluating and fitting the data further, and as several reflections in the full reciprocal space are available we expect extremely good fits of the crystal orientation without a-priori knowledge

6.4 HL4 Fluids in nanoconfinement

Impact of Silica Surface Nanoconfinement on the Microstructure of Alkoxysilane Layers Grafted by Supercritical Carbon Dioxide

D. Rébiscoul, D. Sananes Israel, D. Tardif, V. Larrey, A. Ayral, F. Rieutord, J. Phys. Chem. C ***123****, 19, 12305-12312 (2019)*

Abstract: The impact of nanoconfinement on the microstructure of alkoxysilane layers grafted by supercritical CO_2 was determined using a model system made of silica nanochannels. Using hard X-ray reflectivity, we have directly compared the results obtained on open planar silica surfaces with confined ones. We could thus isolate the effect of the nanoconfinement on the microstructure of different types of grafted layers.

Surface functionalization is intensively used in various technological fields, such as microelectronics, decontamination, medical, catalysis, or biosensor applications. The functionalized surfaces can be either “open” and directly exposed to the environment, or “confined” as in nanopores. The organization (density, microstructure…) of grafted molecules has been intensively studied on open surfaces. For example, the effect of the alkyl chain length and of the surface curvature was demonstrated for alkoxysilane molecules grafted on silica surfaces. However, the organization of the grafted molecules is expected to be different in

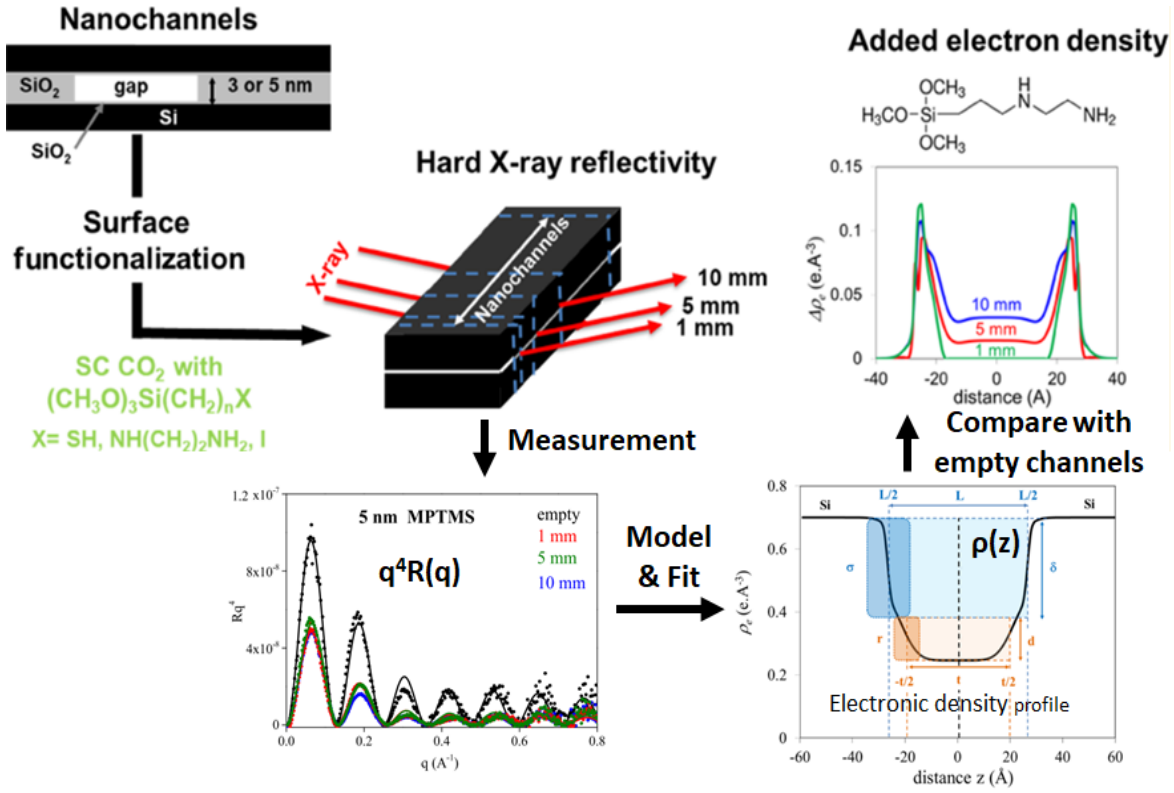

Figure HL4-1. Principle of the experiment: silica nanochannels were made using lithography and direct bonding at the LETI in the CEA-Grenoble, the surfaces were functionalized using supercritical CO_2 (T = 31 °C, P = 74 bar) and different alkoxysilanes. Hard X-ray reflectivity was used to probe the electron density profile across the nanochannel, at different positions along the channel. A two layer model was used to describe the electron density profile. The fitted electron density profile was compared to empty channels to extract the additional electron density from the grafted molecules.

nanoconfinement conditions, due to the reduced dimensionality. In the example mentioned above, the alkoxysilanes molecules may be constrained by the low free space available for their diffusion, hydrolysis, and condensation with surface silanols, which may in turn yield a different organization of the grafted layer. A direct comparison of open versus confined surfaces is thus much needed.

Probing grafted molecule organization in confined surfaces is challenging, as one must access interfaces that are buried in micrometers to millimeters of material, and measure a thin molecular layer with sub-Angström resolution. As we show here, hard X-ray reflectivity is well suited for this type of study. We used arrays of silica nanochannels with 3 or 5 nm (height) x 250 nm (width) x 25 mm (length) to probe the grafting of alkoxysilane molecules, to be compared with our previous results in open, flat silica surface. We used three different alkoxysilane molecules, corresponding to three different organization on open silica surfaces: 3-(mercaptopropyl)trimethoxysilane (MPTMS), [3-(aminoethylamino)propyl]trimethoxysilane (AEAPTMS), and 3- (iodopropyl)triethoxysilane (IPTES), yielding a dense monolayer, a polycondensed layer and a dense bilayer, respectively. We used the GMT setup, an energy of 27 keV and a beamsize of 50 µm (V) x 700 µm (H) to probe the reflectivity along the nanochannel length, as illustrated in Fig. HL4-1. From the measurement in empty channels, we could recover the additional electronic density on the floor and ceiling of the nanochannel, corresponding to the grafted layer.

Assuming an identical density of silanols at the silica surface of all the sample (nanochannels and open surfaces), we found that no matter the molecule, the grafting densities were systematically lower in nanoconfinement conditions, compared to open surfaces. Interestingly, the grafting density also varied along the channel for AEAPTMS and IPTES, while it was constant for MPTMS, even though the molecular length of IPTES and MPTMS are identical (10 Å) and quite similar to that of AEAPTMS (12 Å). This suggested a coupled effect of both the confinement size (nanochannel height) and the nature of the alkoxysilane. We detail here the main results, illustrated in Figure HL4-2:

MPTMS, a dense monolayer: MPTMS forms a dense monolayer on open surfaces. In 5 nm nanochannels, the grafting is homogeneous and close to that of open surfaces. In narrower nanochannels (3 nm), the grafting is also homogeneous by the density is lower, which we explain by the formation of H-bonds between face-to-face thiol groups that prevent an efficient grafting.

AEAPTMS, a polycondensed layer: on open surfaces AEAPTMS forms polycondensed layers, classically explained by the orientation of the amine head groups toward the silicon oxide surface or toward other hydroxylated molecules. In nanoconfinement, an excess electron densities at the center of the nanochannels are observed, decreasing with the distance from the nanochannel entrance, indicating a molecular-transport driven grafting process. In smaller nanochannels, a heterogeneous grafting density tends to indicate channel clogging.

IPTES, a bilayer: IPTES forms two interpenetrating monolayers on open surfaces. In nanoconfinement, we observed much less dense layers with thicknesses close to the molecule size. Nanochannel clogging was deduced from the heterogeneous grafting densities.

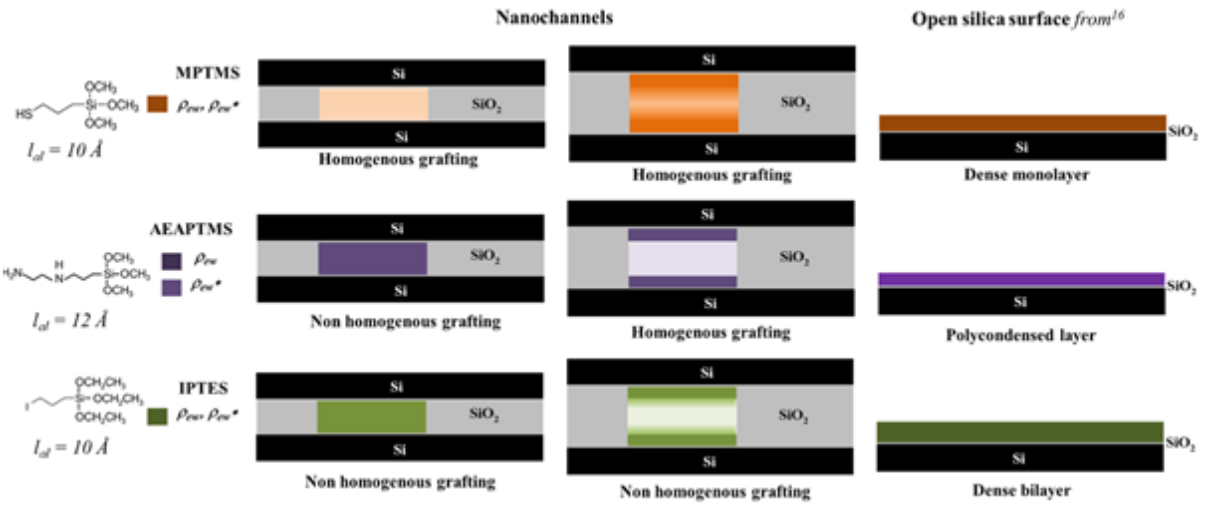

Figure HL4-2. Experimental results: the organization of the different grafted layers (MPTMS, AEAPTMS, IPTES) has been observed, and different behaviors depending on both the nature of the grafted molecule and the height of the nanochannel have been evidenced, quite different from those observed in open surface configuration.

In conclusion, we showed that hard X-ray reflectivity is a very valuable technique to probe confined media. Using bespoke silica nanochannels, we could evidence the factors at play for the efficient grafting of molecules for surface functionalization. We show that the results obtained in open surfaces are not directly applicable to nanoconfined media. Further works will try to evidence the combined effect of surface curvature and nanoconfinement on the grafting efficiency, e.g. using nanoporous silica.

6.5 HL5 Solid/solid wafer bonding interfaces

F. Rieutord[1], M. Tedjini[2], V. Larrey[2], F. Fournel[2]
[1] CEA-Grenoble/IRIG, [2] CEA-Grenoble/LETI

Motivations Hard X-ray synchrotron reflection and scattering are key techniques to obtain information on these so-called buried interfaces,that are difficult to study using other techniques. We have specially developed on the GMT goniometer *interface reflection techniques* that proved very valuable for the study of the mechanics of interface equilibrium and sealing.

Direct bonding is a subject of both applied and fundamental interest:

-as an applied subject: it is a technique that allows the assembling of two different materials, whatever their atomic structure or their physical properties. As such it is a complement to epitaxy when new interfaces are to be built, with extended possibility as for example the possibility of assembling crystalline materials on amorphous substrates. The most famous example is Silicon-on-Insulator substrates (SOI) where a layer of crystalline silicon is on top of an insulating amorphous silicon oxide. The capability of direct bonding does not restrict to producing interfaces between materials. It can be used to put a “lid“ over a patterned surface, resulting in a buried system of channels, voids etc.. that can be used to study nanofluidics or more generally flows in a confined system.

- as a fundamental subject: these interfaces are test vehicles to study the adhesion between solids, especially at small scale. The fundamental issues here concern the role of surface roughness, of long and short distance attractive forces, or the role of a confined adsorbed fluid layer at the interface. Mechanics and elasticity at small scale play a large role. As mentioned, direct bonding on patterned substrate can be used to produce nanochannels, where fundamental research on flow of standard and charged fluids including ion adsorption can be conducted.

Hard X-ray synchrotron reflection and scattering techniques are able to fully characterize the interface parameters (with, depth, roughness spectrum etc..) . The sensitivity is so good that even minute transport of materials along the interface could be evidenced, opening the way to nanofluidics studies. An example will be described below:

Flow of water in nanometer gaps

When bonding two solids together, even flat silicon wafers, an interface is formed between them which exhibits some voids, due to the unmatched roughnesses of the two solids. When bonding two flat and clean (hence hydrophilic) silicon wafers, this gap has sub-nanometric width and is partially filled with water. This can be evidenced using hard X ray reflection, as the beams are able to cross one full wafer thickness to reach the interface.

The reflectivity signal gives information about the width (fringe period), the depth (fringe contrast) of the nanometer interfacial gap. Even more detailed information can be obtained from the full signal analysis, or from off-specular scattering.

Thanks to the high flux of the BM32 beamline, this interface structure can be measured at different points, as a function of time. As a consequence, we could study the dynamics of the water front propagation along the interface.

The sketch of the experiments is shown below (Fig H5-1). At time t=0, an excess of water is put on the open edge of the wafer (the entrance of the nanogap) and the interface electron density profile is probed at different distances and times.

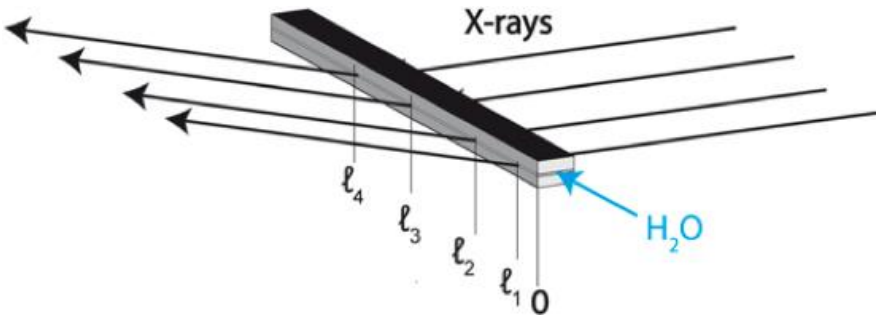

Fig. H5-1: Schematics of the XRR experiment, water intake takes place at l=0and t>=0. XRR measurements of the interface were taken at l1=1mm, l2=4mm,l3=10mm, and l4=17mm from the water input.

As shown Fig. H5-2 a & b, the interface electron density changes as a function of distance or time: this demonstrates that, despite the high confinement (<1nm), the water is still able to flow[1] in the gap.

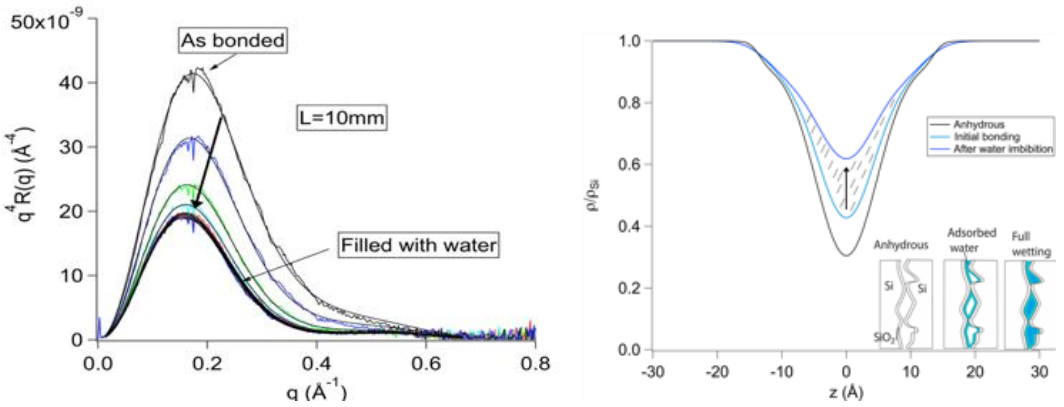

Fig.H5-2: a) Evolution with time of the interfacial reflectivity, at 10mm from the wafer edge due to water intake. Time lag between curves is 1.5h. b) Evolution of interface electron density profile corresponding to the reflection curves of fig H5-2a.

The nature and dynamics of this imbibition flow has been studied. Contrary to flow in microscopic channels, the imbibition front is not sharp but spreads with the wet distance (Fig.H5-3). Yet the mean position of the water front can be easily extracted and plotted as a function of time.

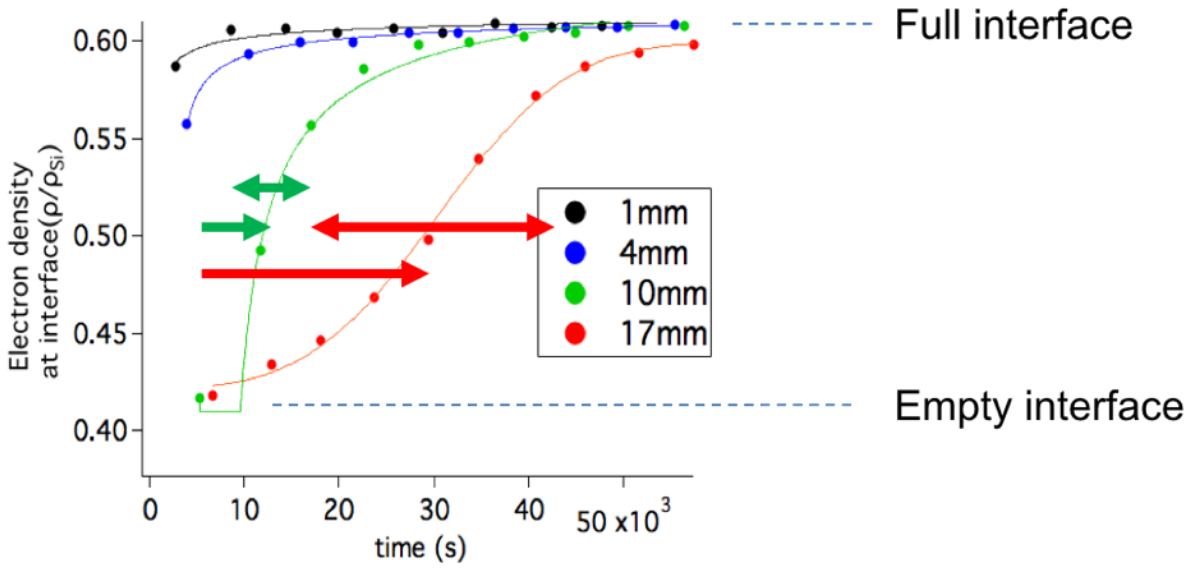

Fig. H5-3: Evolution with time of the interface density associated to the arrival of flowing water. The delay between observation points located at different distance from the edge (saturated with water) is clearly visible, together with the increase of the front width.

It can be shown that distance of the imbibition varies with square root time, as for a diffusion process. Yet the physics is different: the dynamics is here a balance between a driving force (here: wetting of the hydrophilic interface) and a resistive force (the viscous shear force associated to the flow of the liquid between the walls of the channel). The dynamics can be described by an equation which resembles the diffusion except for a square dependence with water amount n.[2]

$$\frac{\partial n}{\partial t} - \frac{D}{2n_0}\frac{\partial^2}{\partial x^2}(n^2) = 0$$

The solution to this equation (so-called Porous Medium Equation, PME) predicts, with our boundary conditions, a profile of finite width, intermediate between the sharp profile of the fluid capillary flow and the infinite width of the diffusion equation solution (see fig H5-4)

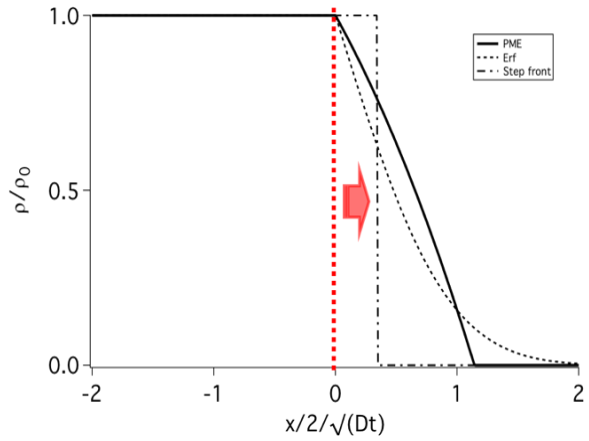

Fig. H5-4: Solution of the different models for fluid propagation in the interface gap. The macroscopic fluid mechanics model predicts a sharp step function (dot-dashed curve), while a diffusion model would predict an infinite breadth erf-like profile (dotted line). The Porous Media Equation predicts a broadening front whose extension remains finite, in between the two previous models (solid line).

References

[1] Tedjini, M.,et al., Appl. Phys. Lett. 109, (2016): 111603.
[2] Rieutord F.,et al., ECS Transactions 86 (2018) 39.

6.6 HL6 Energy storage materials

Operando Raman Spectroscopy and Synchrotron X-ray Diffraction of Lithiation/Delithiation in Silicon Nanoparticle Anodes

S. Tardif, E. Pavlenko, L. Quazuguel, M. Boniface, M. Maréchal, J.-S. Micha, L. Gonon, V. Mareau, G. Gebel, P. Bayle-Guillemaud, F. Rieutord and S. Lyonnard, ACS Nano 2017, 11, 11306-11316

CEA-IRIG and BM32 beamline

Abstract: *Operando Raman spectroscopy and synchrotron X-ray diffraction were combined to probe the evolution of strain in Li-ion battery anodes made of crystalline silicon nanoparticles. Lithiation/delithiation of the silicon under limited capacity conditions triggers the formation of "crystalline core–amorphous shell" particles, which we evidenced as a stepwise decrease in core size, as well as sequences of compressive/tensile strain due to the stress applied by the shell. We experimentally confirmed the two-phase and single-phase models of the lithiation of crystalline and amorphous Si, respectively. We also evidenced critical experimental conditions for accurate operando Raman spectroscopy measurements due to the different heat conductivity of lithiated and delithiated Si. Values of the stress extracted from both operando XRD and Raman are in excellent agreement and valuable for electrochemomechanical modeling of the anodes. Finally we confirmed the continuous increase of the internal compressive strain, unfavorable to the Si lithiation and contributing to the capacity fading.*

The need for “greener” and mobile energy sources has been a massive drive for the research and development of new energy storage technologies. The Li-ion batteries (LiB) are now ubiquitous and the technology is now within the theoretical limits of the usual materials such as graphite electrodes. Silicon has been foreseen as an interesting candidate for the next generation of LiB, as it possesses a theoretical specific capacity (number of stored ion per unit mass) about ten times larger than graphite (3580 mAh/g vs 372 mAh/g). Yet, the Li insertion mechanism in Si is fundamentally different from that in graphite. In graphite, Li ion are reversibly intercalated between the graphene sheets, causing a 10% expansion along the c-axis at full charge (LiC_6). In crystalline Si, the alloying with Li will first amorphize the material (at room temperature) and then possibly recrystallize at the maximum Li content ($Li_{15}Si_4$).

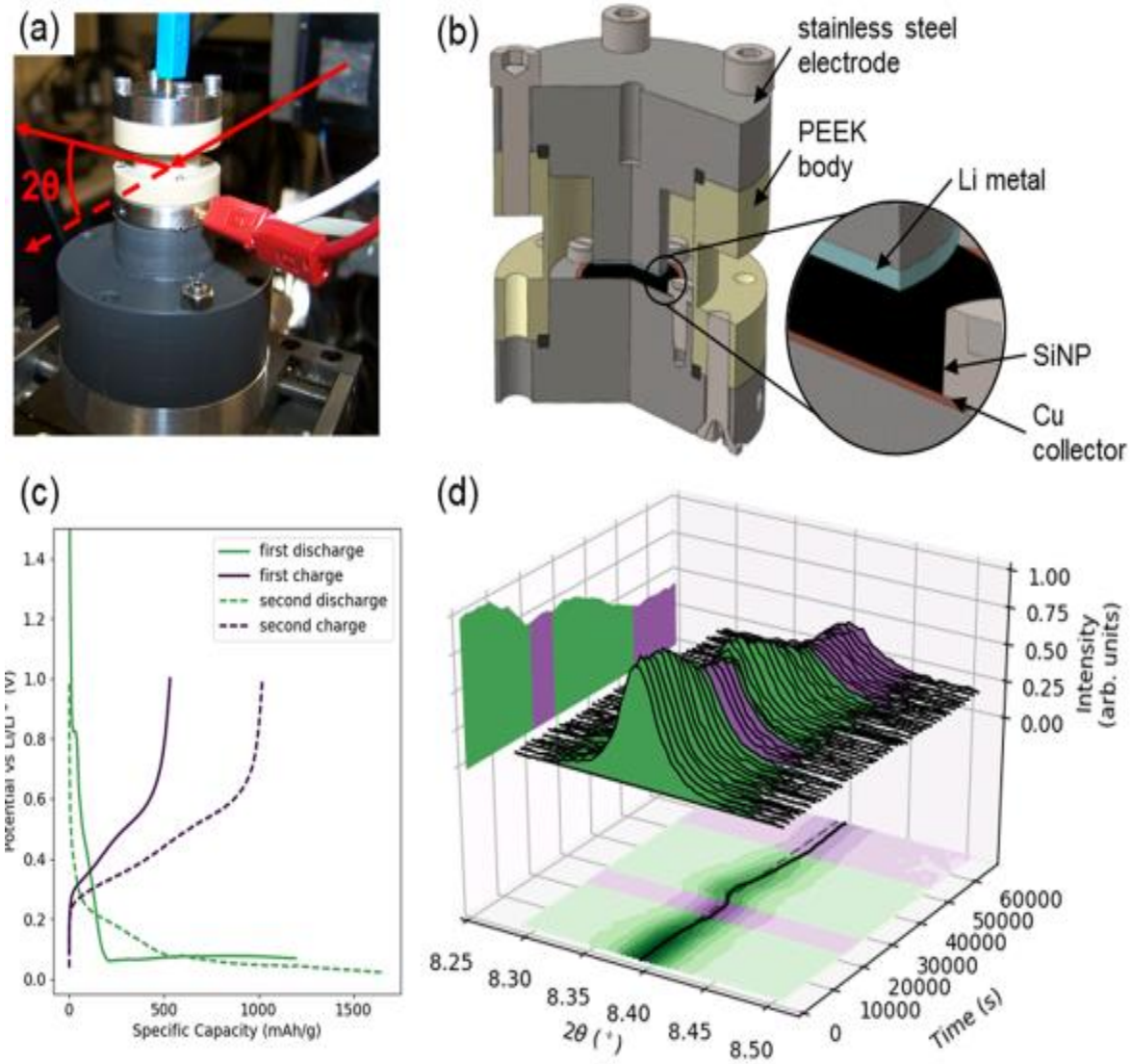

Figure H6-1. Principle of the experiment: (a) photograph and (b) sketch of the electrochemical half-cell, (c) electrochemical cycling of the cell and (d) operando measurement of the Si 111 Bragg reflection.

Upon delithiation the Si remains amorphous. At maximum lithiation, the volume change is tremendous, on the order of 300%. This is highly detrimental to the electrode stability as it can crack the Si which will expose new surfaces to the electrolyte (thereby consuming irreversibly Li ions), or cut the electric contact to the current collector. One common approach to mitigate

these effects is to use nano-sized Si particles (SiNPs). Additionally, stress has a strong impact on the electrochemical potential, on the order of 60-120 mV/GPa. However, no experimental results have been reported so far on the study of strain and stress in crystalline SiNPs during repetitive lithiation/delithiation, and the results from stress/strain models have yet to be experimentally demonstrated over several cycles.

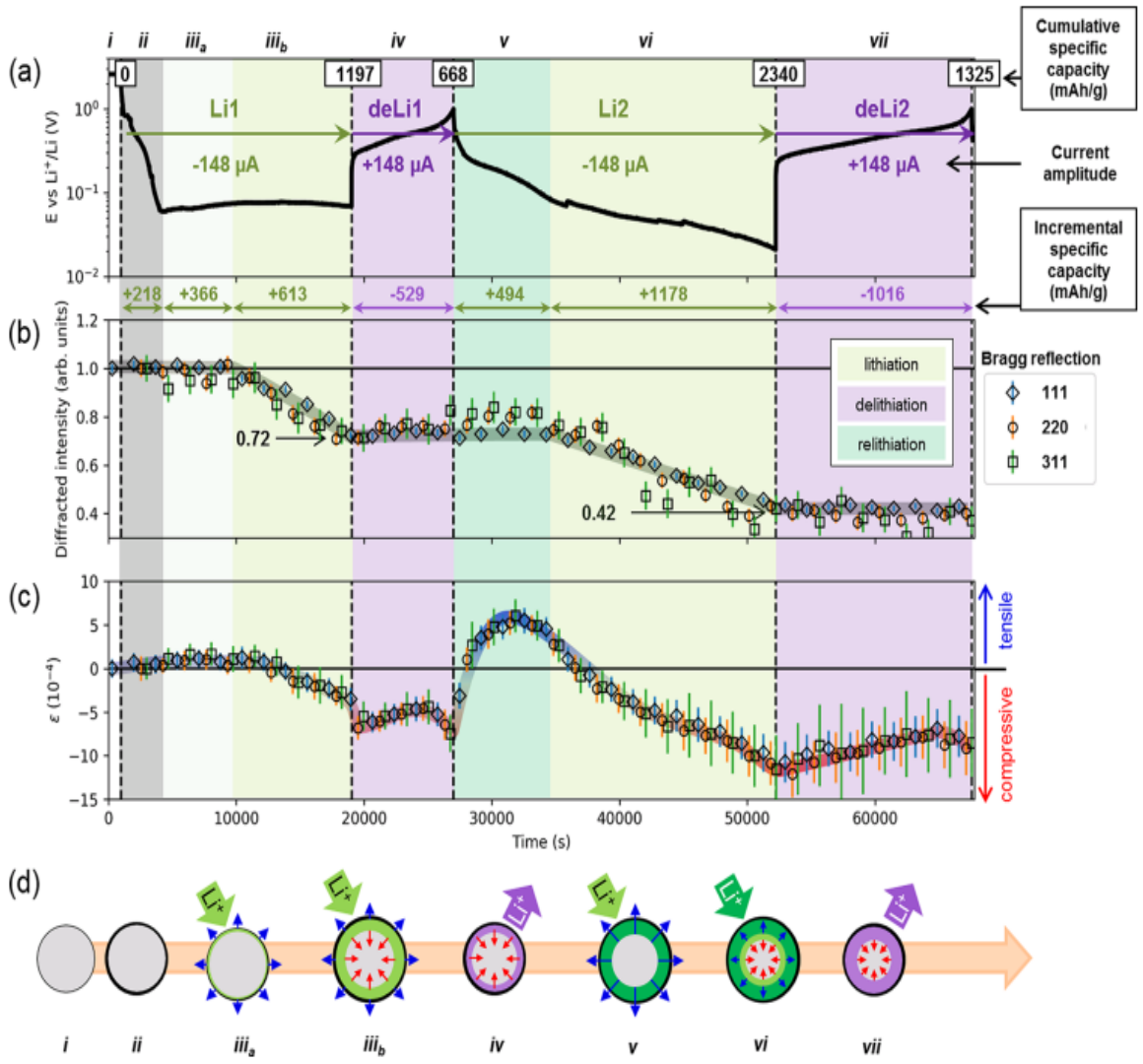

Figure 2. (a) Cell potential, (b) intensity of the SiNP Bragg reflection, and (c) strain in the SiNP over the first two partial lithiation/delithiation cycles, as well as (d) a schematic view of the lithiation/delithiation process in the SiNP. Different steps corresponding to variations in the integrated intensity and/or the strain are identified (colored areas, green for lithiation, purple for delithiation). For each step (i to vii), values of the current amplitude and incremental and cumulative specific capacities are reported. In the cartoon representing the single-core−shell (first cycle) and double-core−shell (second cycle) mechanisms, compressive and tensile states are schematized using red and blue arrows, respectively. The crystalline core is colored in gray, and the outer amorphized shell in green on lithiation and purple on delithiation.

We used operando X-ray diffraction and a bespoke electrochemical cell to probe the evolution of the strain in the crystalline core of SiNPs anodes, as illustrated in Figure H6-1. The anode material consisted in SiNPs mixed with a polymer binder and deposited on a copper foil. The

anode was installed in the cell in a glovebox at the ESRF ElectroChemical-Lab just prior to the experiment, and the cell was set up on the GMT goniometer, with a few degree incidence on the surface (Fig. H6-1a,b). We used hard X-ray (27 keV) to penetrate through the 15 mm diameter cell and also to be able to access higher order reflections without masking by the cell electrodes. The electrochemistry was controlled by a Biologic potentiostat to control the applied current, measure the potential across the cell and calculate the corresponding capacity (Fig.H6-1c). A Ge 111 crystal analyzer and a photomultiplier were used for the detection by scanning the 2θ arm. Several Bragg reflections were measured (Si 111, 220 and 311), and diffraction from the Cu current collector was used as an internal control (Fig. H6-1d). As mentioned before, the lithiation of crystalline silicon results in the amorphization of the crystal, therefore we only used partial cycling (limited lithiation of about 30% of the anode) to observe the evolution of the stress in the crystalline core.

The intensity and peak position from the X-ray diffraction of the SiNPs is shown in Figure H6-2, along with the electrochemical data. We can describe the results as follow: (i) the pristine SiNPs are first measured in open-circuit, then (ii) the initial potential drop corresponds to the Solid-Electrolyte Interphase formation. At step (iii) the potential reaches a plateau: the lithiation of the SiNPs begins. Smaller or disordered particles are probably lithiated first, then the diffraction starts to decrease linearly as the crystalline material becomes amorphous. The resulting strain on the core is compressive, which can be understood from the lithiation mechanism of crystalline Si. During the lithiation of crystalline material, a two-phase model was proposed, where the lithiated, amorphized Si is separated from the pristine, crystalline Si by a sharp lithiation front. This front being trapped between the outer lithiated shell and the pristine core, the volume expansion occurring at the front location applies a compressive strain on the core. Upon delithiation (iv) the compressive stress is maintained by the now plastified shell. The relithiation (v) of the amorphized Si is now a single phase mechanism, that is diffusion-driven. No new Si material is lithiated, as shown by the constant diffraction intensity. Thus the stress is relaxed by the tensile stress applied by the inflating shell. When the shell is fully lithiated, (vi) the lithiation front resumes its progression towards the core, the Si material is amorphized (decreasing diffraction intensity) and a compressive stress is now applied. The second delithiation (vii) is essentially similar to the first one. These results are consistent with additional measurements in the laboratory, using operando Raman spectroscopy.

In conclusion we have evidenced in real time the effects of lithiation and delithiation on crystalline Si nanoparticles for Li-ion batteries with operando X-ray diffraction and Raman spectroscopy. Using progressive limited capacity cycling, we have shown that the initial lithiation of crystalline Si (a two-phase reaction) and subsequent lithiation of amorphous Si (a single-phase reaction) in a confined core−shell geometry result in different strain profiles during the battery cycling, as expected from theoretical models.Our operando diagnosis of the strain and stress in SiNPs provides experimental figures that are much needed for the benchmarking of theoretical models of lithiation/delithiation in SiNPs and for the further rational design of SiNP-based electrodes minimizing the internal stresses via morphology and surface/volume ratio optimization.

6.7 HL7 2D Topological Semimetals Grown by Molecular Beam Epitaxy

Topological Dirac and Weyl semimetals [1], often called the « new 3D graphene», are a new state of matter that shows linear dispersions (Dirac cones) in all three dimensions in the reciprocal space. Weyl fermions predicted by quantum field theory have never been observed in free space, so their low energy « incarnations » in semimetals offers a unique opportunity to merge high energy elementary particle physics with condensed matter. Discovering and engineering topological semimetals from the family of 2D Transition Metal Dichalcogenide materials could open the way for exploitation of their unique topological properties by fabricating thin epitaxial films and devices on suitable crystalline substrates. 2D $HfTe_2$, $ZrTe_2$, $TiTe_2$ and $MoTe_2$ thin films have been grown on technologically important AlN/Si and InAs/Si substrates at the Epitaxy and Surface Science Laboratory (ESSL) of INN / NCSR DEMOKRITOS in Greece. ESRF synchrotron GIXD and STEM at INAC show that the materials are rotationally aligned with the InAs substrates having low in-plane mosaicity (lowest observed so far) and a clear quasi van der Waals (vdW) gap with the substrate indicating high quality vdW epitaxy.

6.7.1 Example 1: Stabilisation at room temperature of the topological weyl semimetal phase in epitaxial MoTe2 atomically thin films

P. Tsipas, S. Fragkos, D. Tsoutsou, C. Alvarez, R. Sant, G. Renaud, H. Okuno, A. Dimoulas

Univ. Athens, Greece, CEA-IRIG and BM32 beamline

Adv. Funct. Mater. ***28****, 1802084 (2018)*

Abstract: Epitaxy of $MoTe_2$ on InAs(111) favours the formation of the orthorhombic (Td) non-centrosymmetric phase, which is a topological type-II Weyl semimetal. Its stability at room temperature is a result of tensile strain from the substrate, which stabilises an elongated interlayer antibonding state characteristic of Td-$MoTe_2$.

It has been shown in the literature that bulk or free-standing films of the 2D material $MoTe_2$ adopt orthorhombic stacking at temperatures lower than 250 K, i.e. non-centrosymmetric, and so $MoTe_2$ is classified as a type-II topological Weyl semimetal. At room temperature, $MoTe_2$ is stable in the monoclinic phase, and is centrosymmetric with trivial topology (no Weyl nodes exist). This work demonstrates that atomically thin $MoTe_2$ films produced by molecular beam epitaxy are stabilised in the Weyl semimetal Td phase at room temperature as a result of the influence of the InAs(111)/Si(111) substrate. The Td-$MoTe_2$ phase has been directly probed by HRSTEM measurements (Figures H7-1), where orthorhombic stacking is clearly observed. In-plane reciprocal space mapping, performed at beamline BM32/INS2, shows a complex diffraction pattern (Figure 2) characterised by closely spaced triple diffraction spots, as a result of the overlapping of 60° and 120° rotated domains. These diffraction spots allow for an accurate estimation of the in-plane lattice constants a and b of the 2x1 reconstructed surface unit cell (Figure H7-2 b-d) characteristic of the Td-$MoTe_2$ phase, while out-of-plane diffraction

(l-scans) yields the out-of-plane lattice constant, c. It is concluded that, due to the influence of the substrate, the lattice parameters of the epitaxial films are enlarged with respect to experimental values obtained from bulk or freestanding films, which has important implications given that the electronic band structure is sensitive to the lattice parameters. Indeed, first principles calculations by density functional theory (DFT) predict that epitaxial films with enlarged lattice parameters have 8 Weyl points with energies only 1.1 and 12.9 meV below the Fermi energy, which makes them accessible to angular-resolved photoelectron spectroscopy (ARPES) and to transport measurements. It is worth noting, however, that the presence of rotation domains adversely affects the resolution of in-situ ARPES, so resolving the closely spaced Weyl points is difficult. Moreover, the enlarged lattice parameters affect the band structure along ΓA direction of the Brillouin zone so that the B1 band (Figure H7-1d) is fully occupied lying below the Fermi energy. The occupation of this band, which is made of interlayer antibonding states (Figure 1d), favours the orthorhombic Td phase with elongated Te-Te distances across the van der Waals gap, thus making the Td phase more stable than the monoclinic one at room temperature [2]. Since prototypical Weyl semimetals (*e.g.* TaAs) are 3D crystal structures mainly found in bulk form, discovering and engineering topological semimetals from the family of 2D transition metal dichalcogenide materials that are stable at room temperature (e.g. Td-$MoTe_2$) could open the way for exploitation of their unique topological properties by fabricating thin epitaxial films and devices on suitable crystalline substrates.

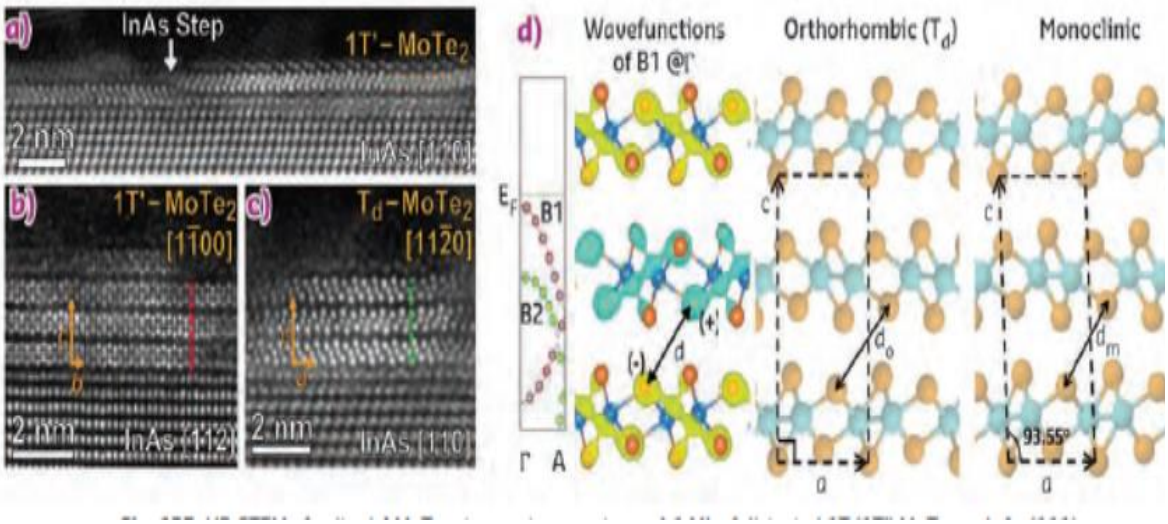

Fig. H7-1: HR-STEM of epitaxial MoTe2 at room temperature. a) 1 ML of distorted 1T (1T') MoTe2 on InAs (111) substrate. b, c) Orthorhombic (Td) stacking of the 1T' MoTe2. d) From left to right: portion of the band structure along ΓA, wave functions of band B1 at Γ showing the interlayer antibonding state between Te, orthorhombic (Td) stacking and monoclinic stacking.

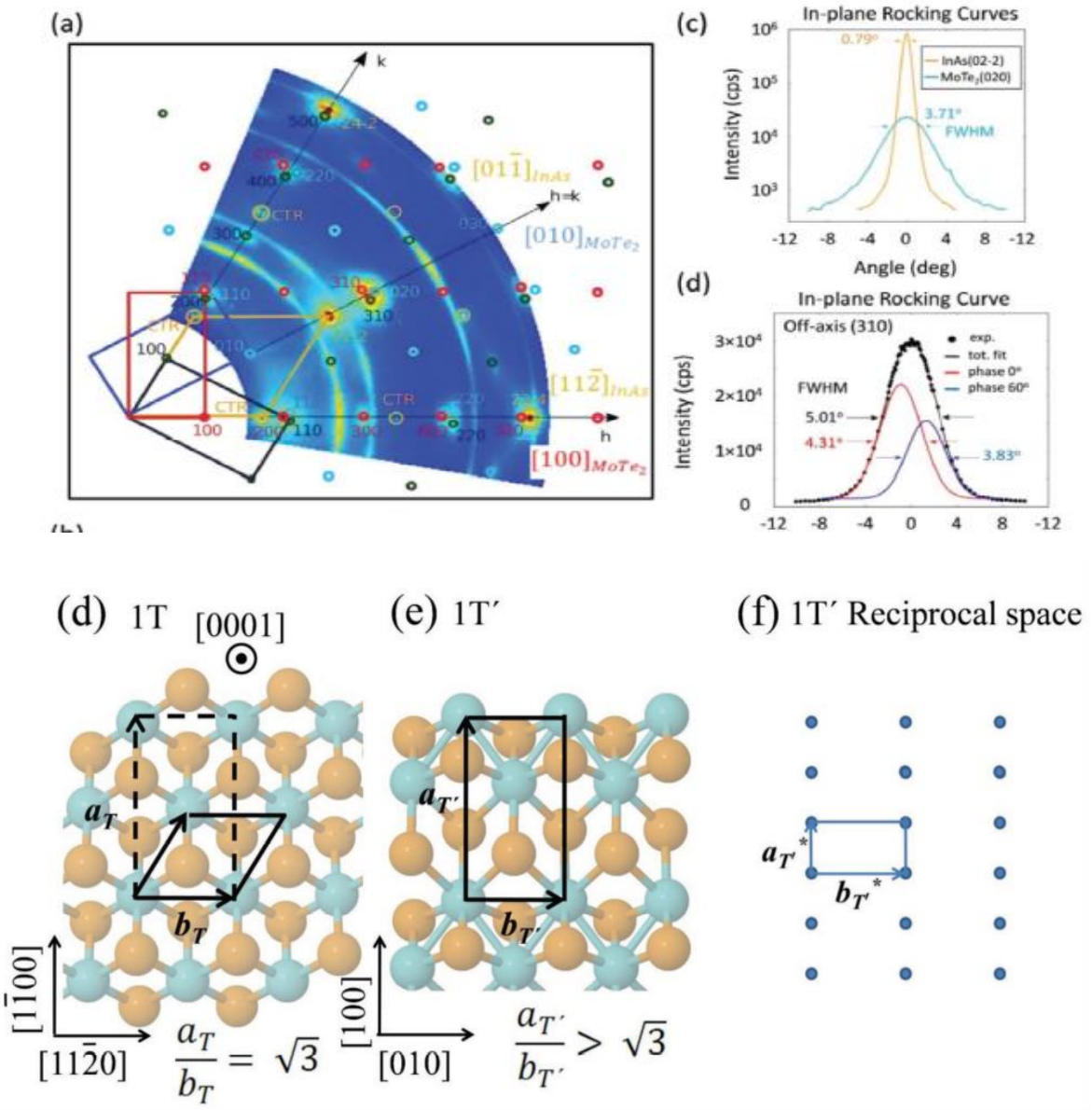

Fig. H7-2: Reciprocal space of epitaxial distorted (1T') MoTe2. a) In-plane reciprocal space mapping by GIXD at BM32. The rectangles show the surface unit cell of the reciprocal space corresponding to domains rotated by 60° between each other. d) The hexagonal surface unit cell of undistorted 1T MoTe2 in real space. e) The 2x1 unit cell of the 1T' MoTe2. f) Reciprocal space of 1T' MoTe2 showing a surface unit cell.

References

[1] N. P. Armitage et al., Rev. Mod. Phys. 90, 015001 (2018).
[2] H.-j. Kim et al., Phys. Rev. B 95, 180101 (R) (2017)

6.7.2 Example 2: Room temperature commensurate charge density wave in epitaxial strained TiTe2 multilayer films

S. Fragkos, R. Sant, Carlos Alvarez, Alexei Bosak, Polychronis Tsipas, Dimitra Tsoutsou, Hanako Okuno, Gilles Renaud, Athanasios Dimoulas

Univ. Athens, Greece, CEA-IRIG, ESRF and BM32 beamline

Adv. Mater. Interfaces ***6, 2019****, 1801850*

Abstract: The group IVB 2D transition metal dichalcogenides (TMD) are considered to be stable in the high symmetry trigonal octahedral (1T) structure due to the lack of unpaired *d*-electrons on the metal site. It is found here that multilayer epitaxial $TiTe_2$ is an exception adopting a commensurate 2×2×2 charge density wave (CDW) structure at room temperature with an ABA type of stacking as evidenced by direct lattice imaging and reciprocal space mapping. The CDW is stabilized by highly anisotropic strain imposed by the substrate with an out-off-plane compression which reduces the van der Waals gap increasing the interlayer coupling. A weaker 2×2 CDW is also confirmed at RT for epitaxial monolayer $TiTe_2$. The addition of epitaxial strained $TiTe_2$ to the family of CDW materials is expected to deepen our understanding on the CDW formation mechanisms in other TMD materials, still under debate and enable real world applications that take advantage of a CDW ground state at room temperature.

After several decades of research on CDW in 2D TMDs and the debate about the associated mechanisms, the common wisdom is that the softening of an acoustic phonon and the electron-phonon interaction are involved in the formation of a PLD and an associated CDW. In our multilayer $TiTe_2$ the stronger intensity superstructure spots are obtained at the L points of the Brillouin zone (Fig. H7-3) implying that softening of an acoustic phonon with wavevector = is at the heart of the commensurate 2×2×2 PLD/CDW formation in multilayer $TiTe_2$ at RT, similar to the $TiSe_2$ case, while hints of localized conduction electrons at the Fermi surface from ARPES measurements indicate polaronic effects likely associated with the CDW. Softening of an acoustic phonon with = as also predicted by theory and evidenced by the very weak superstructure peaks at M (Fig. H7-3) in GIXD could be responsible for the CDW observed at RT in 1 ML $TiTe_2$.

In free-standing $TiTe_2$ multilayer films with relaxed lattice parameters and a sizeable v.d. Waals gap, the weakly coupled Te-Ti-Te (tri)layers do not favor the propagation of the CDW-driving phonons through the layers, probably explaining the absence of CDW in multilayer films. In our epitaxial films though the situation is different, because a significant interaction with the substrate is established producing an anisotropic strain such that the in-plane parameter is enlarged and the out of plane parameter along the *c*-axis is compressed by 2.3% as accurately measured by synchrotron GIXD, yielding an estimated stress ~0.6-0.8 GPa if a measured bulk modulus *B* ~ 0.28-0.40 GPa is assumed. The compression results in an appreciable reduction of van der Waals gap from ~ 3.2 Å to the value of 3.1 Å that we measured by STEM bringing the Te-Ti-Te trilayers closer between each other thus enhancing interlayer Te-Te interactions, signifying a transition from a 2D to a 3D-like $TiTe_2$ crystal. We anticipate that this transition to a 3D structure facilitates the propagation of the important phonon modes along ΓL which are required to propagate across tightly coupled $TiTe_2$ layers

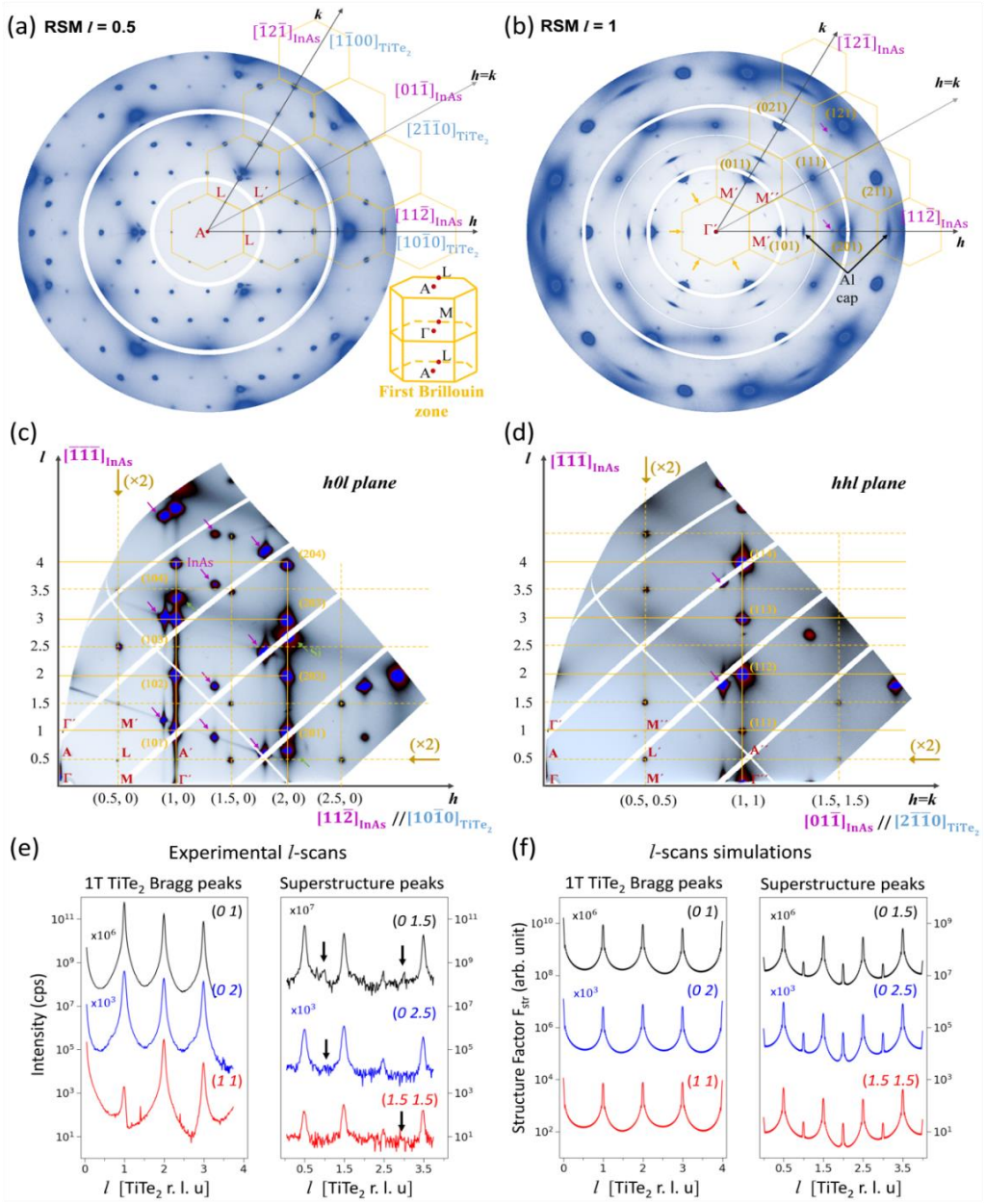

Figure H7-3. *Reciprocal space mapping of CDW 50 ML TiTe2. a) RSM for l = 0.5 (a) and l = 1 b). The honeycomb-like yellow grid shows the projection of the Brillouin zone (BZ) structure (inset) with red letters marking high symmetry points of the first BZ and neighboring BZ (primed and double primed). Yellow numbers in (b) show surface Miller indices of 1T TiTe2 Bragg peaks located at the center (Γ points) of BZ, in contrast to superstructure spots (not indexed) in (a) which are located at the edge (L points) of the BZ. Yellow arrows in (b) show weak superstructure peaks located at the M points of the BZ while magenta arrows show InAs diffraction peaks. Imaging of portion of the h0l c) and hhl planes d). The 1T TiTe2 Bragg peaks are located at the crosspoints of the vertical and horizontal yellow solid lines (guides to the eye) and have all integer hkl values. The superstructure (satellite) peaks are located at the crosspoints of the vertical and horizontal yellow dotted lines and have half integer hkl values. The magenta and green arrows show Bragg peaks of InAs and Si, respectively. e) The experimental l-scans for a selection of (hk) pairs showing peaks at integer or half integer l for 1T TiTe2 Bragg and superstructure peaks, respectively. The black vertical arrows in the right panel indicate very weak superstructure peaks at integer l which are associated with the weak spots at M points seen integer l RSMs. f) Simulation of l-scans in terms of the structure factor using the CDW ABA stacking model showing qualitative agreement with the experimental data in (e).*

in thick films or bulk material to provide the source of instability that drives the CDW distortion at RT which is sustained up to 400 ^{o}C.

The analysis based on the anisotropic strain correlates well with predictions in $TiSe_2$ stating that the CDW critical temperature is enhanced under biaxial tensile (stretching) strain (compression along the c-axis). Our analysis correlates also nicely with the recent experimental results reporting the emergence of CDW in a $TiTe_2$ multilayer under 1.8 GPa non-hydrostatic pressure (effectively uniaxial compression along the *c*-axis as in our films) also providing hints of a re-entrant 2×2 CDW with an estimated critical temperature above RT. The latter appears during the decompression phase around 0.5 GPa, which is similar in magnitude to the epitaxial stress exerted on our films (0.6-0.8 GPa, see above).

6.7.3 Example 3 : Beyond van der Waals Interaction: The Case of MoSe2 Epitaxially Grown on Few-Layer Graphene

MT Dau, M. Gay, D. Di Felice, C. Vergnaud, A. Marty, C. Beigné, G. Renaud, O. Renault, P. Mallet, T. Le Quang, J.-Y. Veuillen, L. Huder, V. T. Renard, C. Chapelier, G. Zamborlini, M. Jugovac, V. Feyer, Y. J. Dappe, P. Pochet, and M. Jamet

CEA-Grenoble/IRIG and LETI, Inst. Néel, Grenoble, CEA-Saclay/SPEC, Paris-Saclay, P. Grünberg Institute, Jülich, Germany

ACS Nano ***2018****, 12, 2319*

Motivations The aim of this proposal was to study vertical 2D heterostructures based on transition metal dichalcogenides and graphene, which is also an attractive structure for exploring new physics in 2 dimensions. We aimed to characterize the structural properties of the top layer $MoSe_2$ and to unveil the van der Waals epitaxial registry between the TMDs layer and graphene-SiC, which has been so far not reported yet.

In the present report, we focus only on the results obtained with the $MoSe_2$/Graphene-SiC heterostructure. Three samples have been characterized, of $MoSe_2$ thicknesses of ~0.7 ML, ~1 ML and 3.5 ML on multilayer graphene on SiC(0001).

The diffraction from three hexagonal lattices is clearly visible on the in-plane rsm: the hardly visible peaks of the SiC(0001) substrate; the peaks from the multilayer graphene grown on it also hardly visible, and finally and those of the $MoSe_2$ thin layer, in the form of wide, in-plane textured, rings of scattering. No other feature is visible. The position of these peaks (together with out-off plane ones, not shown), yields the following epitaxial relationships: SiC[10-10](0001) // Gr[1-100](0001) // $MoSe_2$[1-100](0001). This finding indicates that the in-plane lattices of graphene and MoSe2 commensurately align to each other, whereas the SiC substrate lattice rotates at an angle of 30° with respect to the two adjacent overlayers. The exact lattice parameters of the multilayer graphene and of $MoSe_2$ were deduced by fitting the positions of the corresponding Bragg peaks along radial scans. The widths of these peaks

were also used to estimate the in-plane domain size.The in-plane mosaic spreads were deduced from rocking scan measurements across the graphene and $MoSe_2$ peaks. No evolutions were found with varying momentum transfer Q, thus showing the peak widths are completely dominated by in-plane mosaic spread. The out-off plane thickness and structure, and in particular the stacking sequence, were determined by simulating the rods of scattering by the $MoSe_2$ layer. The position of the out-off plane allowed and forbidden Bragg peaks

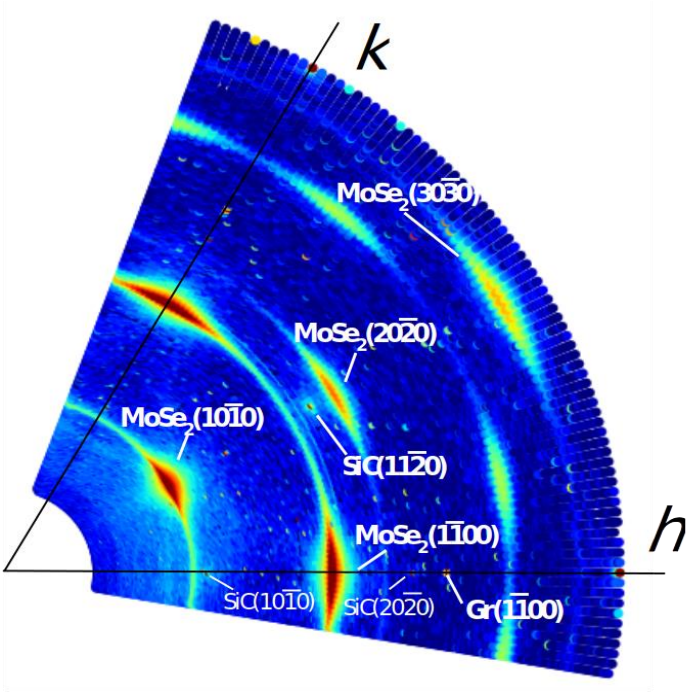

Figure H7-4. In-plane reciprocal space map (rsm) of the 3.5ML–thick $MoSe_2$ sample (right), measured by rocking the sample over 80° at increasing values of the in-plane SiC(0001) reciprocal lattice units h and k with increments of 0.01. The Si(0001) unit cell, is hexagonal with 3.079Å and 10.05Å lengths, respectively in-plane and out-off plane lattice parameters. The out-off plane value is close to zero; the intensity being integrated over =0.1. Note that a 3D measurement is actually performed thanks to the 5° long detector perpendicular to the surface, covering an -range between 0 and 0.75. The color scale is logarithmic, the highest (red) intensity being 106 ph/seconds and the background ~80 ph/s.

allowed to unambiguously demonstrate that the $MoSe_2$ layer is of 1H (2H) structure. Note that these fits yield a 3 to 4 % expansion of the $MoSe_2$ inter-plane distances perpendicular to the surface.

From this study, it was found that crystallographic directions of the $MoSe_2$ lattice align perfectly along the ones of the graphene lattice, resulting in only one commensurate configuration. This reveals a novel feature of the vdW epitaxy where the vdW interaction between the two layers was revised. The latter guides all domains of the $MoSe_2$ layer orienting along the graphene. This finding suggests the unique configuration of epitaxial registry between $MoSe_2$ and graphene which enables for orientation-independent investigation of heterostructure properties without anisotropic effect.

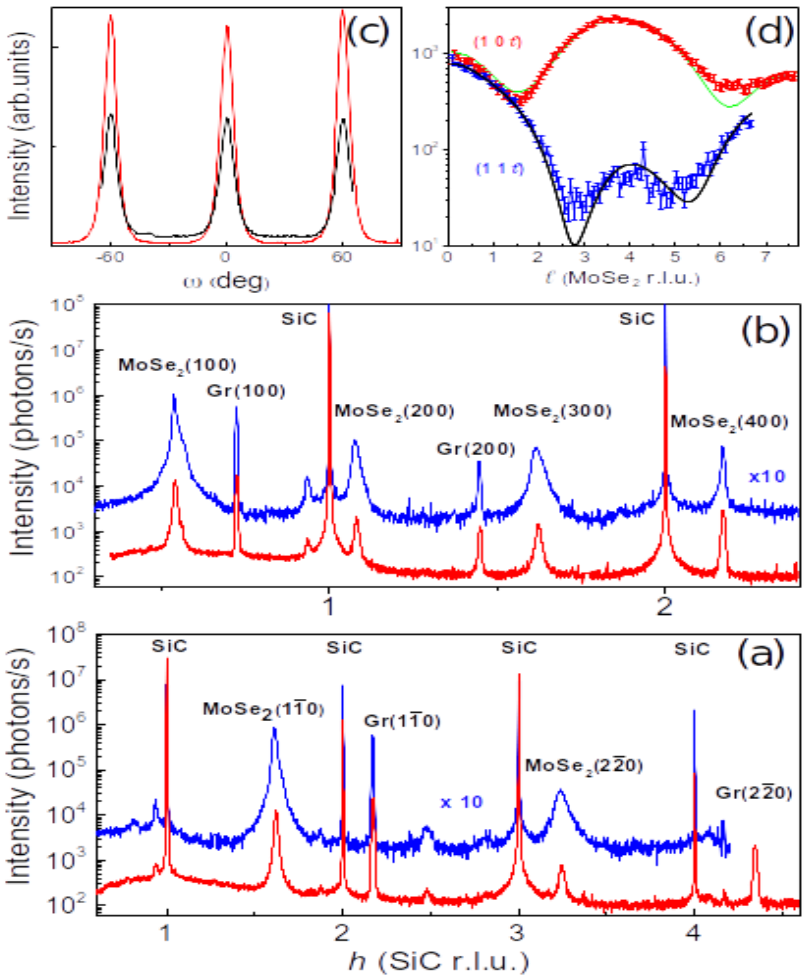

Figure H7-5: (a) Radial scan along the in-plane (h00) direction for the 1 ML (red) and 3.5 ML (blue, multiplied by 10) MoSe2-thick samples, crossing the following Bragg peaks, in order of increasing h : $MoSe_2$(1 00), Gr(1 00), $MoSe_2$(2 00), and Gr(2 00). (b) Radial scan along the in-plane (hh0) direction for the 1 ML (red) and 3.5 ML (blue, multiplied by 10) $MoSe_2$-thick samples, crossing the following Bragg peaks, in order of increasing h=k : $MoSe_2$(H0-H0), Gr(H0-H0),with H=1,2,3 and 4. (c) Azimuthal rocking scans across the $MoSe_2$(10 0) reflection, for 3.5ML (red) and 1 ML (black). (d) Measured intensity along the 10 (red) and 1 (blue) rods of $MoSe_2$ for the 1 ML-thick sample together with simulated rods (green and black lines, respectively) for a perfectly 1ML-thick $MoSe_2$ layer of H-type structure. On the figure, the standard 3 index notation (hkl) is used. The four hexagonal four index notation is (hkil) with i=-(h+k).

6.8 HL8 Structure and chemical order in ultrathin films by resonant x-ray scattering

Inversion parameter in cobalt ferrites thin films

M. De Santis, A. Bailly, I. Coates, S. Grenier, O. Heckmann, K. Hricovini, Y. Joly, V. Langlais, A. Y. Ramos, M. C. Richter, X. Torrelles. S. Garaudée, O. Geaymond, O. Ulrich,

Inst. Néel, Grenoble, LMPS, Cergy-Pontoise, ICMAB Barcelone, Spain, CEMES, Toulouse, BM32 beamline

Acta Cryst. ***B 75****, 8 (2019), DOI: 10.1107/S2052520618016177.*

Abstract: Cobalt ferrite ultrathin films are among the best candidates for spin-filtering at room temperature. A key parameter determining their properties is the inversion degree in their spinel structure. Using the INS2 instrument, $CoFe_2O_4$ thin films were grown on Ag(001), and the cations occupancy distribution was determined through *in situ* x-ray resonant diffraction measurements collected at both the Co and Fe *K* edges. The data analysis was performed using FDMNES, an ab initio code already extensively used to simulate x-ray absorption spectroscopy

Cobalt ferrite is an insulating ferrimagnetic oxide with a high Curie temperature. Alongside its low cost, these properties make it attractive for a wide range of applications. Its spinel crystal structure (space group *Fd-3m*) is comprised of a distorted face-centered cubic sublattice of O^{2-} anions in which, one eighth of the tetrahedral lattice holes and one half of the octahedral lattice holes are occupied by cations (Fe^{3+} or Co^{2+}). This results in the general formula AB_2O_4, where *A* and *B* refer to the cations located in the tetrahedral and octahedral sites respectively. In the normal spinel structure, *A* sites are occupied by divalent cations, and *B* sites by trivalent cations. In the inverse spinel structure, the divalent cations occupy half of *B* sites and the trivalent cations occupy the remaining *A* and *B* sites. The degree of inversion typically depends on the sample preparation conditions. DOS calculations predict that the electronic band gap at the Fermi level differs for majority and minority spins. The size of the band gap, however, depends on the degree of inversion. The use of ferromagnetic or ferrimagnetic insulating films in multilayered structures is an efficient way to generate highly spin-polarized currents due to the exponential relationship between tunneling probability and the spin-dependent barrier height.

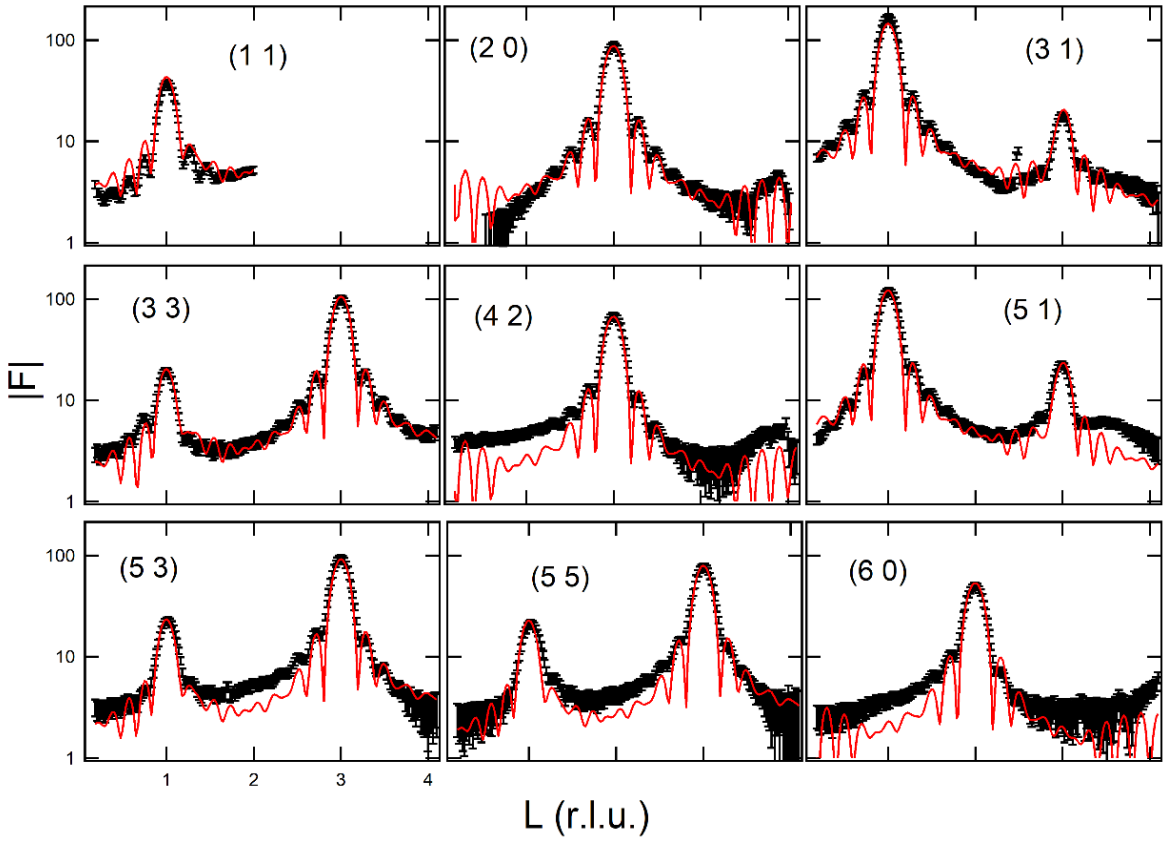

Figure H8-1. Experimental $CoFe_2O_4$ film structure factors measured along 9 inequivalent rods with relative error bars (black symbols), and best fit (continuous, red line).

Cobalt ferrite thin films were grown on a Ag(100) single crystal using the INS2 UHV chamber and following a procedure already employed for the elaboration of magnetite films of similar structure. A cobalt ferrite seed layer was initially prepared by a three-step method. Firstly, 2 Co ML and 4 Fe ML were co-deposited on the substrate kept at room temperature, forming an epitaxial metallic alloy. After deposition, an oxide layer was formed by dosing with O_2 at a pressure of 10^{-6} mbar. Finally, the sample was annealed in oxygen. Following the deposition of the seed layer, the film thickness was increased by reactive codeposition in oxygen at 750 K, until it reached a thickness of about 4 nm.

The film was studied by GIXRD, and its structure was solved by the quantitative analysis of the film diffraction rods (Fig.H8-0) and of the substrate CTR. The oxide film is (001) oriented, and its in-plane [100] direction is aligned with the [100] one of the silver substrate, indicating epitaxial growth. The lattice constant and the structure factors are very close to the cobalt ferrite bulk ones, and both its interface and surface are relatively flat.

However, since the iron and cobalt non-resonant atomic form factors are close in magnitude, standard diffraction methods cannot give reliable values for the film's inversion parameter, i.e. the relative Co and Fe occupancies of tetrahedral and octahedral sites. For this reason, the intensity changes of several ferrite film diffraction peaks were measured by scanning the energy close to both the Fe and the Co absorption K edges. Experimentally, this requires the diffractometer circles to move in such a way that the (HKL) position is kept fixed while scanning

the energy. These energy scans are shown in Fig. H8-2 for a set of 6 peaks at both edges and for 5 additional peaks at the iron edge only. Some of these peaks exhibit a very strong intensity variation, which makes this technique very powerful in determining the stoichiometry of the octahedral and tetrahedral sites of the spinel structure. For example, the (202) and (602) reflections are sensitive to the tetrahedral cation sites only, while the (222) and (622) ones to the octahedral ones only. A quantitative analysis requires the precise knowledge of the resonant contribution to the scattering factors, which is very sensitive to the oxidation state and to the environment of the selected element. Here this resonant contribution was calculated using FDMNES, an ab initio code already extensively used to simulate XANES and RXD. A best fit gives Co tetrahedral and octahedral sites occupancies of 13±5% and 46±3%, respectively. This results in an inversion parameter of 0.88±0.05, a quite large value when compared to that one obtained for bulk samples.

A next step will be the incorporation of such films in a multilayer system to realize a magnetic tunnel junction.

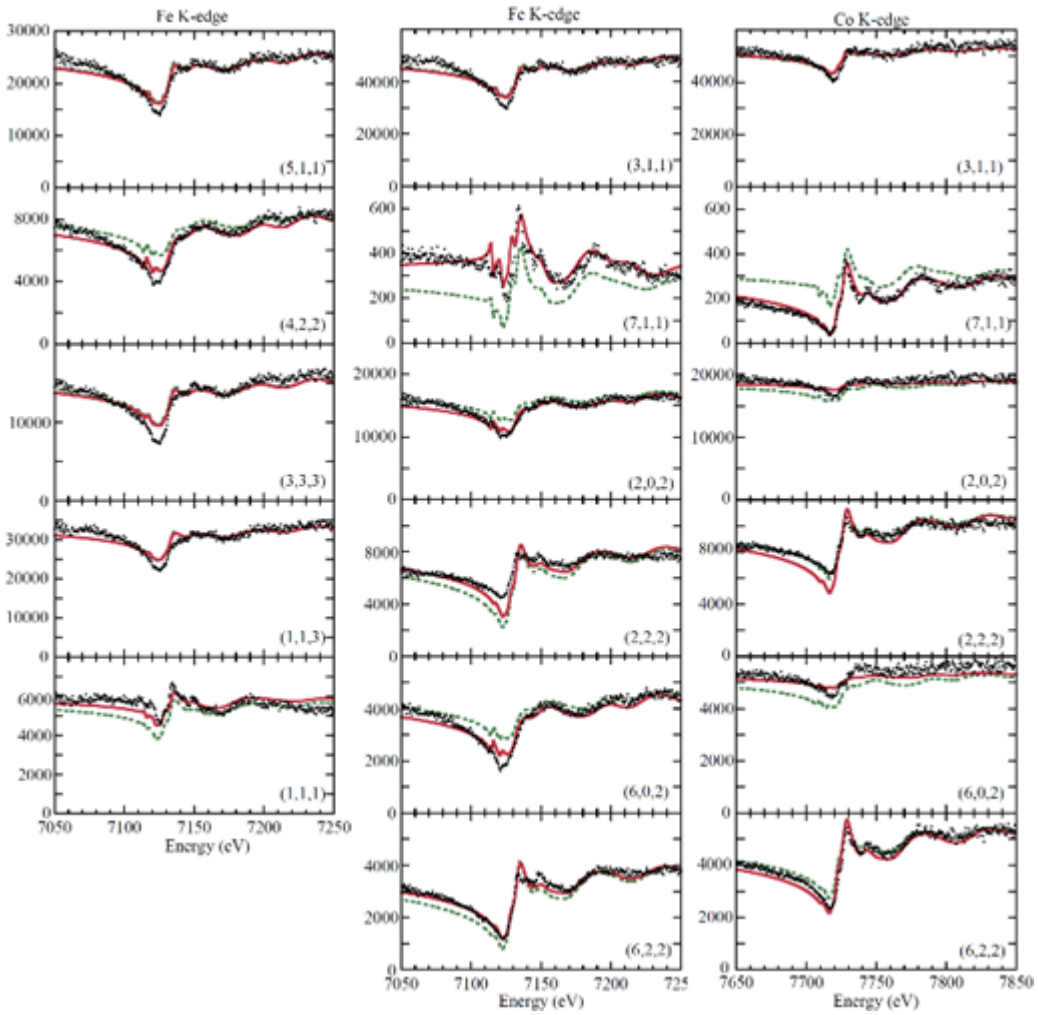

Figure H8-2. Experimental RXD of selected (HKL) reflections at the iron (left and central columns) and cobalt (right) K edges (black symbols), calculated intensity for best fit occupancy (continuous red lines) and for statistical occupancy (dashed green lines).

6.9 HL9 Atomic structure of ultrathin film solved by surface x-ray diffraction

Growth-mode and structure of epitaxial ultrathin MgO/Ag(001) films.

M. De Santis, V. Langlais, K. Schneider and X. Torrelles.
Inst. Néel, Grenoble, ICMAB Barcelone, Spain, CEMES, Toulouse, BM32 beamline

Abstract: MgO ultrathin films are widely used as electron tunneling barriers in electronics and spintronics. They are also well suited for on-surface-synthesis of molecular networks for 2D electronics. Here the structure of a MgO/Ag(001) film in the monolayer thickness range elaborated *in situ* under well-defined conditions is solved quantitatively using the INS2 set-up.

Thin metal oxide films are of great technological importance for applications. Ultrathin insulating films provide precise electrostatic coupling and electron tunneling from a conducting substrate to a second electrode or to adsorbed nanostructures. The ability to engineer nearly perfect ultrathin oxide layers, up to the limit of monolayer thickness, is a key issue. Their increasing technological importance calls for a thorough understanding of their structure. Magnesium oxide is the insulating material of choice in spintronic and is important in catalysis as template for metallic clusters. Growth of non-polar (001) oriented MgO films results in general in a high crystalline quality and in high performances e.g. as tunneling barriers. MgO films grow (001) oriented on Ag(001) and, in the monolayer thickness range, form islands within a large temperature range. The flattest and largest MgO islands are obtained at a growth temperature close to 600 K. This surface has been widely investigated mainly by STM, which however does not allow to resolve some structural details.

Here a MgO film was grown *in situ* by reactive molecular beam epitaxy. About 0.8 Mg ML were evaporated on a clean Ag(001) substrate kept at 620 K, with the chamber backfilled with molecular oxygen at a partial pressure of 10^{-6} mbar. At low coverage, MgO films are in coherent epitaxy on Ag(001), and their structure can be determined by SXRD measuring the substrate CTR. In this experiment a set of 140 reflections were measured, 83 of which non-equivalent, distributed along the (10), (11), and (20) CTR. The capability of surface x-ray diffraction to solve the detailed atomic structure of ultrathin films relies on the collection of precise and accurate structure factors along the CTR. Nowadays and for synchrotron-based x-ray diffraction experiments, the error bar in the measurements is mostly determined by the accuracy and not by the photon statistics. Accuracy is evaluated by the variance $\boldsymbol{\varepsilon}$ of a large enough set of symmetry-equivalent reflections. In the present experiment, which is a test for quantitative structure determination using the new INS2 set-up, we got a variance of 1.7%. This can be considered as the state of art for SXRD, and allowed for solving the structure.

Figure H9-1 shows the experimental MgO/Ag(001) CTR. The data exhibit a bump in the middle between two Bragg peaks, characteristic of a bilayer growth mode. This is confirmed by the quantitative analysis. The structural model consisting of a monoatomic thick MgO layer on top of the silver surface results in quite a bad fit, giving a χ^2 of 22. The agreement improves drastically considering a bilayer growth mode. The final refinement is achieved considering an MgO bilayer covering almost half of the surface and a clean Ag region, resulting in a χ^2 of 2.3. The best fit values (covered fraction S_{MgO}, interlayer spacings *d*, Debye parameters *B*, and roughness parameter $\boldsymbol{\beta}$) are reported in TABLE H9.

TABLE H9. Best fit parameters of the bilayer model.

	MgO-covered	uncovered	Bulk	Clean Ag(001) [1]
$S_{MgO-1,2}$	0.38(8)	-	-	
$d_{Ag2-Ag3}$ (pm)	205.6(4)		2.0425	206(2)
$d_{Ag1-Ag2}$ (pm)	204(1)	201(1)	2.0425	203(2)
$d_{MgO-Ag1}$ (pm)	273(4)	-	-	
d_{MgO} (pm)	213(4)	-	2.1065	
B_{Ag2} ($\times 10^4$ pm^2)	1.1(2)		0.66	0.95
B_{Ag1} ($\times 10^4$ pm^2)	1.5(3)		0.66	0.95
B_{MgO} ($\times 10^4$ pm^2)	0.9(6)	-		
β	0.06(1)			
χ^2	2.3			

The refinement was performed taking oxygen on top of silver and Mg in hollow sited at the interface, as suggested by DFT calculations. A refinement with oxygen in hollow sites results in a relatively good qualitative agreement (blue dotted curves in Fig.1) but in a definitively worst quantitative one with a χ^2 of 7.2. Other interface geometries can be definitively ruled out.

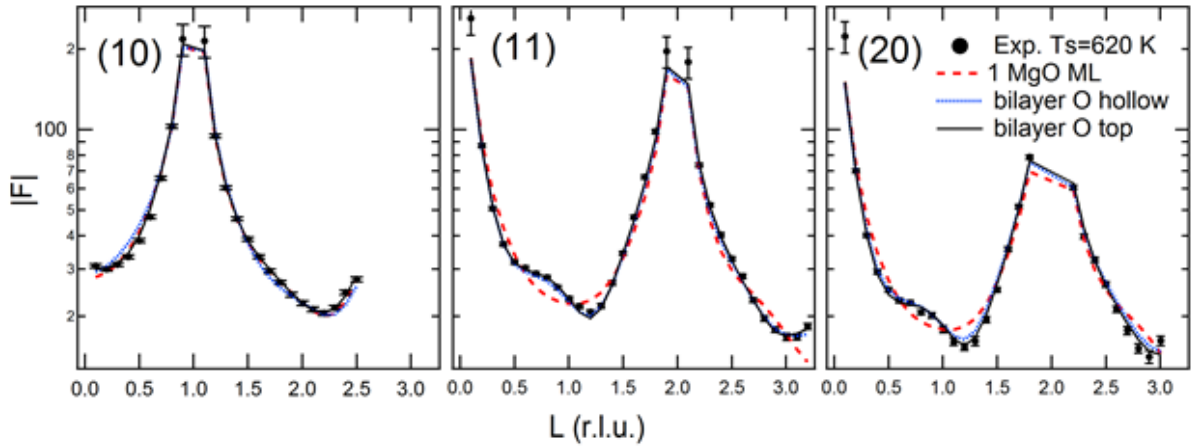

Figure H9-1. Experimental MgO/Ag(001) CTR with error bars (filled black circles) and best fits for the MgO monolayer model (dashed red curves), the bilayer model with oxygen on Ag surface hollow sites (dotted blue curves) and the best model with oxygen on top (black continuous lines).

This example shows as INS2 is well suited to solve the structure of well-ordered ultrathin films in coherent epitaxy on the substrate, also in the unfavorable case of light elements monolayers on heavier substrate atoms, and in the presence of atoms with low atomic scattering contrast as Mg and O.

Reference

*[1] Meyerheim et al. , Z. Kristallogr. **212**, 327 (1997).*

7 Future perspectives and possible plans for further development of the beamline

Based on a choice made in 2017, the BM32 beamline will benefit from a short bending magnet as a new source located in the EBS storage ring with increased brilliance. In June 2020, we have submitted the project MAGNIFIX which aims at upgrading the beamline components (mirrors, monochromator, detector), pushing the actual Laue setup to a higher level of capability and providing efficient tools of data handling for users to interpret their data. In the following paragraphs we will describe the perspectives and the developments that are required to meet the present and future needs of the users on the three instruments without or hopefully with MAGNIFIX funds. First, we report the simulated properties of SBM32 and the first diagnosis made during summer 2020. Then in the first 3 paragraphs we present the minimal perspectives and activities directions on each instrument. Finally, we will draw the main arguments and impacts of MAGNIFIX on the development of the beamline.

7.1 General perspectives seen in the perspective of EBS

The short-bending magnet (SBM). The new EBS machine led to a complete storage ring lattice refurbishment by keeping the public ESRF ID beamline. However, the new lattice has strong impact on BM ports of all CRG beamlines. 4 new source models were designed to fit into a very narrow and constrained space. The choice of the new source has been made in 2017, after X-ray tracing computations according to the X-ray emission model of shadow software and parameters from the ESRF machine division. We rejected the 2-Pole-Wiggler solution - even if it would offer a doubled flux -, due to X-ray signal pollution from a new D2QC element in the storage ring (for deviation and correction electronic trajectory) located a few meters upstream. This parasitic signal could not have been eliminated before reaching the sample by

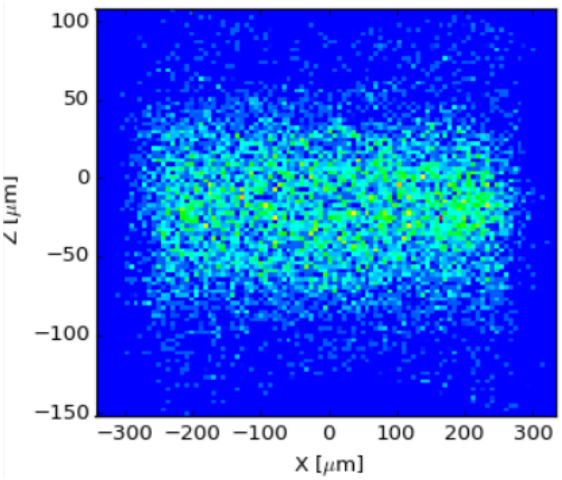

Figure P1: Simulated beam size in monochromatic mode (GMT and INS2 with polished M1) hxv = 500 x 100µm² (with current horizontal focusing scheme). Current vertical size is 200 µm.

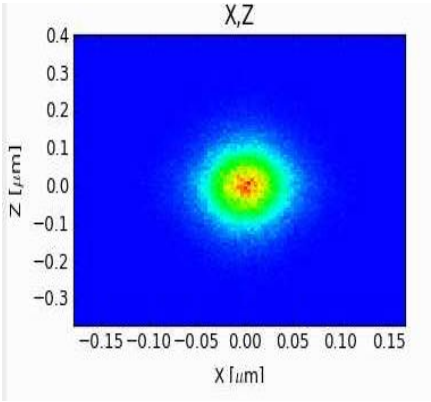

Figure P2: Simulated X-Ray tracing for Laue microdiffraction mode µLaue in Exp. hutch 1 (EH1) with perfect optics elements (no slope errors): Flux X15, beam size (hxv)= 140 x 60 nm². Or Flux X30, beam size = 200 x 100 nm².

any means in our beamline. Sample would have been illuminated by an additional wide beam leading to a high background signal to the detriment of sensitivity of scattering experiments at grazing incidence (performed in INS and GMT). Hence, to keep flux at the same past level, we retained the SBM source that was installed in June and tested in July 2020.

Several comissioning beamtimes from end of August 2020 were dedicated to assess the new beam properties. All optical elements have not been changed but only shifted horizontally. As expected, the flux is rather unchanged with the EBS (first estimation: 3 10^{11} photons/s/3 10^{-4} eV at 27 keV full acceptance, a slightly lower than in 2018), while vertical position beam stability is greatly improved which is very valuable for grazing incidence scattering measurements and Laue microdiffraction. Also simulations of the monochromatic vertical beam size downgrading due to detrimental slope errors along 1 m long mirrors are confirmed by experiments. However in polychromatic mode, the well-polished center part of the last optics mirror (M2) allows to image properly the EBS reduced source. Notably, the vertical size of the secondary source has been divided by two. As a result white beamsize of 200 x 200 nm^2 has been successfully achieved at sample position (also thanks to KB mirrors new polishing).

MAGNIFIX upgrade

In monochromatic mode, hxv = 500 x 200 μm^2 is still observed and will be improved by M1 & M2 state of the art polishing and the reduction of sagittal focusing aberrations (figure P1). We foresee to reach the ultimate beam shape and size by a zero anti-clastic deformation of the illuminated 2nd monochromator crystal area by designing Si/Si molecular bonding which decouple mechanical and x-ray reflective properties. Moreover Ge(111)/Si will also bring a net gain in flux of 2.5 for the majority of experiments performed on the beamline.

Regarding Laue microdiffraction we expect a huge increase of performance in terms of flux (X15-X30) by installing the setup in Exp. Hutch 1 by directly imaging the EBS source (without secondary source). Inserting a toroidal mirror (instead of M2) would also significantly increase the flux at sample by collecting more photons in horizontal direction (currently 50 µm). Studies are in progress to find the best compromise between beamsize and flux taking into account alignment time and stability.

7.2 Foreseen research directions

7.2.1 INS2

As discussed above, the INS2 instrument has been upgraded in 2016 and was operated for 2 years and a half only before the shutdown. This interval was a bit short to display all the functionalities and to have a return from users allowing to plan further developments of the instrument.

One technique that we would like to implement in the next years is resonant x-ray diffraction. XRD is a technique where both the power of site selective diffraction and the power of local absorption spectroscopy regarding atomic species are combined. It has shown its capability to solve questions as the charge ordering in transition metal oxides, or the surface magnetism in metallic alloys, and can give an important contribution to the study of phase transitions in

thin films, whatever their nature – structural, magnetic, metal-insulator, etc. An example is shown in HL8, which demonstrates that BM32 beamline optics is very well suited for resonant scattering experiments. However, in the case of ultrathin films, of weak reflections, or in presence of a substrate fluorescence yield, the signal to analyze can be hindered by the background. For this reason, we plan to install a graphite crystal analyzer on the detector arm to select the elastic signal of interest.

At the same time, we are planning to implement a sample-holder cooling stage in the UHV chamber. This project, which could be realized in the framework of the study of phase transitions in ultrathin films, is in a preliminary stage and its realization will depend on the pressure of the user community.

7.2.2 µLaue

7.2.2.1 Depth Resolution

Within the submitted MAGNIFIX project we plan to install the Laue setup in a new dedicated hutch (EH1) to take advantage of a tenfold flux at sample focal spot (LaueMAX station). We expect then a major improvement of 3D mapping from flux increase for higher sensitivity and/or data collection speed.

7.2.2.2 Energy Resolution

Regarding the energy measurement by a solid state detector mounted on a side of the setup, moderate upgrade would consist in replacing or single punctual energy dispersive detector by a multilelement one (around 7 SSD) so as to reduce significantly the time of translation from a Laue peak to an other and even measure simultaneously two or more peaks.

In case the MAGNIFIX project is funded, we would expect first to take benefit from the increased flux to improve the statistics of diamond filter scan *i.e.* higher dips position resolution. Second we will purchase and custom an Energy-resolved 2D detector (several 100000 pixels) to measure the full strain tensors and consequently derivate the full stress tensor directly from experiments (both isotropic and deviatoric component) as demonstrated by Abboud et al (see HL3). 2D pnCCD detectors exhibit the highest energy resolution (a few % resolution on each pixel) with frame rate ranging from 0.4 to 2kHz, and are well suited for polychromatic beam illumination. The LaueMAX station will be the first instrument worldwide using routinely such X-ray camera open to users, allowing to measure the full tensors in few minutes instead of more than 10 minutes. Moreover, combining angular resolution (small pixel size) with energy resolution opens up also new characterization methods for coupled chemical and structural mapping. For instance powder diffraction with a microbeam (as complementary measurements to Laue diffraction experimental run) can be envisaged for phase identification in heterogeneous system composed by crystals with different size. In the framework of MAGNIFIX, a new postionning system will be built to place the sample at several distances from focusing mirrors at different inclinations covering beamsize from 100nm to 10 µm (with constant flux). Il will allow to adapt the beamsize to the region of interest for faster measurements or when spatial averaging is requested.

7.2.3 GMT

The GMT goniometer is a multipurpose 2+2 surface diffractometer. The large available volume around the sample allows it to accept a large variety of sample environment ranging from furnaces, cryostats, electrochemical cells and mechanical test machines. Being located in 1:1 position on a bending magnet at esrf, the GMT can receive a well-focused beam of medium to high energy X-rays (30keV typically). This allows the study of buried interfaces using grazing incidence scattering techniques: reflectometry, GISAXS, GIXRD, high resolution RSM… Up to now most of the experiments have been carried out using slits and a point detector (NaI scintillator+ PM). The control electronic of the goniometer has been upgraded to icepap controllers.

Our main future development plan concerns the integration of 2D detectors, and specially the new maxipix CdTe detector. This should greatly enhance our photon collection efficiency allowing simultaneous background and (multi) signal collection. However the use of 2D detector in grazing incidence geometries sets specific problems which will have to be tackled:

- A first problem is the large dynamic of the signal to be recorded. We are close to the direct beam and counting dynamics may be close to 10^{10} on a narrow angular range. We shall develop specific automatic filters to protect the detector from overexposure. Several solutions have been developed on other beamlines, such as the fast overflow bit readout at SOLEIL [Dawiec et al., J. Instr. 11, (2016)]. We propose to explore other approaches, based e.g. on the fluorescence signal from the sensor protection windows.

- A second problem is the large footprint on the sample due to the very small incidence. Of course the higher brilliance of the new EBS source should help reduce the size of the beam and hence of the footprint, but some loss of resolution due the length illuminated is unavoidable. Techniques based on the use of knife edges or of a single detector slit located close to the sample will be explored.

Due to the increased flux at sample and increased detector efficiency, we shall also work on a better automation of the sample change and alignment. We are considering replacing the goniometer head by a hexapod and we expect the travel range of several motions to be increased. This should allow performing some 2D stacking of samples, hence a large number of interfaces to be studied in series, taking advantage of the increased EBS photon flux.

Finally, we envisage to set a stroboscopic data-acquisition system for time resolved measurements with no dead time and particularly suited for second generation X-ray source intermediate flux. Following Gorfman's group setup (Choe et al, IUCrJ(2018).5, 417), lattice parameter or reciprocal space map can be obtained by means of a synchronization and a multichannel analyzer system in case of an applied external periodic solication (temperature, electric field…).

7.2.4 Automation & Data Analysis

A net increase of data produced on the beamline is expected due to the more intensive use of 2D detectors. The management of the data and its (temporary and permanent) storage will follow the data policy of ESRF. Metadata will be systematically added to favor open data and

traceability. The µLaue scanning instrument will still produce most of the data from the beamline in terms of volume in the future. It can amount 5To/6days (For energy measurements with 2D detector, we estimate 10To/6days). Software development is mandatory to exploit fully the data and enable users to interpret them in an efficient way (time and reliability). While scattering techniques benefit from common software tools provided by ESRF IT group (Silx, Pymca), one must still design software tools that fit specific needs in terms of visualisation and rapid evaluation of recorded data.

In general also, to train the users, capitalize the users & staff experiences and facilitate the reuse of code, we will pay much attention to elaborate a browsable gallery of data analysis workflows (notebooks, scripts). Moreover, the new control command software BLISS will be operational on the beamline in few months. It opens new ways to build acquisition systems that interact with analysis software (among them LaueTools) to get access rapidly to physical quantities for monitoring, assistance and feedback. Finally, machine learning will be applied to 2D detector data for sorting or filtering purposes (on a single or a set of images).

8 Annexes

8.1 Annex A Statistical information about the use of the beamline

The following statistics cover the last five years period operation of the BM32 beamline. As a CRG beamline, two selection committees hereafter called ESRF and CRG committee allocate beamtime to European and French users (resp. one third and two thirds). Three instruments share the beamtime: INS2, µLaue and GMT (the two latter are hosted in the same experimental hutch and have some common users).

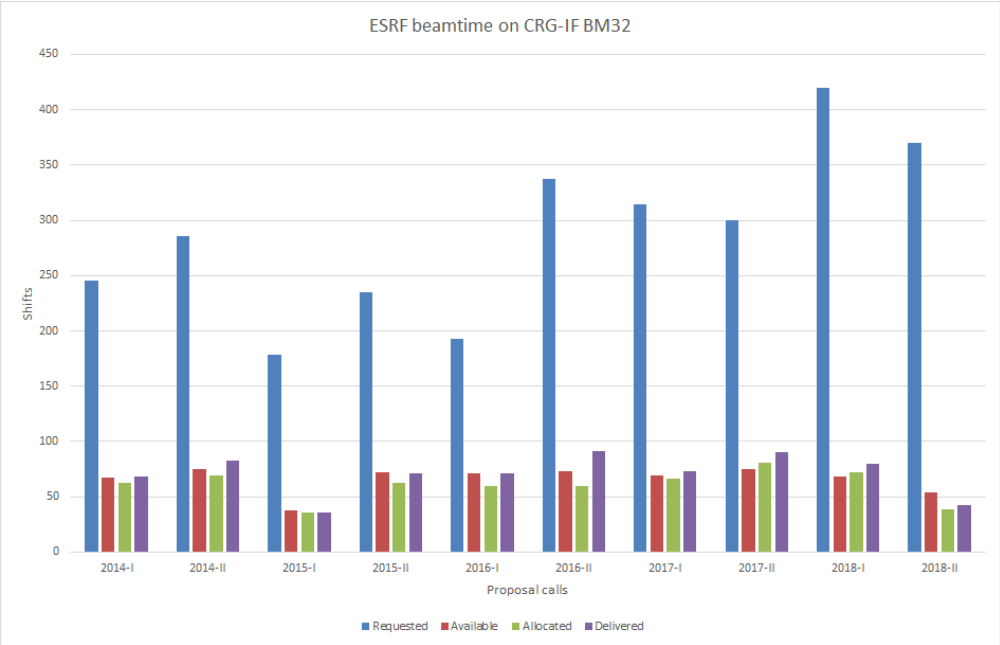

Figure A-1: Evolution of the number of beamtime shifts requested by proposers (blue), available (red) by CRG-ESRF agreement, allocated (green) by ESRF programme committees and actually delivered (violet) to users by the beamline management over the last 5 years calls.

8.1.1 Beamtime exploitation

Beamtime overbooking: 280 shifts (resp. 140 shifts) are allocated for CRG (resp. ESRF) beamtime by program committees of the french synchrotron SOLEIL committee (resp. several ESRF committees) per full operational year. Over the 5 years period. at least 400 shifts per year are requested on BM32 and the mean overbooking ratio (requested/allocated number of shifts ratio) has raised from 3.8 in 2014 and 2015 up to 7.9 in 2018 for ESRF beamtime (fig. A-1). For the CRG beamtime the ratio is respectively lower oscillating around 2. Most of the french users apply to both ESRF and CRG beamtimes. More recently a growing part of them applied only on ESRF beamtime to benefit from travel and accommodation reimbursement. The instruments distribution of requested and allocated beamtime on CRG beamtime in figure A-2 illustrates how the beamtime is shared among the instruments.

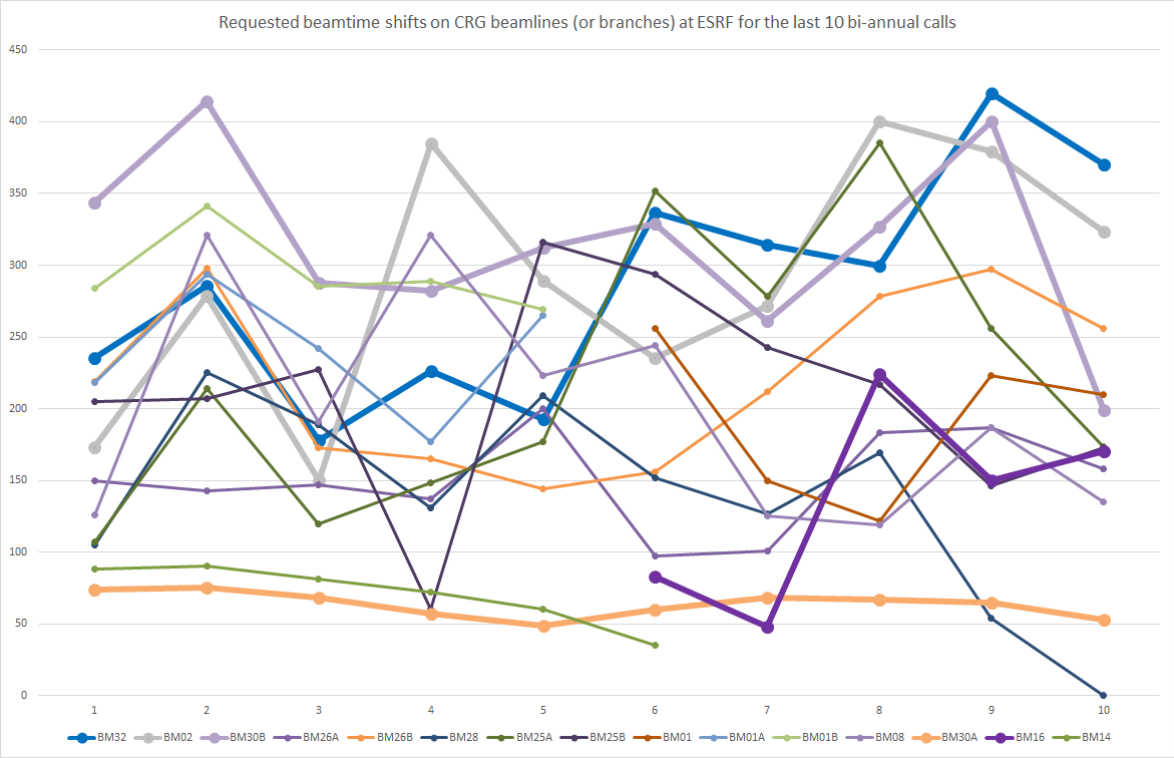

*Figure A-1b: Comparison of requested beamtime on the national CRG branches over the last 10 proposals calls (5 years). Bold lines correspond to french CRG beamlines (**CRG-IF BM32 in blue**) that form the F-CRG group (http://f-crg.fr/).*

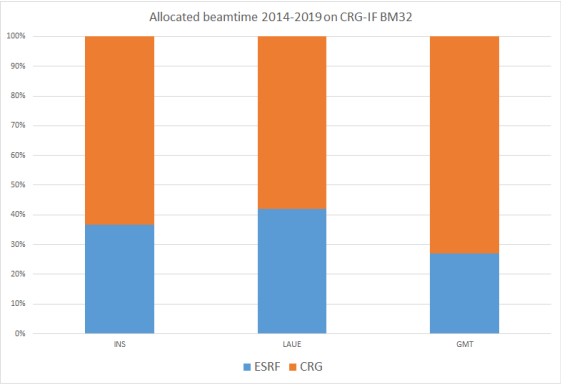

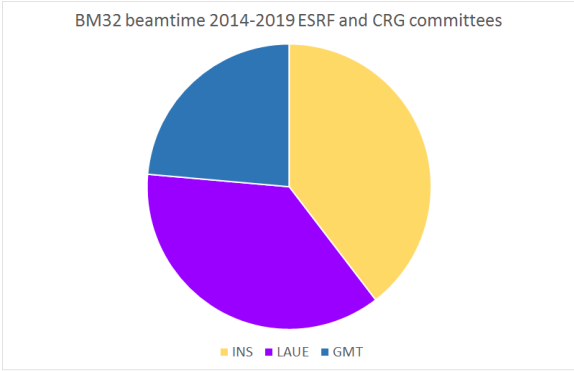

Figure A-2: Distribution of allocated beamtime from CRG and ESRF committees between the three instruments of CRG-IF BM32 (2014-2018).

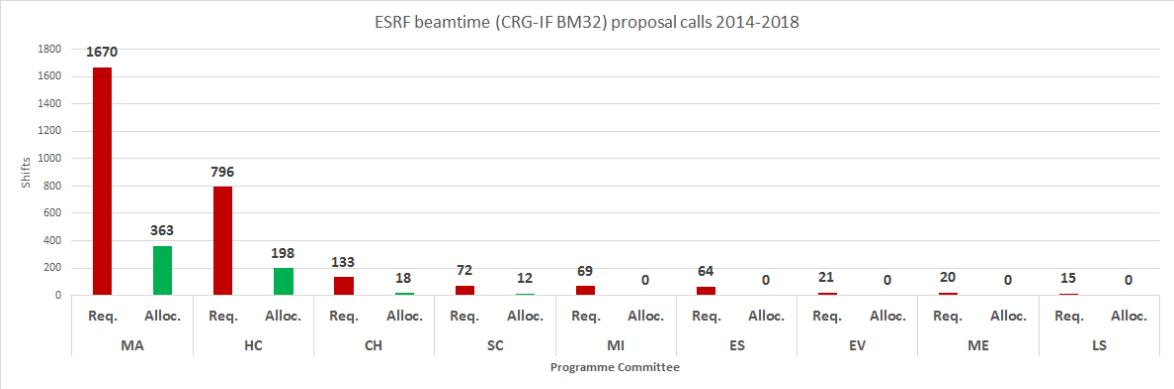

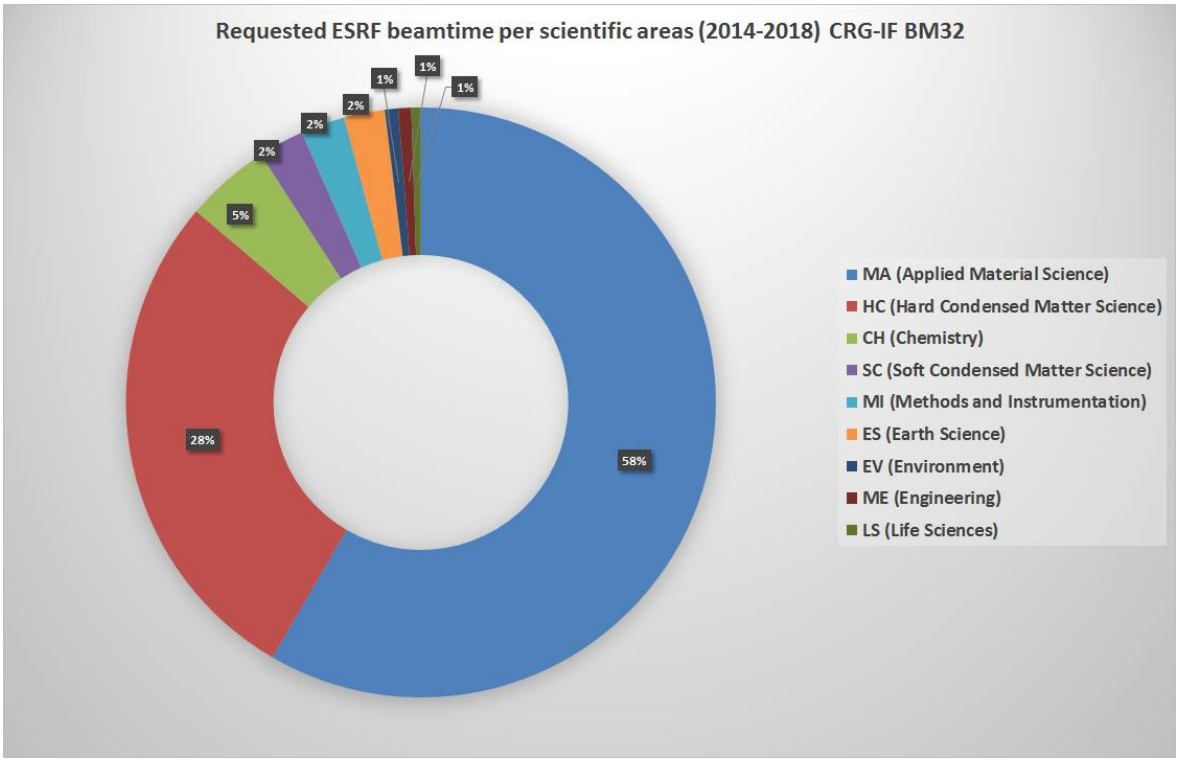

Figures A3-A4 Overbooking per ESRF scientific areas of ESRF beamtime (2014-2018). Committees: (MA) Applied Materials Science, (HC) Hard Condensed Matter Science, (CH) Chemistry, (SC) Soft Condensed Matter Science, (MI) Methods and Instrumentation, (ES) Earth Sciences, (EV) Environment, (ME) Engineering and (LS) Life Sciences.

A quarter (~24%) of the delivered beamtime is devoted to the GMT instrument and the remaining part is equally shared by µLaue (39%) and INS (37%) ones. The mean duration of users experiments is respectively 18, 14 and 15 shifts when performed with INS, µLaue and GMT instruments. BM32/µLaue was several times used for rapid orientation measurements on micro-object for further experiments performed by Bragg Coherent Diffraction Imaging on ID01 or SOLEIL/CRISTAL. Note also that about 5 days have been dedicated to Industrial beamtime with this instrument.

Scientific Fields and Committees: BM32 has been originally dedicated to interface and surface studies. The distribution of allocated ESRF beamtime by ESRF committee is representative of the scientific fields covered by the beamline with its three instruments (Fig A-3 and A-4). For the CRG beamtime the distribution is comparable (not shown). More than one experiment over two is devoted to Applied Materials Science experiments taking advantage of the surface and interface sensitivity of the techniques employed on GMT and microstructure mapping capability on µLaue. Most of the Hard Condensed Matter experiments are carried out on INS station. The versatility of the GMT instrument is reflected by the remaining committees mainly SC committee. The beamline is now clearly optimized for physical and physico-chemistry structural investigations at surfaces and interfaces of materials in both applied and fundamental points of view.

Users Countries and Laboratories: Figure A-5 and A-6 present the panel of countries and laboratories from which the main proposer of the experiment originates. Even if proposers of each experiment come from different laboratories, the distribution retrieved from the main proposer or all users data quite the same. Distribution of ESRF beamtime is shown figure A-5. Two thirds of this beamtime is allocated to French scientists whereas one third of this beamtime is allocated to foreign (non French and European) ones. Actually, some experiments proposed by French teams are submitted in both CRG and ESRF committees and finally obtained by means of ESRF committees. It can be noted the high attraction for BM32 by german and swedish teams respectively from MPIE Düsseldorf and Lund University due to their strong involvement in the µLaue development.

Figure A-6 represents the panel of origin of users with beamtime accepted by both CRG and ESRF committees. Close to 25 % beamtime is allocated to other countries, most of the beamtime being used by French community. One half of French users originates from Grenoble, as beamline staff (BM32), external users or strong collaborators from CEA-IRIG and Institut Néel (which operates the beamline), CNRS labs or applied labs from CEA-LETI-LITEN.

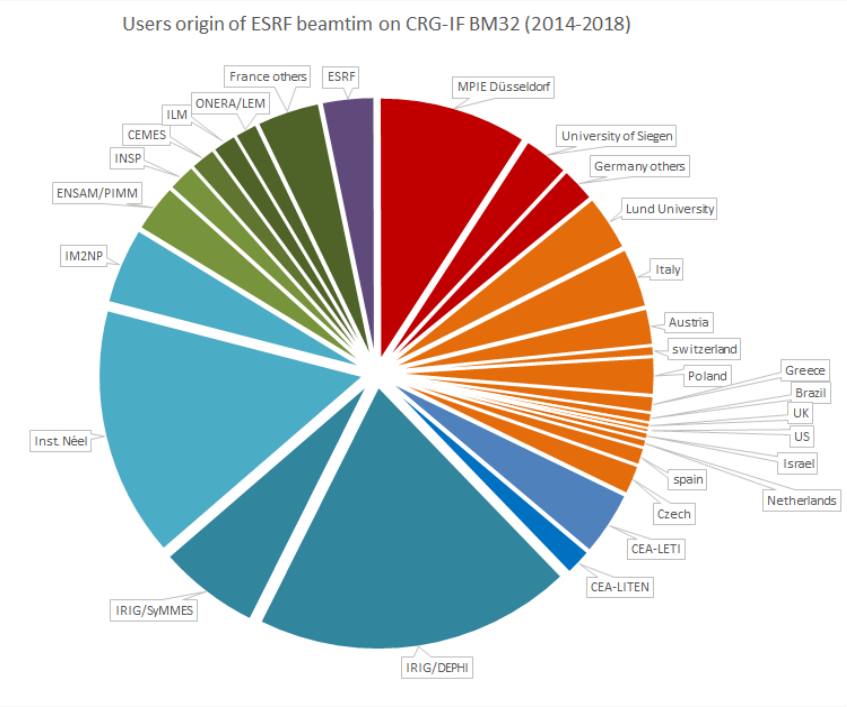

Figure A-5: Panel of laboratories of users of BM32 whose experiments have been accepted by ESRF committees (2014-2018)

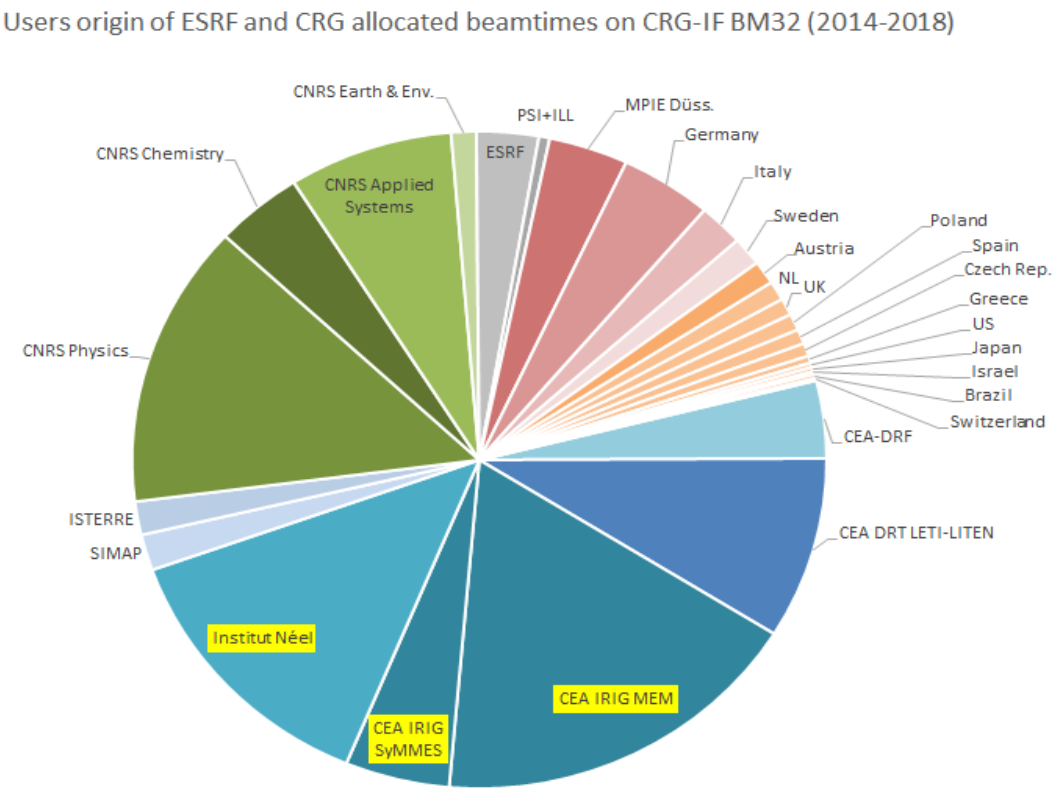

Figure A-6: Panel of laboratories of users of BM32 whose experiments have been accepted by both ESRF and CRG committees (2014-2018). Users from Grenoble laboratories are in blue-like color (~ 50% of total beamtime.user area). Yellow labels correspond to labs in charge of CRG-IF BM32 operation.

8.1.2 Scientific Production

Publications: Beamline staff of BM32 (internal users) and external users with or without strong collaborations with beamline staff produced 94 articles reviewed by peers over the period 2015-sept2020 (equal to 92 in the previous 5 years period) (figures A-7 and A-8). The scientific production does not increase steadily (average rate of 17 articles per year) but with large fluctuations (min. 13 max. 25). Among them, 14 have been published in journals with an impact factor larger than 6 and 2 have been cited more than 30 times (see Annex 3 below). The number of 'high impact' articles produced by the beamline has increased over the last years. The average impact factor is nearly 5. Note that X-ray Measurements performed on BM32 of the two leading articles in the impact factor journal list and most cited one represent a part only of the reported or reviewed results.
The scientific production distribution over the three instruments (figure A-9) shows that the half of publications are related to µLaue instrument. It is likely due to the strong involvement of beamline staff for this emerging technique (compared to GMT techniques), a certain degree of automation, the shortest duration of performed experiments (consequently the highest number of experiments or users teams) and publication journals with relatively less impact.

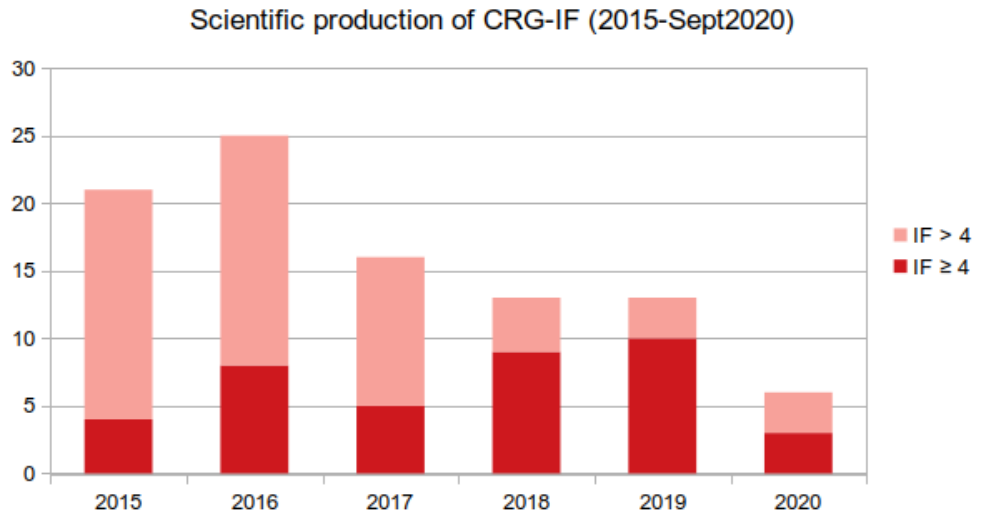

Figure A-7: Number of journal articles published during the period (2015-Sept 2020) using beamtime on CRG-IF BM32 beamline. IF: journal impact factor (2018). Mean production rate: 16.9 articles / year. Note that ESRF shutdown took place from Dec 2018 to Sept 2020.

Three modes of production can be considered in this CRG beamline involving first internal scientists using In-House-Research beamtime and allocated one by CRG or ESRF committees ('IHR' user type), second external users from allocated beamtime only ('EXT' user type), and third beamline staff and external users within the frame of a strong collaboration. This last mode uses mainly allocated beamtime + casual IHR beamtime (Coll user type). It corresponds to a significant beamline staff investment when valuable instrumental and methodological benefits can be obtained for the general beamline development and higher throughput. Compared to the last BLRP period (2005-2010), µLaue gained maturity but a lot of resources are still employed to help users towards autonomy at the expense of internal research activities. According to the distribution of publications over the user type (figure A-10), the CRG-IF BM32 is clearly involved to provide the best assistance to external users since

only 20% of the published works can be considered as in-house research activity (collaboration with beamline staff as principal coordinator/investigator). At the opposite, 25% of articles are published without beamline staff as co-author.

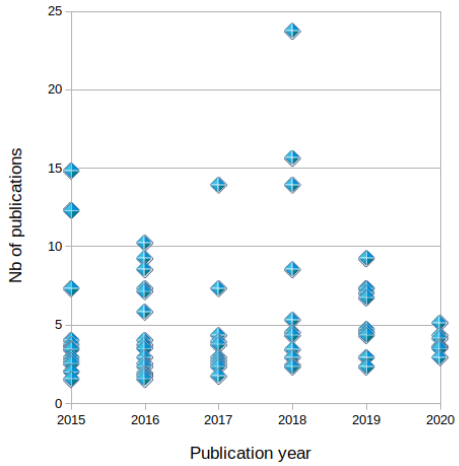

Figure A-8: Distribution of regular papers over publication year (from 2015 to 2019) and journal impact factor evaluated in 2018.

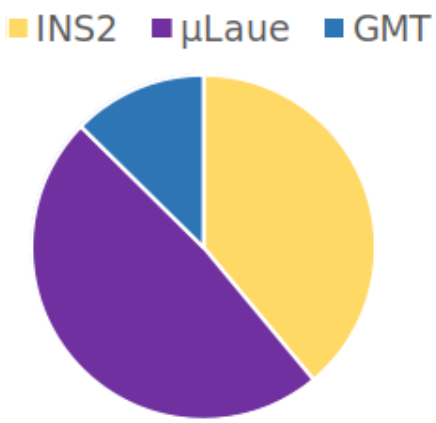

Figure A-9: Distribution of published over the 3 instruments of BM32 beamline during the last 5 years. Half of the reported works are related to µLaue experiments but published in average in journal with less impact than GMT or INS2 publications journals.

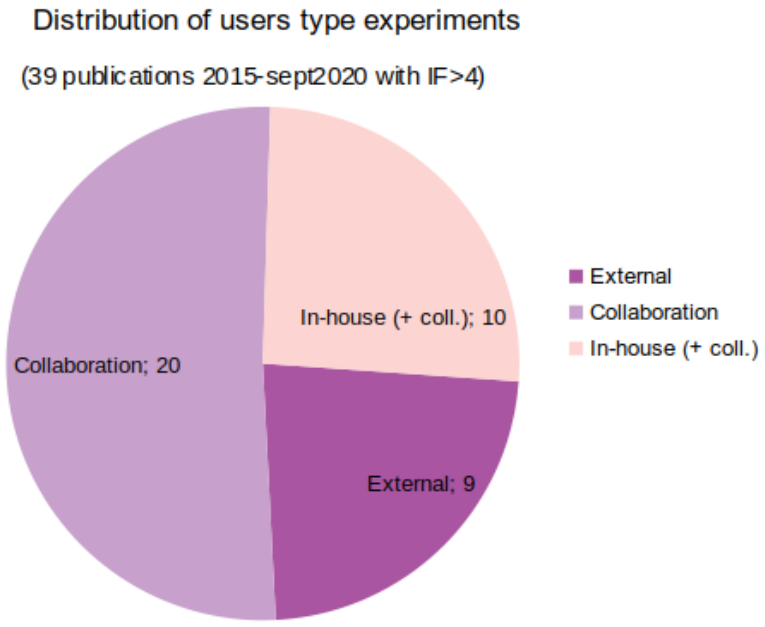

Figure A-10: Distribution of users type on CRG-IF according to the last 5 years 39 high-ranked articles (impact factor higher than 4) over 95 total number of publications.

8.2 Annex B List of Publications, Oral Presentations, Thesis defences (2015-2020)

8.2.1 List of regular papers and proceedings

The list of scientific peer-reviewed articles are sorted by year and impact factor (in brackets) of the journal (most recent factor evaluated in 2018). Additional production are listed in the following: ESRF highlight, Book chapter, Awards, Journal covers, selected thesis from internal and external beamline users, proceedings and selected oral communications.

[] Journal Impact factor 2018

2020

[5.1] Dai Z., Alyabyeva N., Borghetti P., Chenot S., David P., Koltsov A., Renaud G., Jupille J., Cabailh G., Lazzari R. - "*Al-rich Fe0.85Al0.15(1 0 0), (1 1 0) and (1 1 1) surface structures"*
Applied Surface Science 509, 145312-1-145312-7 (2020)
http://dx.doi.org/10.1016/j.apsusc.2020.145312

[4.3] Sant R., Lisi S., Nguyen V.D., Mazaleyrat E., Herrero A.C.G., Geaymond O., Guisset V., David P., Marty A., Jamet M., Chapelier C., Magaud L., Dappe Y.J., Bianchi M., Hofmann P., Renaud G., Coraux J. -" *Decoupling molybdenum disulfide from its substrate by cesium intercalation"*
Journal of Physical Chemistry C 124, 12397-12408 (2020)
http://dx.doi.org/10.1021/acs.jpcc.0c00970

[4.1] Barbier C., Zhou T., Renaud G., Geaymond O., Le Fèvre P., Glas F., Madouri A., Cavanna A., Travers L., Morassi M., Gogneau N., Tchernycheva M., Harmand J.C., Largeau L. -" *In situ X-ray diffraction study of GaN nucleation on transferred graphene"*
Crystal Growth & Design 20, 4013-4019 (2020)
http://dx.doi.org/10.1021/acs.cgd.0c00306

[3.6] Michaud L.G., Castán C., Zussy M., Montméat P., Mareau V.H., Gonon L., Fournel F., Rieutord F., Tardif S. -" *Elaboration and characterization of a 200 mm stretchable and flexible ultra-thin semi-conductor film"*
Nanotechnology 31, 145302-1-145302-7 (2020)
http://dx.doi.org/10.1088/1361-6528/ab647a

[3.5] Ren Z., Cornelius T.W., Leclere C., Davydok A., Micha J.S., Robach O., Richter G., Thomas O. - " First stages of plasticity in three-point bent Au nanowires detected by in situ Laue microdiffraction"
Applied Physics Letters 116, 243101-1-243101-6 (2020)
http://dx.doi.org/10.1063/5.0012816

[2.9] Dai Z.B., Alyabyeva N., Van den Bossche M., Borghetti P., Chenot S., David P., Koltsov A., Renaud G., Jupille J., Cabailh G., Noguera C., Goniakowski J., Lazzari R. - *" Oxide at the Al-rich Fe0.85Al0.15(110) surface"*
Physical Review Materials 4, 074409-1-074409-11 (2020)
http://dx.doi.org/10.1103/PhysRevMaterials.4.074409

2019

[9.2] Capiod, Pierre, Laurent Bardotti, Alexandre Tamion, Olivier Boisron, Clément Albin, Véronique Dupuis, Gilles Renaud, Philippe Ohresser, and Florent Tournus. *"Elaboration of Nanomagnet Arrays: Organization and Magnetic Properties of Mass-Selected FePt Nanoparticles Deposited on Epitaxially Grown Graphene on Ir(111)."*

Physical Review Letters 122, no. 10 (2019): 106802.
https://doi.org/10.1103/PhysRevLett.122.106802.

[7.3] Hektor, Johan, Jean-Sébastien Micha, Stephen A. Hall, Srinivasan Iyengar, and Matti Ristinmaa. "Long Term Evolution of Microstructure and Stress around Tin Whiskers Investigated Using Scanning Laue Microdiffraction."
Acta Materialia 168 (2019): 210–21. https://doi.org/10.1016/j.actamat.2019.02.021.

[7.3] Mukhina, Tetiana, Arnaud Hemmerle, Valeria Rondelli, Yuri Gerelli, Giovanna Fragneto, Jean Daillant, and Thierry Charitat. *"Attractive Interaction between Fully Charged Lipid Bilayers in a Strongly Confined Geometry."*
The Journal of Physical Chemistry Letters 10, no. 22 (2019): 7195–99.
https://doi.org/10.1021/acs.jpclett.9b02804.

[7.0] Wilson, Axel, Aude Bailly, Romain Bernard, Yves Borensztein, Alessandro Coati, Bernard Croset, Hervé Cruguel, et al. *"Gas-Induced Selective Re-Orientation of Au–Cu Nanoparticles on TiO_2 (110)."*
Nanoscale 11, no. 2 (2019): 752–61. https://doi.org/10.1039/C8NR07645F.

[6.7] De Santis, M., A. Bailly, I. Coates, S. Grenier, O. Heckmann, K. Hricovini, Y. Joly, et al. "Epitaxial Growth and Structure of Cobalt Ferrite Thin Films with Large Inversion Parameter on Ag(001)."
Acta Crystallographica Section B: Structural Science, Crystal Engineering and Materials 75, no. 1 (2019): 8–17. https://doi.org/10.1107/S2052520618016177.

[4.7] Fragkos, Sotirios, Roberto Sant, Carlos Alvarez, Alexei Bosak, Polychronis Tsipas, Dimitra Tsoutsou, Hanako Okuno, Gilles Renaud, and Athanasios Dimoulas. *"Room Temperature Commensurate Charge Density Wave in Epitaxial Strained TiTe2 Multilayer Films."*
Advanced Materials Interfaces 6, no. 5 (2019): 1801850. https://doi.org/10.1002/admi.201801850.

[4.5] Niu, Gang, Steven John Leake, Oliver Skibitzki, Tore Niermann, Jerome Carnis, Felix Kießling, Fariba Hatami, et al. "Advanced Coherent X-Ray Diffraction and Electron Microscopy of Individual InP Nanocrystals on Si Nanotips for III-V-on-Si Electronics and Optoelectronics."
Physical Review Applied 11, no. 6 (2019): 064046.
https://doi.org/10.1103/PhysRevApplied.11.064046.

[4.5] Martinez, Nicolas, Gerard Gebel, Nils Blanc, Nathalie Boudet, Jean-Sebastien Micha, Sandrine Lyonnard, and Arnaud Morin. *"Heterogeneous Nanostructural Aging of Fuel Cell Ionomer Revealed by Operando SAXS."*
ACS Applied Energy Materials 2, no. 5 (2019): 3071–80. https://doi.org/10.1021/acsaem.8b02004.

[4.3] Rébiscoul, Diane, Susan Sananes Israel, Samuel Tardif, Vincent Larrey, André Ayral, and Francois Rieutord. "Impact of Silica Surface Nanoconfinement on the Microstructure of Alkoxysilane Layers Grafted by Supercritical Carbon Dioxide."
The Journal of Physical Chemistry C 123, no. 19 (2019): 12305–12.
https://doi.org/10.1021/acs.jpcc.9b01967.

[4.3] Wild, Bastien, Damien Daval, Jean-Sébastien Micha, Ian C. Bourg, Claire E. White, and Alejandro Fernandez-Martinez. "Physical Properties of Interfacial Layers Developed on Weathered Silicates: A Case Study Based on Labradorite Feldspar."
The Journal of Physical Chemistry C 123, no. 40 (2019): 24520–32.
https://doi.org/10.1021/acs.jpcc.9b05491.

[4.3] Sitja, Georges, Aude Bailly, Maurizio De Santis, Vasile Heresanu, and Claude R. Henry. *"Regular Arrays of Pt Clusters on Alumina: A New Superstructure on Al2O3/Ni3Al(111)."*
The Journal of Physical Chemistry C 123, no. 40 (2019): 24487–94.
https://doi.org/10.1021/acs.jpcc.9b05109.

[2.9] Fragkos, Sotirios, Roberto Sant, Carlos Alvarez, Evangelos Golias, Jose Marquez-Velasco, Polychronis Tsipas, Dimitra Tsoutsou, et al. *"Topological Band Crossings in Epitaxial Strained SnTe."*

Physical Review Materials 3, no. 10 (October 14, 2019): 104201.
https://doi.org/10.1103/PhysRevMaterials.3.104201.

[2.3] Plancher, Emeric, Pouya Tajdary, Thierry Auger, Olivier Castelnau, Véronique Favier, Dominique Loisnard, Jean-Baptiste Marijon, et al. *"Validity of Crystal Plasticity Models Near Grain Boundaries: Contribution of Elastic Strain Measurements at Micron Scale."*
JOM 71, no. 10 (2019): 3543–51
https://doi.org/10.1007/s11837-019-03711-5.

2018

[23.7] Cornelius, Thomas W., and Olivier Thomas. "Progress of in Situ Synchrotron X-Ray Diffraction Studies on the Mechanical Behavior of Materials at Small Scales."
Progress in Materials Science 94 (2018): 384–434. https://doi.org/10.1016/j.pmatsci.2018.01.004.

[15.6] Tsipas, Polychronis, Sotirios Fragkos, Dimitra Tsoutsou, Carlos Alvarez, Roberto Sant, Gilles Renaud, Hanako Okuno, and Athanasios Dimoulas. *"Direct Observation at Room Temperature of the Orthorhombic Weyl Semimetal Phase in Thin Epitaxial MoTe2."* Advanced Functional Materials 28, no. 33 (2018): 1802084
https://doi.org/10.1002/adfm.201802084.

[13.9] Dau, Minh Tuan; Gay, Maxime; Di Felice, Daniela; Vergnaud, Céline; Marty, Alain; Beigne, Cyrille; Renaud, Gilles; Renault, Olivier; Mallet, Pierre; Le Quang, Toai; Veuillen, Jean-Yves; Huder, Loïc; Renard, Vincent; Chapelier, Claude; Zamborlini, Giovanni; Jugovac, Matteo; Feyer, Vitaliy; Dappe, Yannick; Pochet, Pascal; Jamet, Matthieu. *"Beyond van Der Waals Interaction: The Case of MoSe2 Epitaxially Grown on Few-Layer Graphene"*
ACS Nano (2018)
https://pubs.acs.org/doi/10.1021/acsnano.7b07446.

[13.9] Tsipas, Polychronis, Dimitra Tsoutsou, Sotirios Fragkos, Roberto Sant, Carlos Alvarez, Hanako Okuno, Gilles Renaud, Reynald Alcotte, Thierry Baron, and Athanasios Dimoulas. *"Massless Dirac Fermions in ZrTe2 Semimetal Grown on InAs(111) by van Der Waals Epitaxy."*
ACS Nano 12, no. 2 (2018): 1696–1703
https://doi.org/10.1021/acsnano.7b08350
.
[8.5] El Kacimi, Amine, Emmanuelle Pauliac-Vaujour, and Joël Eymery. "Flexible Capacitive Piezoelectric Sensor with Vertically Aligned Ultralong GaN Wires."
ACS Applied Materials & Interfaces 10, no. 5 (2018): 4794–4800.
https://doi.org/10.1021/acsami.7b15649.

[5.3] Joly, Yves, Antoine Abisset, Aude Bailly, Maurizio De Santis, Farid Fettar, Stéphane Grenier, Danny Mannix, et al. *"Simulation of Surface Resonant X-Ray Diffraction."*
Journal of Chemical Theory and Computation 14, no. 2 (2018): 973–80.
https://doi.org/10.1021/acs.jctc.7b01032.

[4.5] Hektor, Johan, Jean-Baptiste Marijon, Matti Ristinmaa, Stephen A. Hall, Håkan Hallberg, Srinivasan Iyengar, Jean-Sébastien Micha, Odile Robach, Fanny Grennerat, and Olivier Castelnau. *"Evidence of 3D Strain Gradients Associated with Tin Whisker Growth."* Scripta Materialia 144 (2018): 1–4
https://doi.org/10.1016/j.scriptamat.2017.09.030.

[4.3] Saint-Lager, Marie-Claire, Marie-Angélique Languille, Francisco J. Cadete Santos Aires, Aude Bailly, Stéphanie Garaudee, Eric Ehret, and Odile Robach. *"Oxygen-Induced Changes of the Au30Pd70(110) Surface Structure and Composition under Increasing O2 Pressure."*
The Journal of Physical Chemistry C 122, no. 39 (2018): 22588–96.
https://doi.org/10.1021/acs.jpcc.8b07068.

[3.4] Altinkurt, G., M. Fèvre, G. Geandier, M. Dehmas, O. Robach, and J.-S. Micha. "Local Strain Redistribution in a Coarse-Grained Nickel-Based Superalloy Subjected to Shot-Peening, Fatigue or Thermal Exposure Investigated Using Synchrotron X-Ray Laue Microdiffraction."

Journal of Materials Science 53, no. 11 (2018): 8567–89
https://doi.org/10.1007/s10853-018-2144-4.

[2.9] Ors, T., J.-S. Micha, N. Gey, V. Michel, O. Castelnau, and R. Guinebretiere. *"EBSD-Assisted Laue Microdiffraction for Microstrain Analysis."*
Journal of Applied Crystallography 51, no. 1 (2018): 55–67.
https://doi.org/10.1107/S1600576717017150.

[2.9] Shin, J., T. W. Cornelius, S. Labat, F. Lauraux, M.-I. Richard, G. Richter, N. P. Blanchard, D. S. Gianola, and O. Thomas. *"In Situ Bragg Coherent X-Ray Diffraction during Tensile Testing of an Individual Au Nanowire."*
Journal of Applied Crystallography 51, no. 3 (2018): 781–88.
https://doi.org/10.1107/S1600576718004910.

[2.4] Boullier, Anne-Marie, Odile Robach, Benoît Ildefonse, Fabrice Barou, David Mainprice, Tomoyuki Ohtani, and Koichiro Fujimoto. *"High Stresses Stored in Fault Zones: Example of the Nojima Fault (Japan)."*
Solid Earth 9, no. 2 (2018): 505–29
https://doi.org/10.5194/se-9-505-2018.

[2.3] Ren, Z., T. W. Cornelius, C. Leclere, A. Davydok, J.-S. Micha, O. Robach, G. Richter, and O. Thomas. *"Three-Point Bending Behavior of a Au Nanowire Studied by in-Situ Laue Micro-Diffraction."*
Journal of Applied Physics 124, no. 18 (2018): 185104
https://doi.org/10.1063/1.5054068
.

Proceedings

Tournus, Florent and Capiod, Pierre and Bardotti, Laurent and Tamion, A. and Boisron, O. and Albin, Clement and Dupuis, Véronique and Renaud, Gilles and Ohresser, Philippe (2018). *"Organization and magnetic properties of FePt nanoparticles deposited on graphene/Ir moiré pattern"*
Conference: 2018 IEEE International Magnetic Conference (INTERMAG)
10.1109/INTMAG.2018.8508666.

Reche, Jérôme, Maxime Besacier, Patrice Gergaud, Yoann Blancquaert, Guillaume Freychet, and Thibault Labbaye. *"Programmed LWR Metrology by Multi-Techniques Approach."*
In Metrology, Inspection, and Process Control for Microlithography XXXII, 10585:105850F.
International Society for Optics and Photonics, (2018)
https://doi.org/10.1117/12.2292169.

Ren, Z., T. W. Cornelius, C. Leclere, A. Davydok, J.-S. Micha, O. Robach, G. Richter, and O. Thomas. *"Plasticity in Inhomogeneously Strained Au Nanowires Studied by Laue Microdiffraction."*
MRS Advances 3, no. 39 (ed 2018): 2331–39
https://doi.org/10.1557/adv.2018.465.

2017

[13.9] Tardif, Samuel, Ekaterina Pavlenko, Lucille Quazuguel, Maxime Boniface, Manuel Maréchal, Jean-Sébastien Micha, Laurent Gonon, et al. *"Operando Raman Spectroscopy and Synchrotron X-Ray Diffraction of Lithiation/Delithiation in Silicon Nanoparticle Anodes."* ACS Nano 11, no. 11 (2017): 11306–16
https://doi.org/10.1021/acsnano.7b05796.

[7.3] Malyar, N. V., J. -S. Micha, G. Dehm, and C. Kirchlechner. *"Dislocation-Twin Boundary Interaction in Small Scale Cu Bi-Crystals Loaded in Different Crystallographic Directions."* Acta Materialia 129 (2017): 91–97
https://doi.org/10.1016/j.actamat.2017.02.067.

[7.3] Malyar, N. V., J. S. Micha, G. Dehm, and C. Kirchlechner. "Size Effect in Bi-Crystalline Micropillars with a Penetrable High Angle Grain Boundary."
Acta Materialia 129 (2017): 312–20
https://doi.org/10.1016/j.actamat.2017.03.003.

[4.3] Bailly, Aude, Georges Sitja, Marie-Claire Saint-Lager, Séverine Le Moal, Frédéric Leroy, Maurizio De Santis, Claude R. Henry, and Odile Robach. *"Influence of Palladium on the Ordering, Final Size, and Composition of Pd–Au Nanoparticle Arrays."*
The Journal of Physical Chemistry C 121, no. 46 (2017): 25864–74.
https://doi.org/10.1021/acs.jpcc.7b08254.

[4.3] Daval, Damien, Sylvain Bernard, Laurent Rémusat, Bastien Wild, François Guyot, Jean Sébastien Micha, François Rieutord, Valérie Magnin, and Alejandro Fernandez-Martinez. *"Dynamics of Altered Surface Layer Formation on Dissolving Silicates."*
Geochimica et Cosmochimica Acta 209 (2017): 51–69
https://doi.org/10.1016/j.gca.2017.04.010.

[3.9] Reboud, V., A. Gassenq, J. M. Hartmann, J. Widiez, L. Virot, J. Aubin, K. Guilloy, et al. *"Germanium Based Photonic Components toward a Full Silicon/Germanium Photonic Platform."*
Progress in Crystal Growth and Characterization of Materials 63, no. 2 (2017): 1–24.
https://doi.org/10.1016/j.pcrysgrow.2017.04.004.

[3.7] Camosi, Lorenzo, Stanislas Rohart, Olivier Fruchart, Stefania Pizzini, Mohamed Belmeguenai, Yves Roussigné, Andreï Stashkevich, et al. *"Anisotropic Dzyaloshinskii-Moriya Interaction in Ultrathin Epitaxial Au/Co/W(110)."*
Physical Review B 95, no. 21 (2017): 214422
https://doi.org/10.1103/PhysRevB.95.214422.

[2.9] Abboud, A., C. Kirchlechner, J. Keckes, T. Conka Nurdan, S. Send, J. S. Micha, O. Ulrich, R. Hartmann, L. Strüder, and U. Pietsch. *"Single-Shot Full Strain Tensor Determination with Microbeam X-Ray Laue Diffraction and a Two-Dimensional Energy-Dispersive Detector."*
Journal of Applied Crystallography 50, no. 3 (2017): 901–8.
https://doi.org/10.1107/S1600576717005581.

[2.9] Altinkurt, G., M. Fèvre, O. Robach, J.-S. Micha, G. Geandier, and M. Dehmas. "Full Elastic Strain Tensor Determination at the Phase Scale in a Powder Metallurgy Nickel-Based Superalloy Using X-Ray Laue Microdiffraction."
Journal of Applied Crystallography 50, no. 6 (2017): 1754–65.
https://doi.org/10.1107/S1600576717014558.

[2.9] Plancher, E., V. Favier, C. Maurice, E. Bosso, N. Rupin, J. Stodolna, D. Loisnard, et al. "Direct Measurement of Local Constitutive Relations, at the Micrometre Scale, in Bulk Metallic Alloys."
Journal of Applied Crystallography 50, no. 3 (2017): 940–48.
https://doi.org/10.1107/S1600576717006185.

[2.7] Lamirand, A. D., S. Grenier, A. Y. Ramos, M. De Santis, A. Bailly, E. Mossang, J. M. Tonnerre, et al. *"Growth and Properties of CoO/Fe Perpendicular Exchange Coupled Ultra-Thin Films."*
Journal of Magnetism and Magnetic Materials 443 (2017): 195–201.
https://doi.org/10.1016/j.jmmm.2017.07.079.

[2.5] Zhang, F. G., M. Bornert, J. Petit, and O. Castelnau. "Accuracy of Stress Measurement by Laue Micro-diffraction (Laue-DIC Method): The Influence of Image Noise, Calibration Errors and Spot Number."
Journal of Synchrotron Radiation 24, no. 4 (2017): 802–17.
https://doi.org/10.1107/S1600577517006622.

[2.5] Ibrahim, M., É. Castelier, H. Palancher, M. Bornert, S. Caré, and J. -S. Micha. *"Mechanical Behaviour near Grain Boundaries of He-Implanted UO_2 Ceramic Polycrystals."* Journal of Nuclear Materials 483 (2017): 13–20.
https://doi.org/10.1016/j.jnucmat.2016.10.044
.

[2.3] Gassenq, A., S. Tardif, K. Guilloy, I. Duchemin, N. Pauc, J. M. Hartmann, D. Rouchon, et al. *"Raman-Strain Relations in Highly Strained Ge: Uniaxial (100), (110) and Biaxial (001) Stress."*
Journal of Applied Physics 121, no. 5 (2017): 055702

https://doi.org/10.1063/1.4974202.

[2.3] Guerain, Mathieu, Jean-Luc Grosseau-Poussard, Guillaume Geandier, Benoit Panicaud, Nobumichi Tamura, Martin Kunz, Catherine Dejoie, Jean-Sébastien Micha, Dominique Thiaudière, and Philippe Goudeau. *"Residual Stress Determination in Oxide Layers at Different Length Scales Combining Raman Spectroscopy and X-Ray Diffraction: Application to Chromia-Forming Metallic Alloys."*
Journal of Applied Physics 122, no. 19 (2017): 195105
https://doi.org/10.1063/1.4990146.

[1.7] Tuaz, Aymeric, Philippe Ballet, Xavier Biquard, and François Rieutord. "Micro-Diffraction Investigation of Localized Strain in Mesa-Etched HgCdTe Photodiodes."
Journal of Electronic Materials 46, no. 9 (2017): 5442–47.
https://doi.org/10.1007/s11664-017-5691-6.
Proceedings
Gassenq, A., S. Tardif, K. Guilloy, N. Pauc, M. Bertrand, D. Rouchon, J. M. Hartmann, et al. "High-Quality and Homogeneous 200-Mm GeOI Wafers Processed for High Strain Induction in Ge."
In Silicon Photonics XII, 10108:101081B. International Society for Optics and Photonics, (2017).
https://doi.org/10.1117/12.2251790.

Baum, M., D. Rébiscoul, S. Tardif, N. Tas, L. Mercury, and F. Rieutord. "X-Ray Reflectivity Analysis of SiO_2 Nanochannels Filled with Water and Ions: A New Method for the Determination of the Spatial Distribution of Ions Inside Confined Media."
Procedia Earth and Planetary Science, 15th Water-Rock Interaction International Symposium, WRI-15, 17 (2017): 682–85
https://doi.org/10.1016/j.proeps.2016.12.146.

2016

[10.2] Gueye, Magatte N., Alexandre Carella, Nicolas Massonnet, Etienne Yvenou, Sophie Brenet, Jérôme Faure-Vincent, Stéphanie Pouget, et al. *"Structure and Dopant Engineering in PEDOT Thin Films: Practical Tools for a Dramatic Conductivity Enhancement."*
Chemistry of Materials 28, no. 10 (2016): 3462–68
https://doi.org/10.1021/acs.chemmater.6b01035.

[9.2] Hemmerle, Arnaud, Giovanna Fragneto, Jean Daillant, and Thierry Charitat. "Reduction in Tension and Stiffening of Lipid Membranes in an Electric Field Revealed by X-Ray Scattering."
Physical Review Letters 116, no. 22 (2016): 228101.
https://doi.org/10.1103/PhysRevLett.116.228101.

[8.5] Giammaria, Tommaso Jacopo, Federico Ferrarese Lupi, Gabriele Seguini, Michele Perego, Francesco Vita, Oriano Francescangeli, Brandon Wenning, et al. *"Micrometer-Scale Ordering of Silicon-Containing Block Copolymer Thin Films via High-Temperature Thermal Treatments."*
ACS Applied Materials & Interfaces 8, no. 15 (2016): 9897–9908.
https://doi.org/10.1021/acsami.6b02300.

[7.3] Aminalragia-Giamini, S., J. Marquez-Velasco, P. Tsipas, D. Tsoutsou, G. Renaud, and A. Dimoulas. *"Molecular Beam Epitaxy of Thin $HfTe_2$ semimetal Films."*
2D Materials 4, no. 1 (2016): 015001
https://doi.org/10.1088/2053-1583/4/1/015001.

[7.3] Philippi, Bastian, Christoph Kirchlechner, Jean Sébastien Micha, and Gerhard Dehm. "Size and Orientation Dependent Mechanical Behavior of Body-Centered Tetragonal Sn at 0.6 of the Melting Temperature."
Acta Materialia 115 (2016): 76–82
https://doi.org/10.1016/j.actamat.2016.05.055.

[7.1] Guilloy, Kevin, Nicolas Pauc, Alban Gassenq, Yann-Michel Niquet, Jose-Maria Escalante, Ivan Duchemin, Samuel Tardif, et al. *"Germanium under High Tensile Stress: Nonlinear Dependence of Direct Band Gap vs Strain."*

ACS Photonics 3, no. 10 (2016): 1907–11
https://doi.org/10.1021/acsphotonics.6b00429.

[5.8] Davydok, Anton, Balila Nagamani Jaya, Odile Robach, Olivier Ulrich, Jean-Sébastien Micha, and Christoph Kirchlechner. “Analysis of the Full Stress Tensor in a Micropillar: Ability of and Difficulties Arising during Synchrotron Based MLaue Diffraction.”
Materials & Design 108 (2016): 68–75
https://doi.org/10.1016/j.matdes.2016.06.098.

[4.0] Niu, Gang, Giovanni Capellini, Markus Andreas Schubert, Tore Niermann, Peter Zaumseil, Jens Katzer, Hans-Michael Krause, et al. *“Dislocation-Free Ge Nano-Crystals via Pattern Independent Selective Ge Heteroepitaxy on Si Nano-Tip Wafers.”*
Scientific Reports 6, no. 1 (2016): 1–11
https://doi.org/10.1038/srep22709.

[3.7] Dupraz, Maxime, Roberta Poloni, Kitti Ratter, David Rodney, Maurizio De Santis, Bruno Gilles, Guillaume Beutier, and Marc Verdier. *“Wetting Layer of Copper on the Tantalum (001) Surface.”*
Physical Review B 94, no. 23 (2016): 235427
https://doi.org/10.1103/PhysRevB.94.235427.

[3.7] Franz, Dirk, Nils Blanc, Johann Coraux, Gilles Renaud, Sven Runte, Timm Gerber, Carsten Busse, et al. “Atomic Structure of Pt Nanoclusters Supported by Graphene/Ir(111) and Reversible Transformation under CO Exposure.”
Physical Review B 93, no. 4 (2016): 045426
https://doi.org/10.1103/PhysRevB.93.045426.

[3.7] Leroy, F., Y. Garreau, F. Cheynis, B. Croset, A. Coati, P. Müller, and G. Prévot. *“Elastic Cost of Silicon Step Rebonding.”*
Physical Review B 93, no. 4 (2016): 045416
https://doi.org/10.1103/PhysRevB.93.045416.

[3.5] Gassenq, A., S. Tardif, K. Guilloy, G. Osvaldo Dias, N. Pauc, I. Duchemin, D. Rouchon, et al. *“Accurate Strain Measurements in Highly Strained Ge Microbridges.”*
Applied Physics Letters 108, no. 24 (2016): 241902
https://doi.org/10.1063/1.4953788.

[3.5] Tedjini, M., F. Fournel, H. Moriceau, V. Larrey, D. Landru, O. Kononchuk, S. Tardif, and F. Rieutord. *“Interface Water Diffusion in Silicon Direct Bonding.”*
Applied Physics Letters 109, no. 11 (2016): 111603
https://doi.org/10.1063/1.4962464.

[3.5] Palancher, H., P. Goudeau, A. Boulle, F. Rieutord, V. Favre-Nicolin, N. Blanc, G. Martin, J. Fouet, and C. Onofri. *“Strain Profiles in Ion Implanted Ceramic Polycrystals: An Approach Based on Reciprocal-Space Crystal Selection.”*
Applied Physics Letters 108, no. 3 (2016): 031903
https://doi.org/10.1063/1.4939972.

[2.9] Tardif, S., A. Gassenq, K. Guilloy, N. Pauc, G. Osvaldo Dias, J.-M. Hartmann, J. Widiez, et al. “Lattice Strain and Tilt Mapping in Stressed Ge Microstructures Using X-Ray Laue Micro-Diffraction and Rainbow Filtering.”
Journal of Applied Crystallography 49, no. 5 (2016): 1402–11.
https://doi.org/10.1107/S1600576716010347.

[2.5] Leclere, C., T. W. Cornelius, Z. Ren, O. Robach, J.-S. Micha, A. Davydok, O. Ulrich, G. Richter, and O. Thomas. “KB Scanning of X-Ray Beam for Laue Microdiffraction on Accelero-Phobic Samples: Application to in Situ Mechanically Loaded Nanowires.”
Journal of Synchrotron Radiation 23, no. 6 (2016): 1395–1400.
https://doi.org/10.1107/S1600577516013849.

[2.5] Palancher, H., R. Kachnaoui, G. Martin, A. Richard, J. -C. Richaud, C. Onofri, R. Belin, et al. "Strain Relaxation in He Implanted UO2 Polycrystals under Thermal Treatment: An in Situ XRD Study."
Journal of Nuclear Materials 476 (2016): 63–76
https://doi.org/10.1016/j.jnucmat.2016.04.023.

[2.3] Plancher, E., J. Petit, C. Maurice, V. Favier, L. Saintoyant, D. Loisnard, N. Rupin, et al. "On the Accuracy of Elastic Strain Field Measurements by Laue Microdiffraction and High-Resolution EBSD: A Cross-Validation Experiment."
Experimental Mechanics 56, no. 3 (2016): 483–92
https://doi.org/10.1007/s11340-015-0114-1.

[2.3] Auzelle, Thomas, Xavier Biquard, Edith Bellet-Amalric, Zhihua Fang, Hervé Roussel, Ana Cros, and Bruno Daudin. *"Unraveling the Strain State of GaN down to Single Nanowires."*
Journal of Applied Physics 120, no. 22 (2016): 225701
https://doi.org/10.1063/1.4971967.

[2.3] Deluca, Marco, René Hammer, Jozef Keckes, Jochen Kraft, Franz Schrank, Juraj Todt, Odile Robach, Jean-Sébastien Micha, and Stefan Defregger. *"Integrated Experimental and Computational Approach for Residual Stress Investigation near Through-Silicon Vias."* Journal of Applied Physics 120, no. 19 (2016): 195104.
https://doi.org/10.1063/1.4967927
.
[2.3] Richard M.I., Malachias A., Stoffel M., Merdzhanova T., Schmidt O.G., Renaud G., Metzger T.H., Schülli T.U. *"Temperature Evolution of Defects and Atomic Ordering in Si1−xGex Islands on Si(001)"* Journal of Applied Physics: Vol 119, No 8," (2016)
https://aip.scitation.org/doi/10.1063/1.4942530.

[1.9] Jeffrey M. Wheeler, Christoph Kirchlechner, Jean-Sébastien Micha, Johann Michler & Daniel Kiener *"The effect of size on the strength of FCC metals at elevated temperatures: annealed copper"* Philosophical Magazine, 96:32-34, 3379-3395, (2016)
https://doi.org/10.1080/14786435.2016.1224945

[1.8] Lamirand, A. D., S. Grenier, V. Langlais, A. Y. Ramos, H. C. N. Tolentino, X. Torrelles, and M. De Santis. *"Magnetite Epitaxial Growth on Ag(001): Selected Orientation, Seed Layer, and Interface Sharpness."*
Surface Science 647 (2016): 33–38
https://doi.org/10.1016/j.susc.2015.12.005.

[1.7] Vianne, B., S. Escoubas, C. Krauss, M. -I. Richard, S. Labat, G. Chahine, J. -S. Micha, et al. "Temperature Dependency of the Strain Distribution Induced by TSVs in Silicon: A Comparative Study between Micro-Laue and Monochromatic Nano-Diffraction." Microelectronic Engineering, MAM (Materials for Advanced Metallization) 2015, 156 (2016): 59–64.
https://doi.org/10.1016/j.mee.2016.03.003.

[1.5] Sanchez, Dario Ferreira, Shay Reboh, Monica Larissa Djomeni Weleguela, Jean-Sébastien Micha, Odile Robach, Thierry Mourier, Patrice Gergaud, and Pierre Bleuet. *"In-Situ X-Ray MLaue Diffraction Study of Copper through-Silicon Vias."*
Microelectronics Reliability 56 (2016): 78–84
https://doi.org/10.1016/j.microrel.2015.10.008.
Proceedings
Rieutord, François, Samuel Tardif, Didier Landru, Oleg Kononchuk, Vincent Larrey, Hubert Moriceau, Marwan Tedjini, and Frank Fournel. *"Edge Water Penetration in Direct Bonding Interface."*
ECS Transactions 75, no. 9 (2016): 163
https://doi.org/10.1149/07509.0163ecst.

Rieutord, François, Samuel Tardif, Frédéric Mazen, Didier Landru, and Oleg Kononchuk. (Invited) *"Defect Evolution during Silicon Smartcut™."*
ECS Transactions 75, no. 4 (2016): 155
https://doi.org/10.1149/07504.0155ecst.

Guilloy, K., A. Gassenq, N. Pauc, J. Maria Escalante Fernandez, I. Duchemin, Y.-Michel Niquet, S. Tardif, et al. *"Nonlinear Strain Dependences in Highly Strained Germanium Micromembranes for On-Chip Light Source Applications*"
In Silicon Photonics and Photonic Integrated Circuits V, 9891:98910X. International Society for Optics and Photonics, (2016)
https://doi.org/10.1117/12.2227497.

Montméat, Pierre, Isadora De Nigris Brandolisi, Samuel Tardif, Thierry Enot, Gregory Enyedi, Riadh Kachtouli, Pascal Besson, François Rieutord, and Frank Fournel. *"Transfer of Ultra-Thin Semi-Conductor Films onto Flexible Substrates."*
ECS Transactions 75, no. 9 (2016): 247
https://doi.org/10.1149/07509.0247ecst.

Pavlenko, E.; Quazuguel, L.; Boniface, M.; Tardif, S.; Rieutord, F.; Marechal, M.; Micha, J.-S.; Mareau, V.; Gonon, L.; Lyonnard, S.; "Core-Shell Structural Evolution of Crystalline Silicon Nanoparticles upon Lithiation/Delithiation By Ex Situ Raman Spectroscopy and Operando Synchrotron X-Ray Diffraction"
Meeting Abstracts 2, 262-262 (2016) The Electrochemical Society

Montméat, P.; Brandolisi, I.D.N.; Tardif, S.; Enot, T.; Enyedi, G.; Kachtouli, R.; Besson, P.; Rieutord, F.; Fournel, F. "Transfer of Ultra-Thin Semi-Conductor Films onto Flexible Substrates"
ECS Transactions 75, 9, 247-252 (2016)

Zabel, T; Marin, E; Geiger, R; Bozon, C; Tardif, S; Guilloy, K; Gassenq, A; Escalante, J; Niquet, YM; Duchemin, "Highly strained direct bandgap Germanium cavities for a monolithic laser on Si Group IV Photonics (GFP)"
2016 IEEE 13th International Conference 40-41 (2016)

Reboud, V; Widiez, J; Hartmann, JM; Gomez, E; Gassenq, A; Guilloy, K; Bertrand, M; Tardif, S; Escalante, JM; Pauc, N, "Fabrication of 200 mm Germanium-On-Insulator (GeOI): A step toward a Germanium photonic platform" 2016 IEEE 13th International Conference 140-142 (2016)

Pavlenko, E.; Quazuguel, L.; Boniface, M.; Tardif, S.; Rieutord, F.; Marechal, M.; Micha, J.-S.; Mareau, V.; Gonon, L.; Lyonnard, S. "Evolution of Nano-Crystalline Silicon L.Anode upon Cycling Probed By Ex Situ Raman Spectroscopy and Operando Synchrotron X-Ray Diffraction"
Meeting Abstracts 2, 513-513 (2016) The Electrochemical Society

Reboud, V; Gassenq, A; Dias, G Osvaldo; Guilloy, K; Escalante, JM; Tardif, S; Pauc, N; Hartmann, J-M; Widiez, J; Gomez, E "Ultra-high amplified strains in 200-mm optical germanium-on-insulator (GeOI) substrates: towards CMOS-compatible Ge lasers"
SPIE OPTO 97520F-97520F-8 2016 (2016)

Gassenq, A; Guilloy, K; Tardif, S; Escalante, J; Niquet, YM; Duchemin, I; Hartmann, JM; Rouchon, D; Widiez, J; Rothman, J
"Non-linear bandgap strain dependence in highly strained germanium using strain redistribution in 200 mm GeOI wafers for laser applications"
Group IV Photonics (GFP), 2016 IEEE 13th International Conference, 104-105 (2016)

2015

[14.8] Andreazza, Pascal, Véronique Pierron-Bohnes, Florent Tournus, Caroline Andreazza-Vignolle, and Véronique Dupuis. *"Structure and Order in Cobalt/Platinum-Type Nanoalloys: From Thin Films to Supported Clusters."*
Surface Science Reports 70, no. 2 (2015): 188–258
https://doi.org/10.1016/j.surfrep.2015.02.002.

[12.3] Guilloy, Kevin, Nicolas Pauc, Alban Gassenq, Pascal Gentile, Samuel Tardif, François Rieutord, and Vincent Calvo. *"Tensile Strained Germanium Nanowires Measured by Photocurrent Spectroscopy and X-Ray Microdiffraction."*

Nano Letters 15, no. 4 (2015): 2429–33
https://doi.org/10.1021/nl5048219.

[7.3] Kirchlechner, C., P. J. Imrich, W. Liegl, J. Pörnbacher, J. -S. Micha, O. Ulrich, and C. Motz. *"On the Reversibility of Dislocation Slip during Small Scale Low Cycle Fatigue."*
Acta Materialia 94 (2015): 69–77
https://doi.org/10.1016/j.actamat.2015.04.029.

[4.0] Linas, S., Jean, F., Zhou, T. et al. "Moiré induced organization of size-selected Pt clusters soft landed on epitaxial graphene"
Scientific Reports 5, 13053 (2015)
https://doi.org/10.1038/srep13053

[3.7] Daudin, R., T. Nogaret, A. Vaysset, T. U. Schülli, A. Pasturel, and G. Renaud. "Formation, Stability, and Atomic Structure of the Si(111)-(6x6)Surface Reconstruction: A Quantitative Study Using Synchrotron Radiation."
Physical Review B 91, no. 16 (2015): 165426
https://doi.org/10.1103/PhysRevB.91.165426.

[3.7] Jean, Fabien, Tao Zhou, Nils Blanc, Roberto Felici, Johann Coraux, and Gilles Renaud. *"Topography of the Graphene/Ir(111) Moir\'e Studied by Surface x-Ray Diffraction."*
Physical Review B 91, no. 24 (2015): 245424
https://doi.org/10.1103/PhysRevB.91.245424.

[3.7] Kuświk, P., P. L. Gastelois, M. M. Soares, H. C. N. Tolentino, M. De Santis, A. Y. Ramos, A. D. Lamirand, M. Przybylski, and J. Kirschner. *"Effect of CoO/Ni Orthogonal Exchange Coupling on Perpendicular Anisotropy of Ni Films on Pd(001)."*
Physical Review B 91, no. 13 (2015): 134413
https://doi.org/10.1103/PhysRevB.91.134413.

[3.5] Massy, D., F. Mazen, S. Tardif, J. D. Penot, J. Ragani, F. Madeira, D. Landru, O. Kononchuk, and F. Rieutord. *"Fracture Dynamics in Implanted Silicon."*
Applied Physics Letters 107, no. 9 (2015): 092102
https://doi.org/10.1063/1.4930016.

[3.5] Richard, M.-I., A. Malachias, T. U. Schülli, V. Favre-Nicolin, Z. Zhong, T. H. Metzger, and G. Renaud. *"Ordered Domain Lateral Location, Symmetry, and Thermal Stability in Ge:Si Islands."*
Applied Physics Letters 106, no. 1 (2015): 012108
https://doi.org/10.1063/1.4905844.

[3.4] Zaumseil, P., Y. Yamamoto, M. A. Schubert, G. Capellini, O. Skibitzki, M. H. Zoellner, and T. Schroeder. *"Tailoring the Strain in Si Nano-Structures for Defect-Free Epitaxial Ge over Growth."*
Nanotechnology 26, no. 35 (2015): 355707
https://doi.org/10.1088/0957-4484/26/35/355707.

[2.9] Favre-Nicolin, V., J. Baruchel, H. Renevier, J. Eymery, and A. Borbély. *"XTOP: High-Resolution X-Ray Diffraction and Imaging."*
Journal of Applied Crystallography 48, no. 3 (2015): 620–620.
https://doi.org/10.1107/S160057671500895X.

[2.9] Ferreira Sanchez, D., J. Villanova, J. Laurencin, J.-S. Micha, A. Montani, P. Gergaud, and P. Bleuet. *"X-Ray Micro Laue Diffraction Tomography Analysis of a Solid Oxide Fuel Cell."*
Journal of Applied Crystallography 48, no. 2 (2015): 357–64.
https://doi.org/10.1107/S1600576715002447.

[2.9] Ibrahim, M., É Castelier, H. Palancher, M. Bornert, S. Caré, and J.-S. Micha. *"Laue Pattern Analysis for Two-Dimensional Strain Mapping in Light-Ion-Implanted Polycrystals."* Journal of Applied Crystallography 48, no. 4 (2015): 990–99
https://doi.org/10.1107/S1600576715007736.

[2.9] Leclere, C., T. W. Cornelius, Z. Ren, A. Davydok, J.-S. Micha, O. Robach, G. Richter, L. Belliard, and O. Thomas. *"In Situ Bending of an Au Nanowire Monitored by Micro Laue Diffraction."* Journal of Applied Crystallography 48, no. 1 (2015): 291–96. https://doi.org/10.1107/S1600576715001107.

[2.9] Zhang, F. G., O. Castelnau, M. Bornert, J. Petit, J. B. Marijon, and E. Plancher. *"Determination of Deviatoric Elastic Strain and Lattice Orientation by Applying Digital Image Correlation to Laue Microdiffraction Images: The Enhanced Laue-DIC Method."* Journal of Applied Crystallography 48, no. 6 (2015): 1805–17. https://doi.org/10.1107/S1600576715018397.

[2.7] Lamirand, Anne D., Márcio M. Soares, Aline Y. Ramos, Hélio C. N. Tolentino, Maurizio De Santis, Julio C. Cezar, and Abner de Siervo. *"Spin Orientation in an Ultrathin CoO/PtFe Double-Layer with Perpendicular Exchange Coupling."* Journal of Magnetism and Magnetic Materials, Recent Advances in Nanomagnetism and Spintronics, 373 (2015): 6–9 https://doi.org/10.1016/j.jmmm.2014.02.039.

[2.7] Lamirand, Anne D., Márcio M. Soares, Maurizio De Santis, Aline Y. Ramos, Stéphane Grenier, and Hélio C. N. Tolentino. *"Strain Driven Monoclinic Distortion of Ultrathin CoO Films in the Exchange-Coupled CoO/FePt/Pt(0 0 1) System."* Journal of Physics: Condensed Matter 27, no. 8 (2015): 085001 https://doi.org/10.1088/0953-8984/27/8/085001.

[2.5] Cantelli, V., O. Geaymond, O. Ulrich, T. Zhou, N. Blanc, and G. Renaud. *"The In Situ Growth of Nanostructures on Surfaces (INS) Endstation of the ESRF BM32 Beamline: A Combined UHV–CVD and MBE Reactor for in Situ X-Ray Scattering Investigations of Growing Nanoparticles and Semiconductor Nanowires."* Journal of Synchrotron Radiation 22, no. 3 (2015): 688–700. https://doi.org/10.1107/S1600577515001605.

[2.5] Petit, J., O. Castelnau, M. Bornert, F. G. Zhang, F. Hofmann, A. M. Korsunsky, D. Faurie, et al. *"Laue-DIC: A New Method for Improved Stress Field Measurements at the Micrometer Scale."* Journal of Synchrotron Radiation 22, no. 4 (2015): 980–94. https://doi.org/10.1107/S1600577515005780.

[2.0] Fonović, Matej, Andreas Leineweber, Odile Robach, Eric A. Jägle, and Eric J. Mittemeijer. *"The Nature and Origin of 'Double Expanded Austenite' in Ni-Based Ni-Ti Alloys Developing Upon Low Temperature Gaseous Nitriding."* Metallurgical and Materials Transactions A 46, no. 9 (2015): 4115–31 https://doi.org/10.1007/s11661-015-2999-9.

[1.5] Rauer, C., H. Moriceau, F. Rieutord, J. M. Hartmann, F. Fournel, A. M. Charvet, N. Bernier, et al. *"Mechanism Involved in Direct Hydrophobic Si(100)-2×1:H Bonding."* Microsystem Technologies 21, no. 5 (2015): 961–68 https://doi.org/10.1007/s00542-015-2443-5.

Proceedings

Vianne, B., C. Krauss, S. Escoubas, M.-I. Richard, S. Labat, G. Chahine, T. Schüllli, et al. *"Effect of the Temperature on the Strain Distribution Induced in Silicon Interposer by TSVs: A Comparison between Micro-Laue and Monochromatic Nanodiffraction."* In 2015 IEEE International Interconnect Technology Conference and 2015 IEEE Materials for Advanced Metallization Conference (IITC/MAM), 59–62, (2015) https://doi.org/10.1109/IITC-MAM.2015.7325626.

ESRF Highlights

2018: STABILISATION AT ROOM TEMPERATURE OF THE TOPOLOGICAL WEYL SEMIMETAL PHASE IN EPITAXIAL M o Te2 ATOMICALLY THIN FILMS
from Tsipas *et al*, Adv. Func. Mat., 2018

2015: PROBING THE STRAIN IN GERMANIUM NANOWIRES BY LAUE MICRODIFFRACTION from Guilloy *et al*., Nano Letters 2015

Micha J.S. and Robach O., "La Microdiffraction Laue" in « La cristallographie, science et techniques » Reflets de la physique (n°44-45) [french physical society bulletin]

Thesis

Julien Drieu La Rochelle (**2020**) *"Caractérisation in situ et à différentes échelles de l'évolution sous traction de nanomacles dans un film d'or monocristallin."* Université de Poitiers, February 2020

Lucien Penlap Woguia (**2019**), *"Analyses par faisceaux d'ions de structures tridimensionnelles (3D) pour des applications en nanotechnologie"*, Université Grenoble Alpes, Physique des Matériaux, May 2019

Jérôme Reche (**2019***), "Une nouvelle méthodologie hybride pour la mesure de rugosités sub-nanométriques",* Université Grenoble Alpes École doctorale électronique, électrotechnique, automatique, traitement du signal, October 2019

Tetiana Mukhina (**2019**), *"Active fluctuations and electrostatic interactions in floating lipid membranes",* Université de Strasbourg, École doctorale Physique et chimie-physique, November 2019

Johan Hektor (**2019**), "*Tin whiskers: experiments and modelling*", Lund University, Sweden, March 2019

Jungho Shin (**2019**), "*Etude expérimentale du comportement mécanique et de la nucléation des dislocations dans des nanofils contenant très peu de défauts*", Université Aix-Marseille, Physique et sciences de la matière, August 2019

Roberto Sant (**2019**), "*Exploration par Rayonnement synchrotron X de la croissance et de la structure de dichalcogénures 2D*" Université Grenoble Alpes, December 2019.

Anne Laure Lebaudy (**2018**), "Analyse multi-échelles des déformations et contraintes au sein d'une matrice de détection infrarouge fonctionnant à 100K. Caractérisation expérimentale et numérique", Ecole Nationale Supérieure des Arts et Métiers, Metz, France, June 2018.

Markus Baum (**2018**), "*The role of water properties and specific ion effects on the evolution of silica nanoconfinement*", Université de Montpellier, Sciences Chimiques, November 2018

Susan Sananes-Israel (**2018**), *« Surfaces de silice fonctionnalisées par voie CO_2 supercritique : effets du confinement et comportement en solution aqueuse »*, Université de Montpellier, Sciences Chimiques, September 2018

Gader Altinkurt (**2018**), "*Apport de la microdiffraction Laue pour lad´etermination des contraintes internes dans un superalliage à base de nickel grenaillé : effets de la microstructure et des traitements thermomécaniques*" Université de Lorraine, Science et Ingénierie des Matériaux et Métallurgie, December 2018

Louise Fouquat (**2018**), "*Etude par photoémission d'interfaces métal / oxyde et métal / semiconducteur élaborées par épitaxie par jets moléculaires*", Université de Lyon, Ecole Doctorale Matériaux, December 2018

Aurélien Lardeau-Falcy (**2018**), "*Dopage de couches de GaN sur substrat silicium par implantation ionique*", Université Grenoble Alpes, July 2018

Elodie Bêche (**2017**), "*Etude des collages directs hydrophiles mettant en jeu des couches diélectriques*", Université Grenoble Alpes, October 2017.

Marwan Tedjini (2017), "*Etude du collage direct Silicium Silicium, Gestion de l'eau à l'interface*", Université Grenoble Alpes, September 2017

Wild, Bastien (**2017**), "*Changements microstructuraux et diversité microbienne associés à l'altération des silicates: Influence sur les cinétiques de dissolution du laboratoire au terrain*", Ecole doctorale des sciences de la Terre, de l'Univers et de l'environnement, Strasbourg, February 2017

Magatte Gueye (**2017**), "*Propriétés électriques, optoélectroniques et thermoélectriques de matériaux à base de poly(3,4-éthylènedioxythiophène)PEDOT*",Université Grenoble Alpes, 2MGE : Matériaux, Mécanique, Génie Civil, Electrochimie, December 2017

Jean-Baptiste Marijon (**2017**), *« Caractérisation 3D de la microstructure et des deformations elastiques des polycristaux par microdiffraction Laue* ». Ecole Nationale Supérieure des Arts et Métiers, Paris, France, July 2017

Maxime Boniface (**2017**), "*Suivi à l'échelle nanométrique de l'évolution d'une électrode de silicium dans un accumulateur Li-ion par STEM-EELS*", Université Grenoble Alpes, Ecole Doctorale Physique Grenoble.

Aymeric Tuaz (**2017**), "*Investigations structurales haute-résolution de photodiodes infrarouges de nouvelle génération*", Université Grenoble Alpes, Ecole Doctorale Physique Grenoble, December 2017

Anthony Payet (**2017**), "*Modélisation physique des procédés de fabrication des jonctions FDSOI pour le nœud 10 nm et en-deçà*", Université Grenoble Alpes, Ecole Doctorale Physique Grenoble, May 2017

ZongBei Dai (**2017**), "*Orientation-dependent segregation and oxidation at Fe0.85Al0.15 random alloy surfaces*", Université Paris 6, École doctorale Physique et chimie des matériaux (Paris), December 2017

Amine El Kacimi (**2017**), "*Capteurs piézoélectriques souples à base de microfils de GaN en structure capacitive*", Université Grenoble Alpes, électrotechnique, automatique, traitement du signal (Grenoble), November 2017

Nataliya Malyar (**2017**), "*Dislocation transmission through copper grain boundaries at the micron scale*", Ruhr Universität Bochum, April 2017

Virginie Théry (**2017**), "*Etude de la microstructure et des transitions de phases électroniques et cristallines de couches épitaxiales de VO_2 déposées sur différents substrats*", Ecole Doctorale Sciences et Ingénierie en matériaux, mécanique, énergétique et aéronautique, Poitiers. Biennial **Award best thesis** of French Crystallography Association (AFC)

Kevin Guilloy (**2016**), "*Germanium déformé pour l'émission de lumière*", Université Grenoble Alpes, July 2016

Benjamin vianne (**2016**) "*Intégration d'un interposeur actif silicium pour l'élaboration de circuits électroniques complexes*", Université Aix-Marseille, June 2016

Bastian Philippi (**2016**) "*Micromechanical characterization of lead-free solder and its individual microstructure elements*" Fakultät für Maschnenbau, RUB, Bochum, Germany October 2016

Candice Thomas (**2016**), "*Strained HgTe/CdTe topological insulators, toward spintronic applications*", Université Grenoble Alpes, Ecole Doctorale Physique December 2016

Sara Fernandez (**2016**), "*An insight intro nanostructures through coherent diffraction imaging* ", Université Aix-Marseille, Ecole Doctorale Physique et Sciences de la Matière, December 2016

Virginie Simone (**2016**), "*Développement d'accumulateurs sodium-ion*", Université Grenoble Alpes, November 2016

Florian Dupont (**2016**), "*Nucléation cristalline de nanofils GaN élaborés par MOCVD sur substrats conducteurs pour application LEDs*", Université Grenoble Alpes, 2016

Brice Hugonnet (**2016**), "*Frittage et évolution de la microstructure au cours des traitements thermiques d'aimants NdFeB : influence sur les propriétés magnétiques*" Université Grenoble Alpes, November 2016

Marouane Mastari (**2016**), "*Croissance et caractérisation d'alliages SiGe sur des structures nanométriques pour les applications micro-électronique*" Université Grenoble Alpes, December 2016

Wilgens Sylvain (**2016**), "*Étude de la plasticité du monocristal de phase MAX par déformation aux petites échelles*", Université de Poitiers, École doctorale : Sciences et ingénierie en matériaux, mécanique, énergétique et aéronautique, December 2016

Tao Zhou (**2015**), "*In situ synchrotron X-ray scattering of AiGe NWs: Growth, Strain and Bending*", Université Grenoble Alpes, Ecole Doctorale Physique, December 2015.

Emeric Plancher (**2015**), "*Mesures de champs de déformations élastique et totale pour la détermination du comportement mécanique local de matériaux cristallins.*" Ecole Nationale Supérieure des Arts et Métiers, Paris, December 2015

Fabien Jean (**2015**), "*Growth and structure of graphene on metal and growth of organized nanostructures on top*" Université Grenoble Alpes, Ecole Doctorale Physique, July 2015.

Fengguo Zhang (**2015**), "*Determination of the stress field in polycrystalline materials by Laue microdiffraction*", Ecole Nationale Supérieure des Arts et Métiers, Paris, July 2015

Damien Massy (**2015**), "*Etude de la dynamique de fracture dans la technologie Smart Cut*™", Université Grenoble Alpes, Ecole Doctorale Physique, December 2015

Matej Fonovic (2015), "*Nitriding behavior of Ni and Ni-based binary alloys*", Stuttgart University, Germany, January 2015

Thomas Auzelle (**2015**), "*GaN/AlN nanowires: nucleation, polarity and quantum heterostructures*" Université Grenoble Alpes, Sciences des Nanomatériaux, Décembre 2015.

Zhe Ren (**2015**), "*Nanomechanics : combining mechanical testing in situ with focused X-ray diffraction on a synchrotron beamline*" Université Aix-Marseille, Ecole Doctorale Physique et Sciences de la Matière (Marseille), December 2015

Ali Abboud (**2015**), "*Polychromatic X-ray Diffraction using a pnCCD: Applications for Material Science*", University of Siegen, Germany

Marcelle Ibrahim (**2015**), "*Étude du comportement mécanique d'UO2 implanté en helium par micro-diffraction des rayons X et modélisation par éléments finis*", Université Paris Est, École doctorale Sciences, Ingénierie et Environnement, October 2015

8.2.2 List of featuring or invited oral presentations:

2019

Keynote Talk Kirchlechner et al, "Using experimental small scale mechanics and spatially resolved Laue diffraction to understand dislocation grain boundary interactions"
1st Colloquium on Theoretical and Experimental Micro-Mechanics, Metz/France, 18.-19.11.2019

(invited) C. Kirchlechner et al, "Using experimental small scale mechanics to understand dislocation grain boundary ineractions" Seminar Talk, TU-Eindhoven, Eindhoven/Netherlands 20.11.2019

(invited) C. Kirchlechner et al, "Paving the way to unique, non-destructive 3D-microstructure properties by in situ Laue tomography"
DPG 2019, Regensburg/Germany, 1.-4.4.2019

(invited) C. Kirchlechner et al, "Dislocation slip transmission through coherent Sigma3(111) twin boundaries"
TMS 2019, San Antonio / USA, 12.03.2019

F. Tournus, P. Capiod, L. Bardotti, A. Tamion, V. Dupuis, G. Renaud, P. Ohresser
« Organization and magnetic properties of mass-selected FePt nanoparticles deposited on epitaxially grown graphene on Ir (111) »
Bulletin of the American Physical Society March meeting (2019) Boston MA

L. Renversade, J.-B. Molin, O. Robach, O. Ulrich, C. Kirchlechner, J.-S. Micha
" Cartographie 3D par micro-diffraction Laue "
SOLEIL Users Meeting 17-18 Janvier 2019

Maurizio De Santis, Aude Bailly, Ian Coates, Stephane Grenier, Yves Joly, Veronique Langlais, Aline Ramos, Xavier Torrelles "Growth and structure of cobalt ferrite thin films with large inversion parameter"
IVC−21 (International Vacuum Conference), Malmö (Suède) 1-5 Juillet 2019 (oral).

2018

(invited) A. Dimoulas, D. Tsoutsou, P. Tsipas, S. Fragkos, R. Sant, C. Alvarez, H. Okuno, G. Renaud « Large Area Synthesis of 2D Metal Dichalcogenides By Van Der Waals Molecular Beam Epitaxy »
Seattle, WA, May 2018, ECS Meeting Abstracts, 843-843 2018

(invited) S. Tardif et al., "Synchrotron strain measurements in advanced devices: from Ge micro-bridges for infra-red lasers to Si nanoparticles electrodes for Li-ion batteries",
International Conference Reliability and Stress-Related Phenomena In Novel And Emerging Electronics Systems (a.k.a. The Stress Workshop), 30 Jan. – 01 Feb. 2018, Singapore

(invited) S. Tardif et al., "Measuring Lattice Strain and Orientation Operando at the Sub-Micron Scale"
Spring Meeting of Materials Research Society, 02 – 06 Apr. 2018, Phoenix AZ, USA

(invited) F. Rieutord, S. Tardif, I. Nikitskiy, F. Fournel, M. Tedjini, V. Larrey, C. Bridoux, C. Morales, D. Landru, O. Kononchuk "Water Transport Along Si/Si Direct Wafer Bonding Interfaces"
AIMES 2018, Sep 2018, CANCUN, Mexico. 86 (5), pp.39-47, 2018

(invited) C. Kirchlechner et al, “Dislocation nucleation at and transmission through coherent S3 twin boundaries in Copper”
Symposium honoring George M Pharr on occasion of his 65th birthday, College Station/USA, 7.12.2018

(invited) C. Kirchlechner et al, “Grain size strengthening: Mechanism based descriptions beyond Hall-Petch”
ENGE Conference, Jeju Island / Korea, 12.11.2018

(invited) C. Kirchlechner et al, “Insights into dislocation grain boundary interactions by in situ micromechanics”
Seminar talk, Shenyang national lab, Shenyang / China, 5.11.2018

(invited) C. Kirchlechner et al, “Quantifying dislocation slip transmission by in situ micromechanics”
ICSMA 2018, Ohio State University, Columbus OH, United States of America, 19.07.2018

(invited) C. Kirchlechner et al, Nondestructive 3D information on dislocation density and elastic strain in deforming micro-fatigue specimen
ESMC 2018, Bologna, Italy, 03.07.2018

(invited) C. Kirchlechner et al, “Beyond Hall-Petch: Mechanism based description of dislocation grain-boundary interactions “
DPG-Frühjahrstagung , Berlin, 11.03.2018

Hektor, J., Marijon, J.-B., Ristinmaa, M., Hall, S. A., Hallberg, H., Iyengar, S., Micha, J.-S., Robach, O.,Grennerat, F., Castelnau, O., “Strain Field Around a Tin Whisker Studied Using Differential Aperture X-ray Microscopy (DAXM)”. 4th International Congress on 3D Materials Science (3DMS). 2018.

Hektor, J., Marijon, J.-B., Ristinmaa, M., Hall, S. A., Hallberg, H., Iyengar, S., Micha, J.-S., Robach,O., Grennerat, F., Castelnau, O., “Microdiffraction Studies of the Strain Field Around Tin Whiskers”.ESRF User Meeting. 2018.

F. Tournus, P. Capiod, L. Bardotti, A. Tamion, O. Boisron, C. Albin, V. Dupuis, G. Renaud, P. Ohresser
« Organization and magnetic properties of mass-selected FePt nanoparticles deposited on epitaxially grown graphene on Ir (111) »
Journées de la Matière Condensée (Soc. Française de Physique) 27-31 août 2018 Grenoble

G. Renaud et al, " X-ray investigation of Van der Waals Epitaxy of 2D diselenides and ditellurides"
Conference 3S18, Saint-Christoph, Austria, Feb. 2018,

M. De Santis, A. Bailly, I. Coates, S. Grenier, Y. Joly, V. Langlais, A. Y. Ramos, X. Torrelles
« In situ GIXRD study of cobalt ferrite ultrathin films grown on Ag(001) by MBE »
3rd Joint AIC-SILS Conference - Rome 25 - 28 June 2018
L. Michaud, P. Montméat, F. Fournel, C. Castan, L. Gonon, V. Mareau, S. Tardif, F. Rieutord, *"Mesure de la déformation operando de films ultra-mince silicium sur un polymère flexible",* Matériaux 2018, 19 - 23 Nov. 2018, Strasbourg, France

M. Fèvre, Gader Altinkurt, G. Geandier, M. Dehmas, O. Robach, J.-S. Micha
« Effets de traitements thermomécaniques et de la microstructure sur les champs de déformation d'un superalliage à base de nickel grenaillé »
Matériaux 2018, 19 - 23 Nov. 2018, Strasbourg, France

L. Renversade, O. Robach, O. Ulrich, J.S. Micha

" Cartographie 3D des matériaux polycristallins par micro-diffraction Laue "
Matériaux 2018, 19 - 23 Nov. 2018, Strasbourg, France

L. Renversade, J.-B. Molin, O. Robach, O. Ulrich, C. Kirchlechner, J.-S. Micha
" Cartographie 3D par micro-diffraction Laue "
Colloque de l'Association Française de Cristallographie Lyon, 2018 10-13 juillet

L. Renversade, O. Robach, O. Ulrich, J.-S. Micha « X-ray Laue Diffraction 3D Microscopy »
Journées de la Matière Condensée (Soc. Française de Physique) 27-31 août 2018 Grenoble

J.-S. Micha, D. Cobessi, O. Proux "Perspectives sur les lignes synchrotrons françaises liées à l'upgrade des sources X de l'ESRF »
Journée de l'Association Française des Utilisateurs du Rayonnement Synchrotron 4/06/2018

N.V. Malyar, J.-S. Micha, G. Dehm, C. Kirchlechner
« Quantifying dislocation slip transmission by in situ micromechanics »
ICSMA 2018, Ohio State University

J.B. Molin, L. Renversade, N.V. Malyar, O. Ulrich, J.-S. Micha, C. Kirchlechner
« Nondestructive 3D information on dislocation density and elastic strain in deforming micro-fatigue specimen »
ESMC 2018
2017
C. Kirchlechner et al., "Using nano- and micromechanics to understand interface plasticity"
Hysitron, Nanobrücken 2017, 05.04.2017

C. Kirchlechner, N. Malyar, N. Peter, G. Dehm, J.-S. Micha
New Insights into Plasticity at Grain Boundaries by Nano- and Micromechanics"
TMS 2017, San Diego, 26.02.2017 – 02.03.2017

(invited) S. Tardif, "Operando synchrotron studies of electrodes for ion batteries on the French beamlines @ ESRF"
21st International Conference on Solid State Ionics, Padua, Italy, 18-23 June 2017

Hektor, J., Marijon, J.-B., Ristinmaa, M., Hall, S. A., Hallberg, H., Iyengar, S., Micha, J.-S., Robach,O., Grennerat, F., Castelnau, O., "Differential aperture x-ray microscopy (DAXM) applied to tin whisker growth". Svenska Mekanikdagar. 2017

Hektor, J., Marijon, J.-B., Ristinmaa, M., Hall, S. A., Hallberg, H., Iyengar, S., Micha, J.-S., Robach, O.,Grennerat, F., Castelnau, O., "3D reconstruction of the microstructure, and strain, around a tin whisker,using Differential Aperture X-ray Microscopy (DAXM)". MAX IV Laboratory User Meeting. 2017.

2016

J. Coraux, "Deformations in epitaxial graphene on a metal"
EWEG/2D'16, Bergish-Gladbach, mai 2016, invité

J. Coraux, "Growth, structure & properties of 2D materials at surfaces",
Journées Surfaces et Interfaces, Marseille, janvier 2016, invité

M. De Santis, A.D. Lamirand, A. Ramos, S. Grenier, A. Bailly, X. Torrelles, V. Langlais, "Epitaxial growth of ultrathin magnetite films on Ag(100)"
ECOSS−32, Grenoble, 28 August – 2 September 2016

G. Beutier, M. Dupraz, R. Poloni, K. Ratter, D. Rodney, M. De Santis, B. Gilles, M. Verdier, "Wetting layer of copper on the tantalum (001) surface"
ECOSS−32, Grenoble, 28 August – 2 September 2016

Tardif S. et al., “Mapping the Full Strain Tensor and Lattice Tilts in Ge Microstructures for Photonics Applications”
Materials Research Society Spring Meeting, Phoenix, USA, March 2016

Tardif S. et al.,, “Strain mapping in Ge microstructures using X-ray white beam Laue microdiffraction”
30th Meeting of the European Crystallographic Association, Basel, Switzerland, 28/08-01/09 2016

F. Rieutord, S. Tardif, D.Landru, O. Kononchuk, V. Larrey, H. Moriceau, M. Tedjini and F.Fournel
“Wafer Bonding Symposium Edge Water Penetration in Direct Bonding Interface”
MAM 2016 03/2016 Bruxelles Physics behind SmartCut™
ECS Prime 2016 10/2016 Honolulu

F. Rieutord, S. Tardif, F.Mazen, D.Landru, and O. Kononchuk
“High purity silion symposium Defect Evolution During Silicon SmartCut™”
ECS Prime 2016 10/2016 Honolulu

C. Kirchlechner et al. “What can you learn from a µLaue experiment”
Multiscale Materials Modelling (MMM), Dijon, France, 11.10.2016

C. Kirchlechner, N. Malyar, J.-S. Micha, G. Dehm “Insights into dislocation grain-boundary interaction by X-ray µLaue diffraction”
Dislocations 2016, West Lafayette, USA, 22.09.2016

C. Kirchlechner et al. “Synchrotron ebased µLaue diffraction to probe plasticity at interfaces”
IRSP 2016, Dresden, Germany, 01.06.2016

C. Kirchlechner, N. Malyar, J.S. Micha P.J. Imrich, G. Dehm “X-ray µLaue diffraction to understand plasticity at interfaces”
DPG Frühjahrstagung 2016, Regensburg, Deutschland, 08.03.2016

N. Malyar, J.-S. Micha, G. Dehm, C. Kirchlechner “Slip transfer through coherent 3 (111) twin boundaries loaded in different crystallographic directions”
AK Rasterkraftmikroskopie und nanomechanische Methoden, Saarbrücken, Deutschland, 15.03.2016

Tao Zhou, O. Ulrich, O. Geaymond, & G. Renaud « In situ Synchrotron X-ray Scattering of SiGe Nanowires : Growth, Strain and Bending”
Tailor2016 Mars-Avril 2016, Fontainebleau

Tao Zhou, O. Ulrich, O. Geaymond, & G. Renaud “In situ Synchrotron X-ray Scattering of SiGe Nanowires : Growth, Strain and Bending”
GDR PULSE 2016 Juillet 2016 Marseille

F. Jean, N. Blanc, J. Coraux, G. Renaud “Graphene on Ir structure by synchrotron X-rays”
ECOSS32 Sept 2016 Grenoble

2015

Tournus et al. "Auto-organisation d’agrégats déposés sur le réseau de moiré du graphène"
Colloque Rayons X & Matière, Grenoble décembre 2015,

Bardotti et al. “Self organization of size selected FexPt1-x clusters on graphene”
GDR Nanoalliage réunion Plénière, Porquerolles, mai 2015,

Coraux et al. « Epitaxial graphene on metal hybrid systems"
3S'15, Les Arcs, mars 2015

G. Renaud et al. "Graphene on Ir structure by synchrotron X-rays"
3S'15, Symposium on Surface Science, Les Arcs, Mars 2015

G. Renaud et al. "Graphene on Ir structure by synchrotron X-rays"

European Conference on Surface Science, ECOSS-31, Barcelone, Septembre 2015

(invited) G. Renaud et al. "Structure, morphology and organization of nanoparticles during their growth by MBE or CVD using in situ GISAXS and GIXD"
Institut Lumière-Matière, 10 mars 2015

(invited) G. Renaud "French CRG/IF beamline at the ESRF"
SOLEIL, 16 avril 2015

(invited) G. Renaud “In situ X-ray scattering study of SiGe nanowires: growth, strain and dance"
GDRi MECANO General Meeting Marseille 5-6 Nov. 2015.

GDRI MECANO meeting may 2015, Grenoble: F. Rieutord et al
S. Tardif et al., “Strain mapping in Ge microdevices: a combined experimental study”
GDRi MECANO: Mechanical Issues for Advanced Electron Devices Workshop, Minatec, Grenoble, France, June 29-30th 2015

J. Eymery et al, H. Palancher et al, J.-S. Micha et al, F. Rieutord et al, T. Ors et al, A. Fernandez-Martinez et al
XIème Colloque Rayons X & Matière, Grenoble, France, December 1-4th, 2015

S. Tardif et al., “Full strain tensor mapping in Ge microdevices using X-ray Laue microdiffraction”
XIème Colloque Rayons X & Matière, Grenoble, France, December 1-4th, 2015

J.-S. Micha et al, M. Fèvre et al, T. Ors et al, « µLaue on BM32 capabilities for materials science »
Soleil User Meeting, Saclay
MECASENS VIII septembre 2015 Grenoble

E. Castelier et al, « Strain map in polycrystalline UO2 nuclear fuel »
T. Ors et al, « Combination of EBSD and µLaue in ZrO2 microstructure mapping »
A. Davydok et al, « Evaluation of accuracy in strain by µLaue »
S. Tardif et al., “Strain mapping in Ge microdevices: a combined experimental study”
Size-Strain VII, Oxford, UK, September 21-24th, 2015

H. Palancher et al, « UO2 investigations by µLaue »
EMRS, may 2015, Lille, France :

J.L. Grosseau-Poussard et al 13th International Ceramics Congress Juin 2015, Montecatini terme, Italie : (Advances in Science and Technology 91,162)

J. Eymery et al
11th ICNS (Internat. Conference on Nitride Semiconductors) Sept 2015 Beijing, China

C. Kirchlechner et al
14th International Union of Materials Research Societies-International Conference on Advanced Materials, Jeju Island, South Korea, octobre 2015
International Symposium on Plasticity, Montego Bay, Jamaica, janvier 2015:
ECI Nanomechanical Testing V, Albufeira Portugal, octobre 2015:
Materials Seminar, Department Materials Science and Engineering, UT Knoxville, USA, sept. 2015
European Solid Mechanics Conference, ESMC 2015, Madrid, Spain, juillet 2015
Seminar Lecture at the Institute for Materials, Ruhr-Bochum University, Bochum, Germany, juin 2015:
Gefüge und Bruch 2015, Leoben, Austria, 10.04.2015

C. Kirchlechner et al, N.Malyar et al
ICM12, Karlsruhe, Germany, may.2015

N.Malyar et al., AK Rasterkraftmikroskopie und nanomechanische Methoden, II. Meeting, TU Darmstadt, mars 2015:

8.2.3 Lectures & Tutorials

HERCULES Laue tutorials & practicals

ESRF user meeting tutorials “Laue microdiffraction”

ANF-Laue 26-29 september 2017 CNRS National Training (in french):”Microdiffraction Laue: de la mesure à l’analyse”

2DSchool@Grenoble Grenoble, Juin 2018
"2D Materials studied by X-ray diffraction"
G. Renaud

XTOP 2018, Septembre 2018, Bari, Italie:
"Structure of surfaces and interfaces studied with hard X-rays"
G. Renaud

HERCULES, Grenoble, every spring since 2005
"Surface structures with hard X-rays" et "Nanoobjects with hard X-rays"
G. Renaud

Ecole Thématique CNRS “Réflectivité de Rayons X / neutrons”, October 2018, Marcoule, France
“Grazing Incidence X-ray Diffraction”
S. Tardif

European School of Surface and Nuclear Sciences, May 2018, Porquerolles, France
“Grazing Incidence X-ray Diffraction”
F. Rieutord

8.3 Annexe 3 Most cited articles (published since 2015)

The following list is sorted by decreasing number of citations (estimated in Feb. 2020) with following ‘User type’ codes:

- **EXT** for external users,
- **Coll** for collaboration between beamline staff and external users (mainly driven or initiated by external users). IHR beamtime can be occasionally used.
- **IHR** for activities initiated by beamline staff or strongly dependent on its involvement (in charge of X-ray measurements) in case of collaboration with external users. IHR beamtime is often used.

First author, Journal, year	Instrument	#cited	Scientific field	User type
Gueye, Chem. Mat. 2016	GMT	65	Soft Matter, Surface	Coll
Andreazza, Surf. Sci. Rep., 2015	INS2	35	Fund. Surface science	Coll
Guilloy, Nano Letters, 2015	µLaue	28	Applied Materials	IHR
Guilloy, ACS Photonics, 2016	µLaue	23	Applied Materials	IHR

Camosi, Phys. Rev. B, 2017	INS2	22	Fund. Surface science	Coll
Leclere, J. Appl. Cryst., 2015	µLaue	22	Fund. Materials Mechanics	Coll
Gassenq, Appl. Phys. Lett., 2016	µLaue	20	Applied Materials,	IHR
Tardif, ACS Nano, 2017	GMT	19	Applied Energy Materials	IHR
Malyar, Acta Mat., 2017	µLaue	19	Fund. Materials Mechanics	Coll
Tsipas, ACS Nano, 2018	INS2	16	Applied Materials, Surface	IHR
Reboud, Prog. Cryst. Growth & Charac. Mat., 2017	µLaue	16	Applied Materials,	IHR
Petit, J. Sync. Rad., 2015	µLaue	16	Methods	Coll
Malyar, Acta Mat., 2017	µLaue	15	Fund. Materials Mechanics	Coll
Kuświk, Phys. Rev. B, 2015	INS2	15	Fund. Surface science	Coll
Plancher, Exp. Mech., 2016	µLaue	14	Methods	IHR
Niu, Sci. Rep., 2016	INS2	14	Applied Materials,	EXT
Daval, Geochim & Cosmochim., 2017	GMT	13	Fund. Surface science	Coll

8.4 Annexe 4 List of publications in the highest ranked journals

Journal	IF (2018)	#	Instrument	Users type
Prog. Mat.Sci.	23.7	1	µLaue	EXT
Adv. Func. Mat.	15.6	1	INS2	IHR
Surf.Sci. Rep.	14.8	1	INS2	EXT
ACS Nano	13.9	3	2 INS2, GMT	2 Coll, IHR
Nano Letters	12.3	1	µLaue	IHR
Chem. Mat.	10.2	1	GMT	Coll
Phys. Rev. Lett.	9.2	2	INS2, GMT	Coll, EXT
ACS Appl. Mat. Interf. J. Phys. Chem. Lett.	8.5, 7.3	2	GMT	EXT
Acta Mat.	7.3	5	µLaue	4 Coll, IHR

2D Materials	7.3	1	INS2	Coll
ACS Photonics	7.1	1	µLaue	IHR
Nanoscale, Acta Cryst B	7, 6.7	2	INS2	EXT, IHR
Mat & Design	5.8	1	µLaue	Coll
J. Chem Theo & Comp. Appl. Surf. Sci.	5.3, 5.1	2	INS2	2 Coll
Adv. Mat. Interf.	4.7	1	INS2	Coll
Scripta Mat., Phys. Rev. App ACS Appl. Energy Mater.	4.5	3	2 µLaue, GMT	IHR, EXT, IHR
J. Phys. Chem. C	4.3	6	3 GMT, 3 INS2	5 Coll, IHR
Geochim. et cosmo.	4.3	1	GMT	Coll
Sci. Rep. Cryst. Growth Design	4, 4.1	3	INS2	EXT, IHR, Coll

8.5 Annexe 5: Other bibliometric figures (calculated in Feb. 2020 after beamline database started in 1996)

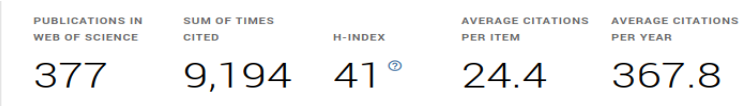

9 Annexe 6: Selected publications: 5 reprints / publications of work accomplished on the beamline

SL 1: P. Capiod *et al.*, Phys. Rev. Lett. **122** 106802 (2019) INS Coll

SL 2: G. Sitja *et al.*, J. Phys. Chem. C, 123, 24487 (2019) INS Coll

SL 3: B. Wild *et al.*, J Phys. Chem. C **123**, 24520 (2019) GMT Coll

SL 4: A. Davydok *et al.*, Materials and Design, **108**, 66 (2016) µLaue Coll

SL 5: J. Hektor *et al.*, Scripta Materialia, **144**, 1 (2018) µLaue Coll

9.1 SL 1: INS2 P. Capiod *et al.*, Phys. Rev. Lett. 122 106802 (2019)

Elaboration of Nanomagnet Arrays: Organization and Magnetic Properties of Mass-Selected FePt Nanoparticles Deposited on Epitaxially Grown Graphene on Ir(111)

Pierre Capiod,[1] Laurent Bardotti,[1] Alexandre Tamion,[1] Olivier Boisron,[1] Clément Albin,[1] Véronique Dupuis,[1] Gilles Renaud,[2] Philippe Ohresser,[3] and Florent Tournus[1]

[1]*Institut Lumière Matière, UMR5306 Université Lyon 1-CNRS, Université de Lyon, 69622 Villeurbanne cedex, France*
[2]*Université Grenoble Alpes, CEA, INAC, MEM, F-38000 Grenoble, France*
[3]*Synchrotron SOLEIL, L'Orme des Merisiers, BP48, Saint-Aubin, 91192 Gif-sur-Yvette, France*

(Received 25 May 2018; revised manuscript received 25 January 2019; published 14 March 2019)

The moiré pattern created by the epitaxy of a graphene sheet on an iridium substrate can be used as a template for the growth of 2D atomic or cluster arrays. We observed for the first time a coherent organization of hard magnetic preformed FePt nanoparticles on the 2D lattice of graphene on Ir(111). Nanoparticles of 2 nm diameter have been mass selected in a gas phase and deposited with low energy on the hexagonal moiré pattern. Their morphology and organization have been investigated using grazing incidence small angle x-ray scattering, while their magnetic properties have been studied by x-ray magnetic circular dichroism, both pointing to a FePt cluster-graphene surface specific interaction. The spatial coherence of the nanoparticles is preserved upon annealing up to 700 °C where the hard magnetic phase of FePt is obtained.

DOI: 10.1103/PhysRevLett.122.106802

Nanoparticles are intensively studied for optical [1–4], catalytic [5–7], magnetic [8–12], and storage applications [13–18]. FePt nanoparticles are interesting candidates for ultrahigh density storage applications due to their extremely high magnetocrystalline anisotropy when chemically ordered in the $L1_0$ phase [19,20]. Another requirement for such applications, as well as for fundamental studies, is to organize magnetic nanoparticles in a 2D array. A great effort is devoted to the bottom-up elaboration of periodic patterned arrays of nanoparticles [21–25]. In this domain, the moiré pattern appearing from the epitaxy of graphene (g) on a transition metal (g/TM) has been used successfully to organize by physical vapor deposition (PVD) on g/Ru(0001), g/Cu(111), or g/Ir(111) a wide variety of pure metallic nanoparticles [21,26–28]. However, organized islands of Fe cannot be grown by PVD on g/Ir(111) [21], so that it is not possible to obtain a superlattice of FePt alloy nanoparticles, even using Pt seeding [26,29].

The MSLECBD (mass-selected low energy cluster beam deposition) technique [30–32] may be used to deposit preformed alloy nanoparticles having a chosen chemical composition. MSLECBD offers opportunities not accessible by PVD: the cluster size can be controlled and is independent of the surface coverage. Recent studies point out the possibility to organize pure nanoclusters on a graphene moiré using soft-landed clusters of Pt on g/Ir(111) or Pd on g/Ru(0001) [33,34], where one of the three high-symmetry sites of the surface is more favorable for adsorption. The same approach could enable to order metallic alloys on graphene, and especially hard-magnetic ones ($L1_0$ FePt) with a strong uniaxial magnetization. Such a possibility would rely on a preferential adsorption of deposited particles on specific sites of the moiré superlattice. In order to study the effect of the graphene substrate on FePt particle organization and magnetic properties, we consider here diluted samples, thus avoiding interparticle interactions. In this Letter, we report on the low-energy deposition of mass-selected FePt clusters (around 2 nm diameter) on the g/Ir(111) moiré superlattice, and their characterization by GISAXS (grazing incidence small angle x-ray scattering) and XMCD (x-ray magnetic circular dichroism). These two complementary experimental techniques allow us to probe, respectively, the organization and magnetic properties (and hence to detect the chemical ordering phase transition upon annealing) of the FePt nanoparticles. A clear tendency to preferential pining and coherent organization is found, as well as specific properties due to the cluster-surface interaction.

The substrate of graphene on a Ir(111) monocrystal has been prepared using chemical vapor deposition (CVD) following a procedure well known in the literature [35]. Chemically disordered FePt clusters of 2 nm diameter, synthesized by the MSLECBD technique, are deposited on the g/Ir(111) surface in a soft-landing regime at various temperatures (see Supplemental Material [36]) with a density of 3×10^4 cluster/μm^2. With this surface coverage and nanoparticle size, a compromise is obtained between a low proportion of multimers [37] and a sufficient signal in x-ray experiments. An amorphous carbon capping layer (a few nanometers thick) is grown after cluster deposition,

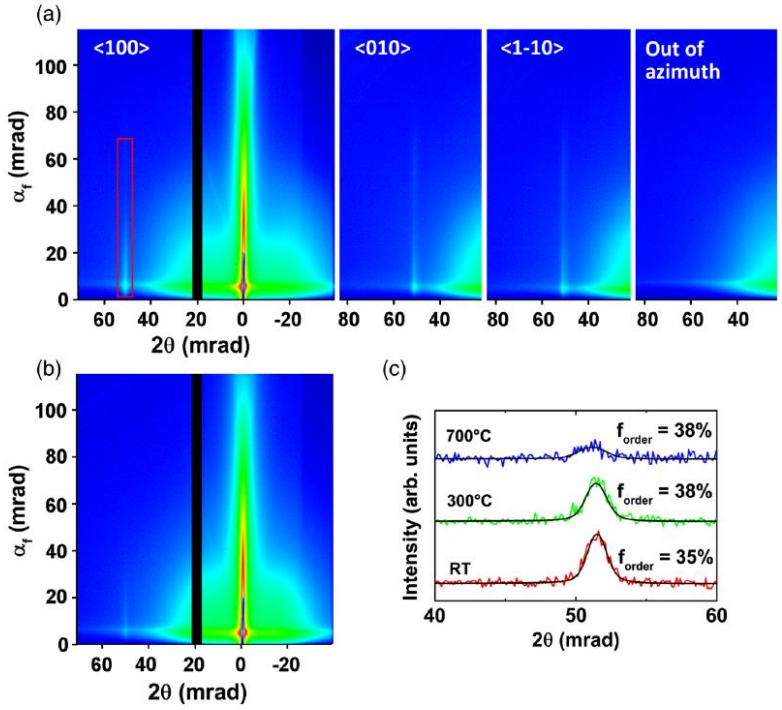

FIG. 1. (a) GISAXS intensities (at room temperature, after deposition at 150 °C) along the ⟨100⟩, ⟨010⟩, and ⟨1-10⟩ directions of the hexagonal moiré lattice. The presence of a correlation peak (highlighted in red) in those directions reflects the hexagonal organization of FePt nanoparticles on the moiré lattice. Out of azimuth, no correlation is visible. (b) GISAXS intensity in the ⟨100⟩ direction at 700 °C. (c) GISAXS intensity profile (fixed α_f) of the correlation peak for three different temperatures with their respective fits represented with the black line. The curves have been shifted for clarity. The fraction f_{order} of particles coherently located on the moiré lattice remains constant around 35% ±3%.

using carbon wire sublimation under vacuum, to avoid any contamination and sintering.

First, the organization and the nanoparticles morphology have been investigated by GISAXS on the BM32 beam line at the European Synchrotron Radiation Facility (ESRF), with an incident x-ray energy of 11 keV and a critical angle of 0.42°. Measurements have been performed on a capped sample, after FePt cluster deposition at 150°C. Once in the beam line UHV chamber, the sample is heated up from room temperature to 700°C.

GISAXS measurements provide information on the lateral correlation, size, and shape of the nanoparticles [38–40]. The central intensity reflects the size and shape of the nanoparticles while the correlation peak in Fig. 1(a) (highlighted in red) corresponds to the coherent organization of the nanoparticles across the sample. The correlation peak appears only in preferential directions (remarkably, in the ⟨100⟩, ⟨010⟩, and ⟨1-10⟩ directions with the h, k, $l = 0$ surface hexagonal lattice notation), and in the vicinity of $2\theta = 51$ mrad which corresponds to the moiré lattice parameter of 2.53 nm [34,35,41]. In other directions (out of azimuth), only the central intensity remains. This indicates that, at room temperature, a 2D hexagonal organization of FePt clusters on the moiré lattice, similar to size-selected Pt clusters on $g/\text{Ir}(111)$ [34] is obtained, and excludes a simple preferential nearest-neighbor distance. This demonstrates that clusters can diffuse on the surface (since they are initially randomly deposited [42,43]) before being pinned on specific sites reflecting the moiré periodicity. The cluster-surface interaction is thus favorable for self-organization and may be described as a chemisorption involving π-d hybridization [44] and local rehybridization from sp^2 carbon to diamond-like sp^3 [33]. The sample was then progressively annealed up to 700 °C, high enough to promote the FePt $L1_0$ chemical ordering [45,46]. As seen in Fig. 1(b), the correlation peak is less intense but a coherent organization still remains. Qualitatively, one can detect moderate changes in the form factor of the particles: the GISAXS signal is more concentrated and intense at low θ angle (near the specular beam).

A quantitative analysis of the GISAXS patterns (using in-plane and out-of-plane line cuts) gives a precise estimation of the form factor (size and shape) and the lateral correlation of the cluster superlattice. Furthermore, it is possible to link the correlation peak intensity to the proportion f_{order} (supposed to be homogeneous over the entire sample) of nanoparticles coherently pinned on the moiré lattice [34].

The total GISAXS intensity can indeed be separated in two contributions: one coming from particles with random locations [47] on the surface (i.e., with no constructive interference and thus no correlation peak) and the other from organized particles on the moiré lattice.

The incident cluster size deduced from transmission electron microscopy (TEM) observations can be modeled with a Gaussian centered on the mean equivalent diameter $D_{\mathrm{TEM}} = 1.9$ nm (see Supplemental Material [36]). First, we want to determine if the incident particle size is preserved on the surface, since diffusion-coalescence processes could produce larger particles. A first quick analysis of the out-of-azimuth GISAXS cuts, by fitting with a simple Gaussian size distribution, indicates that the diameter is globally conserved (mean diameter around 1.9 nm), however, with a presence of some larger particles (relative dispersion of 50%). In fact, it is not surprising to find a particle size distribution different from the incident monomers because even without diffusion, there is a probability (which depends on the cluster density) that a cluster lands on another one and forms a dimer (or multimers) [48]. If clusters diffuse on the surface, they can form additional multimers. Therefore, we can use a better description to analyze GISAXS measurements using two Gaussians: a first one for monomers (main contribution) and a second one corresponding to dimers and multimers. The respective proportion of monomers (X) and dimers ($1\text{-}X$) can be inferred from a best fit, together with the monomers mean size and the dimers relative diameter dispersion [49]. Moreover the particle shape is modeled by truncated spheres with an adjustable H/D ratio, where H is the height and D the in-plane diameter. A value $H/D = 0.74$, coherent with the wetting parameter found for Pt clusters on $g/\mathrm{Ir}(111)$ [34] is obtained. The monomers mean size (spherical equivalent diameter [50]) is found to be $D_{\mathrm{eq}} = 1.9$ nm which is in full agreement with the TEM size histogram while the monomers proportion amounts to 73%. Most of FePt particles on the surface have thus kept their incident size which shows that diffusion, during cluster deposition, is limited but still present. Note that diffusion is indeed required to explain the observed coherent organization and the monomers proportion, slightly lower than expected with a random pinning. Once the size and shape parameters have been determined from the optimal fit of out-of-azimuth GISAXS patterns (see Supplemental Material [36], S3), the proportion f_{order} of particles located on moiré sites is determined from a GISAXS fit along the $\langle 100 \rangle$ direction of the moiré lattice. Here, the form factors are fixed while the interference function is adjusted (it is directly related to the particle organization, i.e., to the moiré crystallographic parameter and the proportion f_{order} [39]).

The intensity of the correlation peak (which depends both on the form factor and on the interference function) and calculated fits are pictured on Fig. 1(c) for three different temperatures. At room temperature $f_{\mathrm{order}} = 35\% \pm 3\%$, which is slightly lower but comparable to Pt particles deposited on $g/\mathrm{Ir}(111)$ where a value of around 50% is found [34]. This difference is probably due to the larger size of nanoparticles and/or to the alloy nature of FePt clusters. The evolution of the form factor between RT and annealing at 300 °C slightly influences the intensity of the correlation peak but f_{order} is in fact almost the same. This is coherent with the fact that at 300 °C the temperature is relatively low and does not induce any important changes in the nanoparticles, graphene, or amorphous carbon capping layer morphology. Remarkably, at 700 °C the organization is preserved and remains visible, with $f_{\mathrm{order}} = 38\% \pm 3\%$. The nanoparticle shape is unchanged, however, with a decrease of the monomers proportion down to 65%. At such a high temperature, atomic displacements can occur allowing some particles to diffuse over a small distance.

The fact that $f_{\mathrm{order}} < 100\%$ indicates that two types of pinning sites coexist: coherent location(s) within the moiré cell and other positions (incoherent contribution). f_{order} is then linked to the relative density of the different possible pinning sites. However, a full description of surface energy potential together with diffusion and coalescence processes is required to infer their density from the f_{order} value, which is out of the scope of this work. Nevertheless, the estimated density of defects in the moiré lattice (moiré domains have sizes in the micrometer range) and/or graphene sheet (wrinkles, step edges…) [35,51,52] is too low to account for the proportion of FePt nanoparticles randomly located. This means that clusters landing in some places inside a moiré cell have a non-negligible probability to end up at many various locations (this supposes some kind of rough potential energy landscape, more complex than with only three high-symmetry pining sites), while other landing areas enable the FePt particles to reach specific pinning sites. In order to reach ultradense (>1 Tbit/in^2) magnetic bit arrays, it is important to understand the pinning mechanisms of preformed clusters as well as the surface energy potential, which governs the diffusion of the nanoparticles on the moiré surface. This may be achieved through theoretical studies or additional experiments (such as STM investigations).

From the GISAXS study, we can tell that the incident particles have been preserved but the surface has a clear influence on their behavior: the random deposition produces, in the end, a partially organized array of particles, even at 700 °C. This cluster-surface interaction may as well have an impact on the magnetic properties, which can be investigated by XMCD. Moreover, if chemical ordering has occurred upon annealing, it should be visible through an evolution of the magnetic properties.

XMCD measurements have been carried out at the DEIMOS beam line at the SOLEIL Synchrotron in Paris-Saclay [53]. By using circularly polarized x rays, the Fe $L_{2,3}$ edges have been probed using total electron yield (fluorescence mode for the hysteresis loops) for several incidence angles, from normal to the sample (0°) to 60° from normal.

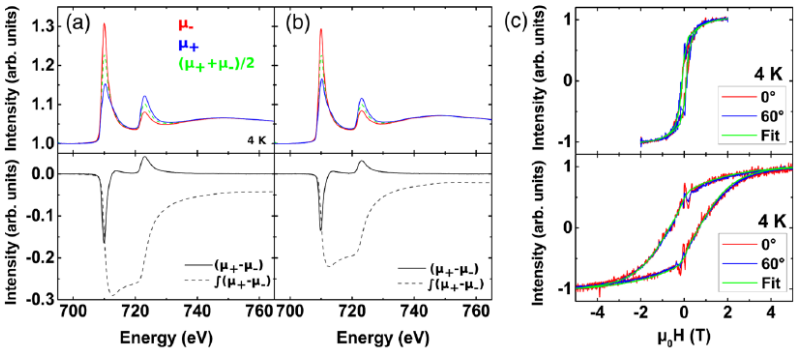

FIG. 2. Top (a) and (b) are, respectively, before and after annealing XAS spectrum at the Fe $L_{3,2}$ edges taken at 4 K for light circularly polarized left (+) and right (−) with the isotropic XAS signal shown in dotted line. Both averaged XAS signals have been normalized for a direct comparison of the XMCD spectrum. The XMCD spectrum [bottom (a) and (b), respectively before and after annealing] is the difference between the two XAS spectra recorded with opposite orientation of the magnetic field and the x-ray polarization (respectively, blue and red for left and right helicity). The dotted lines are the integral of the XMCD spectrum to highlight the modification of the intensity as well as the evolution of the m_L/m_S ratio. (c) Hysteresis loops taken at 4 K for two incidence angles 0° (normal to the surface, in red) and 60° from the normal (in blue), before annealing (top) and after annealing (bottom). The fits are pictured in green for both phase of the nanoparticles.

Those measurements were investigated from room temperature to low temperature (4 K), before and after annealing of the sample up to 700 °C. The sample used for the XMCD characterization, (different from the GISAXS measurements) has been prepared in the same conditions with a higher deposition temperature of 300 °C (the organization is identical, see Supplemental Material [36]).

Figure 2(c) shows the hysteresis loops at low temperature (4 K, i.e., in the blocked regime) before (top) and after annealing at 700 °C (bottom), for two different x-ray incidence angles. The hysteresis loops are completely isotropic which shows that there is neither demagnetizing factor effect, nor any preferential orientation of the nanoparticles. Interactions among the 2D layer of nanoparticles (as for a thin magnetic film) or interface anisotropy with the graphene sheet would have introduced an orientation dependence (anisotropy) of the hysteresis loops. Since none has been observed, this is an other evidence that FePt nanoparticles have kept their individuality even after annealing. Note that the magnetic remanence at 4 K is around 50% of the saturation, which is consistent with the model of isolated nanoparticles having a random distribution of their easy axis.

The effect of annealing on the opening of the loops is clear: the coercive field H_C is increasing from 122 to 650 mT, reflecting an increase of the magnetic anisotropy constant. From the room temperature magnetization curves (in the superparamagnetic regime, see Supplemental Material [36]), we observe that, as expected, the magnetic size distribution is almost unchanged upon annealing and is in full agreement with the geometrical size distribution deduced from GISAXS. To go further, a theoretical model based on a combined Stoner-Wohlfarth and Néel relaxation description, has been used to fit the hysteresis loops, taking into account the magnetic size distribution [54–58]. A biaxial description has been adopted for the magnetic anisotropy [59], in order to reflect the non ideal morphology of the nanoparticles. Before annealing, the mean anisotropy constant is $K_1 = 300$ kJ/m^3 with a relative dispersion of 40% (we use a Gaussian distribution, which reflects the variation of the anisotropy constant among the particles) and a biaxial ratio of $K_2/K_1 = 1.2$.

After annealing, the mean K_1 is 1.4 MJ/m^3 with an increased relative dispersion of 70% and an unchanged biaxial ratio. This large anisotropy dispersion must be due to a chemical order distribution among the FePt particles, in addition to the existence of a variety of geometries (and possible defects) [45]. The two branches of the hysteresis loop only merge at very high field which implies that some particles in the assembly have an anisotropy field higher than 3 T. We estimate the highest anisotropy constant around 3 MJ/m^3 which is close to the bulk value for $L1_0$ FePt [60,61]. The value found for the magnetic anisotropy constant is very large for 2 nm FePt nanoparticles, indicating a transition towards the chemically ordered $L1_0$ phase, already observed for particles embedded in a carbon matrix (with possible defects and multiply twinned chemically ordered particles) [45].

Before annealing, the x-ray absorption spectroscopy (XAS) and XMCD measurements depicted on Fig. 2(a), show well-defined Fe-$L_{2,3}$ absorption edges with no sign of oxidation [62,63] and a clear magnetic Fe signature. All the spectra have been acquired at the saturation regime, respectively 2 and 5 T before and after annealing. The maximum intensity of the XMCD spectrum decreases for annealed FePt nanoparticles [Fig. 2(b)] reflecting a reduced magnetic moment as theoretically expected for $L1_0$ FePt compared to the A1 phase [64,65].

The Fe magnetic moments (spin and orbital moments, respectively m_S and m_L) have been determined by applying the sum rules [66–68] with a number of holes $N_h = 3.705$ [64,69]. The orbital moment is 0.11 ± 0.01 before annealing and decreases to 0.06 ± 0.01 after annealing. The spin moment is 3.0 ± 0.2 before annealing and 2.5 ± 0.2 after annealing. This corresponds to a m_L/m_S ratio of 0.037 ± 0.005 before annealing and 0.024 ± 0.005 after annealing.

The Fe magnetic moment for the disordered A1 FePt nanoparticles is close to the bulk [70]. Such a high value has never been reported for disordered FePt nanoparticles. Nanoparticles are very sensitive to their environment because of the high surface-to-volume ratio, so that an influence of the graphene on the orbital and spin moments cannot be excluded [71]. After annealing, the spin moment is lower and is similar to the value found in the literature for FePt nanoparticles [64,72]. However, m_L is surprisingly low compared to previous studies [64,73], including our results on 3 nm FePt nanoparticles embedded in carbon matrix (0.18 μ_B/at) [72]. m_L/m_S is very close to the value of $L1_0$ bulk (around 2.5% [65,69,74–76]) and smaller than reported for thin films [77–79], which is unexpected, since it is usually assumed that the orbital moment in nano-objects is higher than in bulk due to the broken symmetry. Thus it seems that the presence of graphene has a strong effect on Fe orbital moment in the chemically ordered nanoparticles through modification of the electronic structure. The particle flattening and pining, as revealed by GISAXS, imply that a sizable interaction exist between the FePt clusters and the graphene surface. Charge transfers can occur between the nanoparticles and the graphene and it is very likely to observe a mixing of electronic states as it is observed for clusters and adatoms [80–83]. Magnetic anisotropy energy and orbital moment are closely related: the origin of the MAE comes from the anisotropy of the density of state resulting from the spin-orbit interactions for two distinct directions of the system. The equations derived by Bruno [84] state that for a sizable contribution to the magnetic anisotropy energy, strong spin-orbit coupling and large orbital moment are needed, which is especially true for the Pt atoms in a FePt alloy. Here, we find that the MAE is not directly proportional to the Fe orbital moment in FePt nanoparticles, in full agreement with theoretical studies [69,75,76,78,85,86], even if the question may still be debated [77].

In this study, we have reported the organization of size-selected FePt magnetic nanoparticles on a moiré lattice from the epitaxy of graphene on an iridium monocrystal. The organization has been studied using GISAXS measurements and simulations. We found that after deposition, 38% of the nanoparticles are coherently pinned on the hexagonal moiré lattice. Further theoretical investigation is needed to understand the adsorption energy landscape and the resulting cluster-surface interaction responsible for the organization. A subsequent annealing leads to an impressive increase of the magnetic anisotropy (deduced from XMCD measurements), which can be ascribed to a $L1_0$ chemical ordering transition, while the FePt nanoparticles remain organized on the surface. For the first time, a system made of small FePt nanoparticles, chemically and spatially ordered, has been synthesized and characterized. Moreover, we have illustrated that the magnetic anisotropy and the Fe orbital magnetic moment can exhibit a complex relationship and a subtle dependence on interface effects. Future *ab initio* calculations may give more insight on the electronic and magnetic interactions between FePt nanoparticles and the $g/\mathrm{Ir}(111)$ substrate.

This work is supported by the French state funds Equipex ANR-11-EQPX-0010. The authors acknowledge O. B. and C. A. for their support and assistance at PLateforme LYonnaise de Recherche sur les Agrégats (PLYRA). O. Ulrich and F. Choueikani for their help on, respectively, the BM32 beam line at ESRF and the DEIMOS beam line at SOLEIL.

[1] R. Philip, G. R. Kumar, N. Sandhyarani, and T. Pradeep, Phys. Rev. B **62**, 13160 (2000).
[2] R. Jin, Nanoscale **7**, 1549 (2015).
[3] M. Cui, Y. Zhao, and Q. Song, Trends Anal. Chem. **57**, 73 (2014).
[4] J. L. Menendez, B. Bescos, G. Armelles, A. Cebollada, C. Quintana, E. Navarro, R. Serna, J. Gonzalo, C. N. Alfonso, R. Doole *et al.*, IEEE Trans. Magn. **37**, 1416 (2001).
[5] S. Guo, S. Zhang, L. Wu, and S. Sun, Angew. Chem. **124**, 11940 (2012).
[6] S. Guo and S. Sun, J. Am. Chem. Soc. **134**, 2492 (2012).
[7] L. Xin, F. Yang, S. Rasouli, Y. Qiu, Z.-F. Li, A. Uzunoglu, C.-J. Sun, Y. Liu, P. Ferreira, W. Li *et al.*, ACS Catal. **6**, 2642 (2016).
[8] S. Sun, S. Anders, T. Thomson, J. E. E. Baglin, M. F. Toney, H. F. Hamann, C. B. Murray, and B. D. Terris, J. Phys. Chem. B **107**, 5419 (2003).
[9] S. Sun, C. B. Murray, D. Weller, L. Folks, and A. Moser, Science **287**, 1989 (2000).
[10] S. M. Binz, M. Hupalo, X. Liu, C. Z. Wang, W.-C. Lu, P. A. Thiel, K. M. Ho, E. H. Conrad, and M. C. Tringides, Phys. Rev. Lett. **109**, 026103 (2012).
[11] F. Tournus, Phys. Rev. E **84**, 011612 (2011).
[12] T. T. Trung, D. T. Nhung, N. H. Nam, and N. H. Luong, J. Electron. Mater. **45**, 3621 (2016).
[13] C. Chappert, A. Fert, and F. N. Van Dau, Nat. Mater. **6**, 813 (2007).
[14] G. Reiss and A. Hutten, Nat. Mater. **4**, 725 (2005).
[15] J. Hu, J. Chen, and G. Ju, in *Developments in Data Storage* (John Wiley & Sons Inc., New York, 2011), pp. 223–255.
[16] N. A. Frey, S. Peng, K. Cheng, and S. Sun, Chem. Soc. Rev. **38**, 2532 (2009).
[17] H.-w. Zhang, Y. Liu, and S.-h. Sun, Front. Phys. China **5**, 347 (2010).
[18] S. Sun, Adv. Mater. **18**, 393 (2006).

[19] C.-b. Rong, N. Poudyal, G. S. Chaubey, V. Nandwana, R. Skomski, Y. Q. Wu, M. J. Kramer, and J. P. Liu, J. Appl. Phys. **102**, 043913 (2007).

[20] K. Inomata, T. Sawa, and S. Hashimoto, J. Appl. Phys. **64**, 2537 (1988).

[21] A. T. N'Diaye, T. Gerber, C. Busse, J. Mysliveček, J. Coraux, and T. Michely, New J. Phys. **11**, 103045 (2009).

[22] L. Bardotti, F. Tournus, C. Albin, O. Boisron, and V. Dupuis, Phys. Chem. Chem. Phys. **16**, 26653 (2014).

[23] F. Leroy, G. Renaud, A. Létoublon, and R. Lazzari, Phys. Rev. B **77**, 235429 (2008).

[24] F. Leroy, G. Renaud, A. Létoublon, S. Rohart, Y. Girard, V. Repain, S. Rousset, A. Coati, and Y. Garreau, Phys. Rev. B **77**, 045430 (2008).

[25] S. B. Darling, N. A. Yufa, A. L. Cisse, S. D. Bader, and S. J. Sibener, Adv. Mater. **17**, 2446 (2005).

[26] J. Coraux, L. Marty, N. Bendiab, and V. Bouchiat, Acc. Chem. Res. **46**, 2193 (2013).

[27] E. Soy, Z. Liang, and M. Trenary, J. Phys. Chem. C **119**, 24796 (2015).

[28] Q. Liao, H. J. Zhang, K. Wu, H. Y. Li, S. N. Bao, and P. He, Nanotechnology **22**, 125303 (2011).

[29] C. Vo-Van, S. Schumacher, J. Coraux, V. Sessi, O. Fruchart, N. B. Brookes, P. Ohresser, and T. Michely, Appl. Phys. Lett. **99**, 142504 (2011).

[30] A. Perez, P. Mélinon, V. Dupuis, B. Prével, L. Bardotti, J. Tuaillon-Combes, B. Masenelli, M. Treilleux, M. Pellarin, J. Lermé *et al.*, Mater. Trans., JIM **42**, 1460 (2001).

[31] A. Perez, V. Dupuis, J. Tuaillon-Combes, L. Bardotti, B. Prevel, E. Bernstein, P. Mélinon, L. Favre, A. Hannour, and M. Jamet, Adv. Eng. Mater. **7**, 475 (2005).

[32] A. Perez, P. Melinon, V. Dupuis, L. Bardotti, B. Masenelli, F. Tournus, B. Prevel, J. Tuaillon-Combes, E. Bernstein, A. Tamion *et al.*, Int. J. Nanotechnology **7**, 523 (2010).

[33] B. Wang, B. Yoon, M. König, Y. Fukamori, F. Esch, U. Heiz, and U. Landman, Nano Lett. **12**, 5907 (2012).

[34] S. Linas, F. Jean, T. Zhou, C. Albin, G. Renaud, L. Bardotti, and F. Tournus, Sci. Rep. **5**, 13053 (2015).

[35] J. Coraux, A. T. N'Diaye, M. Engler, C. Busse, D. Wall, N. Buckanie, F.-J. M. zu Heringdorf, R. van Gastel, B. Poelsema, and T. Michely, New J. Phys. **11**, 023006 (2009);

[36] See Supplemental Material at http://link.aps.org/supplemental/10.1103/PhysRevLett.122.106802 describes the elaboration of the samples and all the steps in the experimental process. We included relevant information on the effect of the deposition temperatures (S1), a TEM image with the corresponding equivalent diameter of the deposited nanoparticles (S2), an analysis of GISAXS patterns with the fitted values used in the article (S3), and hysteresis loops taken at 300 K before annealing showing the conservation of magnetic size distribution and the correlation of magnetic and particle size distribution (S4 and S5).

[37] With purely random positions, the proportion of monomers (single nanoparticle of the incident size) would be around 80%.

[38] T. H. Metzger, I. Kegel, R. Paniago, A. Lorke, J. Peisl, J. Schulze, I. Eisele, P. Schittenhelm, and G. Abstreiter, Thin Solid Films **336**, 1 (1998).

[39] G. Renaud, R. Lazzari, C. Revenant, A. Barbier, M. Noblet, O. Ulrich, F. Leroy, J. Jupille, Y. Borensztein, C. R. Henry *et al.*, Science **300**, 1416 (2003).

[40] G. Renaud, R. Lazzari, and F. Leroy, Surf. Sci. Rep. **64**, 255 (2009).

[41] A. T. N'Diaye, S. Bleikamp, P. J. Feibelman, and T. Michely, Phys. Rev. Lett. **97**, 215501 (2006).

[42] F. Tournus, J. Nanopart. Res. **13**, 5211 (2011).

[43] F. Tournus, A. Tamion, N. Blanc, A. Hillion, and V. Dupuis, J. Appl. Phys. **109**, 07B502 (2011).

[44] M. Lattelais and M.-L. Bocquet, J. Phys. Chem. C **119**, 9234 (2015).

[45] F. Tournus, K. Sato, T. Epicier, T. J. Konno, and V. Dupuis, Phys. Rev. Lett. **110**, 055501 (2013).

[46] B. Rellinghaus, S. Stappert, M. Acet, and E. F. Wassermann, J. Magn. Magn. Mater. **266**, 142 (2003).

[47] Truly random positions would produce no correlation peak, but it can also be the case if there are many different sites in the coherently probed zone, which would as well lead to no constructive interference. On the contrary, a statistical occupation of, for instance, three high-symmetry sites would also produce constructive interferences.

[48] F. Tournus, N. Blanc, A. Tamion, M. Hillenkamp, and V. Dupuis, J. Magn. Magn. Mater. **323**, 1868 (2011).

[49] The dimers mean diameter is directly related to the one of monomers (by volume conservation) and the relative diameter dispersion of monomers (incident clusters) is fixed to 10%.

[50] The spherical equivalent diameter D_{eq} (sphere of identical volume) of a truncated sphere of parameter H/D is given by $(D_{eq}/D)^3 = 3(H/D)^2[1-(2/3)(H/D)]$. In the case of $H/D = 0.74$, this corresponds to $D_{eq} = 0.94\ D$.

[51] N. Blanc, J. Coraux, C. Vo-Van, A. T. N'Diaye, O. Geaymond, and G. Renaud, Phys. Rev. B **86**, 235439 (2012).

[52] J. Coraux, A. T. N'Diaye, C. Busse, and T. Michely, Nano Lett. **8**, 565 (2008).

[53] P. Ohresser, E. Otero, F. Choueikani, K. Chen, S. Stanescu, F. Deschamps, T. Moreno, F. Polack, B. Lagarde, J.-P. Daguerre *et al.*, Rev. Sci. Instrum. **85**, 013106 (2014).

[54] A. Tamion, E. Bonet, F. Tournus, C. Raufast, A. Hillion, O. Gaier, and V. Dupuis, Phys. Rev. B **85**, 134430 (2012).

[55] M. Jamet, W. Wernsdorfer, C. Thirion, D. Mailly, V. Dupuis, P. Mélinon, and A. Pérez, Phys. Rev. Lett. **86**, 4676 (2001).

[56] M. Jamet, W. Wernsdorfer, C. Thirion, V. Dupuis, P. Mélinon, A. Pérez, and D. Mailly, Phys. Rev. B **69**, 024401 (2004).

[57] A. Tamion, C. Raufast, E. Bonet, V. Dupuis, T. Fournier, T. Crozes, E. Bernstein, and W. Wernsdorfer, J. Magn. Magn. Mater. **322**, 1315 (2010).

[58] A. Hillion, A. Tamion, F. Tournus, O. Gaier, E. Bonet, C. Albin, and V. Dupuis, Phys. Rev. B **88**, 094419 (2013).

[59] A. Thiaville, Phys. Rev. B **61**, 12221 (2000).

[60] O. A. Ivanov, L. V. Solina, V. A. Demshina, and L. M. Magat, Phys. Met. Metallogr. **35**, 81 (1973).

[61] J. M. D. Coey, IEEE Trans. Magn. **47**, 4671 (2011).

[62] P. S. Miedema and F. M. F. de Groot, J. Electron Spectrosc. Relat. Phenom. **187**, 32 (2013).

[63] W. Karim, A. Kleibert, U. Hartfelder, A. Balan, J. Gobrecht, J. A. van Bokhoven, and Y. Ekinci, Sci. Rep. **6**, 18818 (2016).

[64] C. Antoniak, J. Lindner, M. Spasova, D. Sudfeld, M. Acet, M. Farle, K. Fauth, U. Wiedwald, H.-G. Boyen, P. Ziemann *et al.*, Phys. Rev. Lett. **97**, 117201 (2006).
[65] P. Andreazza, V. Pierron-Bohnes, F. Tournus, C. Andreazza-Vignolle, and V. Dupuis, Surf. Sci. Rep. **70**, 188 (2015).
[66] C. T. Chen, Y. U. Idzerda, H.-J. Lin, N. V. Smith, G. Meigs, E. Chaban, G. H. Ho, E. Pellegrin, and F. Sette, Phys. Rev. Lett. **75**, 152 (1995).
[67] B. T. Thole, P. Carra, F. Sette, and G. van der Laan, Phys. Rev. Lett. **68**, 1943 (1992).
[68] P. Carra, B. T. Thole, M. Altarelli, and X. Wang, Phys. Rev. Lett. **70**, 694 (1993).
[69] I. Galanakis, M. Alouani, and H. Dreyssé, J. Magn. Magn. Mater. **242**, 27 (2002).
[70] C. Antoniak, M. Spasova, A. Trunova, K. Fauth, F. Wilhelm, A. Rogalev, J. Minár, H. Ebert, M. Farle, and H. Wende, J. Phys. Condens. Matter **21**, 336002 (2009).
[71] W. Q. Liu, W. Y. Wang, J. J. Wang, F. Q. Wang, C. Lu, F. Jin, A. Zhang, Q. M. Zhang, G. van der Laan, Y. B. Xu *et al.*, Sci. Rep. **5**, 11911 (2015).
[72] V. Dupuis, G. Khadra, S. Linas, A. Hillion, L. Gragnaniello, A. Tamion, J. Tuaillon-Combes, L. Bardotti, F. Tournus, E. Otero *et al.*, J. Magn. Magn. Mater. **383**, 73 (2015).
[73] C. Antoniak, M. Spasova, A. Trunova, K. Fauth, M. Farle, and H. Wende, J. Phys. Conf. Ser. **190**, 012118 (2009).
[74] I. Galanakis, M. Alouani, and H. Dreyssé, Phys. Rev. B **62**, 6475 (2000).
[75] I. V. Solovyev, P. H. Dederichs, and I. Mertig, Phys. Rev. B **52**, 13419 (1995).
[76] J. M. MacLaren, R. R. Duplessis, R. A. Stern, and S. Willoughby, IEEE Trans. Magn. **41**, 4374 (2005).
[77] M. Soares, A. Lamirand, A. Y. Ramos, M. De Santis, and H. Tolentino, Phys. Rev. B **90**, 214403 (2014).
[78] K. Ikeda, T. Seki, G. Shibata, T. Kadono, K. Ishigami, Y. Takahashi, M. Horio, S. Sakamoto, Y. Nonaka, M. Sakamaki *et al.*, Appl. Phys. Lett. **111**, 142402 (2017).
[79] Y.-S. Chen, C.-H. Lee, and H.-J. Lin, J. Vac. Sci. Technol. **34**, 04J109 (2016).
[80] X. Liu, C.-Z. Wang, H.-Q. Lin, M. Hupalo, P. A. Thiel, K.-M. Ho, and M. C. Tringides, Phys. Rev. B **90**, 155444 (2014).
[81] T. Eelbo, M. Waśniowska, P. Thakur, M. Gyamfi, B. Sachs, T. O. Wehling, S. Forti, U. Starke, C. Tieg, A. I. Lichtenstein *et al.*, Phys. Rev. Lett. **110**, 136804 (2013).
[82] M. Sargolzaei and F. Gudarzi, J. Appl. Phys. **110**, 064303 (2011).
[83] H. Johll, H. C. Kang, and E. S. Tok, Phys. Rev. B **79**, 245416 (2009).
[84] P. Bruno, Phys. Rev. B **39**, 865 (1989).
[85] Y. Kota and A. Sakuma, J. Phys. Soc. Jpn. **81**, 084705 (2012).
[86] S. Ayaz Khan, P. Blaha, H. Ebert, J. Minár, and O. Šipr, Phys. Rev. B **94**, 144436 (2016).

THE JOURNAL OF PHYSICAL CHEMISTRY C

Article

Cite This: *J. Phys. Chem. C* 2019, 123, 24487−24494

pubs.acs.org/JPCC

Regular Arrays of Pt Clusters on Alumina: A New Superstructure on $Al_2O_3/Ni_3Al(111)$

Georges Sitja,*[,†] Aude Bailly,[‡] Maurizio De Santis,[‡] Vasile Heresanu,[†] and Claude R. Henry*[,†]

[†]Aix-Marseille Université, CNRS, CINaM, F-13000 Marseille, France

[‡]Université Grenoble Alpes, CNRS, Grenoble INP, Institut Néel, 38000 Grenoble, France

Supporting Information

ABSTRACT: Alumina ultrathin films obtained by high-temperature oxidation of a $Ni_3Al(111)$ surface are a good template to grow regular arrays of metal clusters. Up to now, two hexagonal organizations called "dot" and "network" structures have been observed with distances between clusters of 4.1 and 2.4 nm, respectively. In the present article, we report on an investigation by in situ grazing incidence small-angle X-ray scattering, showing that Pt deposited at room temperature and for a low coverage forms a new hexagonal structure with a distance between clusters being 1.38 nm. For the first time, an assembly of tiny Pt clusters (1−6 atoms) with a very high density (5.85×10^{13} cm^{-2}) and presenting a good organization on an alumina surface is obtained. This system could be used to investigate by surface science techniques the new emerging field of single-atom catalysis. By deposition at 573 K, small Pt clusters are organized on the network structure. By deposition of Pt at 573 K on preformed Pd seeds, large Pt (Pd) clusters containing about a hundred atoms are organized on the dot structure and they remain organized up to 733 K. We show that the three structures are interrelated. The different organizations of the Pt clusters on the alumina surface are explained by the presence of three types of sites corresponding to different adsorption energies for Pt atoms.

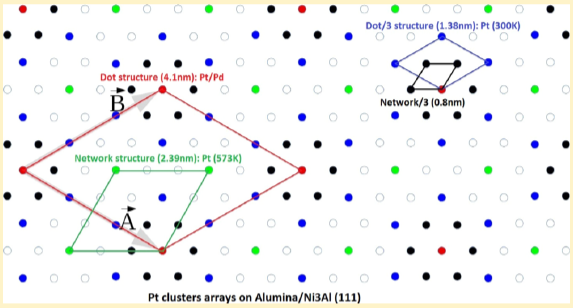

1. INTRODUCTION

Conventionally supported model catalysts are obtained by growing metal clusters on a metal-oxide surface.[1−4] However, nucleation of metal clusters occurs selectively on the randomly distributed defects of the oxide surfaces, leading to a rather large size distribution (in the best case, 25% of the mean size) and the distance between the clusters is variable, which can influence the local reaction kinetics.[5] These limitations can be overcome by using a substrate presenting a regular distribution of defects, which play the role of a template to grow regular arrays of clusters with a sharp size distribution.[5] These arrays of clusters can be used, not only as model catalysts,[5,6] but also for fundamental studies in nanomagnetism.[7,8] Three types of nanostructured surfaces have been recently used as templates: an ultrathin film of alumina obtained by oxidation of a $Ni_3Al(111)$ surface,[9] a graphene monolayer (Gr),[10] or a monolayer of h-BN[11] grown on a metal single crystal. Regular arrays of Pt clusters have been obtained by deposition of Pt atoms on Gr/Ir(111)[12−16] or Gr/Rh(111).[17] The distance between the clusters is 2−3 nm and the cluster size has been varied between 9 and 100 atoms. The cluster organization is stable up to 450 K but CO adsorption at low pressure (10^{-9} mbar) and room temperature (RT) induces coalescence.[13,16] Conversely, the clusters are stable at RT under O_2 or H_2 at 1×10^{-8} mbar.[14] However, under 1×10^{-8} mbar of O_2 at 400 K, intercalation of oxygen atoms between the Gr and the metal substrate occurs, resulting in a disorganization of the cluster array and coalescence.[18] On h-BN/Ir(111), a good organization of Ir clusters has been obtained up to 700 K in ultrahigh vacuum (UHV).[11] To the best of our knowledge, only one scanning tunneling microscopy (STM) image has been published for Pt clusters on h-BN/Rh(111), showing a broad size distribution of the clusters.[19] On $Al_2O_3/Ni_3Al(111)$, no results on regular array of Pt clusters have been reported, whereas arrays of V, Mn, Ag, Cu, Au,[9] Pd,[20] Fe,[8,21] and Co[22] clusters have been obtained. However, only V, Pd, and Cu atoms achieve a good organization. Arrays of bimetallic clusters have been first obtained for PdAu by successively depositing Pd and then Au.[23,24] In fact, Pd acts as a seed for the subsequent deposition of Au. Seeding with Pd clusters has been used to obtain a good organization of Fe,[8,21] Co,[22] and Ni[25] clusters. The organization of the clusters occurs on specific nucleation sites forming two hexagonal superstructures, which have been previously observed by STM on the clean alumina surface for different bias voltages. The first one, observed at $V = 3.2$ V, has a lattice parameter of 2.4 nm and is named the "network" structure, whereas the second one, observed at 2.0 V, has a lattice parameter of 4.1 nm and is

Received: May 29, 2019
Revised: September 12, 2019
Published: September 16, 2019

DOI: 10.1021/acs.jpcc.9b05109
J. Phys. Chem. C 2019, 123, 24487−24494

named the "dot" structure.[26] The two superstructures are interrelated, the large mesh is $(\sqrt{3} \times \sqrt{3})R30°$ relatively to the small one and the densities of sites are 6.5×10^{12} and 1.95×10^{13} cm^{-2}, respectively.[9] Pd clusters perfectly decorate the dot structure, whereas V clusters organize on the network structure.[5] The long-range organization of the arrays has been studied in situ by grazing incidence small angle X-ray scattering (GISAXS) for Pd,[6] Co (seeded by Pd),[22] and PdAu[27,28] clusters. The perfect organization of Pd and PdAu clusters is kept up to 600 K in UHV[27] and in the presence of CO and O_2 at a pressure of 1×10^{-7} mbar.[29] The high stability of the cluster organization is certainly due to the particular surface structure of these films and probably also to their small thickness (0.5 nm). In summary, regular arrays of metal clusters on alumina/$Ni_3Al(111)$ appear to be the best candidates to study accurately the size effect in catalysis with surface science techniques, as it has been already shown for Pd and PdAu clusters.[6,29−31] It is rather astonishing that no attempt of Pt deposition on this alumina film has been reported yet, despite the great interest of Pt in heterogeneous catalysis. Here, we present the first attempt to prepare regular arrays of Pt clusters on alumina ultrathin films on $Ni_3Al(111)$ used as a template. The growth of the Pt clusters is followed in situ by GISAXS. This technique has the great advantage over STM that it reveals the organization of the clusters at the scale of the sample in a few minutes, whereas several days would be necessary using STM. It is shown that depending of the growth conditions (temperature, Pt coverage), different organizations of the Pt clusters appear. In particular, a new organization of Pt clusters containing few atoms and with a very high density is observed for the first time. We show how this new organization is related to the well-known network and dot structures of the alumina films on $Ni_3Al(111)$.

2. EXPERIMENTAL SECTION

The present experimental results have been obtained at the European Synchrotron Radiation Facility (ESRF, Grenoble, France) with the dedicated In Situ Nanostructures and Surfaces (INS) apparatus of the BM32 beamline. The surface of a $Ni_3Al(111)$ single crystal (MaTeck, Jülich, Germany) was cleaned through successive cycles of ion bombardment and annealing at 1100 K.

The sample was subsequently oxidized at an oxygen partial pressure of 5×10^{-8} mbar at 1000 K for 20 min to obtain a nanostructured film of alumina.[32] Atomic deposition of palladium and platinum was performed by thermal evaporation from a water-cooled electron-beam evaporator. The palladium and platinum fluxes have been previously calibrated by using a quartz crystal microbalance. Sample preparation and metal deposition were conducted in situ under UHV in the same chamber used for the GISAXS measurements. The incident X-ray beam energy was set to 19.8 keV, corresponding to a wavelength (λ) of 0.0626 nm. The incidence angle was equal to 0.16° (close to the angle of total external reflection for Ni_3Al at this energy). GISAXS patterns were captured using a two-dimensional (2D) Eiger R1M camera from Dectris. The wavevector transfer $\mathbf{q}$ is defined by its three coordinates: q_x and q_y, parallel with the sample surface, and q_z, perpendicular to it (q_y and q_z being both parallel with the detector plane). The in-plane ($2\theta_f$) and out-of-plane (α_f) scattering angles being small, the q_y and q_z components can be approximated by: $q_y \approx (2\pi/\lambda)\cdot\sin(2\theta_f) \approx (4\pi/\lambda)\theta_f$ and $q_z \approx (2\pi/\lambda)\cdot\alpha_f$. The surface unit cell of the dot structure is hexagonal with the norm of its basis vector equal to 4.1 nm, leading to a distance between nanoparticles rows of $D = 4.1 \times \sqrt{3}/2 = 3.55$ nm. The regular organization of the clusters on the alumina film gives rise to sharp diffraction rods on the GISAXS patterns, perpendicularly to the sample surface.

For any of the superstructures, several diffraction lines corresponding to the nodes (1 0), (2 0), (3 0)... but also (1 1), (2 2), (3 3)... are expected to appear, as long as the sample azimuth ω has been correctly set. In some cases, the 2D camera has also been shifted with respect to the direct and specular beams in order to record the relevant diffraction peaks. The closest scattering rod from the (0 0) specular reflection corresponds to the node (1 0) and is therefore called "1st order" or "order 1"; (2 0) and (3 0) nodes lead to rods that are two and three times farther than order 1, and we will label these lines as order 2 (or 2nd order) and order 3 (or 3rd order). The nodes (1 1) and (2 2) of the reciprocal lattice lead to rods, respectively, $\sqrt{3}$ and $2\sqrt{3}$ farther than order 1. These lines are called order $\sqrt{3}$ and order $2\sqrt{3}$.

To record enough signal in the relevant diffraction rods, the azimuth angle (ω) is slightly tilted from the natural directions of the clusters array on the surface to form the corresponding Bragg angle. However, the azimuth to record order 1, 2, and 3 is nearly 30° away from the one to record $\sqrt{3}$ and $2\sqrt{3}$ rods. Hereafter, we will simplify using only 0° and 30° to label the GISAXS data (the exact value of ω is indicated in the caption for each figure). 0° will stand for order 1, 2, 3... and 30° for $\sqrt{3}$, $2\sqrt{3}$...

The values of ω, which maximize the intensity of the different peaks and the width of the peak intensity ($\Delta\omega$) as a function of ω, are calculated in the Supporting Information. The experimental variation of the order 1 peak as a function of ω is displayed in the Supporting Information (Figure S1). In the intensity profiles, the peak intensity is integrated within a band containing 220 lines from the 1030 lines of the experimental image.

3. RESULTS

3.1. RT Deposition. Figure 1a shows the GISAXS pattern (ω = 0°) after deposition of 0.1 ML Pt at RT on the alumina film. Only one peak is visible, corresponding to the 3rd order in reference to the pattern obtained with the dot structure. On the intensity profile corrected from the baseline of the clean alumina (Figure 1b), the background is flat, indicating that all the scattered intensity from the Pt clusters is in the third-order peak. No disorder or coalescence is observed. As the first- and second-order peaks are not present, the observed peak corresponds to a unit cell three times smaller than the unit cell of the dot structure (in the direction ω = 0°). At ω = 30°, no peak is observed on the GISAXS pattern (see Supporting Information, Figure S2), but a very small peak is visible on the intensity profile at the position $3\sqrt{3}$ (see Figure 5 for the indexation of the peaks). As the $\sqrt{3}$ and $2\sqrt{3}$ peaks are not visible, we deduce that the Pt clusters do not sit on the network structure. The $3\sqrt{3}$ peak corresponds to a second-order scattering peak of the new structure. From these observations, we conclude (see Discussion) that the Pt clusters are on a hexagonal structure parallel to the dot structure, but with unit cell vectors three times smaller (1.37 nm) than those of the dot structure. We call this new structure "dot/3". The density of clusters is therefore nine times larger than for the dot structure and equal to 5.85×10^{13} cm^{-2}. For 0.1 ML of Pt, the clusters contain 2.6 atoms on average. Similar GISAXS

DOI: 10.1021/acs.jpcc.9b05109
J. Phys. Chem. C 2019, 123, 24487−24494

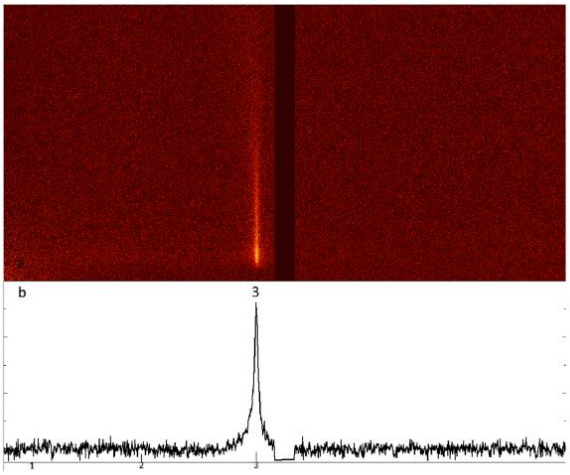

Figure 1. 0.1 ML Pt deposited at RT (a) GISAXS pattern at $\omega \approx 0°$ (b) intensity profile. (The exact value of ω for this figure is $-1.5°$ in order to maximize the intensity of the third-order peak. For this value, if the first- and second-order peaks exist, they would be visible as seen in Figure S3 of the Supporting Information.)

patterns have been clearly observed for 0.05 (1.3 atoms) and 0.15 ML (3.9 atoms)

Figure 2 displays the GISAXS pattern for 0.35 ML of Pt deposited at RT. We now clearly see the 1st- and 3rd-order

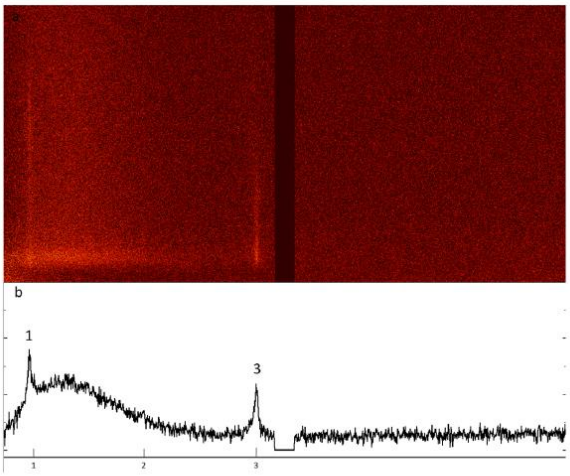

Figure 2. 0.35 ML Pt deposited at RT (a) GISAXS pattern at $\omega \approx 0°$ (b) Intensity profile. (The exact value of ω is $-1.5°$.)

peaks, whereas the 2nd-order peak is hardly visible on top of a broad diffuse component, characteristic of the disorder because of the coalescence of the clusters. No sharp peak is seen at $\omega = 30°$, but only a broad feature in the background. From simulation of GISAXS for a pure dot structure we expect 1st, 2nd, and 3rd peaks at $\omega = 0°$ and $\sqrt{3}$ peak at $\omega = 30°$. For a pure network structure, we expect the 3rd-order peak at $\omega = 0°$ together with $\sqrt{3}$ and $2\sqrt{3}$ peaks at $\omega = 30°$. Thus, we have no pure structure, but we can explain the experimental observations by the following remarks. The presence of peak 1 shows that locally some clusters are on the dot structure and the fact that peak 3 is more intense than peak 2 (taking into account that the Debye–Waller factor is proportional to Q^2) proves that a large fraction of the clusters are still on the "dot/3" structure at 1.37 nm. The absence of $\sqrt{3}$ peak at $\omega = 30°$ shows that locally the clusters are not organized on the network structure. The presence of a wide and intense diffuse peak indicates that the collection of clusters is no longer well-ordered.

3.2. Pt Deposition at 573 K. In Figure 3, the first row displays the GISAXS patterns in two directions ($\omega = 0°$ and ω

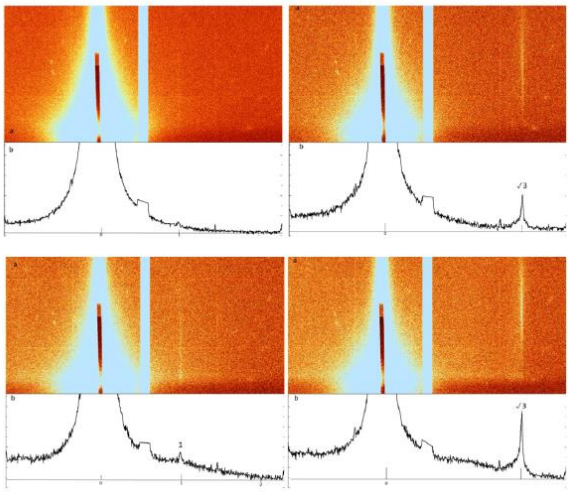

Figure 3. Pt deposition at 573 K. First row: 0.08 ML, $\omega \approx 0°$ (left), and $\omega \approx 30°$ (right). Second row: 0.16 ML, $\omega \approx 0°$ (left), and $\omega \approx 30°$ (right). (a,b) represent the GISAXS pattern and the intensity profile, respectively. (The exact value of ω are $-0.5°$, 28.8° for the left and right parts of the figure, respectively.)

$= 30°$) for 0.08 ML Pt deposited at 573 K. At $\omega = 0°$, no clear peak is visible, whereas at $\omega = 30°$ a $\sqrt{3}$ peak is present. These observations indicate that only the network structure is occupied by the Pt clusters, which contain 6.3 atoms on average. The density of clusters is 1.95×10^{13} cm^{-2}. It should be noticed that in the configuration of the camera used for this series of experiments, the peaks 3 and $2\sqrt{3}$ are out of the field of view of the camera.

After a second deposition of 0.08 ML (total 0.16 ML Pt) the $\sqrt{3}$ peak becomes more intense (Figure 3, second row) and a very small 1st-order peak can be detected close to the baseline. We conclude that for 0.16 ML Pt, the clusters (≈12.6 atoms per cluster) still sit on the network structure, but there is a slight imbalance (in size) between clusters that are on the sites common with the pure dot structure (site A) and those that are specific to the network structure (site B). Coming back to the profile for the initial 0.08 ML deposit at $\omega = 0°$, we can possibly see a tiny peak at the position of the order 1 peak, which is almost merged in the background. This tiny peak would indicate that at 0.08 ML, there is already a small dissymmetry between the size of the clusters in sites A and B, but in both cases the Pt clusters are organized on the network structure.

After deposition of 0.85 ML of Pt at 573 K, the imbalance between the two kinds of clusters is still noticeable but also a wide diffuse peak because of disorder and coalescence is observed (figure not shown).

DOI: 10.1021/acs.jpcc.9b05109
J. Phys. Chem. C 2019, 123, 24487–24494

3.3. Pd Seeding. In the previous section, we have seen that it is not possible to organize Pt clusters containing about a hundred atoms on the network structure. In order to obtain a regular array of large Pt clusters, we tried to use Pd seeding on the dot structure like for Au, Fe, Co, and Ni.[21−23,25]

Figure 4 (first row) shows GISAXS patterns for 0.1 ML of Pd deposited at 363 K. At $\omega = 0°$, 1st- and 2nd-order peaks are

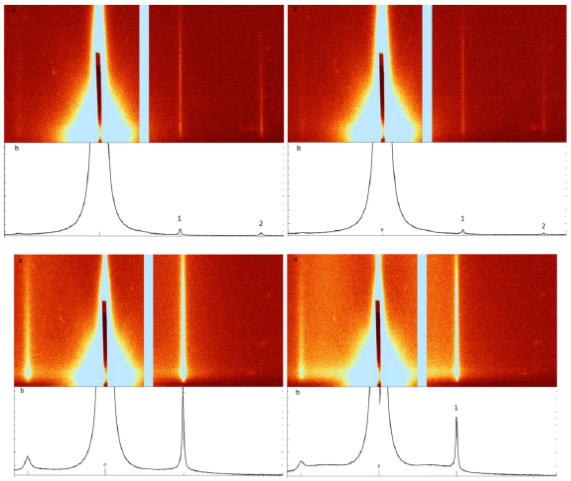

Figure 4. GISAXS pattern and corresponding intensity profiles for Pt cluster arrays seeded with Pd. First row, left: 0.1 ML Pd deposited at 363 K and right: after annealing at 573 K. Second row, left: after deposition of 0.48 ML Pt at 573 K on the Pd seeds and right: after deposition of 0.78 ML Pt at 573 K on the Pd seed. (a,b) represent the GISAXS patterns at $\omega \approx 0°$ and the corresponding intensity profile, respectively. (The exact value of ω is $-0.5°$.)

clearly seen, proving that the clusters containing 23.5 Pd atoms on average are organized on the dot structure. After heating the sample at 573 K, the clusters stay organized on the dot structure (right image on the first row). Then, 0.48 ML of Pt was deposited at 573 K on the preformed Pd clusters. The GISAXS pattern (Figure 4, left of second row) shows that the clusters containing 23.5 Pd atoms and 113 Pt atoms stay organized on the dot structure. The large augmentation of the intensity of the first order peak is due to the important increase of the cluster volume (almost a factor 6). The vanishing of the second-order peak is also due to the large increase of the cluster size, which decreases the visibility of the high-order peaks through the modification of the cluster form factor. After deposition of 0.78 ML of Pt on the Pd seed clusters (23.5 Pd atoms and 184 Pt atoms), the metal clusters stay organized on the dot structure, although some disorder starts to appear (Figure 4, right part of second row). After annealing the sample successively at 711 and 733 K, GISAXS patterns show that the organization on the dot structure is kept up to 733 K. Nevertheless, the intensity of the GISAXS first-order peak decreases when temperature increases, indicating that the organization becomes less perfect.

4. DISCUSSION

4.1. Origin of the New Structure. The first study of ultrathin alumina films on a Ni_3Al surface was made by the group of U. Bardi.[33,34] The films were prepared by oxidation at 900 K of a polycrystalline Ni_3Al surface. By LEED, they observed a surface mesh at ≈3 Å attributed to oxygen atoms of the alumina film with preferential (111) orientation. The thickness of the films has been determined by XPS to be 0.5 nm.[33,34] Later, Becker et al.[35] prepared the alumina film on $Ni_3Al(111)$ by oxidation at 300 K and annealing at 1000 K. They provided the first STM images of the alumina film.[35]

They observed two superstructures at 2.5 and 4.6 nm, which appear at different bias voltages, respectively, 3.1 and 2.2 V.[35] A few months later, J.A. Kelber and collaborators used the same preparation method and observed by STM at RT a hexagonal lattice at 3 Å they identified as O surface atoms.[36] By direct oxidation at 1000 K and STM observation at low temperature, more precise images of the alumina films were obtained.[26] At 3.2 V, a hexagonal arrangement of "dark holes surrounded by smaller hexagonal rings of bright dots"[26] was observed, characterizing the network structure. At 2.0 V, a hexagonal arrangement of bright dots was observed, which is characteristic of the dot structure.[26] The unit cell vectors were more precisely determined as 2.35 nm for the network structure and 4.16 nm for the dot structure.[26] At this time, the question was: do these structures have a pure electronic origin or correspond to topographic surface structures? Noncontact atomic force microscopy (nc-AFM) is the best suited technique to answer this question. In 2006, some of us observed the surface of the alumina films by nc-AFM.[32] Atomic resolution showed the hexagonal surface lattice at 2.9 Å attributed also to O atoms. The self-correlation of the atomic resolution image showed modulation, revealing the network and the dot structures with parameters of 2.39 and 4.1 nm, respectively.[32] The modulation was explained by distortion of the atomic lattice due to the non-perfect accommodation with the Ni_3Al substrate.[32] nc-AFM images in the damping mode clearly showed dot and network superstructures which are defined by two types of features.[32] Hexagons formed by six spots separated by 8 Å appear around the nodes of the dot structure, and the unit mesh of the network structure is formed by three single spots and one hexagon in common with a node of the dot structure unit mesh.[32] From the Fourier transform of the damping AFM image obtained on a single domain, it was deduced that the three different features form three commensurate lattices.[32] We reproduce this Fourier transform (not shown in ref 32) in Figure 5. In this figure, one recognizes

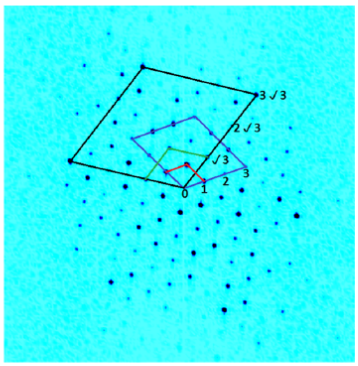

Figure 5. Fourier transform of the nc-AFM image (Figure 1 of ref 32) in damping mode of a single domain of the $Al_2O_3/Ni_3Al(111)$ films (the contrast has been inverted and enhanced). The red, green, blue, and black unit meshes correspond to the dot, network, dot/3, and network/3 structures, respectively.

DOI: 10.1021/acs.jpcc.9b05109
J. Phys. Chem. C 2019, 123, 24487−24494

Table 1. Characteristics of the Hexagonal superstructures Observed on the Alumina Films

superstructure	dot	network	dot/3	network/3
lattice parameter (nm)	4.14	2.39	1.38	0.797
cluster density (cm^{-2})	6.5×10^{12}	1.95×10^{13}	5.85×10^{13}	
relationship	1×1	$(1/\sqrt{3} \times 1/\sqrt{3})R30°$	$1/3 \times 1/3$	$(1/3\sqrt{3} \times 1/3\sqrt{3})R30°$

the reciprocal unit-mesh of the dot structure (a = 4.14 nm), the one of the network structure ($a/\sqrt{3}$ = 2.39 nm), and the one of the smallest structure forming the six hexagonal spots ($a/3\sqrt{3}$ = 0.797 nm) that we call "network/3". We can also recognize the unit cell corresponding to the new structure observed for Pt deposition at RT and at low coverage with a unit cell parameter equal to $a/3$ = 1.38 nm. As said, we name this new structure dot/3. All the four structures are interrelated. The characteristic distance of this new structure (dot/3) corresponds in fact exactly to the one observed in STM images at V = 3.1/3.2 V (in Figure 3a of ref 26 and in Figure 3b or 3d of ref 21) between the six bright spots forming hexagons.

In another nc-AFM study,[37] the atomic hexagonal lattice forming the top surface of the films was also seen with a parameter of 2.9 Å. The network and the dot structures were also recognized. By inverse Fourier transform from selected spots, a hexagonal lattice at 5.1 Å was observed and associated with the Ni_3Al substrate lattice.[37]

The characteristic of the different superstructures are presented in Table 1.

It is interesting to notice that from the reciprocal lattices displayed in Figure 5, one can easily predict the GISAXS peaks that must be observed for the different structures in the two azimuths (ω = 0° and ω = 30°). We have simulated the GISAXS patterns for the different structures and also considered different occupations of the A, B, and C sites (see next paragraph). A good agreement between the simulations and the experimental GISAXS patterns for 0.1 ML of Pt deposited at RT was obtained only for a full occupation of the dot/3 structure (see the Supporting Information, 3rd section).

4.2. Nature of the Different Sites on the Surface of the Alumina Films. In our previous nc-AFM study of the alumina surface, we defined two types of sites (A and B)[32] (see also the Supporting Information). The A sites correspond to the nodes of the dot structure, whereas the unit mesh of the network structure is composed by one A site and three B sites. Now, we define two additional sites (C and D). The C sites are at 1/3 and at 2/3 of the lattice vectors of the unit mesh of the dot structure. Therefore, the nodes of the unit mesh of the "dot/3" structure are one A site and three C sites (see Figure 6). Finally, D sites correspond to the six dots around an A site observed by nc-AFM.[32] The nodes of the unit mesh of the network/3 structure are composed of one A site and three D sites. The different superstructures unit cells, together with the different types of sites, are schematically represented in Figure 6. A real space representation of the different sites can be obtained from the previous nc-AFM study[32] and is given in Figure S5 in the Supporting Information. It is interesting to notice that the B, C, and D sites form hexagons of decreasing size around the A sites and successively rotated by 30°.

An atomic model based on the comparison between near atomic resolution STM images and density functional theory (DFT) calculations has been given by Schmid et al.[21] Following this model, the nodes of the dot structure (A sites) correspond to holes through the alumina films, which are strong adsorption sites for metal atoms like Pd. Further calculations with this model structure showed that it is also the case for Co, Fe, Ni, Cu, Ag, and Au atoms.[38] The high adsorption energy of metal atoms on the holes is mainly because the alumina film does not totally screen the influence of the metallic Ni_3Al substrate. No calculation was made for Pt, but we can expect that it is also the case. Looking carefully at the atomistic model (Figure 2 of ref 21), the B sites forming the network structure correspond to the center of a triangle formed by three surface oxygen atoms. The C sites are also found approximately at the center of a triangle formed by three surface oxygen atoms, but the environment of these three oxygen atoms is really different for the two types of sites (B and C). Therefore, we expect that the adsorption energy of a Pt atom is different on these two sites. However, to explain the fact that at RT the Pt atoms populates the new structure (dot/3) and that at 573 K only the network structure is occupied, we have to assume that the adsorption energy on C sites is smaller than on B sites. The sites corresponding to the smallest structure (D sites) appear to be close to a site between four oxygen atoms forming a square. The adsorption energy of a Pt atom on D sites must be significantly weaker than on the other sites, because at RT they are not occupied by Pt atoms. We assume that there is a hierarchy in the adsorption energy of Pt atoms on the different sites; this value decreases in the order A > B > C > D. From this simple argument, we can tentatively explain the experimental observations. At RT, the A, B, and C sites are occupied by small Pt clusters (typically less than six atoms). From a cluster size of six atoms, the adsorption energy of the cluster is not large enough to stabilize the cluster on C

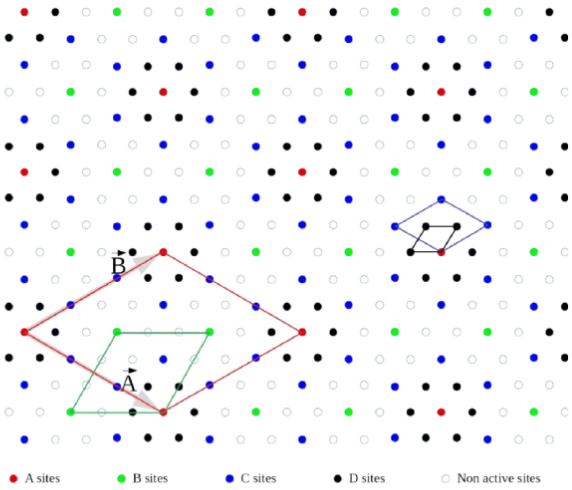

Figure 6. Unit meshes of the dot, network, dot/3, and network/3 superstructures are represented in red, green, blue, and black lines, respectively. The A and B vectors (in gray) are the unit mesh vectors of the dot structure, which is the only true crystallographic surface structure. The A, B, C, and D sites are the red, green, blue, and black dots, respectively.

DOI: 10.1021/acs.jpcc.9b05109
J. Phys. Chem. C 2019, 123, 24487−24494

sites and they start to diffuse and coalesce, leading to some disorder. At 573 K, the C sites cannot stabilize Pt atoms. Then, only B and A sites are occupied and form the network structure for Pt clusters containing up to ≈13 atoms. At larger sizes, Pt clusters are no longer stable on B sites, leading to a mixture of dot and network structures. Some disorder is also present and increases with the Pt coverage. In order to have a regular array of larger Pt clusters, we have to use Pd seeding to form Pd-seeded Pt clusters on the dot structure. In that case, Pd is deposited at 363 K and Pt is subsequently deposited at 573 K. Even if small Pt clusters are originally formed on B sites, they diffuse and coalesce with Pt/Pd clusters on A sites, when they reach a critical size of about 13 atoms and therefore become stable. The Pd-seeded Pt clusters are stable on A sites up to 730 K.

4.3. Comparison between Pd and Pt. For Pd deposition at RT, the dot/3 structure was never observed, contrary to Pt. This difference suggests that the adsorption energy of Pd atoms on the different sites is weaker than for Pt. Several DFT calculations of the adsorption of Pt and Pd atoms on clean α-alumina (0001) surfaces have been published.[39,40] These calculations show that both Pt and Pd bind to oxygen atoms of the alumina surface, but more strongly for Pt (1.99 eV/1.82 eV) than for Pd (1.47 eV/1.19 eV). Ab initio calculation of the adhesion energy of Pt and Pd reaches the same conclusion.[41] On γ-alumina, Pt and Pd atoms are found to bind preferably to oxygen with a stronger binding energy in the case of Pt.[42,43] It is also found that the diffusion energy of metal atoms on γ-alumina is very weak (0.3−0.5 eV).[42,43] From these calculations, we can understand that, at RT, Pt atoms can be stable on C sites and not Pd atoms. Moreover, the weak calculated diffusion energy shows that already at RT, Pd and Pt atoms diffuse rapidly on the surface, as soon as they escape from the B and C sites. For a very thin oxide film supported on a metal substrate, like the alumina used in this study, one would expect an increase of the adsorption energy of a metal atom in comparison with bulk alumina.[44] From calculation on ultrathin alumina films on $Ni_3Al(111)$,[38] the adsorption energy of a Pd atom on the A site (2.75 eV) is much larger than on bulk alumina but for Pd on B sites the calculated value (1.18 eV) is similar to calculations on bulk alumina.

5. CONCLUSIONS

For the first time, regular arrays of Pt clusters have been obtained by deposition of Pt atoms on an ultrathin alumina film grown on $Ni_3Al(111)$. Depending on the deposition temperature, different structures are obtained. At RT, a new structure that we call "dot/3" is observed. Up to now, this new organization had never been observed for the growth of any other metal clusters on this alumina film. The density is nine times larger than the density for the dot structure that gives 5.85×10^{13} clusters cm^{-2}. Only very small Pt clusters (less than six atoms) can be organized on this structure. This system is particularly well suited to study "single atom catalysis"[45] by surface science techniques like molecular beam techniques.[29] Indeed, from single atom catalysts supported on an oxide powder, it is rather difficult to accurately know the geometry of the site where single atoms of catalytic metal are anchored. The use of a flat single crystal under UHV allows to use surface science techniques like low energy electron diffraction (LEED), STM, and nc-AFM to determine the geometry of adsorption sites. For such studies, a few systems have been recently used, like single Au, Ag, Ni, and Pt atoms on Fe_3O_4 (001)[46−49] or Pt on CuO/Cu(110).[50] The new system investigated here has the advantage of presenting a regular organization of few-atom Pt clusters on an alumina surface, which is the most common substrate used in single atom catalysis.

By deposition at 573 K, a regular array of Pt clusters, containing 13 atoms and forming the network structure (1.95×10^{13} clusters·cm^{-2}), is observed. Larger clusters containing 50 atoms are no longer ordered on the network structure. In order to obtain a regular array of large Pt clusters, it is necessary to seed the surface with small Pd clusters. By deposition of Pd at 363 K a regular array of Pd clusters is formed on the dot structure (6.5×10^{12} clusters·cm^{-2}). The subsequent deposition of Pt atoms at 573 K leads exclusively to the growth of the Pd seeded clusters. The organization of Pd seeded Pt clusters on the dot structure is stable up to 730 K.

On the alumina film, four surface structures are observed: the dot structure, the network structure, the dot/3 structure, and the network/3 structure. These four structures are deeply interrelated. Depending on the growth conditions, the organization of Pt clusters on the three larger structures is observed. The formation of these different organizations is tentatively explained by the presence of three types of sites, A, B, and C, having respectively a decreasing interaction with Pt atoms. The dot structure is formed exclusively by A sites, the network structure is formed by A and B sites, and the dot/3 structure is formed by A, B, and C sites. The validity of this model will be tested by further experiments in STM and simulations of the GISAXS patterns.

■ ASSOCIATED CONTENT

Supporting Information

The Supporting Information is available free of charge on the ACS Publications website at DOI: 10.1021/acs.jpcc.9b05109.

Optimal values of ω for the different GISAXS peaks; GISAXS pattern, in the direction $\omega = 0°$, for 0.1 ML of Pt deposited at RT; simulation of the GISAXS pattern; and definition of the different adsorption sites on the alumina film/$Ni_3Al(111)$ (PDF)

■ AUTHOR INFORMATION

Corresponding Authors

*E-mail: sitja@cinam.univ-mrs.fr (G.S.).
*E-mail: henry@cinam.univ-mrs.fr (C.R.H.).

ORCID

Aude Bailly: 0000-0003-1333-7668
Claude R. Henry: 0000-0002-7600-7239

Notes

The authors declare no competing financial interest.

■ ACKNOWLEDGMENTS

Financial support through ANR EQUIPEX ANR-11-EQPX-0010 and beam time on the French CRG-IF beamline at the ESRF are acknowledged. The authors thank the beamline staff.

■ REFERENCES

(1) Campbell, C. T. Ultrathin metal films and particles on oxide surfaces: structural, electronic and chemisorptive properties. *Surf. Sci. Rep.* **1997**, *27*, 1−111.

(2) Henry, C. R. Surface studies of supported model catalysts. *Surf. Sci. Rep.* **1998**, *31*, 231−325.

DOI: 10.1021/acs.jpcc.9b05109
J. Phys. Chem. C 2019, 123, 24487−24494

(3) Gao, F.; Goodman, D. W. Model catalysts: simulating the complexities of heterogeneous catalysts. *Annu. Rev. Phys. Chem.* **2012**, *63*, 265−286.
(4) Wang, H.-F.; Kaden, W. E.; Dowler, R.; Sterrer, M.; Freund, H.-J. Model oxide-supported metal catalysts-comparison of ultrahigh vacuum based preparation of Pd nanoparticles on a single- crystalline oxide substrate. *Phys. Chem. Chem. Phys.* **2012**, *14*, 11525−11533.
(5) Henry, C. R. 2D-arrays of nanoparticles as model catalysts. *Catal. Lett.* **2015**, *145*, 731−749.
(6) Sitja, G.; Le Moal, S.; Marsault, M.; Hamm, G.; Leroy, F.; Henry, C. R. Tranition from molecule to solid state : reactivity of supported metal clusters. *Nano Lett.* **2013**, *13*, 1977−1982.
(7) Vo-Van, C.; Schumacher, S.; Coraux, J.; Sessi, V.; Fruchart, O.; Brookes, N. B.; Ohresser, P.; Michely, T. Magnetism of cobalt nanoclusters on graphene on iridium. *Appl. Phys. Lett.* **2011**, *99*, 142504.
(8) Vlaic, S.; Gragnaniello, L.; Rusponi, S.; Cavallin, A.; Donati, F.; Dubout, Q.; Piamonteze, C.; Dreiser, J.; Nolting, F.; Brune, H. Interlayer exchange coupling in ordered Fe nanocluster arrays grown on $Al_2O_3/Ni_3Al(111)$. *Phys. Rev. B: Condens. Matter Mater. Phys.* **2014**, *89*, 245402.
(9) Becker, C.; Rosenhahn, A.; Wiltner, A.; Bergmann, K. v.; Schneider, J.; Pervan, P.; Milun, M.; Kralj, M.; Wandelt, K. Al_2O_3-films on $Ni_3Al(111)$: a template for nanostructured cluster growth. *New J. Phys.* **2002**, *4*, 75.
(10) Liu, X.; Han, Y.; Evans, J. W.; Engstfeld, A. K.; Behm, R. J.; Tringides, M. C.; Hupalo, M.; Lin, H.-Q.; Huang, L.; Ho, K.-M.; Appy, D.; et al. Growth morphology and properties of metals on graphene. *Prog. Surf. Sci.* **2015**, *90*, 397−443.
(11) Will, M.; Atodiresei, N.; Caciuc, V.; Valerius, P.; Herbig, C.; Michely, T. A monolayer of hexagonal boron nitride on Ir(111) as template for cluster superlattices. *ACS Nano* **2018**, *12*, 6871−6880.
(12) N'Diaye, A. T.; Gerber, T.; Busse, C.; Myslivecek, J.; Coraux, J.; Michely, T. A versatile fabrication method for cluster superlattices. *New J. Phys.* **2009**, *11*, 103045.
(13) Gerber, T.; Knudsen, J.; Feibelman, P. J.; Grånäs, E.; Stratmann, P.; Schulte, K.; Andersen, J. N.; Michely, T. CO-induced Schmoluchowsky ripening of Pt cluster arrays on the graphene/Ir(111) Moiré. *ACS Nano* **2013**, *7*, 2020−2031.
(14) Gerber, T.; Grånäs, E.; Schröder, U. A.; Stratmann, P.; Schulte, K.; Andersen, J. N.; Knudsen, J.; Michely, T. Stability and reactivity of graphene-templated nanoclusters. *J. Phys. Chem. C* **2016**, *120*, 26290−26299.
(15) Franz, D.; Blanc, N.; Coraux, J.; Renaud, G.; Runte, S.; Gerber, T.; Busse, C.; Michely, T.; Feibelman, P. J.; Hejral, U.; et al. Atomic structure of Pt nanoclusters supported by graphene/Ir(111) and reversible transformation under CO exposure. *Phys. Rev. B* **2016**, *93*, 045426.
(16) Podda, N.; Corva, M.; Mohamed, F.; Feng, Z.; Dri, C.; Dvorák, F.; Matolin, V.; Comelli, G.; Peressi, M.; Vesselli, E. Experimental and theoretical investigation of the restructuring process induced by CO at near ambient pressure: Pt nanoclusters on graphene/Ir(111). *ACS Nano* **2017**, *11*, 1041−1053.
(17) Gotterbarm, K.; Späth, F.; Bauer, U.; Bronnbauer, C.; Steinrück, H.-P.; Papp, C. Reactivity of graphene-supported Pt nanocluster arrays. *ACS Catal.* **2015**, *5*, 2397−2403.
(18) Grånäs, E.; Knudsen, J.; Schröder, U. A.; Gerber, T.; Busse, C.; Arman, M. A.; Schulte, K.; Andersen, J. N.; Michely, T. Oxygen intercalation under graphene on Ir(111): Energetics, kinetics, and the role of graphene edges. *ACS Nano* **2012**, *6*, 9951−9963.
(19) McKee, W. C.; Patterson, M. C.; Frick, J. R.; Sprunger, P. T.; Xu, Y. Adsorption of transition metal adatoms on h-BN/Rh(111): Implications for nanocluster self-assembly. *Catal. Today* **2017**, *280*, 220−231.
(20) Degen, S.; Becker, C.; Wandelt, K. Thin alumina films on $Ni_3Al(111)$: A template for nanostructured Pd cluster growth. *Faraday Discuss.* **2004**, *125*, 343−356.
(21) Schmid, M.; Kresse, G.; Buchsbaum, A.; Napetschnig, E.; Gritschneder, S.; Reichling, M.; Varga, P. Nanotemplate with holes: Ultrathin alumina on $Ni_3Al(111)$. *Phys. Rev. Lett.* **2007**, *99*, 196104.
(22) Buchsbaum, A.; De Santis, M.; Tolentino, H. C. N.; Schmid, M.; Varga, P. Highly ordered Pd, Fe, and Co cluters on alumina on $Ni_3Al(111)$. *Phys. Rev. B: Condens. Matter Mater. Phys.* **2010**, *81*, 115420.
(23) Hamm, G.; Becker, C.; Henry, C. R. Bimetallic Pd-Au nanoclusters arrays grown on nanostructured alumina templates. *Nanotechnology* **2006**, *17*, 1943−1947.
(24) Marsault, M.; Hamm, G.; Wörz, A.; Sitja, G.; Barth, C.; Henry, C. R. Preparation of regular arrays of bimetallic clusters independent control of size and chemical composition. *Faraday Discuss.* **2008**, *138*, 407−420.
(25) Gragnaniello, L.; Ma, T.; Barcaro, G.; Semanta, L.; Negreiros, F. R.; Fortunelli, A.; Surnev, S.; Netzer, F. P. Ordered arrays of size-selected oxide nanoparticles. *Phys. Rev. Lett.* **2012**, *108*, 195507.
(26) Degen, S.; Krupski, A.; Kralj, M.; Langner, A.; Becker, C.; Sokolowski, M.; Wandelt, K. Dtermination of the coincidence lattice of an ultrathin Al_2O_3 film on $Ni_3Al(111)$. *Surf. Sci.* **2005**, *576*, L57−L64.
(27) Marsault, M.; Sitja, G.; Henry, C. R. Regular arrays of Pd and PdAu clusters on ultrathin alumina films for reactivity studies. *Phys. Chem. Chem. Phys.* **2014**, *16*, 26458−26466.
(28) Bailly, A.; Sitja, G.; Saint-Lager, M.-C.; Le Moal, S.; Leroy, F.; De Santis, M.; Henry, C. R.; Robach, O. Influence of Palladium on the ordering, final size, and composition of Pd-Au nanoparticle arrays. *J. Phys. Chem. C* **2017**, *121*, 25864−25874.
(29) Sitja, G.; Henry, C. R. Molecular beam study of the oxidation of carbon monoxide on a regular array of Pd clusters on alumina. *J. Phys. Chem. C* **2017**, *121*, 10706−10712.
(30) Alyabyeva, N.; Ouvrard, A.; Zakaria, A.-M.; Bourguignon, B. Probing nanoparticle geometry down to subnanometer size: The benefit of vibrational spectroscopy. *J. Phys. Chem. Lett.* **2019**, *10*, 624−629.
(31) Sitja, G.; Henry, C. R. Molecular beam study of the CO adsorption on a regular array of PdAu clusters on alumina. *J. Phys. Chem. C* **2019**, *123*, 7961−7967.
(32) Hamm, G.; Barth, C.; Becker, C.; Wandelt, K.; Henry, C. R. Surface structure of an ultrathin alumina film on $Ni_3Al(111)$: A dynamic scanning force microscopy study. *Phys. Rev. Lett.* **2006**, *97*, 126106.
(33) Bardi, U.; Atrei, A.; Rovida, G. Initial stage of oxidation of the Ni_3Al alloy : a study by X-ray photoelectron spectroscopy and low energy He+ scattering. *Surf. Sci. Lett.* **1990**, *239*, L511−L516.
(34) Bardi, U.; Atrei, A.; Rovida, G. Initial stage of oxidation of the Ni3Al alloy : structure and composition of the alumina oxide overlayer by XPS, LEIS and LEED. *Surf. Sci.* **1992**, *268*, 87−97.
(35) Rosenhahn, A.; Schneider, J.; Kandler, J.; Becker, C.; Wandelt, K. Interaction of oxygen with Ni3Al(111) at 300K and 1000K. *Surf. Sci.* **1999**, *433*−*435*, 705−710.
(36) Addepalli, S. G.; Ekstrom, B.; Magtoto, N. P.; Lin, J.-S.; Kelber, J. A. STM atomic-scale characterization of the γ'-Al2O3 film on $Ni_3Al(111)$. *Surf. Sci.* **1999**, *442*, 385−399.
(37) Gritschneder, S.; Becker, C.; Wandelt, K.; Reichling, M. Disorder or complexity? Understanding a nanoscale template structure on alumina. *J. Am. Chem. Soc.* **2007**, *129*, 4925−4928.
(38) Olmos-Asar, J. A.; Vesselli, E.; Baldereschi, A.; Peressi, M. Towards optimal seeding for the synthesis of ordered arrays on alumina/$Ni_3Al(111)$. *Phys. Chem. Chem. Phys.* **2015**, *17*, 28154−28161.
(39) Briquet, L. G. V.; Catlow, C. R. A.; French, S. A. Comparison of the adsorption of Ni, Pd and Pt on the (0001) surface of α-alumina. *J. Phys. Chem. C* **2008**, *112*, 18948−18954.
(40) Rivanenkov, V. V.; Nasluzov, V. A.; Shor, A. M.; Neyman, K. M.; Rösch, N. Adsorption of Pd and Pt atoms on α-$Al_2O_3(0001)$: density functional study of cluster models embedded in an elastic polarizable environment. *Surf. Sci.* **2003**, *525*, 173−183.

DOI: 10.1021/acs.jpcc.9b05109
J. Phys. Chem. C 2019, 123, 24487−24494

(41) Li, H.-T.; Chen, L.-F.; Yuan, X.; Zhang, W.-Q.; Smith, J. R.; Evans, A. G. Interfacial stoichiometry and adhesion at metal/α-Al_2O_3 interfaces. *J. Am. Ceram. Soc.* **2011**, *94*, S154−S159.
(42) Deskins, N. A.; Mei, D.; Dupuis, M. Adsorption and diffusion of a single Pt atom on γ-Al_2O_3 surfaces. *Surf. Sci.* **2009**, *603*, 2793−2807.
(43) Valero, M. C.; Raybaud, P.; Sautet, P. Influence of the hydroxilation of γ-Al_2O_3 surfaces on the stability and diffusion of single Pd atoms: A DFT study. *J. Phys. Chem. B* **2006**, *110*, 1759−1767.
(44) Farmer, J. A.; Campbell, C. T. Ceria maintains smaller metal catalysts particles by strong metal-support bonding. *Science* **2010**, *329*, 933−936.
(45) Liu, L.; Corma, A. Metal catalysts for heterogeneous catalysis: From single atoms to nanoclusters and particles. *Chem. Rev.* **2018**, *118*, 4981−5079.
(46) Novotný, Z.; Argentero, G.; Wang, Z.; Schmid, M.; Diebold, U.; Parkinson, G. S. Ordered array of single adatoms with remarkable thermal stability: Au/Fe_3O_4 (001). *Phys. Rev. Lett.* **2012**, *108*, 216103.
(47) Bliem, R.; Kosak, R.; Perneczky, L.; Novotny, Z.; Gamba, O.; Fobes, D.; Mao, Z.; Schmid, M.; Blaha, P.; Diebold, U.; et al. Cluster nucleation and growth from a highly supersaturated adatom phase: silver on magnetite. *ACS Nano* **2014**, *8*, 7531−7537.
(48) Bliem, R.; Pavelec, J.; Gamba, O.; Mc Dermott, E.; Wang, Z.; Gerhold, S.; Wagner, M.; Osiecki, J.; Schulte, K.; Schmid, M.; et al. Adsorption and incorporation of transition metals at the magnetite Fe_3O4 (001) surface. *Phys. Rev. B: Condens. Matter Mater. Phys.* **2015**, *92*, 075440.
(49) Bliem, R.; van der Hoeven, J. E. S.; Hulva, J.; Pavelec, J.; Gamba, O.; de Jongh, P. E.; Schmid, M.; Blaha, P.; Diebold, U.; Parkinson, G. S. Dual role of CO in the stability of subnano Pt clusters at the Fe_3O_4 (001) surface. *Proc. Natl. Acad. Sci. U.S.A.* **2016**, *113*, 8921−8926.
(50) Zhou, X.; Yang, W.; Chen, Q.; Geng, Z.; Shao, X.; Li, J.; Wang, Y.; Dai, D.; Chen, W.; Xu, G.; et al. Stable Pt single atoms and nanoclusters on ultrathin CuO film and their performances in CO oxidation. *J. Phys. Chem. C* **2016**, *120*, 1709−1715.

DOI: 10.1021/acs.jpcc.9b05109
J. Phys. Chem. C 2019, 123, 24487−24494

Physical Properties of Interfacial Layers Developed on Weathered Silicates: A Case Study Based on Labradorite Feldspar

Bastien Wild,[*,†,‡,§] Damien Daval,[§] Jean-Sébastien Micha,[∥] Ian C. Bourg,[‡,⊥] Claire E. White,[†,‡] and Alejandro Fernandez-Martinez[#]

[†]Andlinger Center for Energy and the Environment, [‡]Department of Civil and Environmental Engineering, and [⊥]Princeton Environmental Institute, Princeton University, Princeton, New Jersey 08544, United States

[§]Laboratoire d'Hydrologie et de Géochimie de Strasbourg (LHyGeS), Université de Strasbourg /EOST-CNRS UMR 7517, 1 Rue Blessig, 67000 Strasbourg, France

[∥]CEA—Grenoble/INAC/SPrAM, 17 rue des Martyrs, 38041 Grenoble, France

[#]Université Grenoble Alpes, Université Savoie Mont Blanc, CNRS, IRD, IFSTTAR, ISTerre, Grenoble 38000, France

Supporting Information

ABSTRACT: Amorphous silica-rich surface layers (ASSLs) formed at the interface between silicate materials and reacting fluids are known to strongly influence, at least in some cases, the dissolution rates of silicate phases including soil minerals, glasses, and cements. However, the factors governing the formation of these ASSLs remain largely unknown. Here, we outline a novel approach that uses recent developments in vertical scanning interferometry and in situ synchrotron-based X-ray reflectivity to directly follow the development of ASSLs and the evolution of their physical properties on a representative silicate, labradorite feldspar. Our approach enables independently probing the reactivities of the outer (bulk fluid/ASSL) interface and of the inner (ASSL/pristine mineral) interface in situ, providing a detailed picture of the temporal evolution of the fluid−mineral interface. We investigated the effects of pH, SiO_2(aq) concentration, crystallographic orientation, and temperature on the layer thickness, density, and reactivity as well as on the dissolution rate of the primary mineral. The dissolution rate of labradorite crystals increased with temperature according to an apparent activation energy of ∼57 kJ mol^{-1} and showed no significant difference between crystallographic faces. Both labradorite and ASSL dissolution rates decreased as circum-neutral pH conditions were approached. High SiO_2(aq) concentrations resulted in decreased apparent dissolution rates (even though far-from-equilibrium conditions with respect to labradorite were maintained in the bulk fluid) and in an increased ASSL density at least in some conditions (such as low temperature and close-to-neutral pH values). Our results highlight the importance of ASSLs and their complex impact on the dissolution process. In particular, our results provide evidence of a discrepancy between bulk fluid conditions, generally probed and reported, and those actually operating at the interface with the dissolving primary phase, which are of more direct relevance to the dissolution process but are still largely unknown.

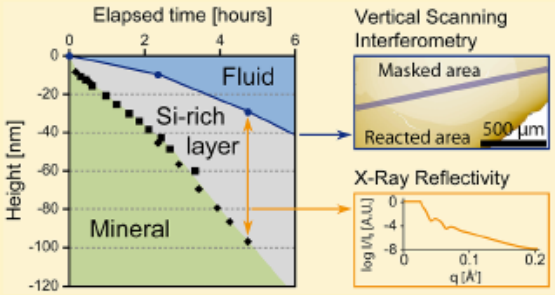

INTRODUCTION

Amorphous silica-rich surface layers (ASSLs) are hydrated, nanoporous, metastable phases that form at the interface between reactive fluids and a variety of silicate materials including olivine,[1−4] wollastonite,[5−9] feldspars,[10−14] and glasses.[15−18] These layers, also called surface alteration layers,[19,20] form ubiquitously from laboratory to field settings.[21−23] They play a key role in controlling the dissolution rates of silicate materials with important implications for several critical environmental and societal challenges including the degradation of cement infrastructure,[24] the long-term storage security of nuclear waste,[18,25] and the feasibility of enhancing silicate weathering as a large-scale CO_2 capture technology.[26,27]

Although the existence of ASSLs has been known or hypothesized for at least 80 years,[28] the mechanisms underlying their formation and their influence on the dissolution rate of the primary material remain poorly understood. This lack of mechanistic understanding is illustrated by two fundamental disagreements. The first of these concerns whether ASSLs form by leaching of soluble elements (e.g., Ca, K, Mg, Na) from the primary mineral or, alternatively, by dissolution of the primary mineral followed by precipitation of an amorphous Si-rich phase. The former

Received: June 9, 2019
Revised: August 11, 2019
Published: October 1, 2019

DOI: 10.1021/acs.jpcc.9b05491
J. Phys. Chem. C 2019, 123, 24520−24532

hypothesis (referred to as the "leached layer" hypothesis) has represented the prevailing paradigm for decades.[29,30] It is consistent with ion and photon probe results suggesting that the elemental profiles of reactive species and reaction products are anticorrelated within the ASSL.[31−40] The alternative "dissolution−reprecipitation" hypothesis[41] is supported by transmission electron microscopy observations that indicate an absence of compositional gradients within the ASSL[13] and by atom-probe tomography measurements of altered glass samples that reveal an atomically sharp inner interface,[42,43] which has led to the suggestion that the compositional gradients observed in the ion and photon probe results may be artifacts associated with low lateral resolution.[22] It is also supported by indirect evidence, in some cases, of fluid−mineral interactions occurring through the layer and of mineral dissolution at the interface between the ASSL and the pristine mineral surface[44] due to the presence of a thin fluid film at the inner interface.[22]

The second fundamental disagreement concerns the extent to which the ASSL behaves as a barrier to transport. The historical approach assumes that the dissolution rate of the pristine silicate mineral surface follows transition state theory (TST) and depends only on the chemistry of the bulk aqueous solution.[45] This "primary dissolution control" approach was based on studies where the presence of ASSLs had little or no effect on the dissolution rate or where evidence of diffusive processes was dismissed as experimental artefacts.[10,46−48] Although challenged more than 20 years ago by both contradictory experimental results[49,50] and theoretical inconsistencies,[51,52] this hypothesis is still widely used in reactive transport codes. An important alternative (referred to as the "ASSL dissolution control" approach) consists of applying TST while treating the thermodynamic properties of the ASSL (rather than the primary mineral) as a driver of the overall weathering process.[49,53−57] In essence, this approach treats the ASSL as an activated complex in the sense of TST, the experimental verification of which is still a subject of debate.[58] A second important alternative (referred to as "primary dissolution and transport control") suggests that, in addition to the dissolution of the primary mineral, transport limitations to the diffusion of reactive species across the ASSL must also be accounted for.[9,18,59−63]

One reason for the existence of competing modeling frameworks outlined above is the relatively limited availability of dissolution data compared with the vast range of conditions to be explored in terms of silicate mineral chemistry, aqueous chemistry, and temperature. For example, with the notable exception of results obtained on wollastonite over a wide pH range,[22] most studies supporting the hypothesis that chemical affinity between the bulk fluid and the primary mineral plays an important role were performed under low pH conditions, which favor the formation of nonpassivating layers,[14] similar to the work by Lagache[10] more than 40 years ago. Similarly, parameters such as the redox potential of the solution that have not been systematically examined may have a direct impact on ASSL texture and resulting diffusivity.[64−66] In short, competing interpretations regarding the mechanism and impact of ASSL formation on the overall silicate dissolution rate for identical materials (e.g., Schott, et al.[8] vs Ruiz-Agudo, et al.[7] or Hellmann, et al.[43] vs Gin, et al.[18]) may simply reflect differences in reacting conditions combined with insufficient information on the thermodynamic and transport properties of ASSLs.

The upshot of this is that an improved understanding of the fundamental properties of ASSLs is likely key to resolving the disagreements outlined above.[27,67] Existing data on the properties of ASSLs remains relatively limited for several reasons. First, standard dissolution experiments yield relatively low accuracy estimates of the growth rate of the ASSL as quantified indirectly from small deviations between the stoichiometric composition of released elements and that of the pristine solid. Second, reconstructions of mineral dissolution rates and ASSL thickness from elemental release data are challenged by uncertainties related to the specific surface area of the reactive interface, typically estimated as the Brunauer−Emmett−Teller (BET) surface area of the fresh mineral powder.[68] Such normalization may not account for the temporal evolution of reactive surface area or spatial variability of the dissolution rate, whereas the surface area measurement itself may be inconsistent and carry large and often poorly constrained uncertainties.[69] Finally, the few existing detailed characterizations of ASSLs have been carried out using destructive techniques and, therefore, they inherently do not reveal the time-dependence of ASSL properties.

To date, the transport properties of nanoporous surface layers developed on silicate materials have represented a recurrent topic for material scientists in general and have been addressed by theoretical and experimental studies beyond the geosciences.[61,70−74] Importantly, such transport properties are critically inherited from the (yet to be determined) physicochemical evolution of the silica-rich surface layers, which represent some of the central insights gained from this study.

The aim of the present study is to utilize a novel combination of approaches to follow the evolution of the physical properties of ASSLs in situ, providing direct information on ASSL thickness and density and indirect insights into the local physicochemical conditions prevailing at the inner (pristine mineral/ASSL) interface. We use X-ray reflectivity (XRR) data to track the temporal evolution of ASSL thickness and density. Complementary vertical scanning interferometry (VSI) measurements are performed to track the evolution of the outer (ASSL/bulk solution) interface. Our methodology circumvents the aforementioned challenges and enables probing of mineral reactivity and layer formation at low solid/fluid ratios (~21 mm^2 for 800 mL of solution), ensuring that far-from-equilibrium conditions with respect to the dissolving crystal can be maintained. Layer thickness and surface retreat data are combined to determine the rate of retreat of the inner interface, enabling the calculation of the dissolution rate of the primary labradorite feldspar located underneath the ASSLs. Overall, this study provides a novel characterization of the physicochemical properties of nanoporous surface layers developed on a reference silicate material (feldspar) and sheds light on the dissolution kinetics of the underlying substrate.

METHODS

Sample Preparation. Labradorite single crystals from Nuevo Casas Grande, Chihuahua (Mexico) were provided by the Mineralogical & Geological Museum of Harvard University (Ref. MGMH#135998). They consist of transparent gem-grade crystals with a composition of $Ab_{39}An_{60}Or_1$.[75] Samples of about 7 mm × 3 mm suited for XRR, VSI, and atomic force microscopy (AFM) measurements were prepared following standard procedures previously described.[14] In brief, euhedral

DOI: 10.1021/acs.jpcc.9b05491
J. Phys. Chem. C 2019, 123, 24520−24532

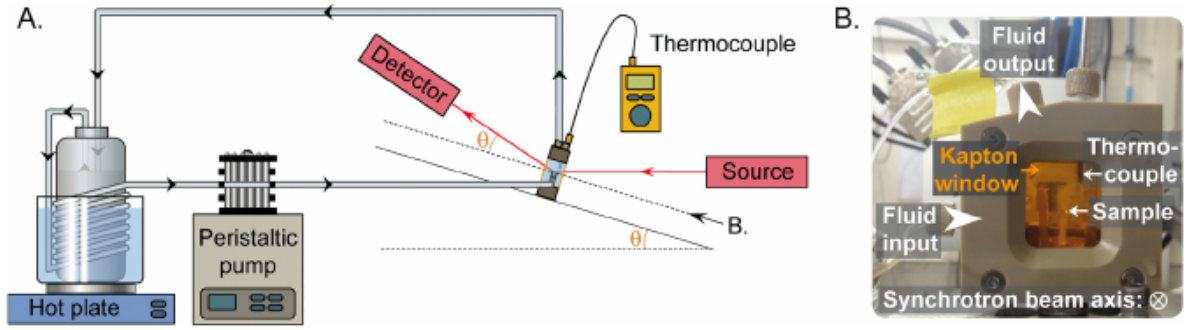

Figure 1. Overview of the experimental setup (A) and front view of the flow-through cell designed for in situ experiments (B). Fluid temperature within the cell was verified with a thermocouple.

crystals were cut with a diamond saw following (001) preferential cleavage planes and polished down to the nanometer scale using colloidal silica polishing suspension. One (010) surface was also prepared. Surface orientation was verified by indexing electron backscatter diffraction (EBSD) patterns obtained on a Tescan Vega 2 scanning electron microscope (SEM).

Labradorite Dissolution and ASSL Formation. Labradorite samples were reacted in pH environments ranging from 1.5 to 4, and experiments were run for durations of about 1 h to more than 35 days as required to form measurable (i.e., >5 nm thick) ASSLs at the fluid−mineral interface. Samples were incubated at 80 °C using polytetrafluoroethylene (PTFE) Savillex reactors equipped with a custom PTFE stirring system.[14] Reactors were filled with a reacting fluid consisting of Milli-Q water whose pH had been previously adjusted with high-grade HCl (37%, ACS reagent) and, for some experiments, saturated with respect to amorphous silica using sodium metasilicate, nonahydrate (Sigma-Aldrich, >98%). The pH was regularly controlled offline at room temperature and adjusted if necessary. A summary of experiments and experimental conditions can be found in Tables S1−S6. The saturation indices for labradorite and amorphous silica at 80 °C were calculated using the Chess software and the Chess tdb database. After reaction, samples were briefly rinsed in Milli-Q water and kept at room temperature in aqueous solutions close to saturation with respect to amorphous silica until XRR measurement to avoid subsequent dehydration or dissolution. For experiments carried out over short durations (up to 94 h), crystals were directly reacted in situ over the course of the XRR measurements with an experimental setup enabling fluid circulation at controlled temperature in a custom flow-through cell with Kapton windows (Figure 1).

Dissolution Rate at the Outer Interface by VSI. The topography of each labradorite sample was measured on a Zygo NewView 7300 VSI prior to the reaction. A portion of the surface of samples summarized in Tables S5 and S6 was then masked with a room-temperature-vulcanizing (RTV) silicone glue spot in order to create a nonreacted reference by avoiding fluid−mineral contact at this specific location. After reaction, the global retreat of the surface due to crystal dissolution was quantified using topography images recorded by VSI on reacted samples after removal of the mask. The absolute dissolution rate at the fluid/layer interface is estimated as $r = (\Delta h/\Delta t) \times (1/V_m)$, where r stands for the absolute dissolution rate (mol m^{-2} s^{-1}), Δh is the surface retreat (m), Δt is the alteration duration (s), and V_m is the molar volume of labradorite (m^3 mol^{-1}).[76] Topography images and profiles were analyzed using SPIP software.

The roughness of the outer interface, σ_{ex}, was determined based on AFM (Bruker MultiMode AFM) and VSI measurements conducted on three representative portions of the surface with dimensions of 1 μm × 1 μm (AFM) and 125 μm × 125 μm (VSI). Roughness values were calculated using Gwyddion software[77] as the root mean square deviation in height, z, from the mean image data plane, z_0. NanoScope Analysis software and Gwyddion were used to visualize and process AFM data including particle size measurements.

Internal Properties of the ASSL by in Situ XRR Experiments. XRR measurements were performed at the European Synchrotron Radiation Facility (ESRF) at the French BM32 beamline (CRG-IF). X-rays (27 keV; wavelength, λ = 0.0459 nm) were used to ensure sufficient transmission ($T \approx 68.5\%$) through the ∼1 cm thick solution in the cell. Reflectivity patterns were acquired for 2θ angles ranging between 0° and 1° (corresponding to scattering vectors ranging between 0.0 and 0.5 $Å^{-1}$). For the prereacted samples (i.e., samples reacted prior to the XRR measurement campaign), the dissolution experiments had different onset times and were all stopped one day prior to the XRR campaign, yielding samples altered for a range of desired time periods. The prereacted samples were then transported to the ESRF in a near-neutral pH solution (pH ≈ 6.5) saturated with respect to amorphous silica. Once at the ESRF, prereacted samples were analyzed in a custom cell (Figure 1B) filled with Milli-Q water at room temperature. For the in situ experiments, unreacted samples were placed in the same cell circulated with a fluid of desired chemistry at 80 °C and patterns were acquired every 5−15 min depending on the growth rate of the ASSL (Figure 1).

Reflectivity data were fitted using the analysis package Motofit,[78] which runs under the IGOR Pro environment. Interfacial roughness, layer density (initially set to that of pure amorphous silica), and layer thickness were refined to match the scattering length density (SLD) profile $q(z)$ in the direction perpendicular to the mineral−water interface. The strategy used to fit the experimental XRR patterns involved identifying the minimum number of layers required to obtain a satisfactory fit following Nelson.[78] Discrepancies between the model and data were quantified by the χ^2 parameter as defined by Nelson,[78] which was minimized by adjusting the thickness and SLD parameters of each layer as well as inner and outer roughness values following a two-step procedure including genetic optimization[79] and the Levenberg−Marquardt meth-

DOI: 10.1021/acs.jpcc.9b05491
J. Phys. Chem. C 2019, 123, 24520−24532

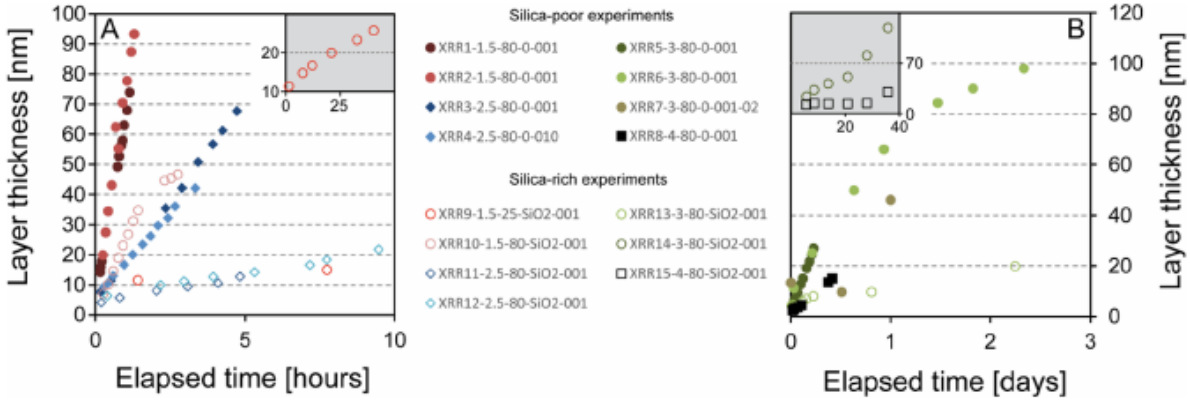

Figure 2. Temporal evolution of layer thickness as measured by XRR. Layer growth was generally faster for experiments at pH ≤ 2.5 (A) compared to experiments at pH > 2.5 (B), and slower for experiments conducted with fluids saturated with respect to amorphous silica (open data points) compared to their nonsaturated counterparts (filled data points). All experiments were conducted at 80 °C with the exception of experiment XRR9-1.5-25-SiO2-001 (red open circles in panel A), conducted at 25 °C. The longest experiments are represented in insets with the same units as the main panel.

od.[80] As shown in Figure S1, some factors (e.g., the existence of local minima) were found to have nonmonotonic influence on fit quality as quantified by the χ^2 value. Hence, the reliability of data modeling was ensured by including genetic optimization as the first step of the fitting procedure. All possible solutions were analyzed manually and discarded if necessary (for instance in the case of nonrealistically high density values).

RESULTS

Formation of ASSLs and in Situ Evolution of Their Physical Properties. The formation of ASSLs at the fluid-mineral interface was observed by XRR for all tested conditions, that is, pH = 1.5 to pH = 4, 80 or 25 °C, in aqueous solutions that were either saturated or not with respect to amorphous silica. As a general trend, ASSL growth rate decreased for experiments conducted at higher pH values, in solutions saturated with respect to amorphous silica, or at lower temperature, all other conditions being kept constant. The ASSL was found to grow at a nearly constant rate in most conditions as revealed by the linear trends in Figure 2, with the notable exception of the longest experiments conducted at pH = 3 and 4 (duration ≥ 1 day). Comparison between results at different pH values revealed a near-linear pH-dependence of the logarithm of the growth rate (Figure 3). Use of a lower temperature (25 vs 80 °C at pH = 1.5) in saturated solution led to a drop of the dissolution rate by a factor of ∼50 (orange symbol, Figure 3). Fluid saturation with respect to amorphous silica led to a decrease of the growth rate by a factor ranging from ∼4 at pH = 1.5 to nearly 30 at pH = 4 (diamonds vs squares, Figure 3).

Measured SLD values ranged from 10.6 to 21.5 × 10^{-6} $Å^{-2}$, which would correspond to densities of ∼1.25 and 2.53 $g{\cdot}cm^{-3}$ under the hypothesis that ASSLs are composed of pure silica (SiO_2) (Figure 4). No significant SLD difference (within the uncertainty of ±5%) was detected between ASSLs grown on different crystallographic surfaces [(001) vs (010)]. Experiments conducted in fluids combining high Si concentrations (∼145 ppm) and weakly acidic pH or low temperature (e.g., experiments XRR10-1.5-25-SiO2, XRR14-3-80-SiO2-001, or XRR15-4-80-SiO2-001) tended to exhibit constant or

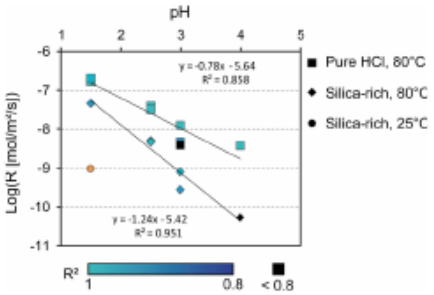

Figure 3. pH-dependence at 80 °C of layer growth rate represented as moles of labradorite per square meter converted each second into layer material (labradorite → layer). Diamonds and squares represent experiments where the fluid was saturated or not with respect to amorphous silica, respectively. For each experiment represented here, the color quantifies the regression coefficient associated to linear regression of the temporal evolution of the layer thickness (cf. Figure 2) according to the color scale below the graph. The orange data point corresponds to the experiment conducted at 25 °C in a silica-rich fluid.

increasing SLD trends over time, suggesting progressive densification. Conversely, experiments conducted in fluids with low Si concentrations (<200 ppb) exhibited decreasing, constant, or nonmonotonous SLD trends. The experiment conducted at 25 °C in a silica-rich fluid at pH = 1.5 exhibited a significantly lower mean SLD compared to its counterpart conducted at 80 °C (12.8 ± 0.9 vs 14.8 ± 0.5 respectively). Measurements performed after completion of experiments XRR9-1.5-80-SiO2-001, XRR11-2.5-80-SiO2-001, and XRR13-3-80-SiO2-001 revealed that layers dried and measured immediately after in situ dissolution tend to exhibit lower SLD values than previous measurements corresponding to their hydrated counterparts (Table S3).

Reactivity and Evolution of the Outer Interface. The global retreat of the outer surface compared to a masked reference (Figure 5), as measured using VSI, was used to probe the reactivity at the outer (ASSL/bulk solution) interface under all tested conditions (see Tables S5 and S6) on a set of samples distinct from those dedicated to XRR measurements.

DOI: 10.1021/acs.jpcc.9b05491
J. Phys. Chem. C 2019, 123, 24520−24532

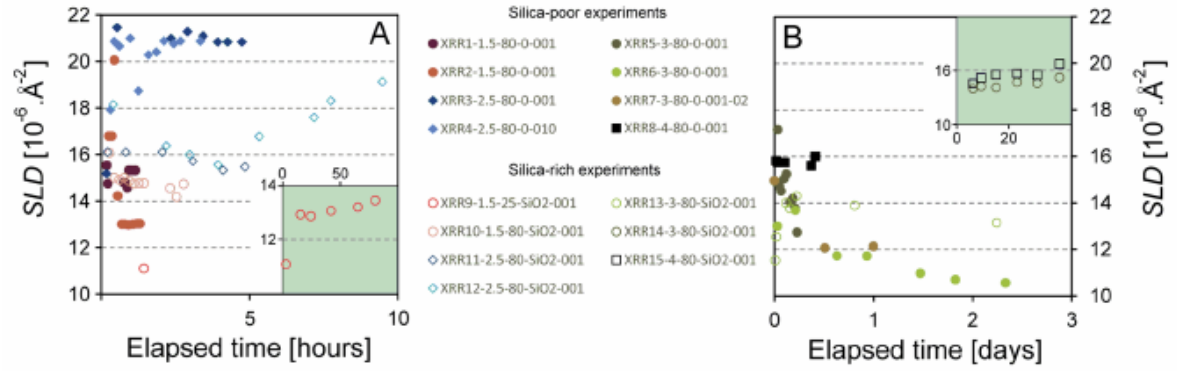

Figure 4. Temporal evolution of the SLD of ASSLs as measured by XRR for experiments at pH ≤ 2.5 (A) and pH > 2.5 (B). Open data points correspond to experiments conducted with fluids saturated with respect to amorphous silica. All experiments were conducted at 80 °C with the exception of experiment XRR9-1.5-25-SiO2-001 (red open circles in panel A) conducted at 25 °C. The longest experiments are represented in insets with the same units as the main panel.

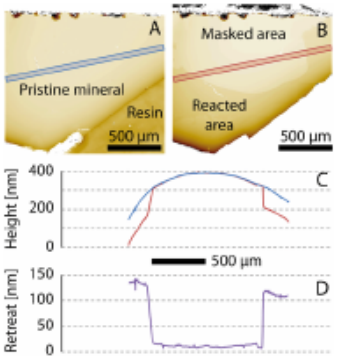

Figure 5. Typical measurement of surface retreat based on topography maps acquired by VSI before (A) and after (B) the dissolution process (here, a labradorite sample weathered for 35 days at 80 °C in a fluid at pH = 3 saturated with respect to amorphous silica). This specific sample was detached from the resin after reaction to facilitate VSI alignment. Height profiles recorded before (blue) and after (red) weathering through the nonreacted masked area are superimposed (C) and subtracted to highlight the overall surface retreat. Some variation on the retreat can be seen, which is consistent with previous results on intrinsic variability of the dissolution rate and profile subtraction at the mm scale.

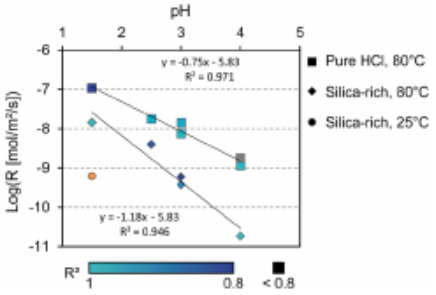

Figure 6. pH-dependence of layer dissolution rate (layer→dissolved species) at 80 °C. Symbol colors and shapes have the same meanings as in Figure 3. Grey square: based on two retreat values.

Dissolution rates of the outer interface were reconstructed from VSI data under the assumption of isovolumetric weathering; the resulting rates showed a significant decrease with increasing pH (Figure 6). Dissolution rates were smaller when the bulk fluid was saturated with respect to amorphous silica, indicating a decreased reactivity of the ASSL at the outer interface by a factor of 4 to 80. The high vertical resolution of the VSI measurements (roughly 3 nm) enabled estimating the apparent activation energy (E_a) of the ASSL dissolution process based on kinetic data collected at T_1 = 80 °C and T_2 = 25 °C for experiments with a fluid at pH = 1.5 saturated with respect to amorphous silica, as

$$E_a = R\frac{T_1T_2}{T_1 - T_2}\ln\left(\frac{r_1}{r_2}\right) \quad (1)$$

where r is the dissolution rate of ASSL. In these conditions, the ~23-fold decrease in ASSL dissolution rate between 80 and 25 °C corresponds to an E_a value of 50 kJ mol^{-1}.

The roughness of the outer interface of a sample reacted at pH = 3 was measured both before and after dissolution based on AFM and VSI data.[14,81] Both techniques yield roughness values of similar order of magnitude, with the VSI values being systematically about twice as large as those obtained by AFM. During the experiments, roughness increased from σ_{ex}^{VSI} = 17 nm and σ_{ex}^{AFM} = 7 nm to σ_{ex}^{VSI} = 65 nm and σ_{ex}^{AFM} = 36 nm as measured using VSI and AFM, respectively. AFM measurements further showed the formation of a nanoscale botryoidal texture of the outer interface exhibiting spherical particles with an average radius of 9.8 ± 1.2 nm (Figure S2). In order to estimate a maximal porosity formed by the silica beads constituting the layer (as opposed to a dense packing of these particles), their arrangement at the outer interface was studied based on AFM data. The intersection of particles with a plane located 9.8 nm below the highest point of a representative portion of the fluid/layer interface yields a pore/particle ratio of 3.2, which yields a rough estimate of ~0.76 as an upper bound on the porosity of the ASSL.

Temporal Evolution of the Fluid−Silicate Interface and Labradorite reactivity. VSI and XRR data were combined to provide one of the first accurate representations of the temporal evolution of the fluid−silicate interface during dissolution and layer formation (Figure 7, Figure S3). In

DOI: 10.1021/acs.jpcc.9b05491
J. Phys. Chem. C 2019, 123, 24520−24532

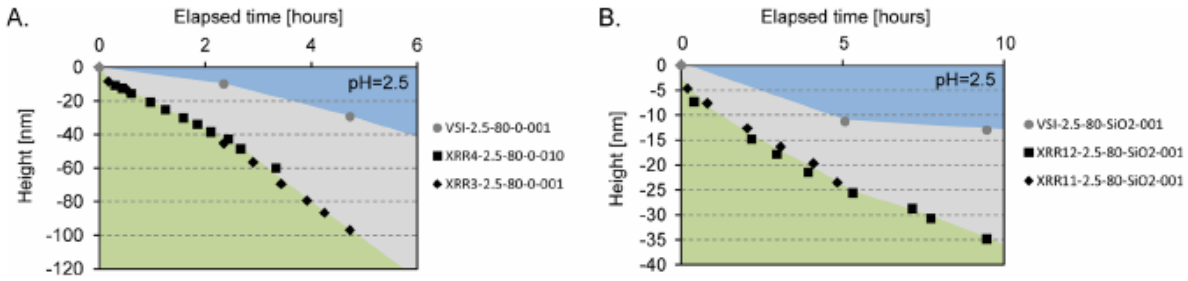

Figure 7. Temporal evolution of ASSL thickness (grey) at the interface between mineral (green) and fluid (blue) for experiments conducted at 80 °C, pH = 2.5, using a fluid that was saturated (SiO_2, panel B) or not (0, panel A) with respect to amorphous silica. Grey dots correspond to VSI measurements of the surface retreat compared to a nonreacted reference (zero height) and track the reactivity of the outer interface. Black diamonds and squares correspond to XRR data corrected for surface retreat and track the temporal evolution of the inner interface. Colored background is used to guide the eye. All experiments were conducted on (001) labradorite faces with the exception of one experiment conducted on (010) (A). A summary of all experimental conditions tested in this study can be found in Figure S3.

particular, the surface retreat, z_{out} measured by VSI was combined with the ASSL thickness, Δz determined from XRR data to evaluate the absolute height of the inner interface, z_{in} (black squares and diamonds, Figure 7) at each timestep, t

$$z_{in}(t) = -\Delta z(t) - \frac{z_{out}(t_{+1}) - z_{out}(t_{-1})}{t_{+1} - t_{-1}} \times t \quad (2)$$

In eq 2, $\Delta z(t)$ is evaluated at time t by XRR, whereas $z_{out}(t_{+1})$ and $z_{out}(t_{-1})$ correspond to absolute values of the surface retreat at the closest VSI measurement before and after XRR measurement, respectively. In most cases, the temporal evolution of the inner interface was linear or made up of linear portions of curves, which indicates constant dissolution rate at given experimental conditions. Linear regression of z_{in} versus time was used as a proxy to estimate the overall reactivity of labradorite (i.e., the dissolution rate of the primary mineral). Of note, this approach considers the ASSL/mineral boundary as a single interface because the two reaction fronts located on each side of the thin fluid film often reported at the inner interface[22] could not be resolved by XRR. The resulting retreat rates of the inner interface revealed a near logarithmic dependence of the dissolution rate on pH (Figure 8). Saturation of the solution with respect to amorphous silica decreased the dissolution rate by a factor ranging from ~5 at pH = 1.5 to ~50 at pH = 4. A temperature decrease from 80 to 25 °C at pH = 1.5 yielded a 37-fold drop in dissolution rate corresponding to an apparent energy of activation of about 57 kJ mol^{-1}.

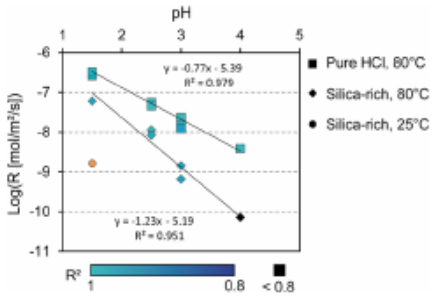

Figure 8. pH-dependence at 80 °C of labradorite dissolution rate (labradorite → layer + dissolved species). Symbol colors and shapes have the same meanings as in Figures 3 and 6.

Fluid Saturation State. To verify that all our experiments were conducted at far-from-equilibrium conditions with respect to labradorite dissolution (i.e., in the region where the dissolution rate should be invariant with saturation state, which defines the dissolution rate plateau), we used the final surface retreat and layer thickness, along with the known sample geometric surface area (~2.8 × 10^{-5} m^2) and labradorite density (~9.8 × 10^{-5} m^3 mol^{-1}), to estimate the maximum possible fluid saturation state with respect to labradorite at the end of our experiments. We note that rough sample edges resulting from diamond saw cutting were washed and covered with RTV glue prior to experiment, which limited their contribution to cation release to the solution composition. As shown in Table S1, Gibbs free energy (ΔG_r) values were all below the ΔG_r threshold value of −41.8 kJ mol^{-1}, where labradorite dissolution should be invariant with saturation as reported by Taylor, et al.[50]

DISCUSSION

Fitting XRR Data. During the XRR fitting procedure, four parameters describing the ASSL were adjusted to match the reflectivity data. These parameters include the layer thickness, density, and inner and outer roughness. As the thickness of the layer primarily affects the periodicity of the signal, which is not significantly impacted by density or roughness, this parameter can be independently assessed with a high degree of confidence. The three other parameters are somewhat correlated, so that the choice of a "best fit" solely based on the χ^2 minimization criterion is nontrivial (see e.g., Figure S1) and sometimes implicitly corresponds to favoring the fitting of one portion of the curve relative to another. Indeed, because the χ^2 value depends on the proportion of data points accurately fitted by the model, it is possible to get a lower χ^2 value with a less relevant fit, if parts of the curve containing little information (as opposed to "features of interest" such as critical angle or well-defined oscillation region) account for a large proportion of the considered data points.

In an attempt to alleviate the issue identified above, we constrained our estimate of the roughness of the outer interface using roughness values measured on the same sample before and after dissolution. We note that these independent roughness measurements had to be performed ex situ, which prevented the acquisition of a time-series during the experiment. We associated as a first approximation, σ_{ex}^{XRR}, either to the linear interpolation of the initial and final AFM-based

DOI: 10.1021/acs.jpcc.9b05491
J. Phys. Chem. C 2019, 123, 24520−24532

roughness (σ_{ex}^{AFM}, cf. dark grey squares, Figure 9) or to the interpolation of the initial and final averages between VSI-

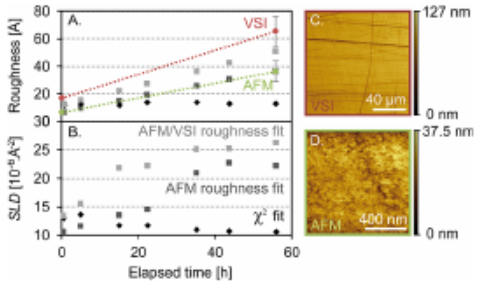

Figure 9. Temporal evolution of roughness (A) and SLD (B) for experiment XRR6-3-80-0-001. Black diamonds correspond to the best fits determined using the lowest χ^2 value as the criterion to assess the validity of the fit, grey squares correspond to best fits obtained using the lowest χ^2 value after imposing at each temporal step the roughness at the outer interface based on topography measurements. In that case, the roughness at the inner interface and the density of the layer were the only adjustable parameters of the model (see text for details). For the "AFM roughness fit" (dark grey squares), the evolution of the outer interface is assimilated to a linear interpolation of AFM roughness measurements acquired before and after the experiment. For the "AFM/VSI roughness fit" (light grey squares), the evolution of the outer interface is associated to the mean value between VSI and AFM measurements, their evolution being supposed linear (see text). The sample roughness measured before and after experiment by VSI and AFM is reported in red and green, respectively, in panel A. Typical fields of view are represented in panels (C,D).

(σ_{ex}^{VSI}) and AFM- (σ_{ex}^{AFM}) based roughness (cf. light grey squares, Figure 9). Reflectivity measurements performed on dried layers (Table S3) were used to verify that any observed discrepancy between σ_{ex}^{XRR} and σ_{ex}^{VSI} or σ_{ex}^{AFM} was unlikely due to dehydration of ASSLs. After applying this constraint, the best fit to the XRR data for both methods (referred to as "AFM/VSI roughness fit" and "AFM roughness fit" and shown as light and dark grey squares in Figure 9B) based on the two remaining parameters (ASSL density and the roughness of the inner interface) suggested that the density of the ASSL invariably increases with time, in contrast with the conclusions reached from the analysis solely based on the χ^2 minimization criterion. However, the resulting density values exceeded those of pure amorphous silica ($\sim 20.6 \times 10^{-6} \cdot A^{-2}$) and even those of unreacted labradorite ($23.5 \times 10^{-6} \cdot A^{-2}$). This likely unphysical result suggests that the roughness values derived by both AFM and VSI overestimate the roughness reflected by the XRR results. Although we note the existence of approaches that can reconcile roughness values obtained using methods with different spatial resolution and field-of-view sizes (e.g., converged roughness parameter approach),[82] these could not be applied in the present case because XRR does not provide a 3D dataset contrary to AFM and VSI. Therefore, we decided to rely on the well-documented "χ^2 fit" approach,[78] which enables direct comparison of our results with literature data.[9,60] We note however that surface roughness may artificially lower the layer apparent density and that further research should be directed at better characterizing in situ the evolution of surface roughness with relevant experimental probes.

Reactivity and Physicochemical Properties of the Fluid/Solid Interface Inferred from XRR and VSI Measurements.

Traditionally, the mechanisms and rates of mineral dissolution have been indirectly monitored through the evolution of fluid composition.[83,84] In these studies, the nonstoichiometry of elemental release was used to indirectly probe the formation of ASSLs at the fluid−mineral interface.[10,33,94] As mentioned in the introduction, this indirect approach suffers from high uncertainties when it comes to determining the evolution of ASSL thickness and density, particularly at low dissolution rates, principally due to the difficulty of accurately determining the stoichiometry of the small elemental release and, also, of constraining the evolving reacting surface area. Our results show that this challenge can be circumvented, to some extent, by using a combination of XRR and VSI measurements to characterize the rate of ASSL formation at the labradorite−water interface. We were able to detect the formation of ASSLs at the surface of labradorite in all tested conditions, in agreement with previous results on a variety of silicate minerals including feldspars.[22] We also probed independently the reactivity of the outer fluid/layer interface and of the inner layer/mineral interface in situ. This provided an accurate picture of the temporal evolution of the fluid−mineral interface (Figures 7 and S3), which enabled unraveling of the reaction kinetics. Our results indicate a reaction order with respect to hydrogen ion (corresponding to the power to which the activity of this ion is raised, see eq 3 and Figure 8) of about 0.77 for the overall dissolution process of labradorite occurring at the inner interface, which is slightly higher than values previously reported for this mineral—typically 0.6—but consistent with the expected range within the feldspar series, typically up to 1.0 for bytownite.[84] Slight differences with previously published data are expected because the protocol used here investigates the reactivity of single cleavage planes, which is known to differ from that of bulk mineral powders.[81]

Most of the mean density values of ASSLs estimated from XRR data fall between 1.29 and 1.89 $g \cdot cm^{-3}$. These measured density values are consistent with the theoretical values for a medium composed of spheres of pure amorphous silica organized with either a "dense packing" (face-centered cubic) or a "minimal packing" (estimated from 2D analysis, see "Reactivity and Evolution of the Outer Interface" section) within an aqueous medium representing 26−76% of the total volume, respectively. Equivalent water−silica ratio may alternatively be associated with a homogeneous product of hydrated silica. Analysis of samples "XRR3-2.5-80-0-001" and "XRR4-2.5-80-0-010" yielded XRR density estimates exceeding the value reported for bulk anhydrous SiO_2 ($2.2\ g \cdot cm^{-3}$, cf. Iler[85]). Such high values may arise from samples with curved interfaces causing total reflection intensity to be detected at angles exceeding the actual critical angle[9] and are therefore not further discussed. Overall, our results indicate that the ASSL is either hydrated or accommodates significant porosity, which, together with the botryoidal texture of the outer interface, is consistent with the hypothesis that ASSL formation involves significant dissolution−reprecipitation.[22,63]

Our experiments show that the dissolution rate of the pristine mineral is impacted by the saturation state of the solution with respect to amorphous silica (Figure 6). From a pure thermodynamic standpoint, only the dissolution rate of the ASSL (and not labradorite) should be impacted by the aqueous silica concentration because the experiments were conducted at far-from-equilibrium conditions with respect to labradorite. This result indicates that the intrinsic dissolution

DOI: 10.1021/acs.jpcc.9b05491
J. Phys. Chem. C 2019, 123, 24520−24532

Table 1. SLD and Associated Estimate of Layer Porosity Measured in Situ or after Drying

measurement	in situ		dried	
experiment	SLD layer [10^{-6}·A^{-2}]	porosity % water (vol)	SLD layer [10^{-6}·A^{-2}]	porosity % air (vol)
XRR9-1.5-80-SiO2-001	14.7	43	14.0	25
XRR11-2.5-80-SiO2-001	15.5	34	10.3	45
XRR13-3-80-SiO2-001	13.2	60	3.4	82

rate of ASSL significantly modulates the reactivity of labradorite (see the section "Passivation by Surface Layers" below).

The dissolution rate of the ASSL was not directly probed by our XRR measurements, which only probed the ASSL thickness. However, the need for frequent z-axis realignment throughout the dissolution experiment to match perfect $\theta-2\theta$ reflection conditions at the surface of the sample provides additional evidence of the progressive retreat of the outer interface, which was tracked more precisely by VSI on separate samples. Our VSI results indicate that the mean ASSL dissolution rate ranged from 1.07×10^{-7} mol m^{-2} s^{-1} at pH = 1.5 to 1.46×10^{-9} mol m^{-2} s^{-1} at pH = 4 at 80 °C in silica-poor solutions. These values are in good agreement with the dissolution rate of amorphous silica observed in other studies. For example, linear extrapolation of our experimental log(rate) = f(pH) model is consistent (within a factor of 0.5 log unit) with the results of Icenhower and Dove[86] for dilute solutions at pH = 5.7 at 80 °C and also (within the same 0.5 log units factor) with estimates based on Rimstidt and Barnes[87] at a pH comprised between 6.5 and 7.1 at 80 °C. In addition, our dissolution rates are consistently 2−3 orders of magnitude greater than that of quartz,[88] as expected for amorphous SiO_2.

Finally, the observation of surface layer dissolution with a fluid at saturation with respect to amorphous silica supports the previous hypothesis, suggesting either an enhanced solubility of the ASSL formed on silicates such as wollastonite compared to pure amorphous silica or that ASSLs dissolve by a different mechanism than amorphous silica.[6] This result, however, is at odds with observations conducted on ASSLs formed on diopside,[89] where the solubility of the ASSLs was suggested to be close to that of α-cristobalite.

In summary, our results suggest that ASSLs formed on labradorite have slightly higher solubility than amorphous SiO_2 but similar dissolution rates. Because the solubility of hydrated amorphous silica would theoretically be lower than pure amorphous silica according to ref 85, we conclude that the presence in our system of a homogenous layer of hydrated amorphous silica is unlikely. Instead, a layer composed of a rather dense packing of silica-rich spheres surrounded by an aqueous solution may form, which would be consistent with a mechanism whereby a botryoidal texture propagates through the layer. Whether the packing, size, or composition of the spheres changes through time still needs to be determined.

As shown in Figure 6, the dissolution rate of ASSL in an acidic solution is also pH-dependent, meaning that hydrogen ions are involved, to some extent, in the dissolution reaction. This feature is generally unexpected for pure amorphous silica.[86] This supports the hypothesis that ASSLs formed on labradorite at pH > 1.5 may not consist of pure hydrated SiO_2.[14] In addition, when the fluid is saturated with respect to amorphous silica (aqueous silica concentrations typically of 5.2×10^{-3} M), the reaction order with respect to hydrogen ion is reduced, showing a reduced impact of the layer on the dissolution rate at more acidic pH values (Figure 8). This is consistent with the formation of different layer-forming phases depending on the pH conditions, the passivating effect of which would be enhanced at conditions closer to neutrality.

The estimate for the activation energy of labradorite dissolution in the present experiments is ~58 kJ mol^{-1}, which is similar to those typically reported for labradorite, at ~42 kJ mol^{-1}.[84] Finally, no difference was detected between the layer growth rate recorded on (001) and (010) faces (Figure 7A). As no anisotropy of dissolution is expected from amorphous phases such as those constituting the ASSL, we conclude that no compelling evidence of dissolution anisotropy for labradorite could be evidenced here.

Effect of Drying on ASSL Properties. Our approach, involving a continuously hydrated fluid−mineral interface, is not completely analogous to environmental settings where minerals, glasses, and concrete materials experience drying/wetting cycles. The effect of drying was therefore investigated at three pH conditions (experiments XRR9-1.5-80-SiO2-001, XRR11-2.5-80-SiO2-001, and XRR13-3-80-SiO2-001). As reported in Table S3, drying of ASSLs tends to decrease their apparent density while having no clear impact on their thickness or roughness. Porosity, defined as the volume proportion of fluid or air in the ASSL, was estimated from SLD values measured in situ or after drying, respectively. The layer was considered to a first approximation as a porous amorphous silica phase, as suggested by its reactivity (cf. previous section). This analysis suggests a drop in porosity during drying for the experiment conducted under acid conditions (pH = 1.5) and an increase at milder pH (pH > 1.5) (Table 1). This behavior cannot be explained by a collapse or dilatation of the porous network during drying because no significant evolution in ASSL thickness was observed. Alternatively, precipitation of distinct phases from the pore solution depending on pH may explain the observed porosity changes. The preliminary results obtained with our approach open interesting avenues for the investigation of the impact of drying/wetting cycles on ASSL textural properties that still need to be explored in depth.

Passivation by Surface Layers. The passivating effect of ASSLs, which results in the reduction of the dissolution rate of primary silicates, has been evidenced in a variety of geological or geochemical contexts.[2,9,14,23,65] In the present study, lower dissolution rates were observed on a reference silicate material (labradorite feldspar) during experiments conducted with silica-rich solutions compared to those that used silica-poor solutions at equivalent pH values. Such contrasting behavior cannot be explained using current analysis approaches, which consist of relating physicochemical properties of the bulk fluid (e.g., T, pH, and other ion activities) to the overall dissolution rate of the silicate materials (R_{min}) following a transition-state theory relation

DOI: 10.1021/acs.jpcc.9b05491
J. Phys. Chem. C 2019, 123, 24520−24532

$$R_{\min} = \left[\sum_i A_{i,\min} \cdot \exp\left(\frac{-E_{a,\min}^{\,i}}{RT}\right) \cdot a_i^{n_{i,\min}}\right] \left(1 - \exp\left(\frac{s \times \Delta G_r}{RT}\right)\right) \quad (3)$$

where $A_{i,\min}$ is an Arrhenius pre-exponential factor; $E_{a,\min}^{\,i}$, a_i, and $n_{i,\min}$ are the activation energy, activity, and reaction order with respect to reactive species, i; R is the ideal gas constant; T is absolute temperature; and ΔG_r and S are the Gibbs free energy of the dissolution reaction and a dimensionless empirical factor. According to the classical theoretical framework of mineral dissolution kinetics, the affinity term $\left(1 - \exp\left(\frac{s \times \Delta G_r}{RT}\right)\right)$ equals ~1 in our experiments because the aqueous solutions were at far-from-equilibrium conditions with respect to the dissolution of the primary phase ($\Delta G_r < -41.8$ kJ mol^{-1}, Table S1). Note that this statement holds true even if more sophisticated empirical functions are used, such as the one determined by Taylor, et al.[50] for labradorite. Moreover, in acidic conditions (pH $\leq$ 4), the only reactive species to be considered is H^+. In short, no effect of the activity of dissolved SiO_2 is anticipated for our system, which is at odds with labradorite dissolution rate in silica-rich solutions being 5−50 times lower compared with silica-poor solutions as described above. Therefore, we conclude that the composition of the solution at the inner (labradorite/ASSL) interface must be different from that of the bulk solution, which is consistent with other recent studies.[20] In particular, as the temperature was maintained constant, we conclude that at least one of the two remaining parameters able to influence the kinetic dissolution rate (namely pH and/or ion concentration) must be significantly higher at the inner interface than in the fluid at least for the silica-rich experiments, and that this discrepancy is higher for experiments conducted in silica-rich fluid than for silica-poor experiments. This hypothesis is supported by the fact that the rate drop observed when saturating the fluid with respect to amorphous silica is more marked for experiments conducted at higher pH, where fluid composition is more sensitive to proton consumption and cation release by the dissolution process. Of note, at pH = 4, with high background concentrations of dissolved silica, pore fluid can only accommodate about 30 ppb of Al^{3+} and Ca^{2+} before reaching the close-to-equilibrium regime domain with respect to labradorite dissolution defined by Taylor, et al.[50] These conclusions may be related to the overall increase of density observed for most experiments conducted in silica-rich solutions, which may indicate a decrease in ASSL porosity and, possibly, transport properties as previously reported for the dissolution of wollastonite.[9] Decreasing density observed for XRR9 and XRR11 experiments suggests, however, that density may not fully determine the transport properties of ASSLs and that other parameters controlling the spatial organization of the porous network (e.g., tortuosity) may need to be investigated in the future using microscopy and surface-sensitive scattering techniques coupled with numerical modeling.

In summary, our results suggest that the decrease of the dissolution rate of labradorite minerals in silica-rich fluids may reflect a passivation by ASSLs formed under these conditions, which decreased the transport properties of reactive species and reaction products through the layer, ultimately leading to higher local pH and/or ion concentration at the inner layer/mineral interface. Therefore, we suggest that the local fluid composition (supposedly at higher pH and closer to labradorite saturation) is the primary driver of the dissolution reaction. In cases where a bijective relationship between fluid chemistry (pH, ΔG_r) and dissolution rate could be demonstrated (e.g., for serpentine[90]), this approach has the potential to enable the determination of the local fluid chemistry at the inner interface.

For experiments conducted in silica-poor fluids, no clear evidence of passivation and ASSL densification was noted. Two possible explanations can be put forward to explain this observation, in contrast with previous data where passivation could be directly observed.[14,23] First, it is likely that the emergence of passivating properties requires a certain minimal duration for the layer to densify, also called "maturing time".[91] Analogous time-dependent processes have been previously observed for amorphous phases such as pre-gibbsite gels.[92] Of note, no clear temporal decrease of the dissolution rate was seen on the timescale of our experiments. Second, it is possible that elemental release from accessory phases included in a given primary mineral or assemblage, and especially iron-containing minerals, plays an important role in the buildup of passivating layers. Indeed, formation of a hematite−amorphous silica assemblage exhibiting passivating properties due to strong Fe(III)−Si chemical interactions[66,93] is one of the few clearly identified mechanisms of silicate passivation to date. In contrast to the present study, both in Wild et al.[14] and Daval, et al.[23] where passivation effect could be observed, the labradorite used contained Fe-bearing mineral inclusions. In short, our results suggest a need for further examination of the potential impact of minor levels of Fe on ASSL passivating properties.

Existing dissolution rate laws are based almost exclusively on laboratory experiments consisting of immersing mineral grains in reactive fluids at high-temperature and low pH conditions and recording dissolution through elemental release into solution. The methodology developed here provides complementary data that can help shed light on silicate dissolution in natural settings. In particular, we were able to precisely quantify two properties critical to extrapolating laboratory results to natural settings and larger time and spatial scales: the rates of dissolution of the pristine mineral and of the ASSL and their associated activation energies. In addition, we provide indirect evidence of changes in the pore fluid chemistry of the ASSL, possibly related to the apparent transport properties of this phase. With regard to implications for silicate weathering in field conditions, our results suggest that circum-neutral pH values, silica-rich fluids, the presence of complex mineralogical assemblages including Fe-rich phases, long time scales, and drying−wetting cycles, all tend to favor the formation of ASSLs with reduced porosity and transport properties. The methodology developed here should enable more detailed characterizations of the physicochemical evolution of silica-rich surface layers on a wide variety of silicate materials and provide new insight into the relationship between the macroscale dissolution rates of silicate materials and the microscale transport properties of nanoporous silica-rich layers, which have been extensively studied both from theoretical and experimental perspectives.[61,70−74]

DOI: 10.1021/acs.jpcc.9b05491
J. Phys. Chem. C 2019, 123, 24520−24532

CONCLUSIONS

The present study tested a novel methodology to probe in situ the formation and properties of ASSLs developed at a fluid−silicate interface. Our approach enabled precise quantification of the formation of ASSLs on labradorite feldspar, a silicate mineral representative of the continental crust. We quantified ASSL density, thickness, and roughness by XRR while independently probing ASSL reactivity by VSI. Our results show that ASSLs have a significant impact on the dissolution rate of the primary mineral: our experiments revealed a drop in the dissolution rate of labradorite in silica-rich solutions compared to silica-poor solutions, where both conditions were far-from-equilibrium with respect to the dissolution of this primary phase in the bulk fluid. Our results suggest that ASSLs formed in silica-rich fluids have distinct transport properties resulting in either higher ion activities, higher pH, or both in the pore solution controlling the dissolution of the primary phase.

Overall, our findings underline the need for an improved understanding of the processes controlling local physicochemical parameters at the interface with the dissolving silicate, which may differ from those recorded in bulk fluid. This has important geochemical and industrial implication. First, it highlights the need to revise current kinetic rate laws, which assume direct bulk fluid−mineral contact. Instead, kinetic models should incorporate the impact of ASSLs, which seems to be condition-dependent. Then, caution should be taken when incorporating such rate laws in models used in the context of onsite studies or important industrial applications, including atmospheric CO_2 drawdown related to silicate mineral weathering, geological carbon capture and storage, or the design of long-term nuclear waste repositories. Finally, and most importantly, the present study highlights the need for a better understanding of the details of micro- to molecular-scale processes in ASSLs in order to gain predictive power in geochemical and industrial contexts.

The methodology developed here is a valuable tool for investigating silicate dissolution. In addition to complementary data, from bulk fluid analysis, and by correlating the theoretical and actual dissolution rates depending on the reaction conditions, it has the potential to enable the determination of the relevant parameters (e.g., local fluid pH and saturation conditions actually driving the dissolution process at the inner layer−silicate interface) to be accounted for to accurately describe fluid−mineral interactions.

ASSOCIATED CONTENT

Supporting Information

The Supporting Information is available free of charge on the ACS Publications website at DOI: 10.1021/acs.jpcc.9b05491.

> Experiments conducted in this study, best fit parameters associated to reflectivity data, surface retreat measured by VSI, treatment of reflectivity data, AFM topography of a reacted portion of labradorite, and temporal evolution of ASSL thickness at the interface between mineral and fluid (PDF)

AUTHOR INFORMATION

Corresponding Author

*E-mail: bwild@princeton.edu. Phone: (609) 986 6332.

ORCID

Bastien Wild: 0000-0002-0187-1110

Ian C. Bourg: 0000-0002-5265-7229

Alejandro Fernandez-Martinez: 0000-0001-5073-9629

Author Contributions

The manuscript was written through contributions of all authors. All authors have given approval to the final version of the manuscript.

Notes

The authors declare no competing financial interest.

ACKNOWLEDGMENTS

A. Aubert and V. Magnin are acknowledged for their technical support during synchrotron measurement campaigns. A. Putnis, J. Hövelmann, K. Czaja, and the Mineralogical & Geological Museum of Harvard University are warmly acknowledged for providing labradorite samples (Ref. MGMH#135998). This project was funded by the VALVE project (EC2CO-BIOHEFECT program coordinated by the CNRS-INSU) attributed to D. Daval. B. Wild was supported by Princeton University's Andlinger Center for Energy and Environment through its Distinguished Postdoctoral Fellows program. The relevance of this study and the quality of the manuscript were significantly improved by insightful comments from Thorsten Geisler-Wierwille, Moritz Fritzsche, and two anonymous reviewers.

ABBREVIATIONS

ASSLs, amorphous silica-rich surface layers; VSI, vertical scanning interferometry; XRR, X-ray reflectivity; TST, transition state theory; BET, Brunauer−Emmett−Teller; AFM, atomic force microscopy; EBSD, electron backscatter diffraction; SEM, scanning electron microscope; PTFE, polytetrafluoroethylene; RTV, room-temperature-vulcanizing; ESRF, European synchrotron radiation facility; SLD, scattering length density; Ab, albite ($NaAlSi_3O_8$); An, anorthite ($CaAl_2Si_2O_8$); Or, orthoclase ($KAlSi_3O_8$)

REFERENCES

(1) Béarat, H.; McKelvy, M. J.; Chizmeshya, A. V. G.; Gormley, D.; Nunez, R.; Carpenter, R. W.; Squires, K.; Wolf, G. H. Carbon sequestration via aqueous olivine mineral carbonation: Role of passivating layer formation. *Environ. Sci. Technol.* **2006**, *40*, 4802−4808.

(2) Daval, D.; Sissmann, O.; Menguy, N.; Saldi, G. D.; Guyot, F.; Martinez, I.; Corvisier, J.; Garcia, B.; Machouk, I.; Knauss, K. G.; et al. Influence of amorphous silica layer formation on the dissolution rate of olivine at 90 °C and elevated pCO2. *Chem. Geol.* **2011**, *284*, 193−209.

(3) Johnson, N. C.; Thomas, B.; Maher, K.; Rosenbauer, R. J.; Bird, D.; Brown, G. E., Jr. Olivine dissolution and carbonation under conditions relevant for in situ carbon storage. *Chem. Geol.* **2014**, *373*, 93−105.

(4) Maher, K.; Johnson, N. C.; Jackson, A.; Lammers, L. N.; Torchinsky, A. B.; Weaver, K. L.; Bird, D. K.; Brown, G. E., Jr. A spatially resolved surface kinetic model for forsterite dissolution. *Geochim. Cosmochim. Acta* **2016**, *174*, 313−334.

(5) Daval, D.; Martinez, I.; Corvisier, J.; Findling, N.; Goffé, B.; Guyot, F. Carbonation of Ca-bearing silicates, the case of wollastonite: Experimental investigations and kinetic modeling. *Chem. Geol.* **2009**, *265*, 63−78.

(6) Weissbart, E. J.; Rimstidt, J. D. Wollastonite: Incongruent dissolution and leached layer formation. *Geochim. Cosmochim. Acta* **2000**, *64*, 4007−4016.

DOI: 10.1021/acs.jpcc.9b05491
J. Phys. Chem. C 2019, 123, 24520−24532

(7) Ruiz-Agudo, E.; Putnis, C. V.; Rodriguez-Navarro, C.; Putnis, A. Mechanism of leached layer formation during chemical weathering of silicate minerals. *Geology* **2012**, *40*, 947−950.
(8) Schott, J.; Pokrovsky, O. S.; Spalla, O.; Devreux, F.; Gloter, A.; Mielczarski, J. A. Formation, growth and transformation of leached layers during silicate minerals dissolution: The example of wollastonite. *Geochim. Cosmochim. Acta* **2012**, *98*, 259−281.
(9) Daval, D.; Bernard, S.; Rémusat, L.; Wild, B.; Guyot, F.; Micha, J. S.; Rieutord, F.; Magnin, V.; Fernandez-Martinez, A. Dynamics of altered surface layer formation on dissolving silicates. *Geochim. Cosmochim. Acta* **2017**, *209*, 51−69.
(10) Lagache, M. New data on the kinetics of the dissolution of alkali feldspars at 200°C in CO2 charged water. *Geochim. Cosmochim. Acta* **1976**, *40*, 157−161.
(11) Casey, W. H.; Westrich, H. R.; Massis, T.; Banfield, J. F.; Arnold, G. W. The surface of labradorite feldspar after acid hydrolysis. *Chem. Geol.* **1989**, *78*, 205−218.
(12) Casey, W. H.; Westrich, H. R.; Banfield, J. F.; Ferruzzi, G.; Arnold, G. W. Leaching and reconstruction at the surfaces of dissolving chain-silicate minerals. *Nature* **1993**, *366*, 253−256.
(13) Hellmann, R.; Penisson, J.-M.; Hervig, R. L.; Thomassin, J.-H.; Abrioux, M.-F. An EFTEM/HRTEM high-resolution study of the near surface of labradorite feldspar altered at acid pH: evidence for interfacial dissolution-reprecipitation. *Phys. Chem. Miner.* **2003**, *30*, 192−197.
(14) Wild, B.; Daval, D.; Guyot, F.; Knauss, K. G.; Pollet-Villard, M.; Imfeld, G. pH-dependent control of feldspar dissolution rate by altered surface layers. *Chem. Geol.* **2016**, *442*, 148−159.
(15) Cailleteau, C.; Angeli, F.; Devreux, F.; Gin, S.; Jestin, J.; Jollivet, P.; Spalla, O. Insight into silicate-glass corrosion mechanisms. *Nat. Mater.* **2008**, *7*, 978−983.
(16) Verney-Carron, A.; Gin, S.; Frugier, P.; Libourel, G. Long-term modeling of alteration-transport coupling: Application to a fractured Roman glass. *Geochim. Cosmochim. Acta* **2010**, *74*, 2291−2315.
(17) Geisler, T.; Nagel, T.; Kilburn, M. R.; Janssen, A.; Icenhower, J. P.; Fonseca, R. O. C.; Grange, M.; Nemchin, A. A. The mechanism of borosilicate glass corrosion revisited. *Geochim. Cosmochim. Acta* **2015**, *158*, 112−129.
(18) Gin, S.; Jollivet, P.; Fournier, M.; Angeli, F.; Frugier, P.; Charpentier, T. Origin and consequences of silicate glass passivation by surface layers. *Nat. Commun.* **2015**, *6*, 6360.
(19) Ruiz-Agudo, E.; Putnis, C. V.; Putnis, A. Coupled dissolution and precipitation at mineral-fluid interfaces. *Chem. Geol.* **2014**, *383*, 132−146.
(20) Geisler, T.; Dohmen, L.; Lenting, C.; Fritzsche, M. B. K. Real-time in situ observations of reaction and transport phenomena during silicate glass corrosion by fluid-cell Raman spectroscopy. *Nat. Mater.* **2019**, *18*, 342−348.
(21) Nugent, M. A.; Brantley, S. L.; Pantano, C. G.; Maurice, P. A. The influence of natural mineral coatings on feldspar weathering. *Nature* **1998**, *395*, 588−591.
(22) Hellmann, R.; Wirth, R.; Daval, D.; Barnes, J.-P.; Penisson, J.-M.; Tisserand, D.; Epicier, T.; Florin, B.; Hervig, R. L. Unifying natural and laboratory chemical weathering with interfacial dissolution-reprecipitation: A study based on the nanometer-scale chemistry of fluid-silicate interfaces. *Chem. Geol.* **2012**, *294*−*295*, 203−216.
(23) Daval, D.; Calvaruso, C.; Guyot, F.; Turpault, M.-P. Time-dependent feldspar dissolution rates resulting from surface passivation: Experimental evidence and geochemical implications. *Earth Planet. Sci. Lett.* **2018**, *498*, 226−236.
(24) Monteiro, P. J. M.; Miller, S. A.; Horvath, A. Towards sustainable concrete. *Nat. Mater.* **2017**, *16*, 698.
(25) Gin, S.; Collin, M.; Jollivet, P.; Fournier, M.; Minet, Y.; Dupuy, L.; Mahadevan, T.; Kerisit, S.; Du, J. Dynamics of self-reorganization explains passivation of silicate glasses. *Nat. Commun.* **2018**, *9*, 2169.
(26) Park, A.-H. A.; Fan, L.-S. CO2 mineral sequestration: physically activated dissolution of serpentine and pH swing process. *Chem. Eng. Sci.* **2004**, *59*, 5241−5247.
(27) Noiriel, C.; Daval, D. Pore-Scale Geochemical Reactivity Associated with CO2 Storage: New Frontiers at the Fluid-Solid Interface. *Acc. Chem. Res.* **2017**, *50*, 759−768.
(28) Correns, C. W.; von Engelhardt, W. Neue Untersuchungen über die Verwitterung des Kalifeldspates. *Naturwissenschaften* **1938**, *26*, 137−138.
(29) Luce, R. W.; Bartlett, R. W.; Parks, G. A. Dissolution kinetics of magnesium silicates. *Geochim. Cosmochim. Acta* **1972**, *36*, 33−50.
(30) Paces, T. Chemical characteristics and equilibration in natural water-felsic rock-CO2 system. *Geochim. Cosmochim. Acta* **1972**, *36*, 217−240.
(31) Muir, I. J.; Michael Bancroft, G.; Wayne Nesbitt, H. Characteristics of altered labradorite surfaces by SIMS and XPS. *Geochim. Cosmochim. Acta* **1989**, *53*, 1235−1241.
(32) Petit, J.-C.; Dran, J.-C.; Schott, J.; Mea, G. D. New evidence on the dissolution mechanism of crystalline silicates by MeV ion beam techniques. *Chem. Geol.* **1989**, *76*, 365−369.
(33) Hellmann, R.; Eggleston, C. M.; Hochella, M. F.; Crerar, D. A. The formation of leached layers on albite surfaces during dissolution under hydrothermal conditions. *Geochim. Cosmochim. Acta* **1990**, *54*, 1267−1281.
(34) Inskeep, W. P.; Nater, E. A.; Bloom, P. R.; Vandervoort, D. S.; Erich, M. S. Characterization of laboratory weathered labradorite surfaces using X-ray photoelectron spectroscopy and transmission electron microscopy. *Geochim. Cosmochim. Acta* **1991**, *55*, 787−800.
(35) Muir, I. J.; Nesbitt, H. W. Effects of aqueous cations on the dissolution of labradorite feldspar. *Geochim. Cosmochim. Acta* **1991**, *55*, 3181−3189.
(36) Shotyk, W.; Nesbitt, H. W. Incongruent and congruent dissolution of plagioclase feldspar: effect of feldspar composition and ligand complexation. *Geoderma* **1992**, *55*, 55−78.
(37) Shotyk, W.; Metson, J. B. Secondary ion mass spectrometry (SIMS) and its application to chemical weathering. *Rev. Geophys.* **1994**, *32*, 197−220.
(38) Schweda, P.; Sjöberg, L.; Södervall, U. Near-surface composition of acid-leached labradorite investigated by SIMS. *Geochim. Cosmochim. Acta* **1997**, *61*, 1985−1994.
(39) Chen, Y.; Brantley, S. L. Dissolution of forsteritic olivine at 65°C and 2 < pH < 5. *Chem. Geol.* **2000**, *165*, 267−281.
(40) Nesbitt, H. W.; Skinner, W. M. Early development of Al, Ca, and Na compositional gradients in labradorite leached in pH 2 HCl solutions. *Geochim. Cosmochim. Acta* **2001**, *65*, 715−727.
(41) Putnis, C. V.; Tsukamoto, K.; Nishimura, Y. Direct observations of pseudomorphism: compositional and textural evolution at a fluid-solid interface. *Am. Mineral.* **2005**, *90*, 1909−1912.
(42) Gin, S.; Jollivet, P.; Barba Rossa, G.; Tribet, M.; Mougnaud, S.; Collin, M.; Fournier, M.; Cadel, E.; Cabie, M.; Dupuy, L. Atom-Probe Tomography, TEM and ToF-SIMS study of borosilicate glass alteration rim: a multiscale approach to investigating rate-limiting mechanisms. *Geochim. Cosmochim. Acta* **2017**, *202*, 57−76.
(43) Hellmann, R.; Cotte, S.; Cadel, E.; Malladi, S.; Karlsson, L. S.; Lozano-Perez, S.; Cabié, M.; Seyeux, A. Nanometre-scale evidence for interfacial dissolution-reprecipitation control of silicate glass corrosion. *Nat. Mater.* **2015**, *14*, 307−311.
(44) Jordan, G.; Higgins, S. R.; Eggleston, C. M.; Swapp, S. M.; Janney, D. E.; Knauss, K. G. Acidic dissolution of plagioclase: in-situ observations by hydrothermal atomic force microscopy. *Geochim. Cosmochim. Acta* **1999**, *63*, 3183−3191.
(45) Aagaard, P.; Helgeson, H. C. Thermodynamic and kinetic constraints on reaction rates among minerals and aqueous solutions; I, Theoretical considerations. *Am. J. Sci.* **1982**, *282*, 237−285.
(46) Berner, R. A.; Holdren, G. R. Mechanism of feldspar weathering: Some observational evidence. *Geology* **1977**, *5*, 369−372.
(47) Berner, R. A.; Holdren, G. R. Mechanism of feldspar weathering-II. Observations of feldspars from soils. *Geochim. Cosmochim. Acta* **1979**, *43*, 1173−1186.
(48) Holdren, G. R.; Berner, R. A. Mechanism of feldspar weathering-I. Experimental studies. *Geochim. Cosmochim. Acta* **1979**, *43*, 1161−1171.

DOI: 10.1021/acs.jpcc.9b05491
J. Phys. Chem. C 2019, 123, 24520−24532

(49) Oelkers, E. H.; Schott, J.; Devidal, J.-L. The effect of aluminum, pH, and chemical affinity on the rates of aluminosilicate dissolution reactions. *Geochim. Cosmochim. Acta* **1994**, *58*, 2011−2024.
(50) Taylor, A. S.; Blum, J. D.; Lasaga, A. C. The dependence of labradorite dissolution and Sr isotope release rates on solution saturation state. *Geochim. Cosmochim. Acta* **2000**, *64*, 2389−2400.
(51) Nagy, K. L.; Blum, A. E.; Lasaga, A. C. Dissolution and precipitation kinetics of kaolinite at 80 degrees C and pH 3; the dependence on solution saturation state. *Am. J. Sci.* **1991**, *291*, 649−686.
(52) Lasaga, A. C. In *Chemical Weathering Rates of Silicate Minerals*; White, A. F., Brantley, S. L., Ed.; Mineralogical Society of America, 1995; Vol. *31*, pp 23−86.
(53) Grambow, B.; Müller, R. First-order dissolution rate law and the role of surface layers in glass performance assessment. *J. Nucl. Mater.* **2001**, *298*, 112−124.
(54) Bourcier, W. L.; Peiffer, D. W.; Knauss, K. G.; McKeegan, K. D.; Smith, D. K. A. Kinetic model for Borosilicate glass dissolution based on the dissolution affinity of a surface alteration layer. *MRS Online Proc. Libr.* **1989**, *176*, 1−10.
(55) Oelkers, E. H.; Schott, J. Experimental study of anorthite dissolution and the relative mechanism of feldspar hydrolysis. *Geochim. Cosmochim. Acta* **1995**, *59*, 5039−5053.
(56) Daux, V.; Guy, C.; Advocat, T.; Crovisier, J.-L.; Stille, P. Kinetic aspects of basaltic glass dissolution at 90 °C: role of aqueous silicon and aluminium. *Chem. Geol.* **1997**, *142*, 109−126.
(57) Oelkers, E. H. General kinetic description of multioxide silicate mineral and glass dissolution. *Geochim. Cosmochim. Acta* **2001**, *65*, 3703−3719.
(58) Lüttge, A. Crystal dissolution kinetics and Gibbs free energy. *J. Electron Spectrosc. Relat. Phenom.* **2006**, *150*, 248−259.
(59) Devreux, F.; Ledieu, A.; Barboux, P.; Minet, Y. Leaching of borosilicate glasses. II. Model and Monte-Carlo simulations. *J. Non-Cryst. Solids* **2004**, *343*, 13−25.
(60) Rebiscoul, D.; Van der Lee, A.; Rieutord, F.; Né, F.; Spalla, O.; El-Mansouri, A.; Frugier, P.; Ayral, A.; Gin, S. Morphological evolution of alteration layers formed during nuclear glass alteration: new evidence of a gel as a diffusive barrier. *J. Nucl. Mater.* **2004**, *326*, 9−18.
(61) Gin, S.; Guittonneau, C.; Godon, N.; Neff, D.; Rebiscoul, D.; Cabié, M.; Mostefaoui, S. Nuclear Glass Durability: New Insight into Alteration Layer Properties. *J. Phys. Chem. C* **2011**, *115*, 18696−18706.
(62) Gin, S.; Neill, L.; Fournier, M.; Frugier, P.; Ducasse, T.; Tribet, M.; Abdelouas, A.; Parruzot, B.; Neeway, J.; Wall, N. The controversial role of inter-diffusion in glass alteration. *Chem. Geol.* **2016**, *440*, 115−123.
(63) Ruiz-Agudo, E.; King, H. E.; Patiño-López, L. D.; Putnis, C. V.; Geisler, T.; Rodriguez-Navarro, C.; Putnis, A. Control of silicate weathering by interface-coupled dissolution-precipitation processes at the mineral-solution interface. *Geology* **2016**, *44*, 567−570.
(64) Sissmann, O.; Daval, D.; Brunet, F.; Guyot, F.; Verlaguet, A.; Pinquier, Y.; Findling, N.; Martinez, I. The deleterious effect of secondary phases on olivine carbonation yield: Insight from time-resolved aqueous-fluid sampling and FIB-TEM characterization. *Chem. Geol.* **2013**, *357*, 186−202.
(65) Saldi, G. D.; Daval, D.; Morvan, G.; Knauss, K. G. The role of Fe and redox conditions in olivine carbonation rates: An experimental study of the rate limiting reactions at 90 and 150 °C in open and closed systems. *Geochim. Cosmochim. Acta* **2013**, *118*, 157−183.
(66) Saldi, G. D.; Daval, D.; Guo, H.; Guyot, F.; Bernard, S.; Le Guillou, C.; Davis, J. A.; Knauss, K. G. Mineralogical evolution of Fe-Si-rich layers at the olivine-water interface during carbonation reactions. *Am. Mineral.* **2015**, *100*, 2655−2669.
(67) Casey, W. H. Glass and mineral corrosion dynamics and durability. *Nat. Mater.* **2008**, *7*, 930−932.
(68) White, A. F.; Brantley, S. L. The effect of time on the weathering of silicate minerals: why do weathering rates differ in the laboratory and field? *Chem. Geol.* **2003**, *202*, 479−506.
(69) Fischer, C.; Arvidson, R. S.; Lüttge, A. How predictable are dissolution rates of crystalline material? *Geochim. Cosmochim. Acta* **2012**, *98*, 177−185.
(70) Cailleteau, C.; Devreux, F.; Spalla, O.; Angeli, F.; Gin, S. Why do certain glasses with a high dissolution rate undergo a low degree of corrosion? *J. Phys. Chem. C* **2011**, *115*, 5846−5855.
(71) Bourg, I. C.; Steefel, C. I. Molecular dynamics simulations of water structure and diffusion in silica nanopores. *J. Phys. Chem. C* **2012**, *116*, 11556−11564.
(72) Rébiscoul, D.; Cambedouzou, J.; Matar Briman, I.; Cabié, M.; Brau, H.-P.; Diat, O. Water dynamics in nanoporous alteration layer coming from glass alteration: an experimental approach. *J. Phys. Chem. C* **2015**, *119*, 15982−15993.
(73) Neeway, J. J.; Kerisit, S. N.; Liu, J.; Zhang, J.; Zhu, Z.; Riley, B. J.; Ryan, J. V. Ion-exchange interdiffusion model with potential application to long-term nuclear waste glass performance. *J. Phys. Chem. C* **2016**, *120*, 9374−9384.
(74) Collin, M.; Gin, S.; Dazas, B.; Mahadevan, T.; Du, J.; Bourg, I. C. Molecular dynamics simulations of water structure and diffusion in a 1 nm diameter silica nanopore as a function of surface charge and alkali metal counterion identity. *J. Phys. Chem. C* **2018**, *122*, 17764−17776.
(75) Hövelmann, J.; Austrheim, H.; Putnis, A. Cordierite formation during the experimental reaction of plagioclase with Mg-rich aqueous solutions. *Contrib. Mineral. Petrol.* **2014**, *168*, 1063.
(76) Arvidson, R. S.; Beig, M. S.; Luttge, A. Single-crystal plagioclase feldspar dissolution rates measured by vertical scanning interferometry. *Am. Mineral.* **2004**, *89*, 51−56.
(77) Nečas, D.; Klapetek, P. Gwyddion: an open-source software for SPM data analysis. *Cent. Eur. J. Phys.* **2012**, *10*, 181−188.
(78) Nelson, A. Co-refinement of multiple-contrast neutron/X-ray reflectivity data using MOTOFIT. *J. Appl. Crystallogr.* **2006**, *39*, 273−276.
(79) Bowen, D. K.; Tanner, B. K.; Wormington, M.; Panaccione, C.; Matney Kevin, M.; Bowen, D. K. Characterization of structures from X-ray scattering data using genetic algorithms. *Philos. Trans. R. Soc., A* **1999**, *357*, 2827−2848.
(80) Marquardt, D. An Algorithm for least-squares estimation of nonlinear parameters. *J. Soc. Ind. Appl. Math.* **1963**, *11*, 431−441.
(81) Pollet-Villard, M.; Daval, D.; Ackerer, P.; Saldi, G. D.; Wild, B.; Knauss, K. G.; Fritz, B. Does crystallographic anisotropy prevent the conventional treatment of aqueous mineral reactivity? A case study based on K-feldspar dissolution kinetics. *Geochim. Cosmochim. Acta* **2016**, *190*, 294−308.
(82) Fischer, C.; Lüttge, A. Converged surface roughness parameters—a new tool to quantify rock surface morphology and reactivity alteration. *Am. J. Sci.* **2007**, *307*, 955−973.
(83) Schott, J.; Pokrovsky, O. S.; Oelkers, E. H. The link between mineral dissolution/precipitation kinetics and solution chemistry. *Thermodynamics and Kinetics of Water−Rock Interaction*; Walter de Gruyter GmbH & Co KG, 2009; Vol. *70*, pp 207−258.
(84) Palandri, J. L.; Kharaka, Y. K. *A compilation of rate parameters of water-mineral interaction kinetics for application to geochemical modeling.* 70 (U.S. Geological Survey, Open File Report 2004), 2004.
(85) Iler, R. K. *The Chemistry of Silica: Solubility, Polymerization, Colloid and Surface Properties, and Biochemistry*; Wiley, 1979.
(86) Icenhower, J. P.; Dove, P. M. The dissolution kinetics of amorphous silica into sodium chloride solutions: effects of temperature and ionic strength. *Geochim. Cosmochim. Acta* **2000**, *64*, 4193−4203.
(87) Rimstidt, J. D.; Barnes, H. L. The kinetics of silica-water reactions. *Geochim. Cosmochim. Acta* **1980**, *44*, 1683−1699.
(88) Tester, J. W.; Worley, W. G.; Robinson, B. A.; Grigsby, C. O.; Feerer, J. L. Correlating quartz dissolution kinetics in pure water from 25 to 625°C. *Geochim. Cosmochim. Acta* **1994**, *58*, 2407−2420.
(89) Daval, D.; Hellmann, R.; Saldi, G. D.; Wirth, R.; Knauss, K. G. Linking nm-scale measurements of the anisotropy of silicate surface reactivity to macroscopic dissolution rate laws: New insights based on diopside. *Geochim. Cosmochim. Acta* **2013**, *107*, 121−134.

DOI: 10.1021/acs.jpcc.9b05491
J. Phys. Chem. C 2019, 123, 24520−24532

(90) Daval, D.; Hellmann, R.; Martinez, I.; Gangloff, S.; Guyot, F. Lizardite serpentine dissolution kinetics as a function of pH and temperature, including effects of elevated pCO_2. *Chem. Geol.* **2013**, *351*, 245−256.
(91) Bottero, J. Y.; Cases, J. M.; Fiessinger, F.; Poirier, J. E. Studies of hydrolyzed aluminum chloride solutions. 1. Nature of aluminum species and composition of aqueous solutions. *J. Phys. Chem.* **1980**, *84*, 2933−2939.
(92) McHardy, W. J.; Thomson, A. P. Conditions for the formation of bayerite and gibbsite. *Mineral. Mag.* **1971**, *38*, 358−368.
(93) Schott, J.; Berner, R. A. X-Ray Photoelectron studies of the mechanism of iron silicate dissolution during weathering. *Geochim. Cosmochim. Acta* **1983**, *47*, 2233−2240.
(94) Chou, L.; Wollast, R. Study of the wctathering of albite at room temperature and pressure with a fluidized bed reactor. *Geochim. Cosmochim. Acta* **1984**, *48*, 2205−2217.

DOI: 10.1021/acs.jpcc.9b05491
J. Phys. Chem. C 2019, 123, 24520−24532

9.4 L 4: µLaue A. Davydok *et al.*, Materials and Design **108** 68 (2016)

Materials and Design 108 (2016) 68–75

Contents lists available at ScienceDirect

Materials and Design

journal homepage: www.elsevier.com/locate/matdes

Analysis of the full stress tensor in a micropillar: Ability of and difficulties arising during synchrotron based µLaue diffraction

Anton Davydok [a], Balila Nagamani Jaya [a], Odile Robach [b,c], Olivier Ulrich [b,c], Jean-Sébastien Micha [b,c], Christoph Kirchlechner [a,d,*]

[a] Max-Planck-Institut für Eisenforschung, Department Structure and Nano-/Micromechanics of Materials, D-40237 Düsseldorf, Germany
[b] Université Grenoble Alpes, Grenoble F-38000, France
[c] CEA/INAC and CNRS, SPrAM, 17 rue des Martyrs, Grenoble F-38054, France
[d] University of Leoben, Department Material Physics, A-8700 Leoben, Austria

HIGHLIGHTS

- Analysis of all deviatoric strain (stress) components in a micron sized pillar during in situ micro-compression
- Calculation of the full stress tensor by the assumption of stress free pillar surfaces
- Comparison of stress component in loading direction with the engineering stresses derived from the load cell

GRAPHICAL ABSTRACT

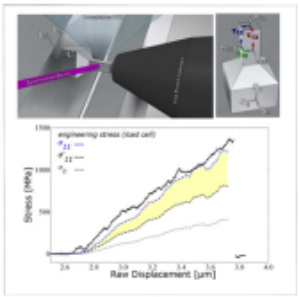

ARTICLE INFO

Article history:
Received 27 April 2016
Received in revised form 20 June 2016
Accepted 23 June 2016
Available online 24 June 2016

Keywords:
In situ micro compression
Experimental micromechanics
Synchrotron radiation
Laue microdiffraction

ABSTRACT

The full strain tensor present in a $2 \cdot 2 \cdot 6\ \mu m^3$ sized germanium micro pillar was measured by X-ray microdiffraction Laue during in situ loading. Initial orientation gradients, residual strains and diffraction peak streaking were found negligible. The obtained strain values from Laue pattern analysis have been used to calculate the deviatoric stress tensor. The collected patterns show a pillar rotation and a build-up of shear stress components acting parallel to the contact surface of the flat punch, which is both an indication for misalignment of the sample and counter-body during loading. Based on the assumption of stress free pillar-side faces the full stress tensor was further evaluated. The stresses acting in loading direction derived from the Laue patterns compared to engineering stresses calculated from the continuously recorded signal of the load cell are in agreement within 9%. The discrepancy is explained by the initial experimental misalignment of the pillar with respect to the counter-body. Finally, difficulties arising during such an in situ experiment are discussed.

1. Introduction

The size dependence of mechanical properties at the micro- and nanometer length-scale has gained enormous attention during the last decade due to the trend of continuous downscaling of components in

* Corresponding author at: Max-Planck-Institut für Eisenforschung GmbH, Max-Planck-Str. 1, 40237 Düsseldorf, Germany.
E-mail address: kirchlechner@mpie.de (C. Kirchlechner).

http://dx.doi.org/10.1016/j.matdes.2016.06.098
0264-1275/

micro- and nano-electronics as well as decreasing internal length scales in structural materials. Among all types of crystalline materials containing lattice defects, a transition from a bulk-like to small scale mechanical behavior is observed. This size-effect is manifested by novel properties like high strength [1–4] or a size dependent brittle-to-ductile transition [5], which are not observed in bulk. Life time and probability of failure in micron-sized devices for electronic applications are strongly connected to the internal defect structures at small length scales. Thus, a fundamental understanding of the impact of a limited number of defects on the mechanical endurance of micron sized objects is vital for future applications.

In situ micromechanical investigations of materials at small length scales are challenging, but provide unique information on the mechanical behavior of constituents composing real microstructures. Typically, the global stress-strain response of a focused ion beam (FIB) milled micro-pillar is monitored by a loading instrument. However, local stress heterogeneities (due to e.g. the internal grain structure, dislocation pile-ups or loading constraints etc.) complicate the analysis of such experiments. Due to experimental uncertainties [6], lateral constraints [6,7] and microstructural inhomogeneity [8], the local elastic strains remain unknown. Therefore it is challenging to estimate the impact of applied stress on the underlying defects in micron sized samples. Thus, techniques which are able to probe the local elastic strains and resolve the full stress tensor during loading are required.

There are several techniques for strain measurements of single crystalline small scale objects that have been reported in literature. Local strain determination can be realized using scanning electron microscopy (SEM), transmission electron microscopy (TEM) and performing X-ray diffraction experiments. Various techniques and their strain sensitivity are summarized in Table 1, whereas the reader is referred to the mentioned publications for further information.

Common drawback of all electron-based techniques is the surface sensitivity and/or requirement of electron transparent samples for TEM investigations, which often leads to a strain relaxation during specimen preparation. During monochromatic X-ray diffraction measurements at fixed photon-energies sample rotation is required, which could (i) lead to significant vibrations of the loading rig and (ii) to a change in illuminated volume. (i) clearly should be avoided as it often results in an unintended sample destruction. Instead of rocking to prevent (i) an energy scanning using a tunable monochromator could be performed, however, also in this case a constant illuminated volume cannot be assured. An alternative way to perform local strain measurements within selected grains of a microstructure is polychromatic beam X-ray micro diffraction Laue (μLaue) [16–18], which is able to probe the strains with a sensitivity of $5 \cdot 10^{-5}$ [14] at a spatial resolution of 500 nm [19]. In a μLaue standard experiment the spot energy is unknown, however, an estimation for spot energies can be made during Laue pattern analysis and indexation. Thus, only the direction of reciprocal lattice vectors is determined but not their length, which gives access to the deviatoric strains only. Due to the use of a wide energy bandpass all illuminated crystals automatically fulfill Bragg's law and thus, no sample rotation is required. As a consequence also unintended sample rotations do not cause the loss of the diffracted signal as in case of coherent diffraction, which makes μLaue a perfect tool for in situ observations [20].

Capabilities of μLaue diffraction for strain measurements are well-known and were demonstrated on several different systems in the past. Examples comprise the stress measurements during thermal cycling of an Al film [21], local stresses in a buckled W film [22,23], full stress tensor measurements in micro-electro-mechanical-systems (MEMS) [24] or of ion-implanted UO_2 [25]. Also in the field of semi-conductors Laue diffraction was employed to probe local strains controlling the optical properties [26].

While Laue diffraction is frequently used to monitor the deformation of micron sized compression pillars in situ [20,27–29] to study the storage of geometrically necessary dislocations (GNDs) and geometrically necessary boundaries (GNBs), no analysis on the stress tensor is reported. Thus, aim of this work is to extract the stresses present in a micron sized compression pillar during loading in order to explore difficulties arising during in situ micro-deformation of micron sized objects. Therefore, the obtained Laue patterns are used to evaluate the deviatoric strain tensor. Based on the assumption of stress free pillar side surfaces the full stress tensor present in the sample is calculated. Finally, the stress obtained from Laue pattern analysis is compared to the nominal applied engineering stress along the loading direction during the micro-compression experiment.

2. Experimental setup

Rectangular, nominally $2 \cdot 2 \cdot 6\,\mu m^3$ sized germanium micro pillars were prepared by FIB milling from an ⟨111⟩ oriented germanium wafer, applying coarse (2 nA) and fine (100pA) 30 keV Ga^+ ion currents using a Zeiss Auriga® cross-beam microscope. A SEM image of a selected pillar is shown in Fig. 1a. The surface finish of the pillar is poor, however, as shown by Maaß and co-workers [30] a poor surface quality does not necessarily imply a high crystalline defect density.

The experiments were performed at the μLaue station of the French CRG-IF BM32 beamline at the European Synchrotron Radiation Facility (ESRF, Grenoble, France) [19]. The reflection mode of the μLaue setup was used. The sample stage together with the deformation device was tilted by 40° with respect to the incoming synchrotron beam. A polychromatic X-ray beam with an energy bandpass of 5–22 keV (pink-beam) was focused down to 500 · 500 nm using Kirkpatrick–Baez mirrors [19]. Sample alignment was assisted by optical microscopy and X-ray fluorescence mapping (see Fig. 1b) prior to the mechanical testing. During μLaue pattern acquisition the optical microscope was brought into a remote position and a MAR 165 mm CCD detector (now rayonix) with $2048 \cdot 2048$ pixel^2 with a pixel size of 80 μm was placed 60.973 mm away from the sample (determined during setup calibration).

A bulk and strain-free Germanium wafer was also used to calibrate the μLaue diffraction setup, namely the CCD position and tilts with respect to sample position and incoming beam direction. The Laue diffraction patterns were analyzed following peak search and index refinement procedures with the LaueTools software package [31] developed at the beamline. As first step, a blurred image was created by digital

Table 1
Various non-destructive methods to measure lattice strains in small dimensions.

Method	Instrument	Probe	Lateral resolution [nm]	Strain resolution [1]	Comments	Ref.
Kossel microdiffraction	SEM	Electrons	2…50	$2 \cdot 10^{-4}$		[9]
High resolution electron backscatter diffraction (EBSD)	SEM	Electrons	~5	$2 \cdot 10^{-4}$	Reference pattern required	[10]
Convergent-beam electron diffraction	TEM	Electrons	<2	$2 \cdot 10^{-4}$		[11]
High-resolution TEM	TEM	Electrons	0.5	$1 \cdot 10^{-4}$		[12]
Dark-field-electron holography	TEM	Electrons	2–4	$2 \cdot 10^{-4}$	Reference wave from undistorted material?	[11]
Coherent X-ray diffraction	Synchrotron	Photons	<30	$< 1 \cdot 10^{-4}$	A priori knowledge of the grain shape	[13]
μLaue diffraction	Synchrotron	Photons	500 - 500	$< 5 \cdot 10^{-5}$		[14]
Laue DIC	Synchrotron	Photons	500 - 500	10^{-5}	Reference pattern required	[15]

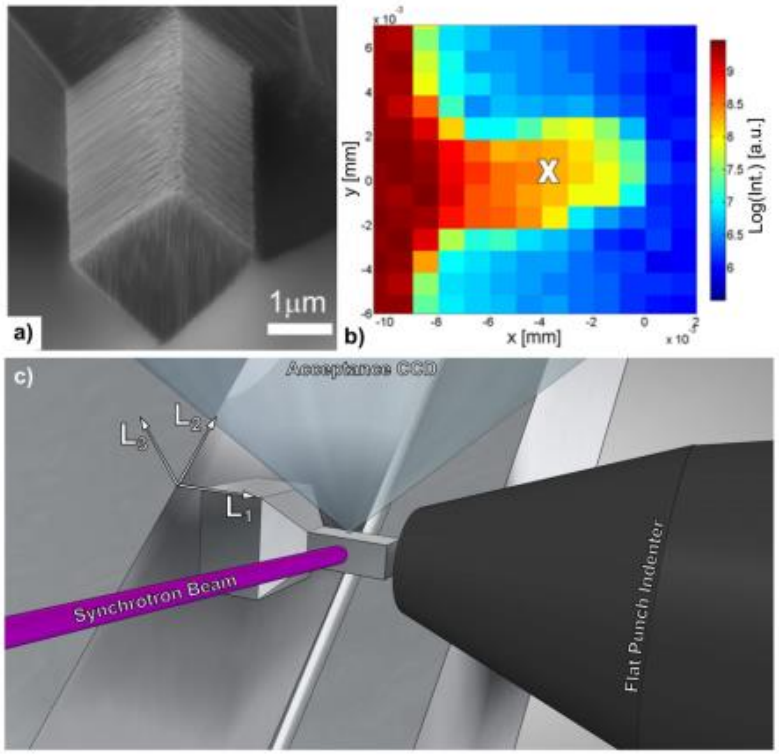

Fig. 1. a) SEM micrograph of a Ge micropillar; the poor surface quality is clearly visible. b) Fluorescence map recorded close Ge K-edge (white cross showing the position during in situ measurements). c) Schematic showing the in situ setup including the laboratory coordinate system, the incoming synchrotron beam and the angular acceptance of the detector.

filtering (minimum filter). The blurred image was subtracted as background in order to obtain local maxima as initial guesses of peaks positions for subsequent refinement with a 2D elliptical Gaussian model as peak shape. This procedure yielded 80–100 reflections which were then used for indexation, i.e. to assign a crystallographic reflection (*hkl*) to each individual spot. Finally, during unit cell orientation and strain refinement the deviatoric lattice strains components were obtained.

Mechanical loading was done by a custom built straining device dedicated to compression, tensile, bending and bending fatigue experiments [32]. The provided force resolution is below 10 µN inside the experimental hutch at the ESRF. Fig. 1c shows a detailed view on the germanium micro-pillar, the flat punch indenter, the incoming pink-beam and accepted diffracted beams. More details on the used instrumentation are provided elsewhere [19,32].

Two different operation modes were used during the experiment: (i) deformation scans, revealing local information during mechanical deformation; (ii) raster scans, imaging the global changes in the sample in an unloaded state:

(i) During deformation scans, applied force and displacement of flat punch, as well as Laue patterns were recorded simultaneously. The acquisition time for recording a signal Laue pattern was composed of 0.1 s exposure time and readout time of the detector and in total took 4.5 s. The X-ray beam was focused on a single position on the pillar measured with submicron precision and is marked in the fluorescence scan in Fig. 1b. Subsequently, the sample was deformed in displacement controlled mode with a strain-rate of $3.3 \cdot 10^{-4}\,s^{-1}$.

(ii) To capture global changes of the orientation, residual stresses and peak shape a raster scan along the L_1 and L_2 axis with a step size of 1 µm was performed prior and post the mechanical experiment. To avoid interference from vibrations of the translation motors, such scans are carried out only in an unloaded state. Also, the flat-punch indenter tip was retracted by at least 3 µm before these scans.

3. Results & interpretation

3.1. Pillar microstructure after FIB milling

Initially, i.e. after FIB milling and before deformation, the pillar does not exhibit pronounced orientation gradients (Fig. 2a). The point to origin misorientation angle is calculated similar as presented in [33] and in all cases is below 0.0075°. This indicates that there are essentially no geometrically necessary dislocation (GNDs) and no geometrically necessary boundaries (GNBs) present here, which is in contrast to previous observations in metallic micro pillars by Maaß [34].

Also the residual deviatoric stresses across the pillar are analyzed as exemplarily shown for the σ_{11}' component (loading direction) in Fig. 2c. The stresses locally vary between 0 and 25 MPa, which is close to the resolution limit of roughly 10 MPa, assumed based on a strain resolution of 10^{-4}.

The main intensities of the Laue spots exhibit a circular peak shape. Representative peaks are shown in Fig. 3b and c both recorded at the position for in situ loading. The peaks are circular in the unloaded state across the entire sample, as shown in Fig. 3b, c for the (112) diffraction spot. The variation in peak FWHM is <0.4 pixels being 15% for the (112) peak width across the entire sample. At some positions slight tails (not visible in the color coding of Fig. 3 and not captured by the Gaussian fit

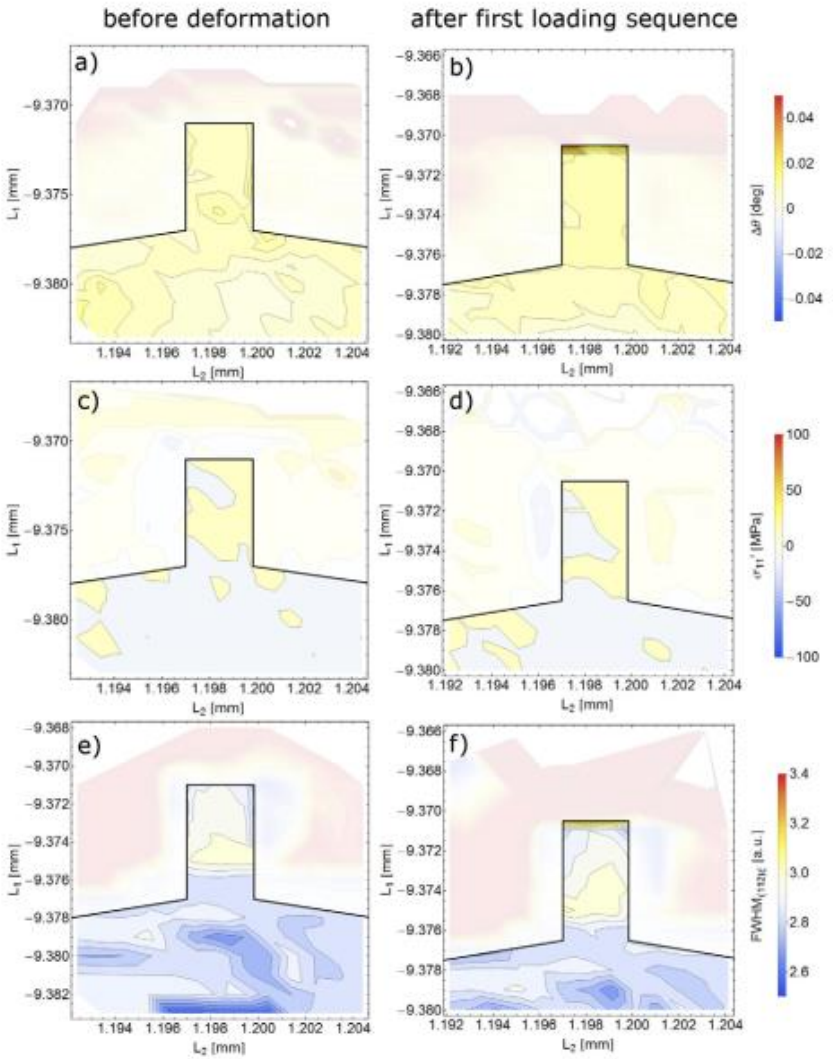

Fig. 2. Several measures extracted from the mesh scans before and after the first loading sequence. The pillar geometry is schematically shown based on the fluorescence signal recorded during the experiment. (a, b) Point to origin misorientation with a contour step size of 25·10^{-3}; (c,d) residual deviatoric stress component σ_{11}' in the unloaded state with contour step size of 25 MPa. (d, e) Full-width-at-half-maximum (FWHM) of the major peak axis (ξ) of the (112) diffraction spot with a step size of 0.05 [pxl].

presented in Fig. 2e) are visible. This behavior is similar to the one previously observed by Maaß and co-workers in silicon [30]. In our case, however, since the diffracted intensity of the tails with respect to the total diffracted intensity per spot is $<10^{-3}$ it can be assumed that this is not stemming from a volumetric effect (e.g. geometrically necessary dislocations) but rather by a thin surface layer, or some signature of X-ray beam tail. Possible candidates for thin layers are a FIB introduced damage layer [35] or a redisposition layer, as also indicated by the SEM images (see Fig. 1a).

Thus, from the X-ray scattering Laue point of view the pillar neither possesses orientation gradients nor residual stresses or peak streaking in the as-formed state.

3.2. In situ loading experiment

The mechanical experiment was performed in displacement controlled mode up to varying maximum displacements. The engineering stress is defined as the applied load over the initial cross-section of the pillar. During the first loading sequence (Fig. 4a) the sample is deformed elastically only, i.e. no plastic hysteresis is found after unloading. After a mesh scan past the first loading sequence a second one was performed to an increased maximum displacement, which led to a catastrophic failure of the sample. Therefore, neither unloading curves nor post-mortem analysis of the sample after the second loading sequence is available.

During mechanical loading several changes of the Laue pattern can be observed and are exemplarily shown in Fig. 3: (i) a rotation of the entire pattern as indicated by the trajectories, (ii) a relative shift of the individual spots and (iii) peak streaking (Fig. 3d, e).

3.2.1. Crystal rotation

The crystal rotation is manifested by a collective peak shift. The trajectories of the individual Laue spots (Fig. 3a, arrows) as well as the calculated orientation matrix were used to identify the rotation axis and angle. From both, a maximum rotation of 1.1° within the first deformation step to a maximum engineering stress of 425 MPa

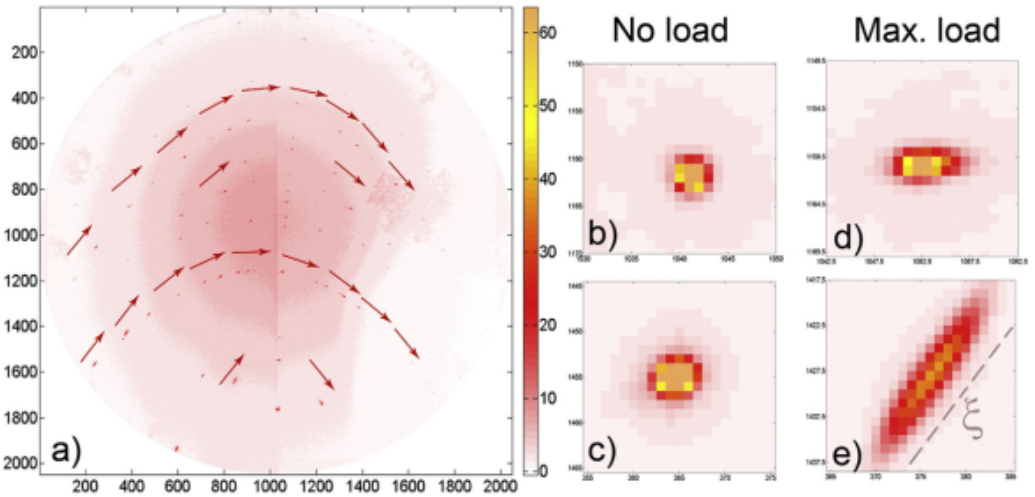

Fig. 3. (a) Entire Laue pattern recorded in the loaded state. Trajectories of Laue peaks and streaking direction ξ are indicated by arrows. Representative Laue spots in the unloaded state close to the detector center (b) and off-centered (c) as well as during loading (d, e) are shown.

was determined. The rotation of the sample center is induced by a misalignment of the flat punch indenter with respect to the pillar top surface. The unintentional misalignment is stemming from a miscut of the top surface of the pillar. The miscut originates from a deviation of our standard experimental procedure described in the supporting online material of [3], which typically prevents similar experimental uncertainties. However, for this sample milled in a massive Ge wafer the aforementioned approach was unfortunately not possible.

The sensitivity of μLaue diffraction allows tracking rotations well below 0.01°, hence, this kind of in situ experiments directly point to imperfections like misalignments of the experiments. However, similar small misalignments as observed here (1.1°) are difficult to be detected by in situ SEM setups. Even if the experiments are performed with the highest care, such misalignments cannot easily be corrected and, hence, might be present in all in situ compression experiments.

It is noteworthy that after the first unloading (see stress vs. displacement curve in Fig. 3a) the entire pattern rotation recovered resulting in a very similar misorientation map as before (compare Fig. 2a and b). This reversibility supports the findings of the stress-displacement diagram of a purely elastic loading during the first loading sequence.

During the second loading the sample rotation increases further until fracture of the sample.

3.2.2. Elastic strains

The relative shift of spots with respect to each other is a sign of deviatoric strains, which were analyzed by the standard Laue pattern analysis using the LaueTools software [31]. The sample coordinate system S is defined according to the schematic(s) presented in Fig. 5d with S_1 as compression axis. From the components of the deviatoric strain tensor obtained by Laue diffraction, the deviatoric stresses σ' can be calculated applying the single crystalline elastic stiffness tensor of Ge [36].

During the first loading sequence (shown in Supporting online material Fig. S1) the deviatoric component σ'_{11} reaches up to 120 MPa. The increase is thereby linear and the unloading behavior mainly follows the loading behavior. Both the other normal stress components remain below 50 MPa. The shear components are zero within the resolution of the method. All stress components entirely recover, which is also evident in Fig. 2c–d presenting the unchanged distribution of residual stresses in the unloaded state (σ'_{11} component). Fig. 5 shows the evolution of the deviatoric components during the second loading sequence. Similar to the first loading, the shear stresses are not affected at low displacements (<3 μm), however – in contrast to an ideal loading experiment – non-zero shear components build up being pronounced at displacements > 3.2 μm. Noteworthy, the shear components acting parallel to the contact surface are affected most, while the other one essentially stays zero. A more detailed discussion on the origin of the non-zero shear stresses is provided in the following discussion section of this paper.

Finally, the deviatoric stress data allows for calculating the full stress tensor composed of the hydrostatic stress tensor ($\sigma_H \cdot I_3$) and the accessible deviatoric tensor, according to:

$$\underline{\underline{\sigma}} = \begin{pmatrix} \sigma_{11} & \tau_{12} & \tau_{13} \\ - & \sigma_{22} & \tau_{23} \\ - & - & \sigma_{33} \end{pmatrix} = \begin{pmatrix} \sigma_H & 0 & 0 \\ 0 & \sigma_H & 0 \\ 0 & 0 & \sigma_H \end{pmatrix} + \begin{pmatrix} \sigma'_{11} & \tau_{12} & \tau_{13} \\ - & \sigma'_{22} & \tau_{23} \\ - & - & \sigma'_{33} \end{pmatrix} \tag{1}$$

Since the side surfaces of the pillar need to be stress free, the only non-zero stress component of the full stress tensor is the σ_{11}, i.e. $\sigma_{22} = \sigma_{33} = 0$.[1] This gives access to the hydrostatic component σ_H, which is calculated as the mean of the analyzed deviatoric stress components σ'_{22} and σ'_{33} here. Thus, the stress in loading direction σ_{11} derived from the deviatoric strains obtained from the Laue patterns analysis is:

$$\sigma_{11} = \sigma'_{11} + \frac{-\sigma'_{22} - \sigma'_{33}}{2} \tag{2}$$

For further analysis we compare σ_{11} (from the Laue diffraction experiment) with the measured engineering stresses (derived by the force measured via the load cell) during the compression experiment (Fig. 4b). Besides the engineering stress-time curve, all components of Eq. (2), namely σ_{11}, σ'_{11}, and $^1/_2(\sigma'_{22} + \sigma'_{33})$ are also plotted. Even though significantly deviating at low stresses, the deviation of the σ_{11} from the engineering stress gets increasingly smaller with a relative error as low as 2%. On average above a cut-off stress of 500 MPa, the deviation from the Laue-based σ_{11} and the engineering stress derived via load cell is within 9%.

[1] This assumption only holds true for regions close to the sample surface.

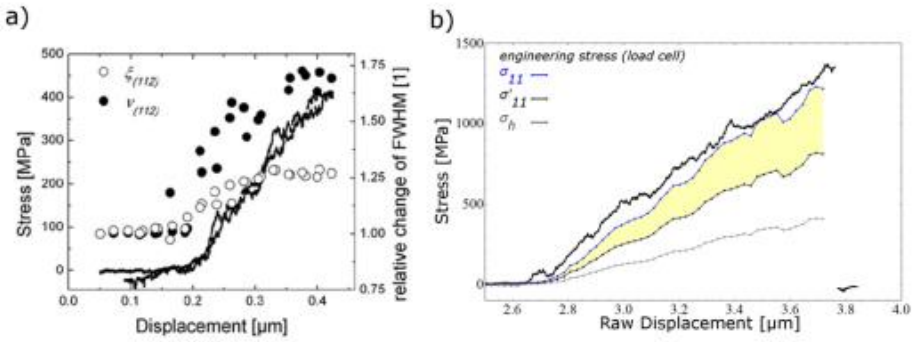

Fig. 4. a) Stress vs. punch displacement curve of the first loading sequence (continuous line) and peak widths of the (1 1 2) Laue reflection in both directions (ξ,ν being perpendicular to ξ). b) Engineering stress and several stress components (σ_{11},σ'_{11},σ_h) extracted from the Laue patterns as a function of punch displacement.

3.2.3. Laue peak streaking

During deformation several Laue spots are elongated with an elliptical footprint exhibiting a major streaking direction ξ (see Fig. 2e). Thereby, Laue spots behave differently: the peak shape of diffraction peaks captured at the detector center show less streaking (Fig. 3d) than off-centered peaks (Fig. 3e). A detailed analysis of the (1 1 2) peak width in both, the main streaking axis ξ and the minor axis ν is presented in Fig. 4a. During loading, a very pronounced streaking with a relative peak width increase by the factor of 1.75 is observed. The peak width increase is not linear but seems to start saturating at higher displacements. The saturation of the peak-width increase strongly supports the idea of a miscut of the pillar top surface. Noteworthy, the peak shape upon unloading follows the loading path and entirely recovers. The fact, that neither the load displacement curves, the residual stress components, the orientation distribution across the pillar, nor the diffraction peak shape shows irreversible changes documents the purely elastic loading of the sample in the first cycle and an absence of plastic accommodation of the misalignment.

Thus, we assume that the diffraction peak streaking originates from elastic bending of the sample only. This is consistent for materials with a high strength/stiffness ratio as previously discussed in [37]. The high strength to stiffness ratio of germanium allows for detectable elastic lattice curvatures in 2 µm sized compression pillars and therefore, a meaningful GND analysis as for instance shown in [38] is generally prevented in this sample.

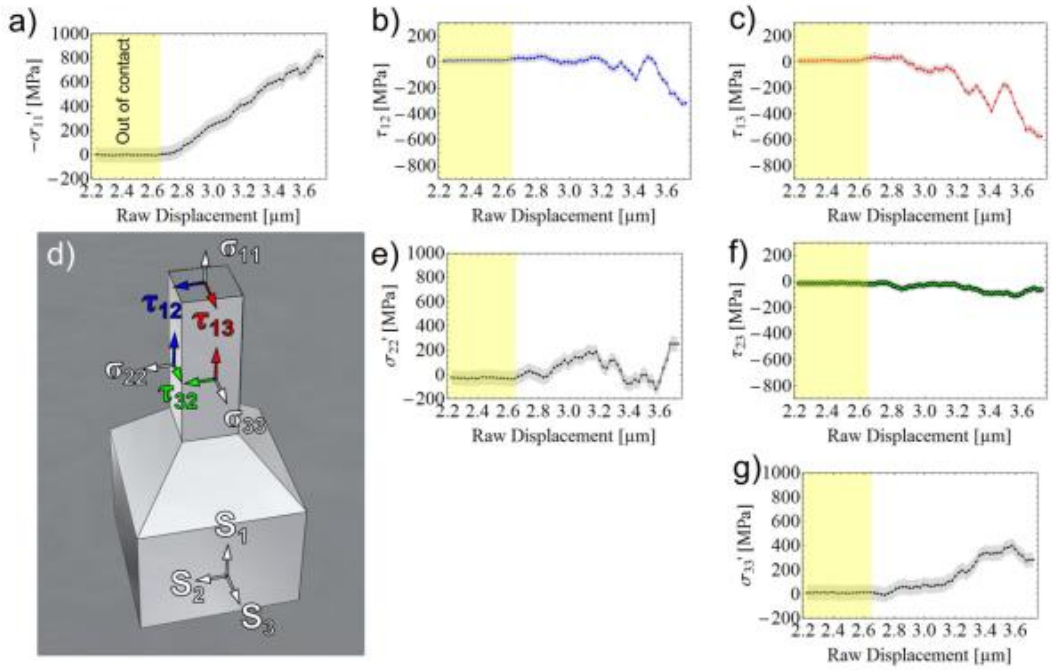

Fig. 5. Analyzed deviatoric stress components from in situ µLaue diffraction as a function of raw punch displacement (second loading sequence). a) σ_{11}', b) τ_{12}, c) τ_{13}, d) corresponding schematic of the pillar and its sample coordinate system S, e) σ_{22}', f) τ_{23} and g) σ_{33}'. The gray shaded region indicates a strain resolution of $5\cdot10^{-4}$, which is assumed to be a worst case scenario here. Yellow region corresponds to punch out of contact of the pillar.

As mentioned above, all data captured during the first deformation sequence to a maximum engineering stress of 425 MPa do not indicate any plastic deformation or phase transition of the Ge micropillar. Also a raster scan in between the first and the catastrophic second deformation is presented in Fig. 2b, d, e and supports this finding. The entire pillar shows a maximum point to origin misorientation of $2.5 \cdot 10^{-3}$°, which is comparable to the initial misorientations. Unfortunately, due to the loss of the sample after its fracture data after the second cycle are not available.

3.3. After loading sequence

The mesh scans performed after the first loading sequence suggest that neither the misorientation across the sample, nor the stress distribution and peak width changed during loading and we therefore assume that the sample had globally been deformed elastically only.

4. Discussion

4.1. Origin of shear stress

In an ideal compression experiment the buildup of shear stresses as observed here is not expected. However, experimental imperfections can cause the development of an undesired stress. To confirm the experimental findings accompanying finite element modelling (FEM) have been performed assuming a misaligned (2°) rigid indenter in frictionless contact. Isotropic material properties and pure elasticity was assumed. The stress tensor was then averaged over a $500 \cdot 500 \cdot 2000$ nm^3 sized rod similar to the illuminated volume during Laue diffraction. The simulations – as presented in the supporting online material Fig. S2 – confirm the absence of shear stresses at low displacements, and the build-up of shear stresses in the plane parallel to the top surface in case of misalignment.

This behavior is different to ductile materials (e.g. copper), where misalignments are quickly accommodated by plastic deformation and storage of GNDs. This was previously shown to result in the formation of a complicated sub-structure with several satellite peaks. In case of high strength brittle materials the stored elastic strain energy leads to catastrophic failure – as observed in the underlying work.

4.2. Experimental errors affecting the comparability of stresses analyzed via Laue and load cell

The stresses derived from Laue microdiffraction and the engineering stresses measured via the load cell deviate on average by 9%. Possible origins of the difference are manifold: errors in measuring (a) the pillar cross-section or (b) the force provided by the load cell, (c) strongly inhomogeneous stresses caused by misalignment (d) averaging over an inhomogeneous state and (e) bad peak fitting due to streaking. (a) The experimental error on the cross-sectional dimensions (a) is <1% for the applied imaging conditions (EHT 5 keV and 5.1 mm working distance in the Zeiss Auriga®) assuming a rectangular cross-section. (b) The force provided by the load cell is subjected to an experimental error < 2%, which has been proven by 5 standard weights in the range of 10 mN to 196 mN. The sum of uncertainties in the measured signal via a non-linear uncertainty propagation yields a possible error of 4% for the engineering stress, and in the order of 2% at maximum load for the stresses derived from Laue diffraction. This is still well below the observed discrepancy, which can be attributed to (c and d) the misalignment of the pillar top surface with respect to the flat punch, yielding considerable stress concentrations locally, which is differently averaged in both cases. As the misalignment is entirely accommodated by an elastic distortion, the relative differences of the engineering stress with respect to σ_{11} is continuously reduced being smallest at high applied loads.

4.3. Beam stability

Within this work no systematic investigation on the X-ray beam position stability during the experiment had been performed. However, it could be noted that the drift along the L_1 axis is <14 nm/h averaged over a 6 days period, which is negligible. However, the compliance (12 mN/μm) of the sample sitting on the load cell leads to a shift of the illuminated region of roughly 1 μm, i.e. the beam footprint moves 16% of the pillar length towards the top. As the entire sample had been homogenous prior and after the deformation scan we assume that this effect can be neglected.

The beam drift in L_2 direction is more pronounced. Even though the long term stability is comparable to the L_1 direction, along the L_2 axis a residual beam movement of ~1 μm during scanning could be observed even though an automatic table tilt inclination compensation was used. The results presented within this work are not affected by this beam drift, as in the worst case the beam footprint would fall of the sample and wouldn't interact with other materials. Thus, the in situ experiments and its homogenous illumination during the experiment prove that also the L_2 beam position was stable during this experiment.

5. Conclusions

We report the successful measurement of the full stress tensor in a $2 \cdot 2 \cdot 6$ μm^3 sized germanium pillar by X-ray μLaue diffraction during deformation. The aim of the experiment was to identify difficulties during local stress tensor measurements in micron sized compression pillars loaded in situ at the BM32 beamline of the ESRF. Germanium was used as model-material for evaluating the effects of experimental imperfections and uncertainties during the in situ mechanical test on the stress tensor determination at the micrometer scale. The findings can be summarized as below:

- The deviatoric stresses have successfully been measured. The deviatoric stress tensor has been used to calculate the normal stress acting along the compression direction based on the assumption of stress-free pillar side walls. Differences of 9% with respect to the engineering strain are partly addressed to misalignment and averaging of the inhomogeneous stress state. Surprisingly, the analysis of deviatoric stresses work even in severely (elastically) streaked Laue patterns.
- During deformation the sample rotates due to an initial experimental misalignment of the sample with respect to the flat punch indenter. The misalignment is of the order of 1.1° and causes a non-centrosymmetric loading. The misalignment causes the final fracture of the sample. While at low displacements no shear stresses are built up, significant shear stresses parallel to the contact surface are formed at higher flat punch displacements.
- The misalignment causes pronounced peak streaking in the loaded state which saturates at higher strains. Unloading leads to a complete reversibility of the peak streaking. The peak streaking is thus addressed to elastically caused lattice curvature.
- After elastic loading, neither the orientation distribution, nor residual stresses nor peak shape changed across the entire sample.

In the future we plan to perform similar experiments on metallic micropillars to investigate the acting shear stresses close to the leading dislocation of a dislocation pile-up, e.g. close to a grain or twin boundary.

Acknowledgement

The authors gratefully acknowledge the European Synchrotron Radiation Facility for allocation of the beamtime MA2096, as well as N. Malyar for assistance during the beamtime. This work was funded by the German Research Foundation (DFG) within the project KI-1889/1-1.

Appendix A. Supplementary data

Supplementary data to this article can be found online at http://dx.doi.org/10.1016/j.matdes.2016.06.098.

References

[1] M.D. Uchic, D.M. Dimiduk, J.N. Florando, W.D. Nix, Sample dimensions influence strength and crystal plasticity, Science 305 (2004) 986–989.
[2] J.R. Greer, J.T.M. De Hosson, Plasticity in small-sized metallic systems: intrinsic versus extrinsic size effect, Prog. Mater. Sci. 56 (2011) 654–724.
[3] M.D. Uchic, P.A. Shade, D.M. Dimiduk, Plasticity of micrometer-scale single crystals in compression, Annu. Rev. Mater. Res. 39 (2009) 361–386.
[4] O. Kraft, P.A. Gruber, R. Mönig, D. Weygand, Plasticity in confined dimensions, Annu. Rev. Mater. Res. 40 (2010) 293–317.
[5] F. Östlund, K. Rzepiejewska-Malyska, K. Leifer, L.M. Hale, Y. Tang, R. Ballarini, W.W. Gerberich, J. Michler, Brittle-to-ductile transition in uniaxial compression of silicon pillars at room temperature, Adv. Funct. Mater. 19 (2009) 2439–2444.
[6] C. Kirchlechner, J. Keckes, C. Motz, W. Grosinger, M.W. Kapp, J.S. Micha, O. Ulrich, G. Dehm, Impact of instrumental constraints and imperfections on the dislocation structure in micron-sized Cu compression pillars, Acta Mater. 59 (2011) 5618–5626.
[7] D. Kiener, C. Motz, G. Dehm, Micro-compression testing: a critical discussion of experimental constraints, Mater. Sci. Eng. A 505 (2009) 79–87.
[8] I. Tiba, T. Richeton, C. Motz, H. Vehoff, S. Berbenni, Incompatibility stresses at grain boundaries in Ni bicrystalline micropillars analyzed by an anisotropic model and slip activity, Acta Mater. 83 (2015) 227–238.
[9] D. Bouscaud, A. Morawiec, R. Pesci, S. Berveiller, E. Patoor, Strain resolution of scanning electron microscopy based Kossel microdiffraction, JAC 47 (2014) 1699–1707.
[10] A.J. Wilkinson, G. Meaden, D.J. Dingley, High-resolution elastic strain measurement from electron backscatter diffraction patterns: new levels of sensitivity, Ultramicroscopy 106 (2006) 307–313.
[11] M.J. Hÿtch, A.M. Minor, Observing and measuring strain in nanostructures and devices with transmission electron microscopy, MRS Bull. 39 (2014) 138–146.
[12] X.Y. Peng, L.Q. Zhou, X. Li, X.F. Tao, L.L. Ren, W.H. Cao, G.F. Xu, Strain study of gold nanomaterials as HR-TEM calibration standard, Micron 79 (2015) 46–52.
[13] V. Chamard, M. Allain, P. Godard, A. Talneau, G. Patriarche, M. Burghammer, Strain in a silicon-on-insulator nanostructure revealed by 3D X-ray Bragg ptychography, Sci. Report. 5 (2015).
[14] F. Hofmann, S. Eve, J. Belnoue, J.S. Micha, A.M. Korsunsky, Analysis of strain error sources in micro-beam Laue diffraction, Nuclear Instruments and Methods in Physics Research, Section A: Accelerators, Spectrometers, Detectors and Associated Equipment 660 (2011) 130–137.
[15] J. Petit, O. Castelnau, M. Bornert, F.G. Zhang, F. Hofmann, A.M. Korsunsky, D. Faurie, C. Le Bourlot, J.S. Micha, O. Robach, O. Ulrich, Laue-DIC: a new method for improved stress field measurements at the micrometer scale, J. Synchrotron Radiat. 22 (2015) 980–994.
[16] G.E. Ice, J.W.L. Pang, Tutorial on X-ray microLaue diffraction, Mater. Charact. 60 (2009) 1191–1201.
[17] A.A. MacDowell, R.S. Celestre, N. Tamura, R. Spolenak, B. Valek, W.L. Brown, J.C. Bravman, H.A. Padmore, B.W. Batterman, J.R. P, Submicron X-ray diffraction, Nuclear Instruments and Methods in Physics Research, Section A: Accelerators, Spectrometers, Detectors and Associated Equipment 467–468 (2001) 936–943.
[18] N. Tamura, R.S. Celestre, A.A. MacDowell, H.A. Padmore, R. Spolenak, B.C. Valek, N.M. Chang, A. Manceau, J.R. Patel, Submicron X-ray diffraction and its applications to problems in materials and environmental science, Rev. Sci. Instrum. 73 (2002) 1369.
[19] O. Ulrich, X. Biquard, P. Bleuet, O. Geaymond, P. Gergaud, J.S. Micha, O. Robach, F. Rieutord, A new white beam X-ray microdiffraction setup on the BM32 beamline at the European Synchrotron Radiation Facility, Rev. Sci. Instrum. 82 (2011) 033908–033916.
[20] R. Maaß, S. Van Petegem, H. Van Swygenhoven, P.M. Derlet, C.A. Volkert, D. Grolimund, Time-resolved Laue diffraction of deforming micropillars, Phys. Rev. Lett. 99 (2007).
[21] N. Tamura, A.A. MacDowell, R. Spolenak, B.C. Valek, J.C. Bravman, W.L. Brown, R.S. Celestre, H.A. Padmore, B.W. Batterman, J.R. Patel, Scanning X-ray microdiffraction with submicrometer white beam for strain/stress and orientation mapping in thin films, J. Synchrotron Radiat. 10 (2003) 137–143.
[22] N. Tamura, H.A. Padmore, J.R. Patel, High spatial resolution stress measurements using synchrotron based scanning X-ray microdiffraction with white or monochromatic beam, Mater. Sci. Eng. A 399 (2005) 92–98.
[23] P. Goudeau, P. Villain, N. Tamura, R.S. Celestre, H. Padmore, Residual stress mapping by micro X-ray diffraction: application to the study of thin film buckling, J. Phys. IV 12 (2002) (p.Pr6-409-Pr406-416).
[24] O. Perroud, R. Vayrette, C. Rivero, O. Thomas, J.-S. Micha, O. Ulrich, X-ray microbeam strain investigation on Cu–MEMS structures, Microelectron. Eng. 87 (2010) 394–397.
[25] M. Ibrahim, E. Castelier, H. Palancher, M. Bornert, S. Caré, J.S. Micha, Laue pattern analysis for two-dimensional strain mapping in light-ion-implanted polycrystals, JAC 48 (2015) 990–999.
[26] K. Guilloy, N. Pauc, A. Gassenq, P. Gentile, S. Tardif, F. Rieutord, V. Calvo, Tensile strained germanium nanowires measured by photocurrent spectroscopy and X-ray microdiffraction, Nano Lett. 15 (2015) 2429–2433.
[27] H.E. Weekes, V.A. Vorontsov, I.P. Dolbnya, J.D. Plummer, F. Giuliani, T.B. Britton, D. Dye, In situ micropillar deformation of hydrides in Zircaloy-4, Acta Mater. 92 (2015) 81–96.
[28] C. Kirchlechner, P.J. Imrich, W. Grosinger, M.W. Kapp, J. Keckes, J.S. Micha, O. Ulrich, O. Thomas, S. Labat, C. Motz, G. Dehm, Expected and unexpected plastic behavior at the micron scale: an in situ μLaue tensile study, Acta Mater. 60 (2012) 1252–1258.
[29] C. Marichal, H. Van Swygenhoven, S. Van Petegem, C. Borca, {110} slip with {112} slip traces in bcc Tungsten, Sci. Rep. 3 (2013).
[30] R. Maaß, D. Grolimund, S. Van Petegem, M. Willimann, M. Jensen, H. Van Swygenhoven, T. Lehnert, M.A.M. Gijs, C.A. Volkert, E.T. Lilleodden, R. Schwaiger, Defect structure in micropillars using X-ray microdiffraction, APL 89 (2006).
[31] J.S. Micha, LaueTools, Open Source Python Packages for X-ray MicroLaue Diffraction Analysis, 2015.
[32] C. Kirchlechner, J. Keckes, J.S. Micha, G. Dehm, In situ μLaue: instrumental setup for the deformation of micron sized sample, Adv. Eng. Mater. 13 (2011) 837–844.
[33] C. Kirchlechner, P.J. Imrich, W. Liegl, J. Pörnbacher, J.S. Micha, O. Ulrich, C. Motz, On the reversibility of dislocation slip during small scale low cycle fatigue, Acta Mater. 94 (2015) 69–77.
[34] R. Maaß, S. Van Petegem, J. Zimmermann, C.N. Borca, H. Van Swygenhoven, On the initial microstructure of metallic micropillars, Scr. Mater. 59 (2008) 471–474.
[35] D. Kiener, Z. Zhang, S. Šturm, S. Cazottes, P.J. Imrich, C. Kirchlechner, G. Dehm, Advanced nanomechanics in the TEM: effects of thermal annealing on FIB prepared Cu samples, Philos. Mag. 92 (2012) 3269–3289.
[36] W.A. Brantley, Calculated elastic constants for stress problems associated with semiconductor devices, J. Appl. Phys. 44 (1973) 534–535.
[37] C. Kirchlechner, W. Grosinger, M.W. Kapp, P.J. Imrich, J.S. Micha, O. Ulrich, J. Keckes, G. Dehm, C. Motz, Investigation of reversible plasticity in a micron-sized, single crystalline copper bending beam by X-ray mu Laue diffraction, Philos. Mag. 92 (2012) 3231–3242.
[38] G.E. Ice, R.I. Barabash, White beam microdiffraction and dislocations gradients, in: F. Nabarro, J. Hirth (Eds.),Dislocations in Solids, vol. 13 2007, pp. 499–601.

9.5 SL 5: µLaue J. Hektor et al., Scripta Materialia, **144**, 1 (2018)

Scripta Materialia 144 (2018) 1–4

Contents lists available at ScienceDirect

Scripta Materialia

journal homepage: www.elsevier.com/locate/scriptamat

Regular Article

Evidence of 3D strain gradients associated with tin whisker growth

Johan Hektor[a,*], Jean-Baptiste Marijon[b], Matti Ristinmaa[a], Stephen A. Hall[a], Håkan Hallberg[a], Srinivasan Iyengar[c], Jean-Sébastien Micha[d,e], Odile Robach[d,f], Fanny Grennerat[g], Olivier Castelnau[b]

[a] Division of Solid Mechanics, Lund University, Box 118, Lund 221 00, Sweden
[b] Laboratory PiMM, UMR CNRS 8006, Arts & Métiers ParisTech – CNAM, Paris, France
[c] Division of Materials Engineering, Lund University, Box 118, Lund 221 00, Sweden
[d] CEA-CNRS CRG-IF BM32 Beamline at ESRF, Grenoble, France
[e] Université Grenoble Alpes, INAC-SPrAM and CNRS, SPrAM and CEA, INAC-SPrAM, PCI, Grenoble, France
[f] Université Grenoble Alpes, INAC-SP2M and CEA, INAC-SP2M, NRS, Grenoble, France
[g] LGT Argouges, Éducation Nationale, Grenoble, France

ARTICLE INFO

Article history:
Received 18 August 2017
Received in revised form 18 September 2017
Accepted 18 September 2017
Available online 23 September 2017

Keywords:
Whiskers
Intermetallic compounds
Lead-free solder
X-ray diffraction

ABSTRACT

We have used Differential Aperture X-ray Microscopy (DAXM) to measure grain orientations and deviatoric elastic strains in 3D around a tin whisker. The results show strain gradients through the depth of the tin coating, revealing a higher strain deeper in the Sn layer. These higher strains are explained by the volume change occurring during growth of the intermetallic phase Cu_6Sn_5 at the interface between the Cu substrate and the Sn coating and at grain boundaries between Sn grains.

Tin whiskers are filamentary tin grains, only a few micrometers wide, but capable of growing to several millimeters in length. Whiskers grow spontaneously from tin coated surfaces and are electrically conducting. This may cause issues due to short-circuiting between components of electronic devices. A number of failures of electronic products due to short circuiting caused by whisker growth have been reported [1]. Until recently, the problem of whisker growth was effectively solved by using Pb–Sn alloys rather than pure Sn. However, due to environmental concerns this solution is no longer available. The ban on the use of lead in electronic devices and components, combined with the current trend of miniaturization, can be envisaged to increase the problems caused by whisker growth in the near future.

Tin whiskers have been an active area of research for over 60 years [2]. Despite this, several questions remain to be resolved regarding the mechanisms causing the whiskers to form and grow. The main hypothesis is that whiskers grow to relax stresses in the tin layer [2–5]. In the case of tin coatings on copper substrates, which is the system studied in this work, the stress is often associated with the volume change caused by the formation and growth of the intermetallic phase Cu_6Sn_5. It has been shown both experimentally [6–9] and by numerical simulations [10,11] that the growth of Cu_6Sn_5 at the interface between the Sn layer and the Cu substrate and at grain boundaries between Sn grains generates compressive stress in the tin layer. However, formation of intermetallic phases is not a necessary condition for whisker growth. Williams et al. [12] report whisker growth on Sn–W samples not forming intermetallic phases. Sobiech et al. [13,14] and Sun et al. [15] claim that the state of stress (tensile or compressive) is unimportant for whisker growth. Instead, they argue that whisker growth is driven by negative strain gradients in the tin layer, i.e. that the strain at the root of the whisker should be more tensile/less compressive than in the surrounding microstructure.

Previous X-ray diffraction studies of tin whiskers have used techniques that only provide spatial resolution in the two dimensions parallel to the Sn coating [4,14,16-18]. This means that the results are averaged over the penetration depth of the X-rays, which is typically on the order of 10 µm. By using Differential Aperture X-ray Microscopy (DAXM) [19–21] diffraction patterns from different depths in a sample can be reconstructed, thus obtaining spatial resolution in three dimensions. This makes it possible to study the grain structure and the strain field around whiskers in greater detail.

* Corresponding author.
E-mail address: johan.hektor@solid.lth.se (J. Hektor).

https://doi.org/10.1016/j.scriptamat.2017.09.030
1359-6462/

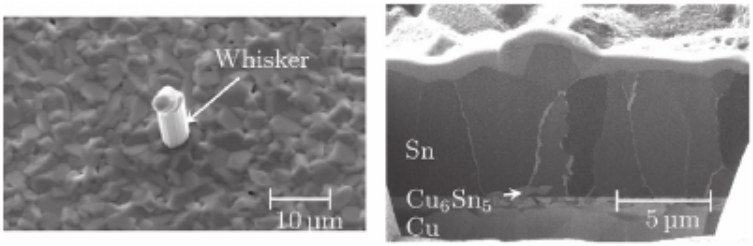

Fig. 1. Left: SEM image of the tin whisker selected for the microdiffraction measurements. Right: FIB cross section showing the columnar grain structure of the Sn layer and the formation of Cu_6Sn_5 at the Cu–Sn interface and at grain boundaries between Sn grains.

In the present work, tin coatings with a thickness of approximately 6.5 µm were deposited on polished 1 mm thick Cu sheets by means of electron beam evaporation. The microstructure of the Sn layer consists of columnar grains, typical for Sn coatings [7,22,23], see Fig. 1. After deposition, the samples were left to age for four months under ambient conditions during which whisker formation took place. Prior to the X-ray experiment, a suitable whisker was located using a scanning electron microscope, see Fig. 1.

The X-ray measurements were performed using the Laue microdiffraction setup on the CRG-IF BM32 beamline at the European Synchrotron Radiation Facility (ESRF) [24]. A polychromatic X-ray beam of 5–23 keV was focused to a spot of 0.7 µm size on the sample using a pair of Kirkpatrick-Baez (KB) mirrors. The sample was mounted at an angle of 40° with respect to the incoming beam and the diffracted X-rays were measured by a Mar CCD 2D detector comprising 2048 × 2048 pixels with a pixel size of about 80 µm, placed at an angle of 90° with respect to the incident beam. This geometry allowed for measurements of reflections in the range $41° \leq 2\theta \leq 139°$.

Conventional Laue microdiffraction can provide information about the crystal structure, orientation, and deviatoric elastic strains of a sample. Due to the penetration depth of the X-rays, the measurements are averaged over the volume probed by the beam [18]. Furthermore, strain determination is less accurate for grains below the surface of the sample. To remedy these limitations, a wire acting as a 'differential-aperture' can be placed between the sample and the detector [19], the experimental setup for DAXM measurements is illustrated in Fig. 2. During the measurement the wire is moved in 1 µm steps parallel to the sample surface and a diffraction pattern is measured for each wire position. By comparing the differential intensity of given detector pixels between two successive wire positions, it is possible to determine the scattering contribution as a function of depth along the beam [20]. The resolution in depth is essentially governed by the distances between the wire, the incident beam and the detector, by the number of steps scanned with the wire, the scanning direction, and (an effect neglected here) by the non-zero transmission of the wire edges [21].

The measured diffraction patterns were analyzed using the LaueTools software [25], being developed at the BM32 synchrotron beamline. The depth-resolved diffraction patterns can be indexed to obtain the crystallographic orientation of each of the grains illuminated by the X-rays. For each reciprocal unit cell an orientation matrix describing the orientation of the unit cell is obtained. From the orientation matrix the direct, $(a, b, c, \alpha, \beta, \gamma)$, and reciprocal, $(a^*, b^*, c^*, \alpha^*, \beta^*, \gamma^*)$, lattice parameters of the deformed crystal can be extracted. Following Ice and Pang [26], the elastic strains, in a frame attached to the crystal lattice and assuming small deformations, can be calculated as

$$\boldsymbol{\varepsilon} = \frac{1}{2}\left(\boldsymbol{A}\boldsymbol{A}_0^{-1} + \left(\boldsymbol{A}\boldsymbol{A}_0^{-1}\right)^T\right) - \boldsymbol{I}, \tag{1}$$

with $\boldsymbol{I}$ being the identity matrix and

$$\boldsymbol{A} = \begin{bmatrix} a & b\cos\gamma & c\cos\beta \\ 0 & b\sin\gamma & -c\sin\beta\cos\alpha^* \\ 0 & 0 & c\sin\beta\sin\alpha^* \end{bmatrix}. \tag{2}$$

the matrix $\boldsymbol{A}_0$ in Eq. (1) is constructed as in Eq. (2) but using the lattice parameters of an unstrained crystal. Unstrained Sn has a body-centered tetragonal structure with lattice parameters $a = b = 5.83$ Å, $c = 3.18$ Å and $\alpha = \beta = \gamma = 90°$ [4]. Since each Laue spot is related to a unique family of lattice planes, variation of the angles between Laue spots directly corresponds to the strain of the unit cell. However, due to the polychromatic beam used in the experiment, it is not possible to determine the volume of the unit cell. For this reason only the deviatoric part of the elastic strain tensor can be determined,

$$\boldsymbol{\varepsilon}^{dev} = \boldsymbol{\varepsilon} - \frac{1}{3}\mathrm{tr}(\boldsymbol{\varepsilon})\boldsymbol{I}, \tag{3}$$

where $\mathrm{tr}(\boldsymbol{\varepsilon})$ denotes the trace of the strain tensor. The effective strain, which is an invariant of the strain tensor, is defined by

$$\varepsilon_{eff} = \sqrt{\frac{2}{3}\boldsymbol{\varepsilon}^{dev} : \boldsymbol{\varepsilon}^{dev}}, \tag{4}$$

with : denoting the double contraction operator.

Two orthogonal lines, 8 µm and 16 µm long, intersecting at the whisker root, were scanned at steps of 0.8 µm using DAXM. In Fig. 3, the reconstruction in depth of four diffraction peaks belonging to two different Sn grains is shown. The diffraction patterns were reconstructed with 1 µm resolution in depth. The first two rows of the figure show Laue spots coming from a grain at the surface of the sample, while the lower two rows show spots from a grain beneath the

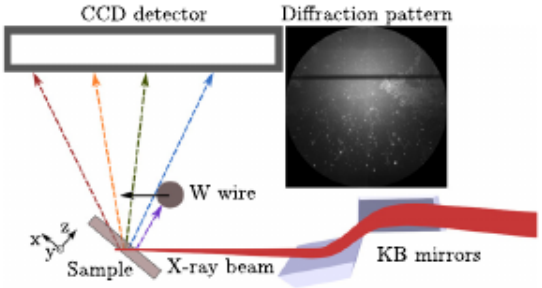

Fig. 2. Schematic view of the experimental setup for Laue microdiffraction. The W wire is only used during the 3D measurements. The wire is seen as a horizontal shadow on the diffraction pattern.

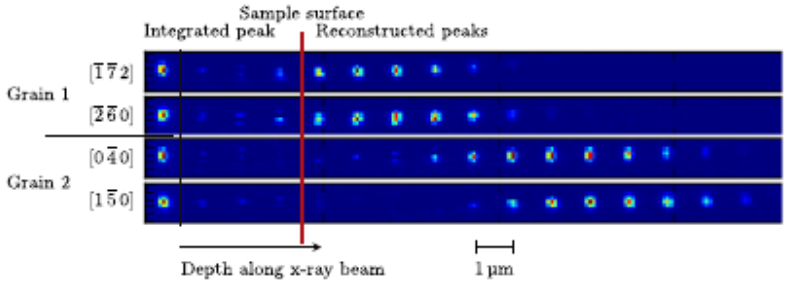

Fig. 3. Laue spots from two different Sn grains, reconstructed in depth along the X-ray beam. The red line indicates the sample surface. To the left the integrated peak is shown, i.e. the peak as measured by the detector when the W wire has been removed.

surface, positioned 5–10 µm below the surface along the incoming beam. Note that due to the 40° tilt of the sample, the depth along the beam is greater than the depth perpendicular to the surface. The slight vertical shift in peak position with increasing depth corresponds to an elongation of the integrated peak and is an indication of strain gradients or rotation within the grains.

In panels b and d in Fig. 4, 2D maps of the grain orientation and effective strain of the Sn grains in a region of 20 × 20 µm around the whisker are shown. The maps were obtained using conventional Laue microdiffraction, i.e. without depth resolution. The grains in the orientation map are color coded based on their Euler angles and it is assumed that the most intense diffraction spots come from the grains on the surface. From the orientation map we see that the grain size is about 3 µm with a few of the grains being elongated in one direction. This is in agreement with the SEM image in Fig. 1. The 2D map of the effective strain shows strain variations across grain boundaries. There are also some grains with strain gradients within the grain. This could be an indication of Cu_6Sn_5 growing at the grain boundaries, thus deforming the region around the grain boundary more than the central part of the grain.

Fig. 4a shows 3D plots of the grain orientations in the Sn coating from the DAXM measurements. It is seen that the DAXM measurements define a columnar grain structure in the tin layer, similar to that obtained by FIB, on a different region of the sample, in Fig. 1. The grain structure is also similar to previous FIB observations published in the literature [27–29]. The whisker grain does not extend all the way through the tin layer, but rather seems to sit on top of another grain. It is also seen that the grain boundaries of the whisker grain are inclined approximately 50° with respect to the surface. This is in good agreement with the growth model proposed by Sarobol et al. [30] in which whiskers form from surface grains with oblique grain boundaries. Note that only a small part of the whisker was scanned using DAXM, as seen in Fig. 4b most of the whisker is located at $x > 0$.

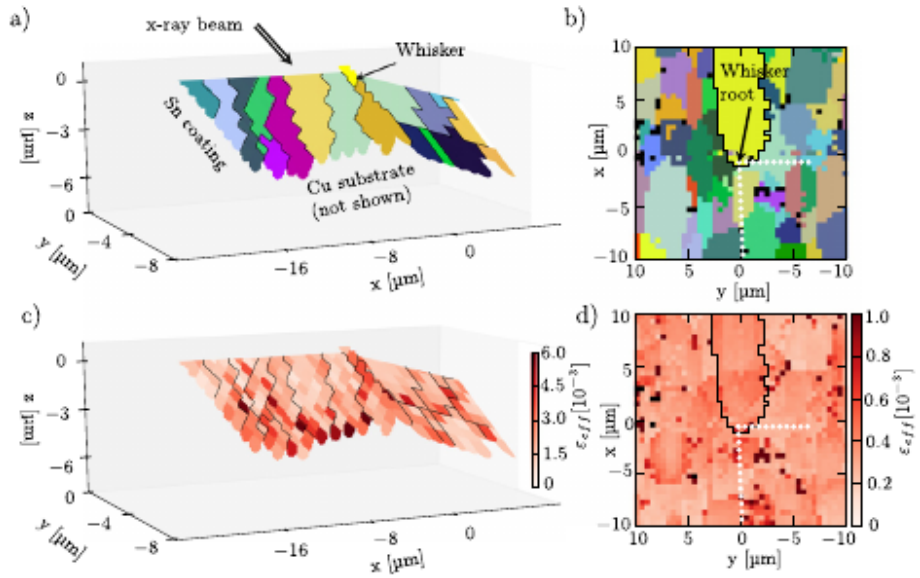

Fig. 4. a): 3D map showing the grain orientations in the Sn coating, obtained from the DAXM measurements. The grains are colored based on their Euler angles. The double lined arrow indicates the direction of the incoming X-ray beam. The coordinates are referring to the coordinate system in Fig. 2, with the origin placed in the whisker root. The surface of the sample is at $z = 0$. b): 2D map of the orientation of the Sn grains around the whisker, obtained by conventional Laue microdiffraction. The black pixels correspond to points where the indexing was not possible. The filled white circles indicate the positions scanned with DAXM. The yellow grain indicated by black lines is the whisker. c): 3D map of the effective strain in the Sn coating. d): 2D map of the effective strain in the region around the whisker.

By comparing the 2D surface map to the 3D map it is possible to identify the same grains in both maps. However, at some positions the 2D map shows a grain which is not located at the surface. For example, the pink grain in Fig. 4a is not found at the correct position in the 2D map in Fig. 4b. This is a consequence of the volume averaging of the diffraction pattern, as grains with a large probed volume will give intense diffraction spots even though they are located below the surface. This indicates that DAXM measurements are necessary even to get a correct representation of the grain structure at the surface. Depth resolution will also increase the credibility of the strain determination.

From the maps of the effective strain in Fig. 4c it is evident that the strain is low at the surface and higher deep in the sample, i.e. there exists a strain gradient in the depth direction. Again, due to the averaging over the probed volume, strain gradients through the depth of the coating can not be seen using conventional Laue microdiffraction. This observation further highlights the need for 3D spatial resolution. The high strain close to the bottom of the tin layer can be explained by the volume change due to formation of the intermetallic compound Cu_6Sn_5, occurring by diffusion of Cu atoms into the Sn layer. Regions of higher strain around some grain boundaries are also present. It is also seen in Fig. 4c that the whisker is not completely strain free, the part of the whisker that is above the sample surface has very low strains, but there is some strain in the root and in the grain below the root. In Fig. 1, Cu_6Sn_5 is forming along grain boundaries between Sn grains, and a Cu_6Sn_5 precipitate is present just below the whisker. Similar formation of Cu_6Sn_5 in the region studied with DAXM could explain the strain in the whisker root and around grain boundaries. High effective strain can also be an indication of plastic deformation. In fact, previous TEM studies of Sn coatings [6,7] reveal dislocation movement from the region close to the intermetallic phase towards the surface of the Sn layer. Furthermore, dislocation pile-ups at the surface can lead to cracking of the surface oxide, which is believed to be a precursor for whisker growth [3,5].

Even though only a single whisker was investigated, the results are consistent with those from other studies and so can be considered to be representative for other whiskers growing from pure tin coatings of similar thickness deposited by e-beam evaporation. The mechanisms behind whisker growth and formation of Cu_6Sn_5 are considered to be the same even for coatings manufactured using other techniques, although additional driving forces, such as additional stress due to plating impurities in the case of electroplating, might be present.

In this work the first successful 3D characterization using DAXM of the grain orientations and deviatoric strain around a tin whisker has been presented. The predicted microstructure, columnar Sn grains with the whisker grain having oblique grain boundaries, corresponds well with FIB studies of a different region on the sample, both in terms of grain shape and grain size. The whisker having angular grain boundaries is also in agreement with theoretical models for whisker formation. Furthermore, the measurements confirm the existence of strain gradients in the depth direction. The strain gradients are believed to be caused by the volume change associated with growth of the intermetallic phase Cu_6Sn_5. The high strain will lead to plastic deformation of the Sn layer and dislocations will pile up at the surface, leading to cracking of the surface oxide. Cracks in the surface oxide are believed to be potential nucleation sites for tin whiskers.

Acknowledgments

The authors would like to thank the company Evatec AG in Trübbach, Switzerland, for sample preparation. The funding provided by the Swedish Research Council (Vetenskapsrådet, VR) under grant nos. 2011-05512 and 2015-05390 is gratefully acknowledged. We are also grateful for the beamtime provided by the ESRF, beamline BM32.

References

[1] D. Bunyan, M.A. Ashworth, G. Wilcox, R.L. Higginson, R. Heath, C. Liu, Trans. Inst. Met. Finish. 91 (2013) 249–259.
[2] G.T. Galyon, IEEE Trans. Electron. Packag. Manuf. 28 (2005) 94–122.
[3] B.-Z. Lee, D. Lee, Acta Mater. 46 (1998) 3701–3714. https://doi.org/10.1016/S1359-6454(98)00045-7.
[4] W. Choi, T. Lee, K. Tu, N. Tamura, R. Celestre, A. MacDowell, Y. Bong, L. Nguyen, Acta Mater. 51 (2003) 6253–6261.
[5] K. Tu, J. Li, Mater. Sci. Eng. A 409 (2005) 131–139.
[6] E. Chason, N. Jadhav, W. Chan, L. Reinbold, K. Kumar, Appl. Phys. Lett. 92 (2008) 171901.
[7] K. Kumar, L. Reinbold, A. Bower, E. Chason, J. Mater. Res. 23 (2008) 2916–2934. https://doi.org/10.1557/JMR.2008.0351.
[8] W. Boettinger, C. Johnson, L. Bendersky, K.-W. Moon, M. Williams, G. Stafford, Acta Mater. 53 (2005) 5033–5050.
[9] G.T. Galyon, L. Palmer, IEEE Trans. Electron. Packag. Manuf. 28 (2005) 17–30.
[10] J. Hektor, M. Ristinmaa, H. Hallberg, S.A. Hall, S. Iyengar, Acta Mater. 108 (2016) 98–109.
[11] E. Buchovecky, N. Jadhav, A.F. Bower, E. Chason, J. Electron. Mater. 38 (2009) 2676–2684.
[12] M. Williams, K.-W. Moon, W. Boettinger, D. Josell, A. Deal, J. Electron. Mater. 36 (2007) 214–219.
[13] M. Sobiech, U. Welzel, E. Mittemeijer, W. Hügel, A. Seekamp, Appl. Phys. Lett. 93 (2008) 011906.
[14] M. Sobiech, M. Wohlschlögel, U. Welzel, E. Mittemeijer, W. Hügel, A. Seekamp, W. Liu, G.E. Ice, Appl. Phys. Lett. 94 (2009) 221901.
[15] Y. Sun, E.N. Hoffman, P.-S. Lam, X. Li, Scr. Mater. 65 (2011) 388–391.
[16] P. Sarobol, W.-H. Chen, A.E. Pedigo, P. Su, J.E. Blendell, C.A. Handwerker, J. Mater. Res. 28 (2013) 747–756.
[17] P. Sarobol, W.-H. Chen, A.E. Pedigo, P. Su, J.E. Blendell, C.A. Handwerker, J. Mater. Res. 28 (2013) 785.
[18] F. Pei, N. Jadhav, E. Buchovecky, A.F. Bower, E. Chason, W. Liu, J.Z. Tischler, G.E. Ice, R. Xu, J. Appl. Phys. 119 (2016) 105302.
[19] B. Larson, W. Yang, G. Ice, J. Budai, J. Tischler, Nature 415 (2002) 887–890.
[20] B.C. Larson, L.E. Levine, J. Appl. Crystallogr. 46 (2013) 153–164.
[21] J.-B. Marijon, (Ph.D. thesis), Ecole Nationale Supérieure d'Arts et Métiers, Paris, France, 2017.
[22] L. Reinbold, N. Jadhav, E. Chason, K.S. Kumar, J. Mater. Res. 24 (2009) 3583–3589. https://doi.org/10.1557/jmr.2009.0431.
[23] M.A. Ashworth, G.D. Wilcox, R.L. Higginson, R.J. Heath, C. Liu, R.J. Mortimer, Microelectron. Reliab. 55 (2015) 180–191. https://doi.org/10.1016/j.microrel.2014.10.005.
[24] O. Ulrich, X. Biquard, P. Bleuet, O. Geaymond, P. Gergaud, J. Micha, O. Robach, F. Rieutord, Rev. Sci. Instrum. 82 (2011) 033908. https://doi.org/10.1063/1.3555068.
[25] J.-S. Micha, LaueTools, Open Source Python Packages for X-ray MicroLaue Diffraction Analysis, 2017, https://sourceforge.net/projects/lauetools/.
[26] G.E. Ice, J.W. Pang, Mater. Charact. 60 (2009) 1191–1201.
[27] G.T. Sheng, C. Hu, W. Choi, K. Tu, Y. Bong, L. Nguyen, J. Appl. Phys. 92 (2002) 64–69.
[28] S.-K. Lin, Y. Yorikado, J. Jiang, K.-S. Kim, K. Suganuma, S.-W. Chen, M. Tsujimoto, I. Yanada, J. Electron. Mater. 36 (2007) 1732–1734.
[29] K. Kim, C. Yu, S. Han, K. Yang, J. Kim, Microelectron. Reliab. 48 (2008) 111–118.
[30] P. Sarobol, J. Blendell, C. Handwerker, Acta Mater. 61 (2013) 1991–2003.